Electrospray ion beam deposition and preparation of model molecular solar cells surfaces

Thesis submitted to the University of Nottingham for the degree of
Doctor of Philosophy, December 2022.

Nouf Alharbi

4309466

Supervised by

James O'Shea
Philip Moriarty

Abstract

Studying the fundamental science of surface science of dye-sensitised solar cells requires placing complex molecules on surfaces in an ultra-high vacuum. Since most dye molecules are fragile and non-volatile to be deposited by thermal evaporation or sublimation technique, electrospray deposition was therefore explored as an alternative method. This thesis aims to work on developing the electrospray deposition technique to obtain high-quality monolayers in situ in high vacuum environments.

Image charge detection mass spectrometry (CDMS) has been used to measure the speed and charge distributions of molecular ions. Image charge drift tube measurements formed large clusters giving strong transient signals with a narrow velocity distribution of cluster sizes ranging from 300 ms^{-1} and 330 ms^{-1}. The charge-to-speed relationship showed fitting with a $1/\text{v}^2$, meaning that all clusters have constant kinetic energy. In the case of the small clusters or individual molecular ions travelling through the drift tube, advanced electronics are required to see the weak signals hidden in the background noise.

The electrostatic ion deflector experiments, highlighting the capabilities of bending the ion beam in order to work towards separating two components of the beam, showed the formation of large clusters in the beam. These clusters have required a higher voltage in order to be deflected by the same amount based on SIMION simulations and a smooth range of charge distributions. Small molecular ions are worth studying in the future - via the discovery of low voltage range since these deflection experiments have concentrated on the high voltage regime.

In the second section, the XPS measurements of defocussing experiments showed an incapability of the Einzel lens to diverge the beam over a large area on the sample, especially when the SIMION simulation achieved this. As well as, the defocussing experiment using a long tube exhibited the success of the Einzel lens to spread the beam over the entire sample. In the last section, AFM and optical images displayed the deposition of graphene oxide successfully with heterogeneous deposition coverage across the surface.

Dye-sensitisers adsorbed onto rutile TiO_2 (110) were deposited in situ in UHV using electrospray deposition. Adsorption geometries and determining the dispersion of these molecules with this titanium surface were investigated using X-ray photoemission spectroscopy (XPS). The results of O 1*s* photoemission in the monolayer coverages showed that dye complexes bind onto TiO_2 (110) by deprotonation of the carboxylic acid and phosphonic acid groups so that their oxygen atoms bond to titanium atoms of the substrate. Photoemission of C 1*s*, together with N 1*s*, indicated that the molecule is intact on the surface.

List of Publications

The adsorption and XPS of triphenylamine-based organic dye molecules on rutile TiO_2 (110) prepared by UHV-compatible electrospray deposition.

Nouf Alharbi, Jack Hart, and James N. O'Shea, (in preparation/ Manuscript Draft).

Acknowledgements

First and foremost I would like to thank my supervisor, Dr. James O'Shea, for his continued support and encouragement throughout my Ph.D. Thanks also to my fellow PhD students Robert Temperton, Jack Hart, and my supervisor again, who have always been willing to discuss or explain to me the principles behind electrospray ionization and x-ray photoelectron spectroscopy techniques and how to apply them to avoid potential risks during the project implementation. I am also fortunate to have some friends who have always been my source of support abroad and spent a lot of quality time with them. In the end, I am very grateful to my entire family, especially, my parents for their love and moral support throughout my long time at university.

Abbreviations

AFM Atomic Force Microscopy.

BE Binding Energy.

CCD Charge-Coupled Device.

CRM Charge Residue Model.

DC Direct Current.

DLD Delay Line Detector.

DSSCs Dye Sensitised Solar Cells.

EP Pass Energy.

ES-IBD Electrospray Ion Beam Deposition.

ESI Electrospray Ionisation.

ESIMS Electrospray Ionisation Mass Spectrometry.

HOMO Highest Occupied Molecular Orbital.

IEM Ion Evaporation Model.

K-cell Knudsen-cell.

KE Kinetic Energy.

LUMO Lowest Unoccupied Molecular Orbital.

MCP Microchannel plate.

MF MicroFocus.

PE Potential Energy.

PES Photoemission Spectroscopy.

RF-DC Direct Current / Radio Frequency.

ToF Time of Flight.

UHV Ultra-High Vacuum.

XPS X-ray Photoelectron Spectroscopy.

Contents

List of Tables

List of Figures

Chapter 1

Dye-Sensitised Solar Cells

1.1 Introduction

Solar cells are devices that transform the energy of light from the sun into electricity via the photovoltaic effect, and therefore they are named photovoltaic cells. Electricity generated by means of solar cells is commonly employed rather alongside renewable energy sources like wind and hydroelectric, as well as pollution-producing non-renewables, such as oil, coal, gas and nuclear. In the early 1990s, dye-sensitised solar cells (DSSCs) received great interest until perovskite solar cells started to take over near 2010 [1]. However, DSSCs still have very promising properties, including low cost, colourful appearance, high power conversion systems, simple manufacture, high flexibility and semi-transparent quality [2–5]. They probably will not replace traditional silicon solar cells for rooftop installations, but they could be integrated into windows and glass facades. Brian O'Regan and Michael Grätzel, who manufactured TiO_2 electrodes from a colloidal solution of TiO_2 films, initially created the first DSSCs in 1991 [4, 6, 7]. This type of solar cell, commonly known as a Grätzel cell, is seen in Figure 1.1.

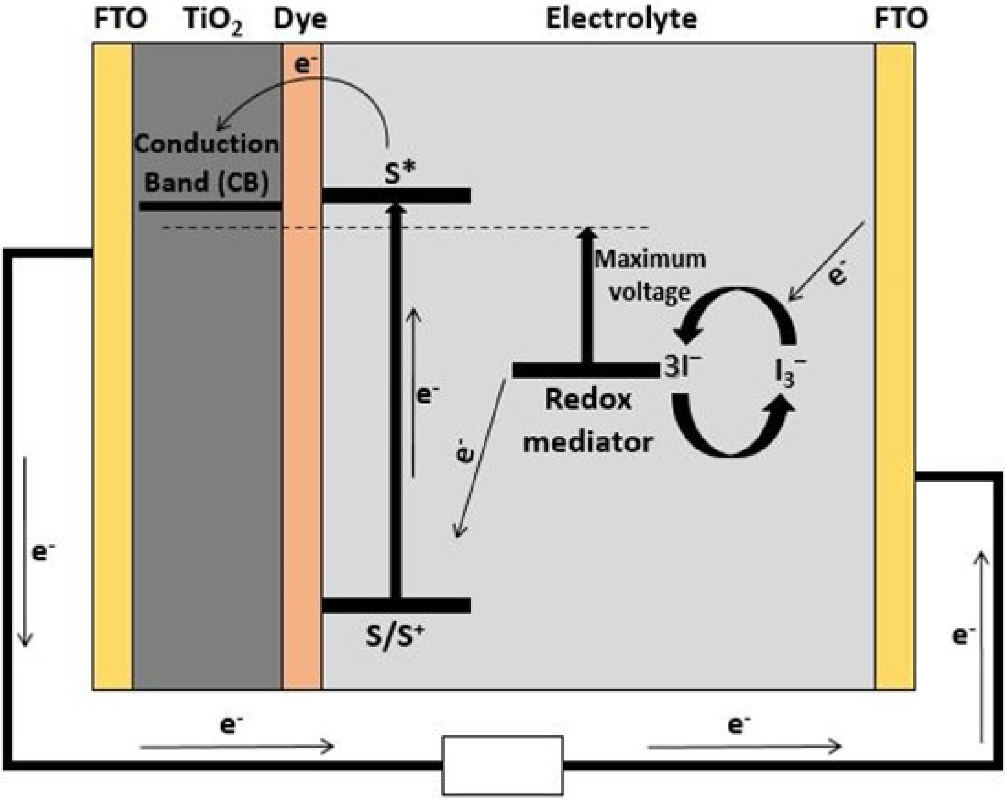

Fig. 1.1. A schematic diagram shows dye-sensitised solar cell working principle, as electron transfer is indicated with arrows. Maximum voltage is the difference between the redox potential of electrolyte and the semiconductor conduction band (TiO_2), allowing work to be carried out. The electrodes are transparent conducting glass plates manufactured of fluorine-doped tin oxide (FTO).

1.2 Operating Principle of the DSSCs

The operating principle of DSSCs is based on injecting electrons into the conduction band of titanium dioxide. The typical DSSC layout (as shown in Fig.1.1) involves the photon exciting an electron from the dye layer, transitioning the photosensitizer or dye responsible for absorbing light in the visible spectrum from its ground state (S) to an excited state (S^*) [6, 8]. The excited conduction band electron of the semiconductor is transferred into the TiO_2 state (S^+) given by the following relation [9]:

$$S^+ + e^- \rightarrow S \tag{1.1}$$

The electrons from TiO_2 flow into the counter electrode, which is usually made of platinum or carbon, via the external circuit and then move into the electrolyte (redox mediator such as I^-/I_3^-). The electrolyte carries electrons back to the dye molecules in order to regenerate the oxidised dye, which can be expressed as:

$$3I^- \rightarrow I_3^- + 2e^- \tag{1.2}$$

The tri-iodide, (I_3^-), is reduced again to iodide, (I^-), at the counter electrode, allowing the dye molecules to be regenerated in the same way [8], as follows

$$I_3^- + 2e^- \rightarrow 3I^- \tag{1.3}$$

In 1993, Nazeeruddin et al. [10] found the most extensively used dye molecule, N3, known as Ru 535, as seen in Figure 1.2. The use of the N3 at the TiO_2 surface produces a high cell efficiency of 11% [11]. According to O'Shea and his group's research, it has been demonstrated that N3 on the surface of TiO_2 is bonded by the carboxylic acid group of bi-isonicotinic acid ligands and the sulphur atom of thiocyanate ligands [12], while thiocyanate only bonded with the Au surface [13] and only the carboxylic group bonded with the aluminium oxide layer [14]. This dye molecule could not be deposited using the conventional evaporation technique due to its being large, fragile, non-volatile and thermally labile, which means that it breaks down with heat, so the electrospray deposition technique (discussed later in Chapter 2) is the best way to deposit it.

A lot of research had been done on bi-isonicotinic acid ligand that can be sublimed in the ultra-high vacuum (UHV) before these investigations. A rutile $TiO_2(110)$ single-crystal surface [15, 16] and anatase TiO_2 nanoparticles [17] were used in these investigations to determine the molecule bonding geometry to the

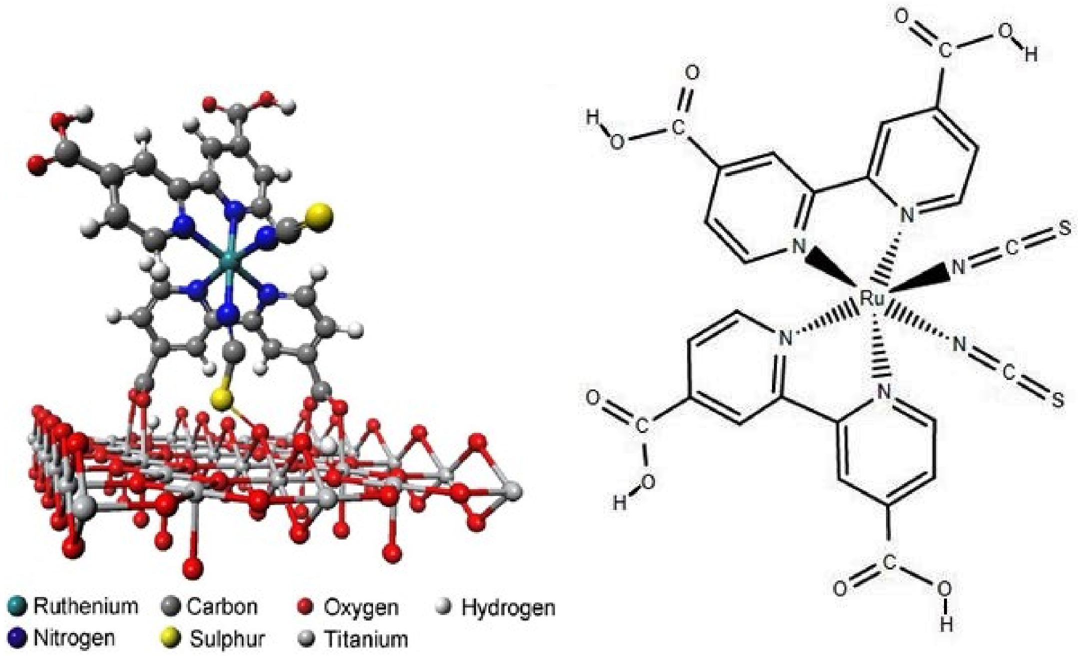

(a) **(b)**

Fig. 1.2. (a) N3 molecule adsorbed on rutile titanium dioxide TiO_2 (110), reproduced from [12], and (b) chemical structure of the N3 molecule cis-di(thiocyanato)bis(2,2'-bipyridyl-4,4'-dicarboxylate) ruthenium (II), reproduced from [6].

titanium dioxide surface. The study of charge transfer dynamics from molecule to the rutile surface showed that transmission happens in less than 3 fs [18]. The Au(111) surface has been studied in the same way. The scientists report that carboxylic acid groups are not bonded to the substrate. The charge is likely to be transferred between the molecule and a gold surface in both directions (i.e. from the molecular state to the single-crystal Au(111) and from the Fermi level of the metal into the lowest unoccupied molecular orbital (LUMO)) [19].

Many different dyes may be used as sensitisers in DSSCs; however, the most commercially used dye sensitisers are based on an N3 dye, such as N719 and N749. Compared with N3, N719 (often described as the industry standard dye) is the most frequently used high-performance dye because it dissolves more easily in polar solvents and enables increased cell voltage. Likewise, N749, known as a black dye, exhibits a wider spectrum absorption range and near-infrared photoresponse [20, 21]. N3 and RuP are dark purple powder-colored organometallic semiconductor sensitisers, and they contain ruthenium atoms, which are rare. Conversely, SQ2, RK1, D5, SC4 and R6 are examples of green-, red-, orange- and blue- coloured purely organic dyes that are less effective but have the benefit of being less expensive since they do not include rare earth elements. Transition-metal photosensitisers, namely copper (Cu) [22] and iron (Fe) [23, 24], are considered extremely interesting owing to their abundance, low cost and non-toxicity.

Although traditional organic solvent-based liquid electrolytes in DSSCs produce highly efficient cells, they have been replaced by other substances, such as polymers [25], that dissolve the iodine/iodide pair, binary ionic liquids, such as non-volatile and thermally steady electrolytes [26]; and hole-conducting solids (hole transporting materials), such as TPD (N,N'-Bis(3-methylphenyl)- N,N'-diphenylbenzidine) or spiro-TAD (2,2',7,7'-Tetrakis[N,N-di (4-methoxyphenyl) amino]-9,9'-spirobifluorene) [27–29], since they drain devices.

Organic solar cells use molecules other than dye molecules in the same context as DSSCs. Researchers have used Poly(3-hexylthiophene-2,5-diyl) (P3HT) and Phenyl-C61-butyric acid methyl ester (PCBM), respectively [30, 31], as candidates for organic solar cells, which can also be integrated into DSSCs due to their favorable properties. The charge transfers to the anode through the donor molecules (holes), whereas it transfers to the cathode through the acceptor molecules (electrons) [32]. C_{60}, called fullerene, is worth investigating further as a possible building component for future solar cell systems, as it was added in DSSCs between porphyrin molecules and TiO_2 to improve efficiency [33]. C_{60} is an electron acceptor that can be covalently linked to a porphyrin, an efficient photosensitiser for TiO_2, which acts as an electron donor [34–37]. Charge-separation occurs as a result of injecting the electron from the excited dye into the titanium dioxide semiconductor conduction band, which leads to enhanced energy conversion. Donor–acceptor-linked molecules interact with the TiO_2 substrate of the cell by COOH groups in the C_{60}, where the photoexcited electrons created by porphyrin are transmitted to the C_{60} and then to TiO_2 [33].

1.3 Aims of this Thesis

Pollution and climate change mean the need to stop burning fossil fuels like coal and gas and harnessing energy from the sun is much needed. The solar cell is not just for making electricity. It is also included in dye-sensitised photovoltaics and solar water splitting to generate hydrogen as a fuel for transport and to convert to electricity in fuel cells. The overall aim of this project is to find low-cost, simple ways to filter and manipulate an electrospray beam to control to some extent what lands on the surface. The premise of the approach is by accelerating the ions all to the same speed, then their kinetic energy will be determined by their mass. So, electrostatic deflection plates can be used to bend the beam into a radius that will be inversely proportional to its mass and therefore, filter it accordingly.

1.4 Scheme of the Thesis

This thesis is organised as follows:

Chapter 1 is intended to provide insights into the study of DSSCs to understand the behavior of this system, considered an effective alternative to provide energy from the sun. The research aims and structure of the thesis are also covered.

Chapter 2 presents a brief background of electrospray, where the characterisation and development of the UHV electrospray deposition technique are necessary steps in studying fragile and complex molecules. This includes depositing a wide range of complex molecules that cannot be deposited using traditional thermal evaporation/sublimation techniques.

Chapter 3 describes key experimental methods and some background used in this thesis including X-ray photoelectron spectroscopy (XPS) and atomic force microscopy (AFM) devices. The SIMION simulation required to implement these methods is also presented.

Chapter 4 aims to understand electrospray by investigating an image charge detection spectrometer to determine ions' speed distribution using a high-speed amplifier to measure the charge of ions' image to determine how fast the molecules are going and whether all the ions can reach the same speed.

Chapter 5 presents the filtering of molecules by their kinetic energy using electrostatic ion deflection plates that facilitate the deviation of the ions beam. The ion optics is applied to explore defocusing within the Einzel lens using sodium chloride (NaCl) solution with XPS measurements. AFM is used to analyse the morphology of graphene oxide films.

Chapter 6 investigates the study of the adsorption of dye molecules such as N3, RuP, D5, SC4 and R6 onto a TiO_2 surface using a unique combination of electrospray deposition systems to form thin films of dye molecules on the surface and in situ XPS to investigate the bonding geometry and chemical interaction.

Chapter 7 gives a brief summary of the research work carried out in this thesis and presents suggestions for future work.

Chapter 2

Fundamental Concepts of Electrospray Ionisation

2.1 Introduction to Electrospray Ionisation

Electrospray ionisation (ESI) is considered the most common method of ionisation used in analytical chemistry. A wide range of analytes may be studied with it, including inorganic ions, ionised polymers, nucleic acids, peptides and proteins. The analytes existing in the electrospray solution may be ions or compounds not ionised [38]. ESI is a process that uses a liquid solution to produce a flow of small droplets charged by the electric field. The main point of this system lies in applying a high voltage between a capillary needle tip and a target. The physics behind the electrospray is derived from Rayleigh's theoretical studies [39], which studied the physics of isolated charged droplets. During the period between 1914 and 1917, Zeleny published three articles describing multi-jet modes utilising a mechanism comparable to current electrospray systems [40–42].

In 1968, Dole et al. [43] predicted that a beam of large molecules would be generated by ESI, but they could not provide convincing experiments to support this prediction. Fenn et al. proved definitively in 1988 that large molecules such as proteins could be transferred using a quadrupole mass spectrometer into gas-phase molecular ions without breaking them apart [44, 45]. Fenn was awarded the Nobel Prize for the development of ESI mass spectrometry (ESIMS) analyses of biological macromolecules in chemistry in 2002 [46]. In 1992, Fenn first discovered that ESIMS, which is still in use today, could generate up to five million ions with vast multiple charges [47]. The basic ESI mechanism is demonstrated in the schematic illustrations of Figure 2.1. This mechanism indicates a liquid passing through an electrospray emitter capillary with a high voltage of 2 – 4 kV applied to it and the entrance capillary is at a distance of about 2 – 5 mm from the emitter capillary exit.

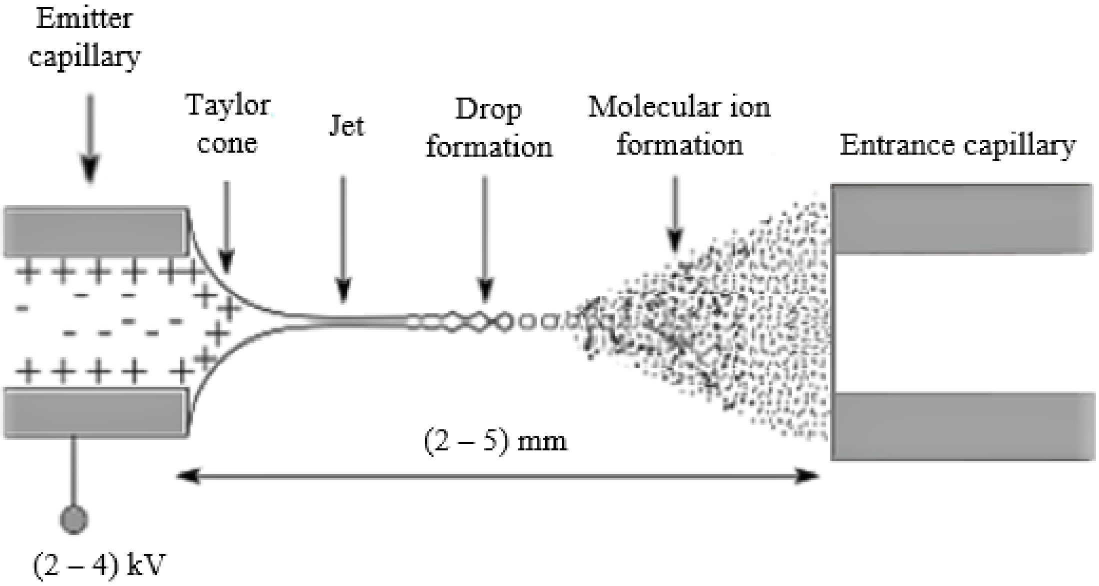

Fig. 2.1. Electrospray ionisation mechanism experiment. The liquid passes via the capillary tube that is placed (2 – 5) mm away from the entrance capillary. A large voltage (2 – 4) kV was applied to a liquid causing to form a Taylor cone, divided into a jet and emits a mist of droplets. Image modified from [6].

2.1.1 Taylor Cone-Jet Formation

The main first step of the ESI process is molecular ion formation by spraying liquid that exits the emitter capillary. Using a large electric field disintegrates charged droplets, leading to aerosol formation. Surface tension and electrostatic coulomb are dominating forces on the liquid. The surface tension returns the liquid into the capillary in order to minimise the surface area, while the electrostatic forces pull the liquid to the counter electrode. The liquid is formed into an elliptic shape when lower voltages are applied to the liquid that is held inside the capillary. At a certain voltage, the elliptic shape suddenly changes to a sharp cone called a Taylor cone. In 1964, Taylor showed that at all points of its surface, a balance of surface tension and electrostatic forces can be achieved at an angle of 49.3° [48].

The Taylor cone is inherently unstable because it tends to be infinitely sharp due to the apex of the cone and the electric field at the tip constituting a singularity. A charged liquid jet is expelled from the Taylor cone tip by the strong electric field, as seen in the Figure 2.1. Repulsion of the surplus of charged ions existing on the jet's surface makes the jet split into a series of newly generated droplets that are charged near the theoretical Rayleigh limit. The maximum charge for the droplet before the fission process is given by:

$$Q = 8\pi(\epsilon\gamma R^3)^{\frac{1}{2}} \tag{2.1}$$

where Q is droplet charge at the Rayleigh limit of radius R; ϵ is electric permittivity; and γ is the liquid surface tension. This expression demonstrates the main concept of transforming charged droplets into molecular ions, which is that multiple smaller drops are more stable than one big drop [49].

The jet mode at the tip of the needle is formed based on the solution properties and the process conditions, such as needle size, distance, flow rate and applied voltage [50]. Figure 2.2 shows different cone-jet modes created by electrospray. The spray mode in ESI goes through three stages: from the dripping stage into multi-jet and ultimately to cone-jet. The cone-jet mode is regarded as the best due to the stability of the liquid jet [51]. Dripping and spindle modes may occur because of a high-viscosity solution, which may block the needle or entrance capillary. Additionally, dripping generally takes place at low-liquid flow rates as opposed to the spindle that happens at high flow rates [52]. Moreover, low surface tension and high viscosity led to multi-jet and precession modes [53], but the oscillating mode appears as a result of the increase in surface tension and viscosity.

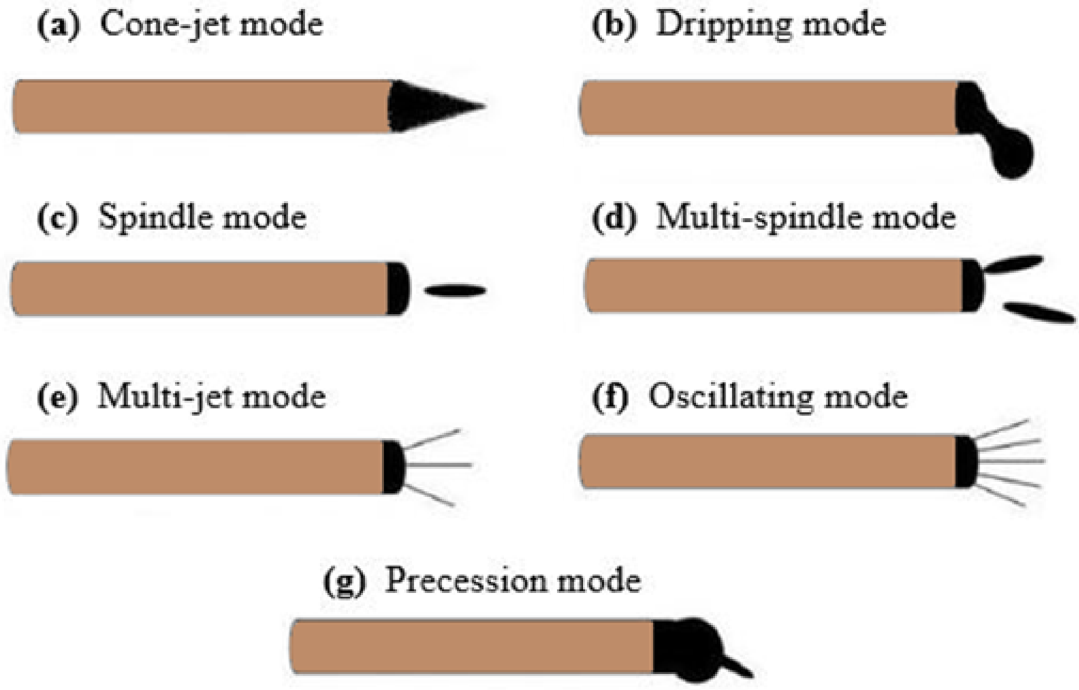

Fig. 2.2. (a-g) Subsequent frames showing different cone-jet modes through electrospray system. Image adapted from [54].

2.1.2 Gas-Phase Ions Production

Two models for the generation of gas-phase molecular ions from small and large charged droplets in the ESI process have been proposed: the ion evaporation model (IEM) and charged residue model (CRM), shown in Figure 2.3 [38, 45]. Iribarne and Thomson [55, 56] established the IEM in the 1970s to illustrate how a spray atomiser generated atomic ions from charged droplets. IEM usually applies to species with low molecular weight and works when the radius of droplets decreases below 10 nm, whereas the electric field at the drop surface is sufficiently large to eject a small ion from the surface [45].

The CRM is applicable for very large macromolecular species ions above 1,000 Dalton (Da), such as proteins. Droplets containing only one analytical molecule according to the CRM are generated by the electrospray mechanism. The electrospray system breaks up the droplets where solvent evaporation leads to shrinkage, increasing the charge on the surface towards the Rayleigh limit, and the emission of the Taylor cone expels charged liquid from the origin drop. The solvent of the final droplet evaporates after many cycles in CRM to generate analyte ions in the gas phase [45]. According to some studies, the CRM is a poor description of the process for long-chain and non-spherical molecules, which have larger and wider distributions of charge than the CRM would predict [57].

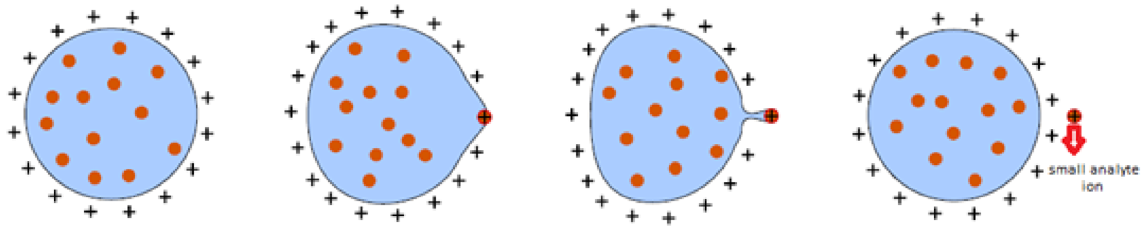

(a) Ion Evaporation Model (IEM)

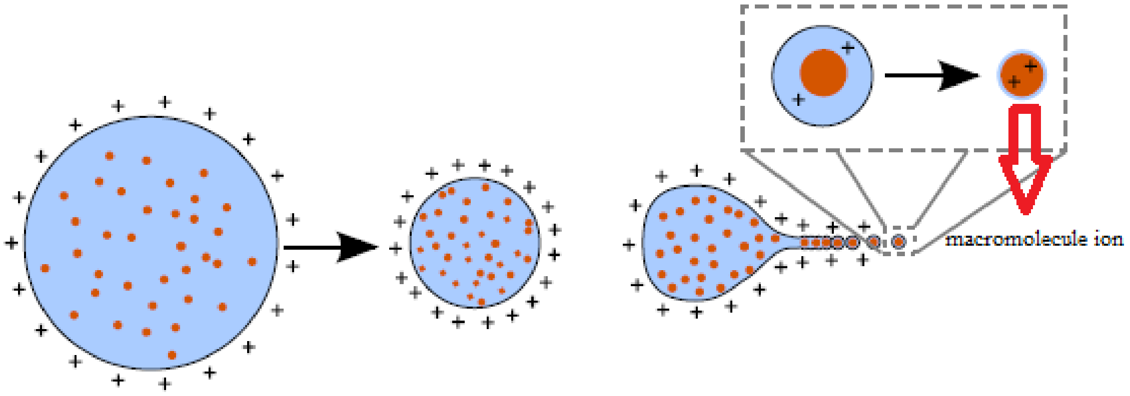

(b) Charge Residue Model (CRM)

Fig. 2.3. Two mechanisms for molecular ions generation from charge droplets. (a) IEM: Small analyte ion ejection from a charged nanodroplet. (b) CRM: Release of a globular protein ion into the gas phase. Figure reproduced from [6].

2.2 Electrospray Deposition

The first common application was discovered by ESI use as a source of mass spectrometry. Mass spectrometry is based on converting highly non-volatile analytes, such as biological molecules, into ions in a vacuum and measuring their path reactions to electric and magnetic fields [44]. Another advantage of ESIMS is the enabling of a chemical analysis of molecular species directly in the solution [58]. ESI is currently utilised as suitable source of deposition appropriate with an ambient and UHV by using a substrate as the counter electrode. In the case of vacuum, the counter electrode is the entrance. Vacuum deposition is based on comparable instruments with applications for mass spectroscopy through minimising the pressure until it reaches the high-vacuum environments required using a group from pumped chambers. Also, it has been commonly used to produce an ion beam from a solution comprising molecules to be deposited.

Electrospray ion beam deposition (ES-IBD) is a more efficient way to deposit big molecules instead of the conventional approach, which depends on converting molecules from a solid or liquid state to a gaseous state, called sublimation or thermal evaporation. If the molecule is big, the temperature needed to sublimate or evaporate it will be higher, where raising the temperature leads to the destruction of the molecule before converting it to the gas phase.

In this thesis, a standard basic electrospray deposition source was introduced, which demonstrated remarkable capability to overcome the vapour deposition difficulties for large organic biological molecules or inorganic clusters. During the electrospray deposition process, as shown in Figure 2.4 , the solution passes into the emitter capillary (needle) and then applies 2 kV and drives the liquid into the entrance capillary followed by three pumping vacuum stages separated by skimmer cones. Compared with many of the developed electrospray deposition instruments, this machine is characterised as easy to operate, low cost, small and portable.

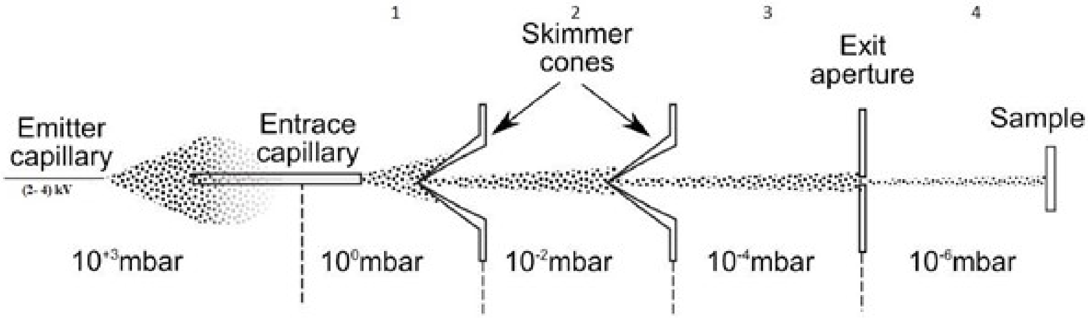

Fig. 2.4. Schematic of the vacuum electrospray deposition system showing the solution enters through a capillary and a series of differentially pumped skimmer cones minimizes the pressure at all stages. Figure reproduced from [59].

The electrospray method generally occurs in the air, and thus the spray moves to a lower pressure chamber for analysis. In fact, many materials can be deposited using electrospray deposition depending on the availability of appropriate solvents. Ku and Kim [60–62] found that the solutions with low viscosity, such as water and methanol, are perfect solvents for spraying in a vacuum as compared with high-viscosity solutions, such as glycerol. Moreover, scientists have attempted to overcome the freezing of organic solvents at the tip of the capillary emitter during low pressure and high evaporation by heating the tip.

2.2.1 Vacuum interface

Electrospray vacuum ionisation is performed through differential pumping, beginning from a capillary inlet. A capillary tube with a 0.25 mm inner diameter and length of 5 cm transfers the ions into a vacuum chamber. It is important to use a capillary because it reduces the amount of gas leaking into the chamber, and the amount of pumping, in order to obtain a sensible pressure in the chamber compared with a pinhole or a skimmer cone. Further modifications can be made to the entrance capillary, including forming the capillary with a funnel-shaped inlet, but this was not feasible during this project. The funnel-shaped inlet is used to develop nanoelectrospray capillary vacuum interfaces. The hydrodynamic flow will collimate the ion cloud and minimise the space charge expansion because of the axial acceleration of the ions. The funnel design produces a huge volume of high speed, allowing for efficient sampling. Moreover, vacuum transmittance can reach 100% of the ions created by the electrospray and, thus, can be transmitted to the vacuum through a funnel capillary, which transfers higher currents compared with an inlet capillary (a non-funnelled capillary) [63].

The ions and gas are subject to free jet expansion when they leave the entrance capillary and proceed into the first stage of the vacuum where they move more quickly, equal to the sound speed (Mach number M=1) at the capillary exit and supersonic speeds towards M>1, as shown in Figure 2.5. Gas is being expanded to such an extent that the particles no longer collide because of increasing speed and decreasing density, which is known as a quitting surface [64].

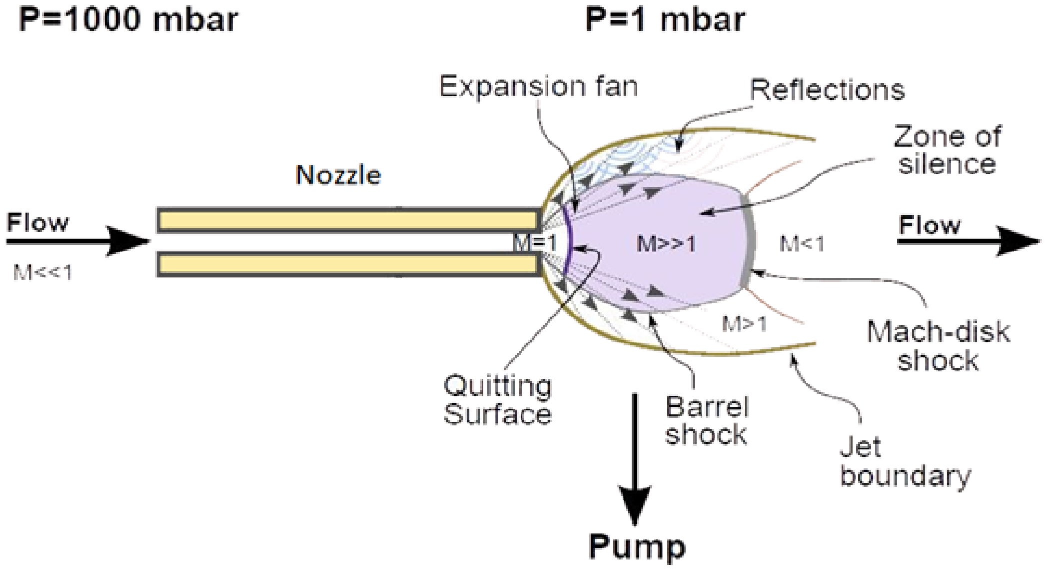

Fig. 2.5. A typical free-jet expansion. The beam's thermodynamic characteristics are constant between quitting surface and zone of silence (shown in purple) where samples are taken from the molecular ions. Figure reproduced from [6].

Reducing the region of cross-sectional expansion and increasing the pressure leads to the so-called Mach disc. The position of the Mach disc can be analytically described by the following equation [64]:

$$x \approx 0.67d\sqrt{\frac{P_{\text{ambient}}}{P_{\text{vacuum}}}} \tag{2.2}$$

where x is the distance, d is the capillary diameter and $P_{ambient}$ and P_{vacuum} are the system's pressures.

Barrel shock is caused at the capillary exit by forming a sequence of waves that propagate outward and reflect off the jet boundary causing gas recompression. The region outside the quitting surface and inside barrel shock is called the zone of silence, where the gas is completely unaffected by any exterior impacts. The expansion implies that the particles flow in one direction, and thus, collisions are less likely. A skimmer cone is inserted into the silence zone to sample the ions in order to reduce disturbances and other unwanted flows. Perhaps inserting the skimmer cone will change the shape of the Mach disc [65].

2.2.2 Applications

The electrospray technique offers a quite promising method for depositing a wide range of complex molecules in an UHV as dye sensitisers, nanoparticles, polymers, biological molecules and high-energy chemistry. These molecules will be discussed in more detail below.

2.2.2.1 Dye Sensitisers

O'Shea's group has developed an electrospray deposition device to investigate the 'N3' sensitiser dye sprayed on rutile titanium dioxide surface ($TiO_2(110)$). In 2008, XPS was used to study bonding/interaction sites and charge transfer dynamics between molecules with this surface [12]. Moreover, N3 on anatase surfaces has been studied using scanning tunneling microscopy (STM) and spectroscopy [66]. In the case of adsorption of N3 dye on the Au(111) surface, researchers have not only looked at molecules' ligands but have also studied charge transfer dynamics. They observed that only the sulphur in these compounds forms an effective connection with N3 [13] and that charge transfer from molecule into the surface was ultra-fast [67]. In the same way, the bonding and charge transfer of an ultra-thin aluminium oxide layer into a NiAl(110) was studied [14]. Dye molecules for photocatalytic water splitting [68–71] and photovoltaic dye molecules, such as zinc protoporphyrins [72], have also been studied using the electrospray system.

2.2.2.2 Nanoparticles and Macromolecules

Electrospray deposition experiments focused on the production of solid collagen nanoparticles, where spraying collagen led to the formation of nanofibers [73]. Some electrospray deposition studies were also conducted on fullerenes [74] and carbon-based nanomaterial (carbon nanotubes) [75]. Electrospray deposition source in situ is suitable for giant porphyrin nanorings, as discussed in some literature [76–80], single-molecule magnets [81–85] and clusters [86]. Moreover, scientists have been interested in depositing polymers by electrospray mechanism in the form of simple chains, such as poly(ethylene) oxide [60], and complex ones, such as porphyrins [87]. A blend of P3HT and PCBM are commonly used in polymer-fullerene bulk heterojunction solar cells prepared by electrospray deposition as well [88].

2.2.2.3 Biological Molecules

Novel advances in UHV deposition methods have introduced new potential applications in biotechnology to deposit large biological molecules such as peptides [89] and proteins without affecting their activity or functional properties [59, 90]. Unfortunately, it is difficult for researchers to obtain high-resolution scanning microscopy images of individual protein molecules by STM because of the proteins' incompatibility with the vacuum environment [91, 92]. However, the ES-IBD of unfolded proteins allows for controlling their conformation by changing the deposition energy [93].

2.2.2.4 High Energy Chemistry

According to results from STM and spectroscopy, UHV ESI of N3 dye on Au(111) does not break down at kinetic energy lower than 2.5 eV, but fragmentation begins when the impact energy is ∼7eV per molecule. Consequently, it is necessary to optimise the ion kinetic energy in order to prevent fragmentation throughout the deposition process [94]. As for the molecules less susceptible to fragmentation, functionalisation of graphene was employed via hyperthermal molecular reaction with azopyridyl groups by the collision of azopyridinium ions onto the surface at considerably high energy. According to XPS and Raman spectra, a 3% degree of the carbon atoms in graphene was highly functionalised, whereas AFM observations showed that chemical vapour-deposited graphene retained its topographic characteristics after exposure to azopyridinium [95]. In electrospray studies presented in Chapter 6 of this thesis, no fragmentation of the molecules is observed. For example, all the N3 data suggest that the molecule is completely intact and it has not fragmented since there is not enough energy to break it apart (where the kinetic energy is 0.34 eV).

Chapter 3

Instrumental Techniques and Methods

3.1 Surface Cleaning

The surfaces in UHV are often cleaned by argon sputtering, where the beam energy is between 500 eV up to 4 KeV per ion. This creates defects on the surface and then the surface usually needs to be restructured, which is achieved by heating it typically above 600℃. At various stages, the surface cleanliness is verified using XPS (see section 3.4). The series of sputter and anneal cycles with Ar^+ions is different for every material. For example, to clean titanium dioxide, a 2 kV followed by 1 kV and annealing up to 600℃ have been used.

3.2 Ultra High Vacuum (UHV) Pumps

For accurate measurements of the desired properties, the experiments must be operated in a UHV environment, which ensures that contaminants do not interfere with measurements and that any extra particles in the system are removed after deposition as well. Scroll pumps, often called dry-scroll pumps and commercially available from companies such as Edwards, are needed to reduce the system pressure from atmospheric pressure of 1,000 mbar down to 10^{-2} mbar. Scroll pumps are capable of compressing the air inside the pump chamber to the atmosphere, allowing for the removal of large volumes of gas. These pumps are used to avoid backstreaming of pump oil (used in rotary vein pumps) into the system. This is especially substantial in this project, as a molecular beam of molecules is formed to deposit on the surface, so we do not want oil vapour to be part of the deposition.

In addition to rotary pumps, there are turbomolecular vacuum pumps that can also be used to reduce the pressure of a high vacuum to a UHV between 10^{-3} and 10^{-9} mbar by spinning rotor blades. The working principle of this pump is that a series of rotary blades transport the molecules through the system, and they are expelled from the system by hitting the underside of these blades. The pump comprises stator blades that are used to assure that only molecules moving in the right direction are allowed to progress to the next stage and eventually the backing pump.

An ion gauge measures vacuum pressure by attracting electrons from a heated cathode to an anode with a direct current (DC) potential of approximately 150V. The XPS system uses the hot filament ion gauge. Most of the electrons are transmitted through the mesh, whilst some of them collide with the remaining gas-forming ions. Increasing the negative voltage on the collector, which is generally –30V, causes the gas ions to accelerate in the direction of the central ion collector. The ion current amplifier is commonly used to provide measurements of the gas pressure in the high vacuum range. A cold cathode gauge is engaged in the electrospray system of this project due to the pressure range in the two turbopumped electrospray stages not being low enough. The working principle of a cold cathode gauge is that the ionisation results from the electron plasma created by the random release of an electron at the cathode where the discharge is carried out slowly by applying a DC high voltage. The electrons move quickly in a cycloidal way around the anode, where they have enough energy to ionise gas molecules. The slow ions are captured by the cathode, and the discharge ion current is used for pressure measurements. The cold cathode gauge is considered less accurate than the hot cathode gauge but more robust where it does not use hot filament and works perfectly to achieve stable pressure measurement from high vacuum to UHV. The absence of hot filaments releases less outgassing compared to the hot cathode gauges.

3.3 Deposition Methods

3.3.1 Thermal Evaporation/ Molecular Beam Deposition

It is possible to sublimate many small molecules from sources of vaporisation, such as Knudsen cells (K-cells), which are considered one of the most commonly used techniques for molecular deposition on surfaces in UHV environment [96, 97]. Typically, in this method, the substance for deposition is placed in a crucible heated by a current-operated filament heater. The temperature of the material can be measured using a thermocouple connected to the K-cell, supposing that the solid molecule is generally a powder and it has been fully degassed. Throughout this process, a limited increase in chamber pressure should occur due to the molecules usually tending to remain where they land. Thus, it is necessary to have a direct line of sight between the source and the sample by heating at the sublimation temperature of molecules. Heating facilitates the molecules along a straight line towards the substrate surface. Sublimation deposition is popular because it allows for precise control of the deposition rate. This method enables the production of a uniform layer over a wide surface of the substrate. The deposition time and the K-cell's temperature are two important factors that affect the amount of chemical deposition. Thermal evaporation is not suitable for large molecules, which has motivated the development of UHV-compatible ESD. The most previously studied example for comparison of sublimation and electrospray is C_{60} onto Au(111) by Satterley et al. [98]. The results for the UHV-ESD of C_{60} show that it is possible to deposit molecules onto a hydrogen-bonded supramolecular network. The STM images show that heptamers and C_{60} dimers might be trapped in the hexagonal and parallelogram network pore almost as if they were thermally evaporated. It is also noticed in this study that there is some reorganisation of the underlying network because of the residual solvent.

3.3.2 Ultra-High Vacuum Electrospray Deposition

The disadvantage of using a molecular beam deposition method is that the intramolecular binding energies are lower than the sublimation and dissociation energy, as is the situation for large molecules [99]. The appropriate alternative to deposit large molecules, which will be addressed here, is UHV-ESD, which can be found in the literature [74, 86, 100, 101]. The simplest electrospray deposition system, used in this thesis, is based on a very similar configuration to the commercially available Molecularspray system developed in Nottingham, and will be discussed later in this context. This technique has achieved great success, allowing the study of non-volatile and complex molecules using UHV techniques from STM to synchrotrons [12, 13, 67–70, 72, 74, 75, 81, 98, 102].

The ESI interface creates the ion beam and carries it out to the first stage of the differentially pumped system (discussed in more detail in Section 2.1.1). As shown in Figure 3.1, this interface was built using PEEK (PolyEtherEtherKetone) microfluidic parts that supply liquid feed from a glass syringe pump used to control the liquid flow and an electrical potential attached in a T junction, which applied the high voltage to the liquid to deliver it to the emitter capillary where ions were generated. The emitter was placed a few millimeters away from the inlet capillary, and the T junction was mounted on a three-axis manipulator to control its position as the perfectly aligned emitter and inlet capillary. A flow rate of approximately 0.3 mL/hr and a large voltage (2–4 kV) were usually used.

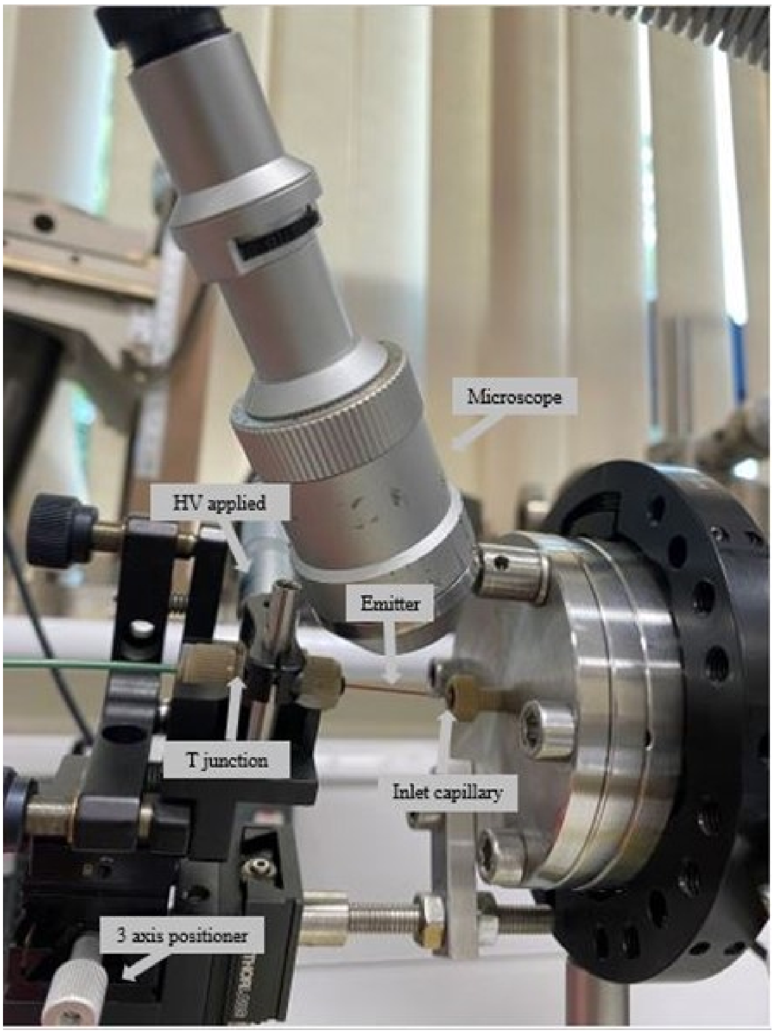

Fig. 3.1. Photograph showing the key components of the electrospray ionization source interface.

As shown in the schematic diagram in Figure 3.2, the electrospray system enables the pressure to be lowered through a series of differentially pumped chambers from the atmospheric pressure to 10^{-6} mbar in the deposition chamber. The electrospray system has a capillary tube with an inner and outer diameter of 0.25 mm and 1.6 mm, respectively, and a length of 5-cm stainless steel. A heater has been used around the inlet capillary to help desolvation of the droplets. Electrospray occurs in ambient gas, and it is common in almost all electrospray deposition sources worldwide [86, 101]. The only exception is in Swarbrick's paper, in which deposited carbon nanotubes using electrospray deposition in a vacuum was carried out by the O'Shea group in Nottingham [75]. The drawback of this method is that the electrospray solution could freeze and block the capillary, so almost all ESI takes place at ambient pressure. Some studies applied an extractor ring underneath the emitter capillary in order to steady the spraying process [103–106].

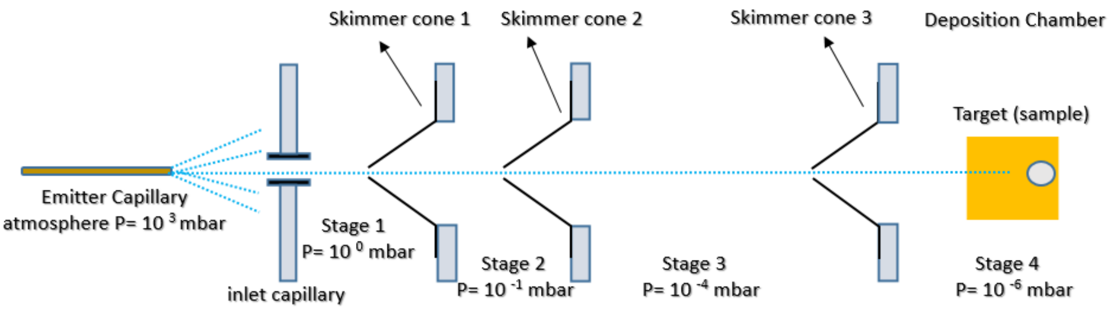

Fig. 3.2. Schematic drawing of the electrospray deposition process that shows the liquid passing through the entrance capillary and a group of differentially pumped at all stages into the deposition chamber to be deposited on the surface.

In this work, three skimmer cones with aperture diameters of 0.4 mm, 0.6 mm and 0.6 mm, respectively, were placed to four separate differentially pumped stages (two roughing pumps and two turbomolecular pumps). Vacuum stages 1 and 2 are pumped by a dry-scroll pump to a pressure of 1 mbar in the first stage, and the second stage achieves a pressure of 0.1 mbar. The third and fourth chambers are pumped by turbomolecular pumps, allowing the pressure to decrease from 10^{-4} mbar in the third chamber to 10^{-6} mbar range in the fourth chamber, which provides a pressure of roughly 10^{-6} mbar in the chamber where the deposition sample is held. It is worth noting that when the source is coupled to a preparation chamber with a larger pumping capacity, the deposition pressure can be reduced to the 10^{-8} mbar range.

Some systems placed an ion funnel between the entrance capillary and the first skimmer. The ion funnel consists of spaced ring electrodes that gradually decrease in internal diameter whilst working to restrict the ions radially (see Figure 3.3) [107]. The ion funnel compresses the beam into a smaller diameter so that more of it passes through the skimmer cone. The disadvantage of this instrument is that it is quite big and has to be used in a large tube relation. The ion funnel cannot insert into the skimmer cone; therefore, skimmer cones have been chosen as a way to overcome the complexity of the ion funnel. The other disadvantage is that the control electronics are complex and expensive.

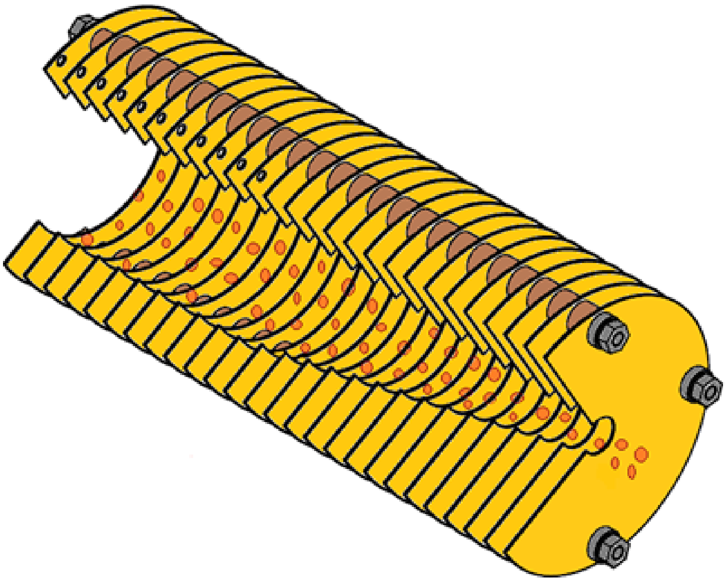

Fig. 3.3. Schematic of the ion funnel showing ring electrodes and the direction of the ion diffusion.

Deposition time differs depending on the desired film thickness. Monolayer coverage was accomplished after approximately 20 minutes, whereas multilayer coverage occurred after several hours. The deposition was observed by keeping an eye on the changes in the pressure of the deposition chamber or through the immediate measuring of the sample drain current. Two deposition approaches were carried out in this thesis: an electrospray rig and by attaching the electrospray to the XPS chamber. In the first approach, the sample is transferred ex situ from an electrospray rig and introduced into the XPS via a load-lock to study bonding/interaction sites on the surface. The sample here may be susceptible to contamination from the air. However, an advantage of using this method is the possibility of depositing a lot of materials, thus focusing only on XPS measurements. In the other approach, the deposition onto the surface takes place in situ inside the XPS, where the sample only has to be moved a little bit to move from the deposition spot to the analysis spot (a few mm), so the sample is never exposed to the atmosphere. The disadvantage of using this approach is that it is more time-consuming because the same system is used to conduct the deposition, therefore it is impossible to take any measurements.

A solvent such as isopropanol was utilised to clean the entrance capillary to unblock clogging due to the high liquid concentration, so dilute solutions that have concentrations beneath 0.1% (w.t.) can be used instead. A broad variety of molecules from different solvents can be deposited, such as methanol, ethanol, tetrahydrofuran, water (with 10% methanol added), acetone, toluene (with 10% methanol added) and chlorobenzene (with 10% methanol or acetone added). There is a wide range of molecules that have been deposited by electrospray deposition from various solvent mixtures, for example, C_{60} from toluene/acetonitrile [98], N3 from 200 ml of 3(methanol):1(water) mixture [12, 13], ∼1 mg of single-molecule magnet in 10 ml of pure methanol [81], zinc protoporphyrin from 10 ml of 1:1 methanol/toluene mixture [72], graphene oxide from propylene glycol methylether acetate, acetone, ethanol [108] and sodium chloride (NaCl) from water/methanol/acetic acid [109].

3.4 Photoemission Spectroscopy

In 1887, Hertz [110] studied how light interacts with electrons when he discovered that exposure of zinc to ultraviolet radiation causes it to lose its negative charge. Experiments conducted in the late nineteenth century revealed that shining light on a metal surface enabled the emission of electrons. Einstein analysed this phenomenon, known as the photoelectric effect, in 1905 [111] using plank's equation of the black body radiation, for which he was awarded the Nobel Prize in 1921. The photoelectric effect contributed to the development of photoelectron spectroscopy, which has been used to investigate chemical interactions and charge transfer dynamics between molecules and surfaces.

The photoionisation process of electrons may only occur if the photon source has high energy. Photoemission spectroscopy (PES) probes the energy distribution of occupied states of atoms by measuring the photoionisation process. The energy level diagram of these states is shown in Figure 3.4.

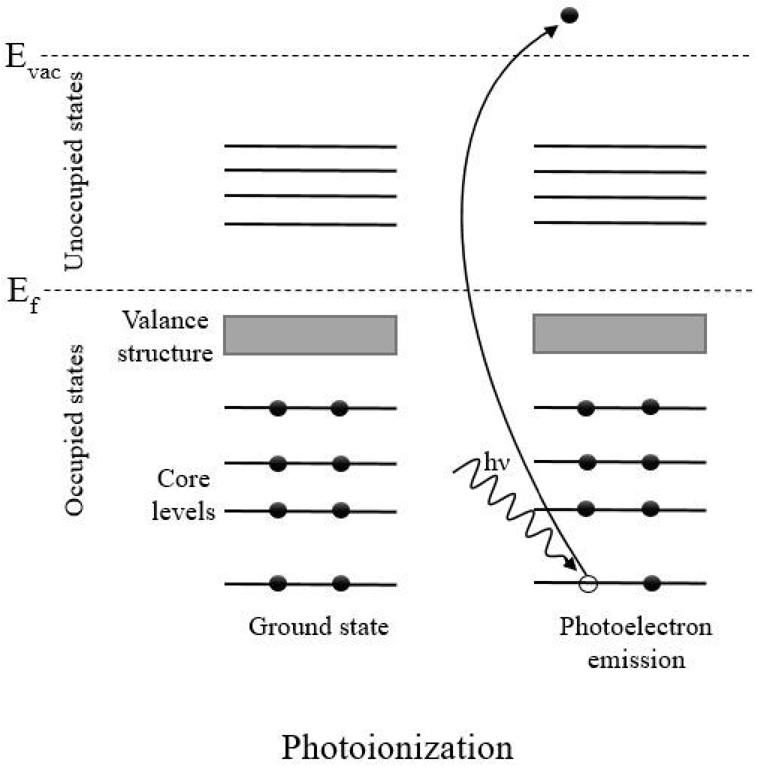

Fig. 3.4. Energy level diagram showing the ground state where the molecule absorbs a photon with energy hν. This energy is transmitted to an electron in the form of a photoelectron.

3.4.1 Uses of Photoemission Spectroscopy

The PES technique, also known as photoelectron spectroscopy, is widely used for measuring the binding energy of electrons in atoms and molecules. Scientists often use PES to identify chemical composition, studying surface contamination, organic layers, catalysis and corrosion. This method might be used for identifying the ingredients in a historical artefact, such as a painting, which may reveal the kind of paint used and, consequently, the period and place of the artwork's creation.

Additionally, PES may reveal the chemical states of atoms bound together. The electrons of atoms can form stronger and more energetic bonds by sharing with other atoms. But, as a result of this, a simple shift of electrons occurs in the binding energy, which can be discovered by measuring the binding energy of the electrons. For instance, it has been proven that positively charged atoms lead to shifting electrons' binding energy to higher values, which is coupled with a rise in the coulombic attraction between the electrons and the nucleus.

In this work, PES is used to ensure that the surface is free from contaminants after the sputtering and annealing process and before depositing molecules. More importantly, it determines the chemical states of the atoms in the dye molecules adsorbed on a crystal surface, such as the rutile $TiO_2(110)$, having been used in the Chapter 6 experiments to study their bonding.

3.4.2 X-ray Photoelectron Spectroscopy

XPS is one of the most frequently applied methods for analysing the chemistry of the surface of the material. It also measures the electronic state of the atoms, as well as their kinetic energy. The photoelectric effect, in which electrons are emitted from the substance as a consequence of the absorption of photons, is the fundamental mechanism underpinning PES. The photoionised electrons' kinetic energy is given by:

$$E_{\mathrm{K}} = hv - \phi - E_{\mathrm{B}} \tag{3.1}$$

where hν is the energy of the absorbed photon. Each electron has a specific ionisation potential required to remove it from the atom or molecule. The ionisation potential has been divided into binding energy, E_B, of the excited electron with respect to the Fermi level and the work function, ϕ, of the material required to transfer electrons from the Fermi level to the vacuum level. The basic concept of these levels and energies is shown schematically in Figure 3.5.

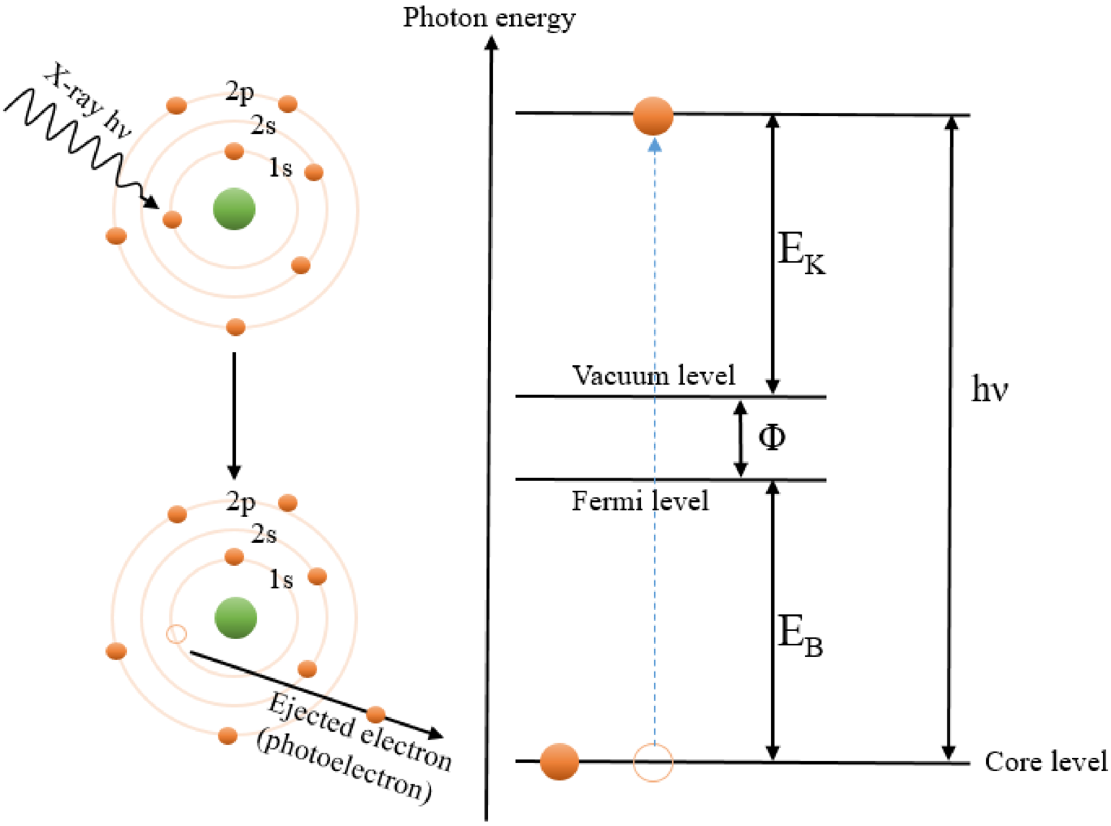

Fig. 3.5. Schematic energy levels diagram for spectrometer showing removal of a core level electron during an XPS experiment.

The Fermi level can be considered the energy level of an electron at which it has a 50% probability of being occupied. The Fermi level of metals tends to be located above the highest occupied electronic level. However, for insulators and semiconductors, it tends to be in the centre of the bandgap, whereas doped semiconductors move nearer to the conduction band or the valence band depending on the carrier's charged dopant. For example, in the case of TiO_2, the natural dopant is oxygen vacancies, which makes it n-type, and therefore, the Fermi level is usually very close to the conduction band edge.

The vacuum level refers to the energy level of a free-electron far enough away from neighbouring particles that it is at rest with zero kinetic energy. Any additional energy gained by the electron would be in the form of kinetic energy, which enables the electron to transmit through the vacuum and then be positioned above the vacuum level. The unoccupied and bound electronic state lies between the Fermi and the vacuum levels [112].

Electrons may exist in atomic or molecular energy levels. The atomic energy levels are well-defined by a finite number of electrons before the extra electrons start moving to the next level. The inner-shell electrons (1s orbital), called core levels, have a higher binding energy than outer-shell electrons such as 2s and 2p electrons due to their proximity to the nucleus. On the other hand, the electrons farthest from the nucleus have low binding energy and are named valence electrons, relating to their location in the valence levels. Molecular energy levels, also called molecular orbitals, comprise electrons that are weakly bonded in mixed energy levels. The electrons distribute over neighbouring atoms or the entire molecule.

Photons can penetrate quite deep into the solid before being absorbed, but excited electrons can only travel through a few layers of matter. Hence, it is necessary to prepare the sample carefully and eliminate contamination as much as possible because the XPS technique is very sensitive to the surface. Surface sensitivity in XPS can be increased by altering the angle at which electrons are detected from the surface with respect to the analyser, and therefore, the route of electrons changes before arriving at the detector and decreasing the depth from which the detected electrons can be released.

3.4.3 Hemispherical Electron Energy Analyser

The photoelectron energy distribution is essentially measured with a hemispherical analyser. Electrons pass through an electrostatic lens system that bends the inbound electrons entering a narrow slit to prevent unusual paths, and then via an analyser which consists of two concentric hemispheres with two different radii, see Figure 3.6. Potentials applied to the inner and outer hemispheres apply an electrostatic force to the electrons. The electrons only flow through to the detector if the electrons' centripetal forces nearly match the electrostatic forces, enabling the measurement of the number of electrons and their kinetic energy; on the contrary, an imbalance causes electrons to collide into one of the two hemispheres depending on how much kinetic energy they have. A retardation voltage is used to slow down the photoelectrons to pass energy, which will detect kinetic energies in addition to the pass energy.

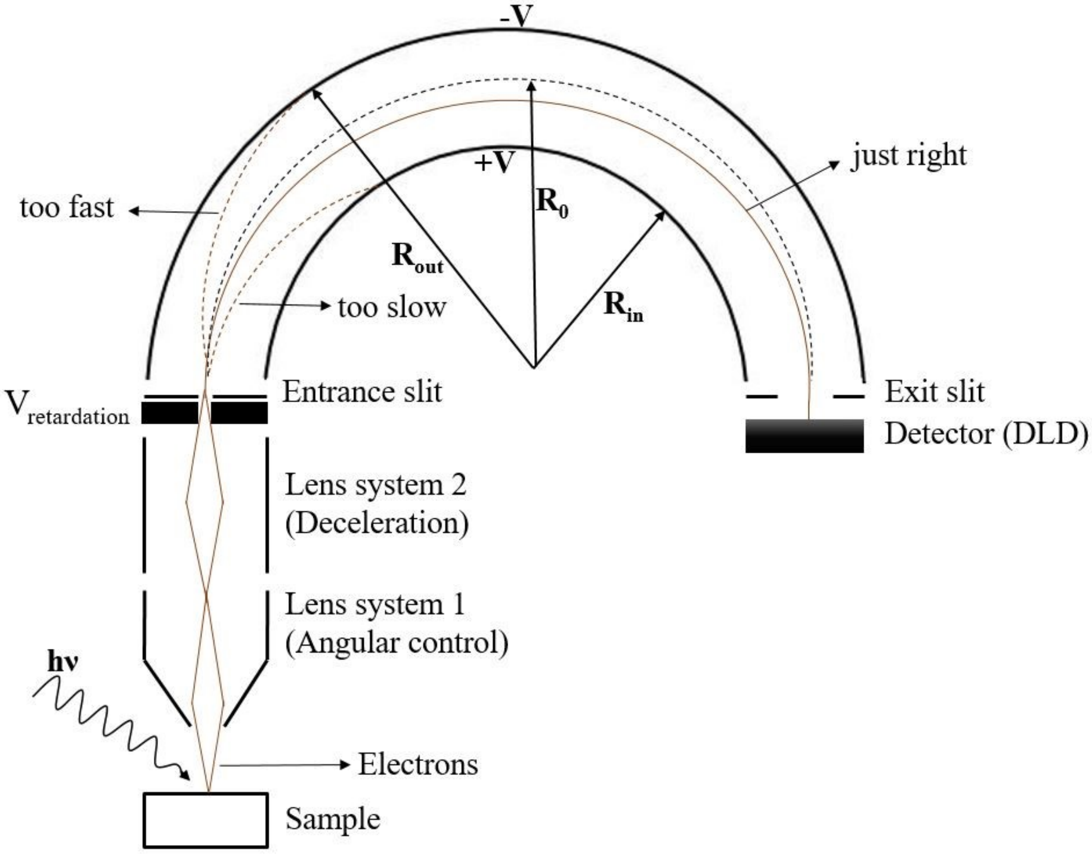

Fig. 3.6. Schematic diagram of a hemispherical electron analyser. The photoelectrons that are emitted from the surface are accelerated into the analyser. Electrons are decelerated and focused via a slit with applying a voltage in between. Just electrons that are in the pass energy range will reach the DLD detector to be counted.

A swept-tuned mode is the most significant detection mode used in XPS. The retardation potential of the reaching electrons on the detector is changed, allowing their number to be measured, whilst the hemisphere's pass energy remains constant. XPS measures the whole range of electron kinetic energies at one fixed pass energy level on the detector. There is another detection mode known as fixed-tuned mode but it was never used. It is not suitable for obtaining the correct shape of the spectrum; rather, it is appropriate for very fast data acquisition.

In this study, a 2D delay-line detector (DLD) is the most employed piece of equipment in the detector composition. The 2D-DLD can be used instead of charged coupled device (CCD) camera. The design of the DLDs is a modern innovation in physics detectors, unlike most microchannel plate (MCP) detector systems. DLDs may be either single- or multi-dimension devices. The feature of the DLD detector is that it defines the electrons' effect position on the detector in two dimensions with a high capability for detecting numerous particle hits and analysing the position and time coordinates of every single particle. A DLD comprises two delay lines that are perpendicular to each other, where every delay line consists of a pair of wires applying a voltage between two thin wires. In the DLD, electron-pulsed signals strike two layers of thin wires, causing flashes of light on the detector surface. The distance of the electron cloud colliding with the wire is determined via reading the pulses of induced current from the end of the wire. Moreover, the information received from both wires is used to identify the location of the incident charge on the detector surface. Single-channel electron multiplier devices (e.g. a 1D array of channeltrons) are the most used conventional detectors. These detectors are best suited for applications requiring high-intensity measurements.

The term 'pass energy' (EP) refers to the energy carried by electrons when they flow along a central axis between the two hemispheres. This energy is generally set between 5 eV and 200 eV based on the type of the chosen application. High pass energy provides more count rates and gives the analyser a worse accuracy, but low pass energy loses more electrons and provides a higher resolution.

In addition to the pass energy, the spectrometer's final energy resolution can be calculated using the equation for the sum of the two slits' widths ($\mathrm{W_{entrance}}$ and $\mathrm{W_{exit}}$) and the spectrometer's size.

$$W = W_{entrance} + W_{exit} \tag{3.2}$$

Higher-resolution spectra can be provided by using smaller slit apertures and bigger spectrometers based on the following equation, where the smallest full width at half-maximum (FWHM) is given by ΔE.

$$\Delta E/E_p = W/2R_0 \tag{3.3}$$

where $\mathrm{E_p}$ is pass energy of the electrons through the analyser. $\mathrm{R_0}$, as indicated in Figure 3.6 by a black dashed line, is the radius of the electrons with the pass energy that can get to the exit slit along the median path through the spectrometer where $\mathrm{R_0} = \frac{1}{2}$ ($\mathrm{R_{in}}$ + $\mathrm{R_{out}}$) [113, 114]. $\mathrm{R_{in}}$ and $\mathrm{R_{out}}$ are the radii of the inner and outer hemispheres, respectively.

3.4.4 X-ray tube Anode

The single X-ray source (called microfocus X-ray) generates high-intensity and high-resolution X-ray with small spot sizes less than 200µm, which can achieve monochromatic resolution of 0.25eV. 200W is determined as the maximum power dissipation to prevent anode damage. The MF single X-ray is made of filament due to its thermal properties, tungsten (target material – it is a single aluminum anode) and an emitter. The emitter includes a crystal connected to wires that create a high flux of electrons with a low-energy diffusion. The MF single X-ray anode operates by electron flows that are boiled off by the X-ray tube filament using a sufficiently high voltage to hit the target area in a steady electron beam. The emitted electrons released due to thermionic emission process are controlled using a grid bias. There are two types of X-rays generated: characteristic radiation and bremsstrahlung radiation, as summarised for aluminium in Figure 3.7. A bremsstrahlung X-ray is created when bombarded electrons slow down due to electrostatic interactions with the target's electrons. X-ray photons are released as a result of the electrons' change in momentum, whereas characteristic X-ray takes place when electrons expelled from filaments smash with the electrons within the target in order to excite them from low to high atomic energy levels. X-ray photons with energy levels equivalent to the energy gap are released when electrons decay back to their ground states.

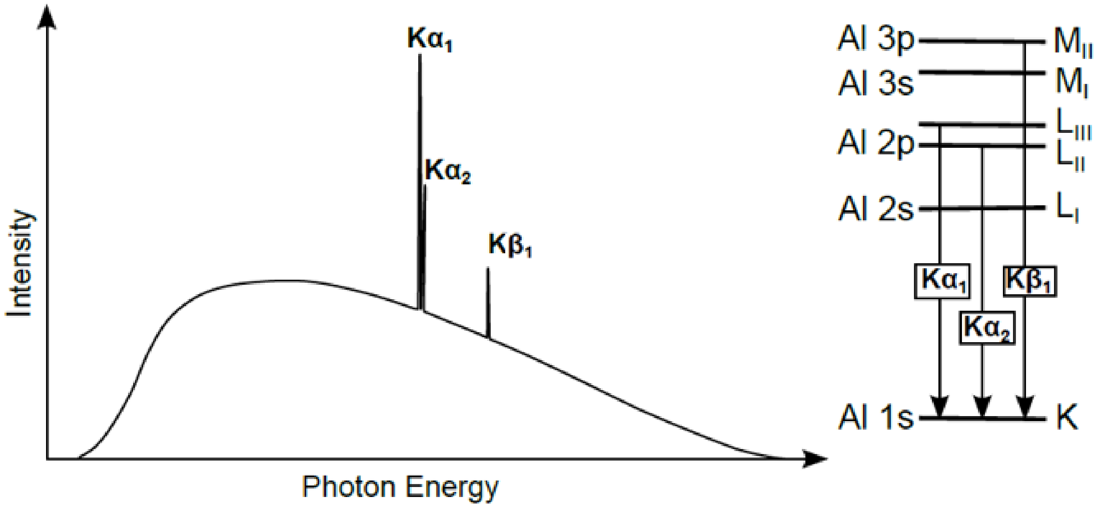

Fig. 3.7. Diagram outlines characteristic X-ray emission and Bremsstrahlung background for Aluminium. Kα_1, Kα_2 and Kβ_1 correspond to transitions L$_{\mathrm{III}}$, L$_{\mathrm{II}}$ and M$_{\mathrm{II}}$ energy levels down to the core hole 1s.

The characteristic X-rays enter the analysis chamber by penetrating a very thin aluminium-coated silicon nitride window, which is one of the components of the anode. Monochromatic x-rays have been used to remove undesired characteristic peaks and for imaging studies, especially for increasing energy resolution and minimising the background to obtain sharper images. A point-to-point focusing crystal geometry is introduced in the Rowland circle [115], e.g. a toroidal quartz crystal to concentrate the X-ray beam onto the sample, as outlined in Figure 3.8.

Constructive interference in the X-ray reflection in accordance with Bragg's law (used to measure variations in scattering angles of crystals) for the general case of hkl planes, $n\lambda = 2d_{hkl} \sin(\vartheta_{hkl})$, is permitted when the total path difference ($2d_{hkl} \sin(\vartheta)$) between light diffracted by parallel crystal plates matches the integer wavelengths. Where n (an integer) is the order of diffraction, λ is the wavelength of the incident X-ray, d is the spacing of the crystal layers and ϑ is the angle between the incident ray and the scattering crystal plane. The undesirable spectral contribution may be greatly decreased by adjusting the incidence angle ϑ such that the path length difference matches the wavelength of the required emission line.

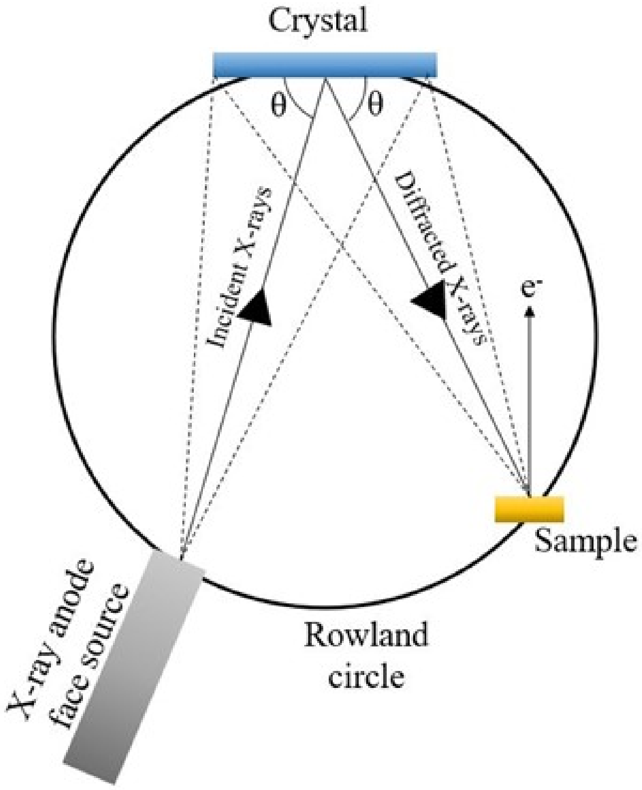

Fig. 3.8. Configuration of the sample and analytical crystal on the Rowland circle geometry within X-ray emission spectroscopy from an anode.

3.4.5 Surface Sensitivity

The surface sensitivity approach is one of the main advantages of using PES in surface science experiments, as this technique is more sensitive to atoms close to the surface than to atoms in the bulk that are farther away from the surface. It has to be noted that photoelectrons have a smaller escape depth despite the fact that the soft X-rays' regime is able to penetrate a surface at a depth of microns [116] because of the strength of the interaction between electrons and material.

Inelastic scattering of electrons may occur as they move through a solid material. Subsequently, the origin of these electrons is no longer known due to their missing Auger transition or energy level information, and as a result, a background of uninteresting secondary electrons is created. With regard to electrons that are not inelastically dispersed, which take part in photoelectron and Auger peaks, they come from the crystal's surface rather than its bulk. So, electrons that move a short space before scattering are favoured over those that move a long space and, hence, may be originating from deeper in the specimen. Because of the definition of the inelastic mean free path, $\lambda(E)$, which states the average distance travelled by the electron through the material before losing energy and reducing its intensity to 1/e, it is presented by:

$$I(d) = I_0 \; exp(-d/\lambda(E)) \tag{3.4}$$

where I(d) is the intensity after the electron beam has travelled through the material to a distance d, and I_0 is the initial intensity.

The mean free path of the electrons is more dependent on the kinetic energy than on what form of matter they exist in. The graph in Figure 3.9 illustrates the general curve for the electron inelastic mean free path in a different metal as a function of kinetic energy.

The inelastic mean free path on the plot shows a minimum for electrons with kinetic energy at roughly 50 eV-100 eV. At higher kinetic energies, the electrons can travel rapidly and spend less time in the metal so that they are less likely to interact, whereas at lower kinetic energies, the probability of inelastic scattering reduces since the electron has insufficient energy to excite loss processes and consequently originates from the minimum in the sample. In the experiment, the kinetic energies are determined by the fact that the photon energy cannot be changed. It is always a fixed aluminium KAl for photon energy, for example, the kinetic energy for the C1s level calculated from E_K=hν-E_B that appears on the universal curve at 1,203 eV.

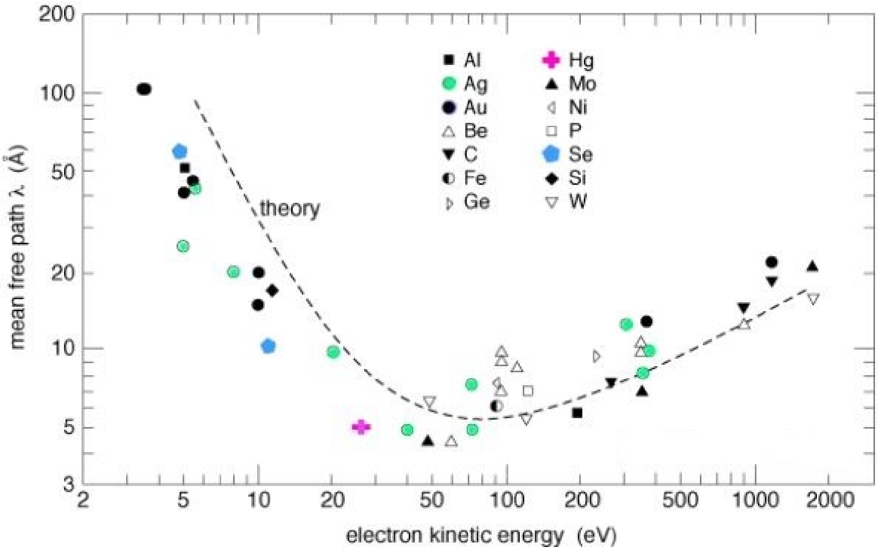

Fig. 3.9. The curve showing the inelastic mean free path of an electron travelling through metals (solid) as a function of kinetic energy. The graph is adapted from reference [117].

3.4.6 Final State Effects

3.4.6.1 Spin-orbit Coupling/Splitting

XPS peak splitting is expected to occur for other orbitals (e.g. p, d and f orbitals) other than s orbital due to spin-orbit coupling. This forms as a result of an electron's spin, s, coupled with its angular momentum, l; in other words, it is an interaction between electrons' spin and angular momentum to give the total angular momentum, j, such that j = l + s [118, 119]. After an electron is emitted from a core atomic orbital by photoemission, two distinct states are involved, either s = +1/2 (spin-up) or s = -1/2 (spin-down), and $l = 0$ in the case of s orbital, which means that there is no degeneracy between the two electrons since they have the same kinetic energy. However, degeneracy is apparent for energy levels with $l > 0$, such as p, d and f orbitals (i.e. $l = 1$, 2 and 3, respectively), causing a split in the final state energy. Degeneracy can be calculated by:

$$Degeneracy = 2j + 1 \tag{3.5}$$

If the emitted electrons with two different energies, two distinct peaks are observed for p, d and f orbitals at different binding energies measured in XPS rather than the single peak obtained for s orbital. Two peaks' size ratios is defined by the degeneracy value's ratio, as seen in Table 3.1.

Orbital	**J values**	**Degeneracy**	**Peak ratio**
s (l=0)	1/2	0	
p (l=1)	1/2, 3/2	2, 4	1:2
d (l=2)	3/2, 5/2	4, 6	2:3
f (l=3)	5/2, 7/2	6, 8	3:4

Table 3.1. Total angular momentum (j), electron degeneracy, and peak intensity ratio of s, p, d, and f orbitals for X-ray photoemission spectroscopy.

For example, Ti $2p$ splits into discrete peaks corresponding to the Ti $2p_{1/2}$ and Ti $2p_{3/2}$, calculated using the total angular momentum, j = l + s. In this case, $l = 1$ and the intensity ratio between the two Ti $2p$ peaks is given by the equation (3.5), resulting in an intensity ratio of 1:2, as shown in a titania spectrum in Figure 3.10. A low total angular momentum makes the two peaks small with high binding energy.

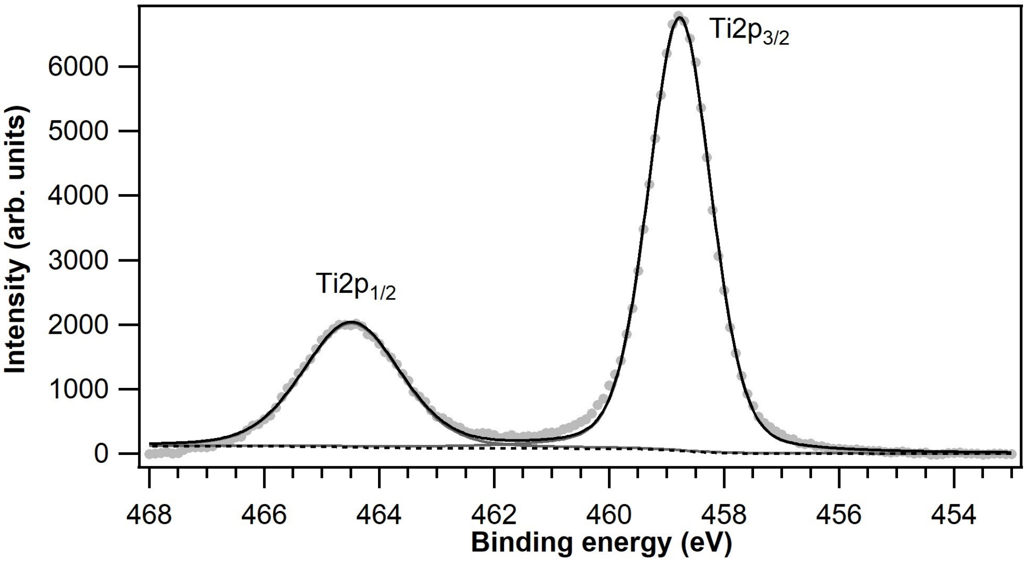

Fig. 3.10. A photoemission spectrum of a titanium sample is shown, where Ti $2p_{1/2}$ peak on the left and Ti $2p_{3/2}$ peak on the right has computed using the total angular momentum j = l+ s.

3.4.6.2 Shake-up and Shake-off Features

Satellites are formed when a core electron is removed through a photoionisation process, where a sudden change in coulomb potential occurs due to the loss of shielded electrons. This disturbance causes the electron to shift from a bonding orbital to an anti-bonding orbital simultaneously. Two types of satellite peaks created by satellite lines in the XPS spectrum have been detected: shake-up and shake-off, as outlined in Figure 3.11. The shake-up satellites in a photoelectron spectrum of an atom can arise when the core electron that is emitted from the atom loses some energy through excitations of valence band electrons into the unoccupied valence levels, so the photoelectron has kinetic energy less than it would normally be by an amount equal to the cost of the HOMO-LUMO (highest occupied molecular orbital-lowest unoccupied molecular orbital) excitation. Lower kinetic energy looks like higher binding energy, so these features are always found to be the high binding energy side of the main peaks that are related to them. The shake-off is a similar process but the valence electron is fully ejected from the ion into the continuum of unbound energy states above the vacuum level; hence, the loss structure can disappear into contributing to the scattered background.

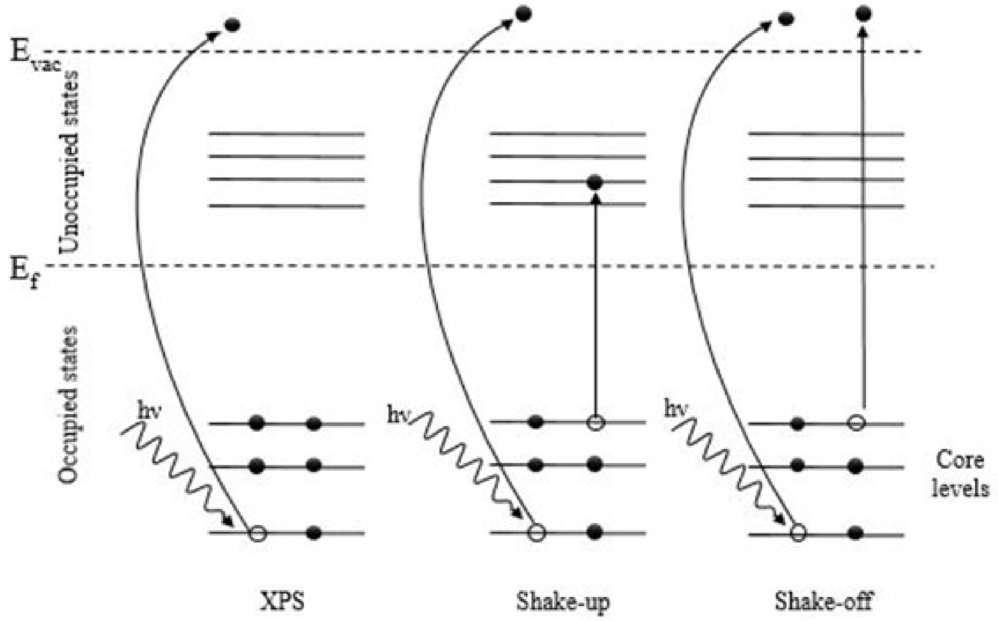

Fig. 3.11. Schematic of energy level diagram showing XPS (main peak), shake-up, and shake-off (satellites peaks).

3.5 Atomic Force Microscopy (AFM) and Optical Microscopy

AFM has been used in a wide range of sciences around the world, including physics, chemistry, biology, as well as engineering. In this thesis, AFM data on the morphology of graphene deposition will be shown in Chapter 5. AFM can precisely identify a sample surface's electrical, magnetic, chemical, optical, topographic and mechanical characteristics [120] in air, liquids and UHV environments. Binnig et al. invented AFM, a very high-resolution imaging method, in 1985 [121] using a tiny probe, known as a cantilever, for scanning the sample. The AFM may be sensitive to vibrations conveyed by the floor, resulting in restriction of measurement sites and, subsequently, defection on images, so they are placed on isolators to prevent vibration.

The typical AFM techniques operate [122] as represented in Figure 3.12, by scanning a sample's surface using a sharp tip (commonly made of silicon or silicon nitride) on the end of the cantilever. A piezoelectric tube scanner is made of ceramic material which has been used to move the sample in the three coordinates (XYZ stage or scanning stage). In most cases, a laser beam reflected from the cantilever's backside is used for observing the AFM tip's height and then directing the reflected beam to hit the photodiode. A feedback loop is employed to maintain a constant interaction force between the tip and the sample. A 3D topographic image is created by incorporating the coordinates of the AFM tip by scanning with a magnification greater than 1,000x compared to the compound optical microscope. On the other hand, AFM cannot measure regions greater than 100 µm.

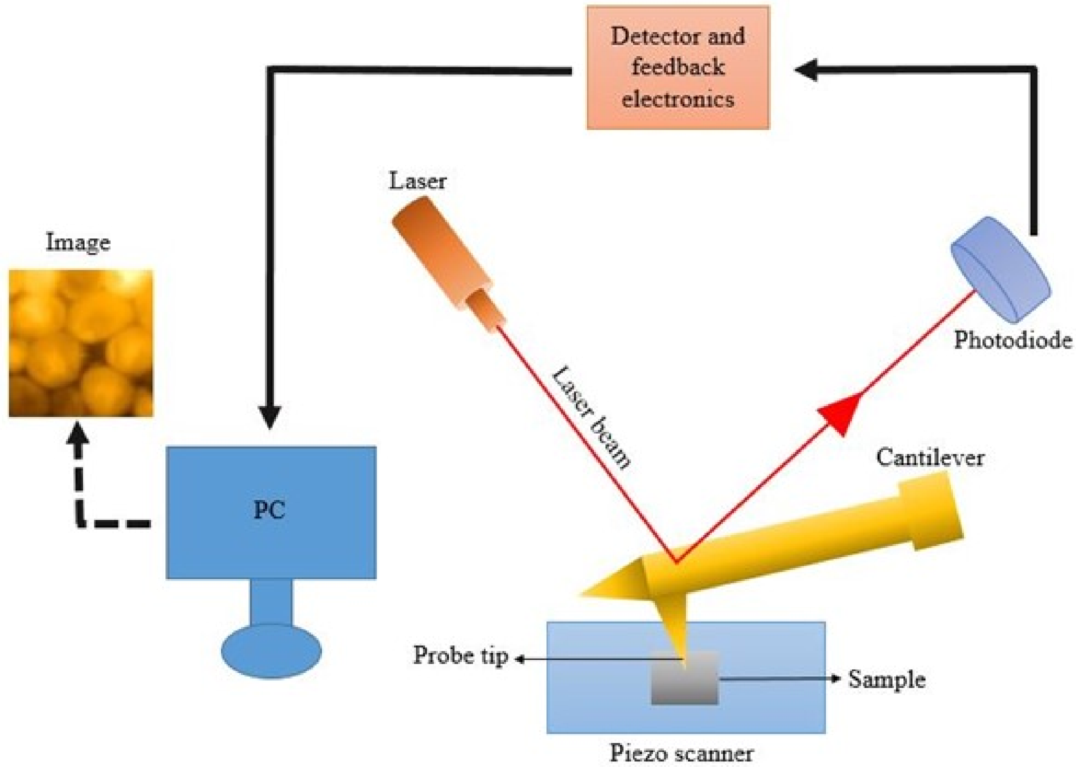

Fig. 3.12. Schematic of basic AFM setup components.

An optical microscope (also called a light microscopy) is a common technique that uses visible light and lenses to produce 2D images that are magnified about 1,000x due to the limited resolving power of visible light. Optical images can be captured by a camera such as a CCD. It is employed in many science and technology fields, including physics, biology, pharmaceutical, nanotechnology, materials science and many others.

3.6 SIMION simulation

Ion optics can be modelled with 2D symmetrical and 3D asymmetrical electrostatic potential arrays using the SIMION simulation program. It is suitable for simulating a wide variety of systems, such as mass spectrometers and particle optic lenses. This software is used to calculate the virtual electrostatic fields and to determine the paths of charged particles [123]. The trajectories of ions in electrostatic fields can be calculated in SIMION according to the Lorentz Force law. The equation is given as:

$$F = qE + qv \times B \tag{3.6}$$

where q is the electric charge of the particle moving with velocity v. E and B are electric and magnetic fields. The path of ion charge can be defined by the Lorentz Force equation and Newton's second law equation. Newton's second law can be expressed as follows:

$$F = ma \tag{3.7}$$

where m and a are the mass and acceleration of the object, respectively.

3.6.1 Electrode Geometry

The first step in SIMION is to create electrostatic potential arrays by drawing 3D geometric shapes in the grid point. 3D arrays can be defined as electrodes (poles) by inserting electrode numbers with 1 volt or 2 volts, etc. or non-electrode (non-pole) of 0 volts to erase the wrong points. The geometry of the electrodes, empty space and applied voltage helps to calculate the electric field in SIMION. Figure 3.13 presents the creation of the electrodes in the grid points in SIMION, and Figure 3.14 shows view of the potential 3D array generated from Figure 3.13. SIMION provides another way to define electrode geometry in a potential array using geometry files. Geometry files are usually employed for sophisticated 3D geometry, or any geometry definitions that need to be resized. Because symmetry is different in different parts of the instruments, geometry files have been used in order to assemble them together into one array. For instance, cylindrical symmetry for the Einzel lens and mirror symmetry for the deflection has been applied.

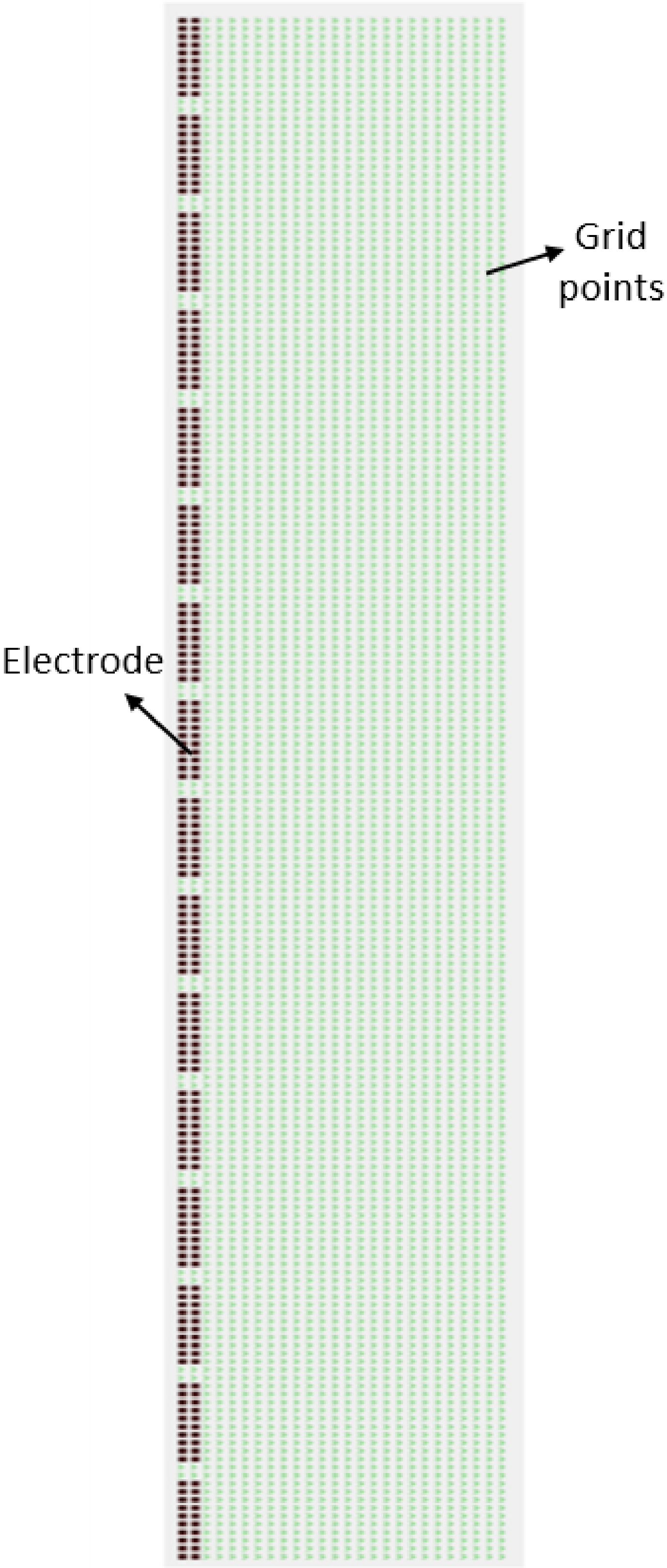

Fig. 3.13. Example of a potential array form of the generating electrodes (black) in the grid points (green) in SIMION software.

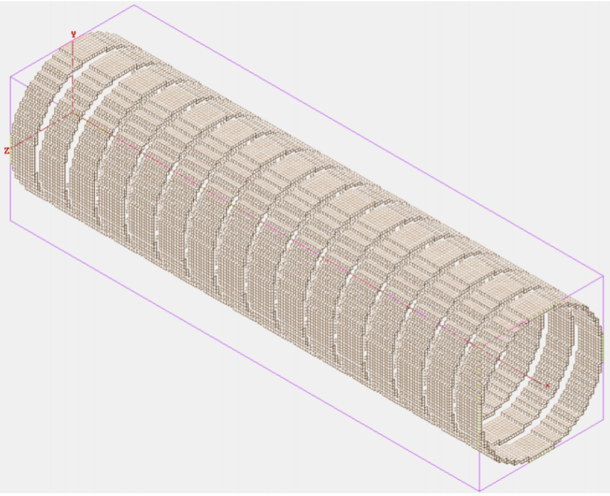

Fig. 3.14. View of the 3D electrodes introduced from Figure 3.13.

3.6.2 Flying Ions

Before flying ions in SIMION's ion optics workbench (WB), potential arrays should be refined. To simulate the trajectory of the ions, it is necessary to define some parameters for the ions' simulation, such as the number of particles and values of ions' mass, charge, position distribution and kinetic energy or velocity. Ions can be defined either in groups of similar ions or individually. Electrons, protons and defaults all give ions in the selected ion group resting mass and charge, except the defaults transform the definition of the group of the selected ions to a SIMION default. After setting up all parameters, ions can be flying through the potential field in SIMION. SIMION uses the fourth-order Runge–Kutta calculator technique to compute ion trajectories.

After the ion's flight is finished, SIMION permits a view of these trajectories in WB or potential energy (PE) surface views. The WB view (see Figure Figure 3.15) allows 2D and 3D views, even for interior ion trajectory. There are many viewing choices, such as 3D pointing, cutaway clipping and others. Figure Figure 3.15 illustrates ion trajectory within the Einzel lens, which has been built by a 2D cylindrical array. The PE surface view (see Figure 3.16) lets us see the ion pathways of a 2D plane. The PE surface view has physical importance for the electrostatic fields due to graphically showing the electrostatic forces acting on the ions. Figure 3.16 shows a PE surface view of the Einzel lens trajectory, which aids in understanding the electrostatic focusing of ions. It is easy to learn the ion paths in the Einzel lens by imagining that the shape of the PE surface is a bit like a golf course where golf balls interact with hills in the same way that ions interact with the PE surface.

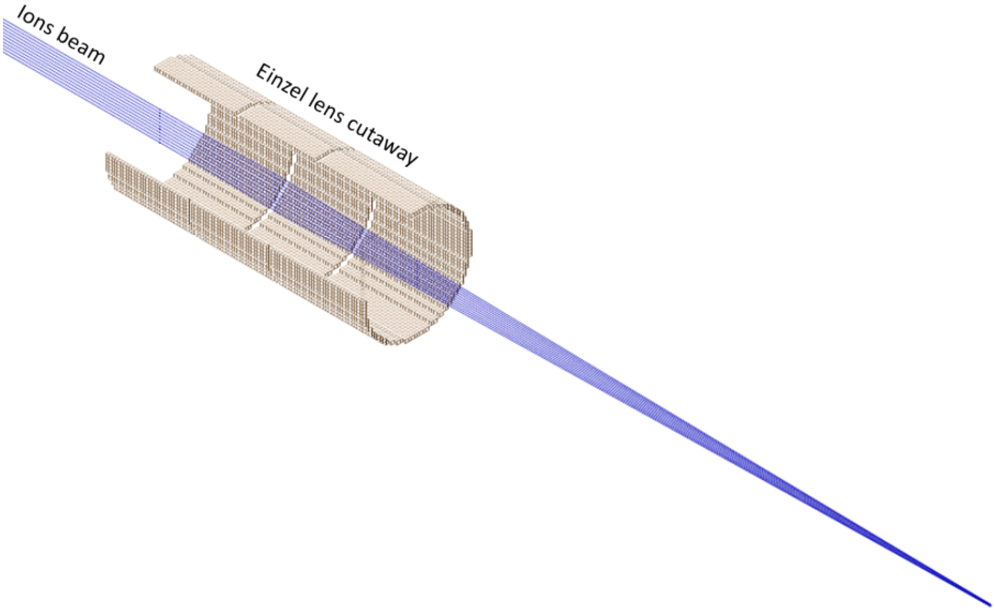

Fig. 3.15. Workbench (WB) view of ion trajectories flown through Einzel lens cutaway. Image modified from [124].

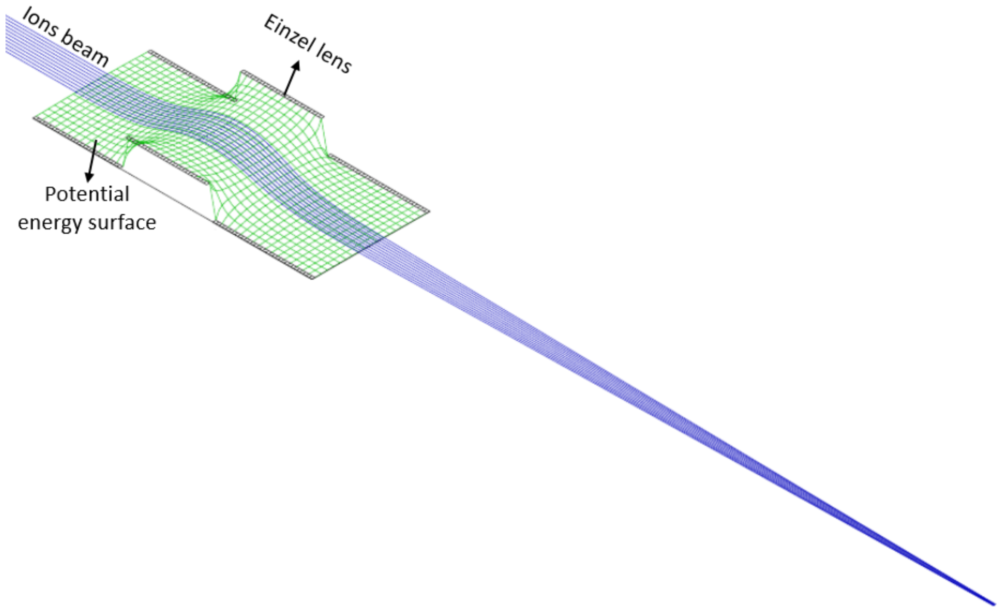

Fig. 3.16. Potential energy (PE) surface view of ion trajectories flown through the Einzel lens. Image modified from [124].

In this chapter, the key experimental methods and techniques of electrospray deposition, some background underlying PES and AFM are outlined, including a discussion of the instrumentation used. All of these will underpin the experimental work presented in Chapters 4, 5 and 6. SIMION calculations will also be exhibited in Chapter 5. At this point, the next chapters begin discussing experimental studies.

Chapter 4

The Characterisation of Velocity Distributions in Electrospray Ionisation

4.1 Introduction

Depositing molecules on surfaces supports an enormous variety of science and technology fields, from solar cells to heterogeneous catalysis. Ion beam deposition in a vacuum is considered a technology that produces surface coating for a large range of applications and enables researchers to study complex molecules on surfaces, especially in situ using high-resolution techniques requiring a high vacuum, such as scanning probe microscopy and PES. Depositing functional molecules, dye sensitisers of photovoltaics, water-splitting solar cells, biomolecules and nanoparticles onto surfaces under UHV conditions is not readily feasible because they are typically fragile and non-volatile.

Small volatile and thermally stable molecules can be vaporised onto surfaces in the conventional deposition because most of the traditional methods depend on thermal evaporation or sublimation. The liquid or solid in the case of small molecules is softly heated in order to reach the fractional pressure of molecules in the gas stage, where raising the molecule's temperature leads to its destruction or dissociation before the necessary energies are reached to achieve the gas phase. Using this technique could be ineffective with large molecules or nanoparticles since a high temperature is required for sublimation and evaporation - i.e they are thermally unstable, and their vapour pressure is low. Electrospray is a soft ionization technique that can use with non-volatile materials to produce the molecules into the gas phase non-thermally. Rauschenbach [125] proved that it is possible to deposit non-volatile molecules, such as proteins and peptides, onto surfaces and retain their structure (i.e. even the very weak bonds that give proteins their shape are not broken) or successfully soft land them from ion beams under vacuum.

Image charge detection mass spectrometry is a general technique used to calculate m/z (i.e. mass to charge ratio) for each ion. Also, it enables measurement of the ion charges that go through the system. The image charge detector consists of a metal tube connected to a charge-sensitive amplifier, as can be found in the literature [126–128]. The simple description of the image charge detection spectrometer is shown in Figure 4.1. When charged ion passes through the tube, it impresses an image charge that the amplifier detects on the tube. If the tube is long enough, the image charge then has time to build up a charge that corresponds to an ion charge on the tube but with an opposite sign, which can be measured as a voltage. In addition, it measures interval time when the ion enters the tube and gives a measurement of the speed when the ion leaves the tube. Differentiating the voltage signal can reveal the time-of-flight (TOF) of the ions from the distance between peaks where, in turn, the velocity of the ions is calculated where the area under the peaks is proportional to the ion charge [126].

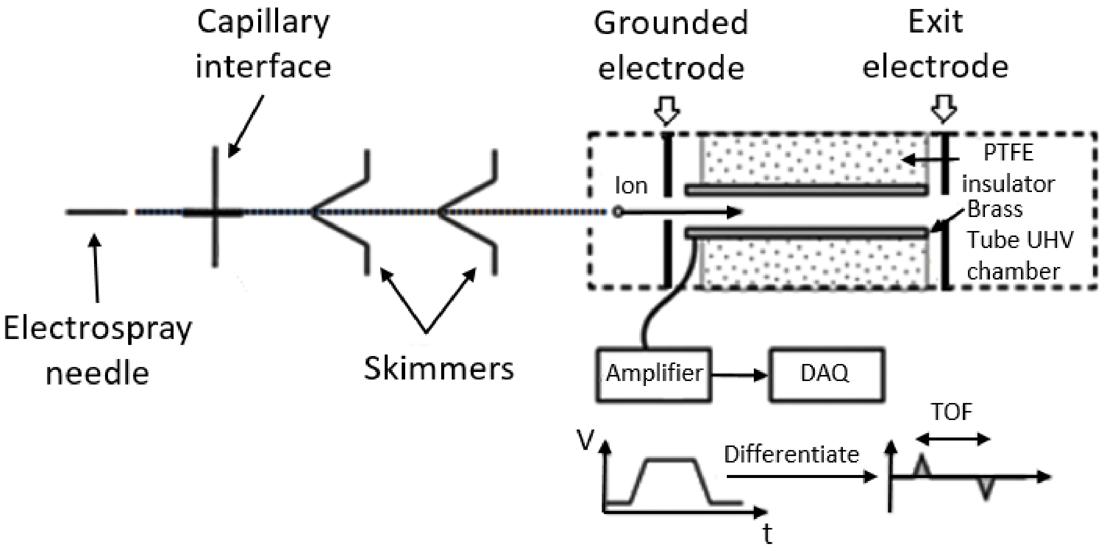

Fig. 4.1. Schematic diagram of image charge detection spectrometer showing the ion passes through the tube. A sensitive amplifier and high-speed data acquisition card (DAQ) can be used to measure an image charge of the ion on the tube. The lower portion of the Figure shows the signal obtained from the image charge detector which is known as time-of-flight (TOF).

The electrospray deposition source (see Figure 3.2 in section 3.3.2) has been developed by including a homemade image charge drift tube in order to determine the ions' velocity distribution using an amplifier to measure image charge, which will be discussed in more detail in the method section. The aim of developing this instrument is to build a low-price, small-scale electrospray deposition system, designed to be mounted on a wide range of UHV instruments.

The main goal of this work is an exploration of speed and, indirectly, the size of the ions in stages 3 and 4 as a result of changes to the geometry of stage 1. Therefore, the charge tube has been used to determine the velocities and to determine if it is possible to accelerate them to a similar speed. In addition, the position of the first skimmer cone relative to the entrance capillary to sample inside the Mach disc has been changed in order to see whether obtaining more control over the speed will be possible. The sample takes place inside the Mach disc because the ions are still under the influence of the supersonic expansion, so they are probably accelerated to a similar speed. Alternatively, outside the Mach disc, there are other air molecules that will slow them down, where they will collide and thus begin to thermalise – details of which are outlined in section 2.2.1. However, if the distance is too large, they will all be reduced to the same energy and therefore have different speeds based on their mass according to the kinetic energy equation $\mathrm{KE} = \frac{1}{2}\,\mathrm{mv}^2$, where m and v are the mass and velocity of an object.

4.2 Experimental Methods

The electrospray deposition setup used for these studies is shown in Figure 4.2. The source is equipped with a 250 µm internal diameter entrance capillary in stage 1 using a heater around the entrance to assist desolvation of the droplets. The first two vacuum stages are pumped by roughing pumps, such as dry scroll pumps, where pressures around 1 mbar in stage 1 and 0.1 mbar in stage 2 have been achieved. In this experiment, the position of the skimmer cone has been changed with respect to the Mach disc of the supersonic expansion in order to gain some control over the ions' speed, which can be measured with an image charge drift tube. The second skimmer (aperture diameter of 0.6 mm) is placed near the first skimmer (aperture diameter of 0.4 mm) to increase the ion range to the maximum and reduce any thermal revolution.

Stage 3 and 4 are pumped by a turbomolecular pump to pressures around 10^{-4} mbar and 10^{-6} mbar, respectively. The third stage constitutes an image charge drift tube. This instrument allows for determining the speed distribution of ions using a high-speed amplifier to measure the charge of the ion image when entering the tube and losing the charge when leaving. Moreover, the ion charge can be qualitatively estimated from the volume of the induced image charge.

The strategy of Maze et al. [129], who utilised image charge detection spectrometry to investigate the charge and velocity distributions of electrosprayed pure water droplets, was employed in this experiment but with spraying fluores-

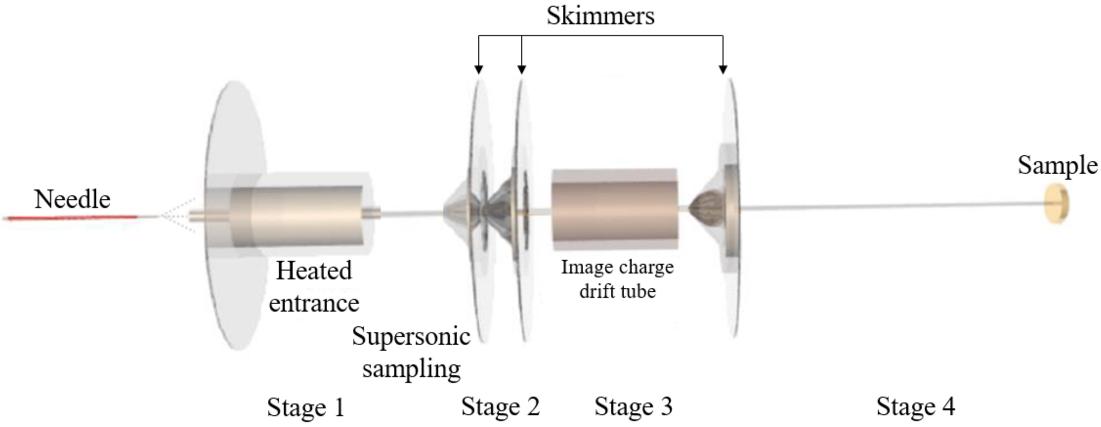

Fig. 4.2. Schematic of the electrospray deposition source. A supersonic sampling stage speeds up molecules to a narrow speed distribution that is measured by a drift tube of image charge. The beam of molecules enters into the system to the final skimmer aperture to deposit on the sample in the deposition chamber (UHV chamber).

cein dye. The TOF between two peaks gives the speed of the droplet; additionally, the charge amount on the drops can be determined from the region beneath peaks in the differentiated signal by applying a small voltage pulse using a known capacitance of the preamplifier.

An example of data collected using an image charge detector is shown in Figure 4.3. The device in Figure 4.1 comprises a 50 mm long brass tube installed in the vacuum chamber by a PTFE (Polytetrafluoroethylene) insert and attached to a charge-sensitive amplifier. Further, a data acquisition (DAQ) card is applied until the amplifier's voltage output can be measured. Since the instrument is extremely affected by vibrations that mostly came from vacuum pumps, the chamber is placed on a vibration isolation table, so it was necessary to conduct a careful study of the pumping to reduce this. Dry-scroll pumps (previously discussed in section 3.2) have been used in the main chamber, whereas the turbomolecular pump is installed in the third stage and connected through bellows to the electrospray system to pull vibration out from the system. All support pumps are connected through plastic tubes rather than metal tubes because the metal tubes allow the transferring of further vibrations.

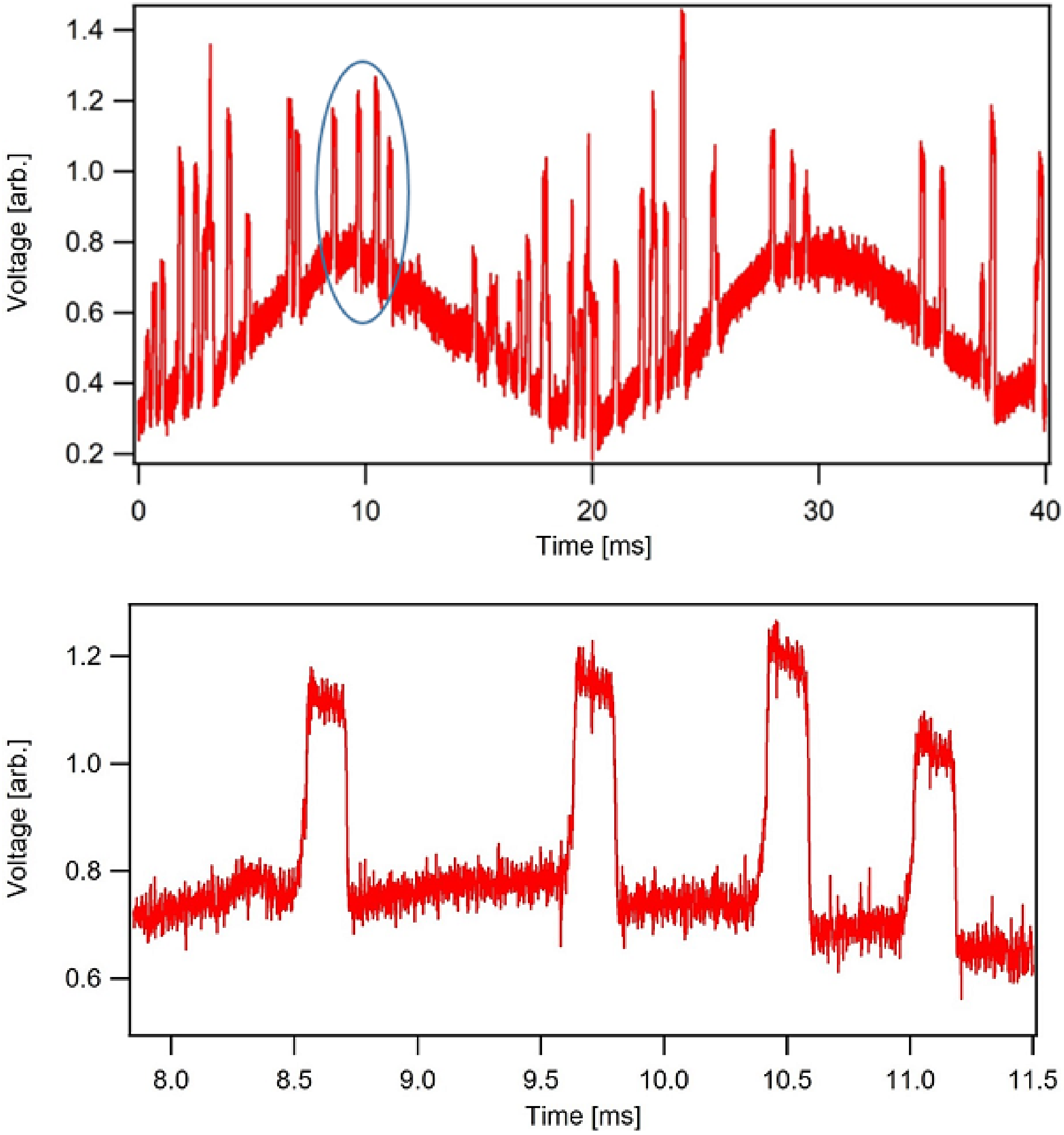

Fig. 4.3. Example data collected using an image charge detector for 1 mM of a standard fluorescein solution (50:50 water: methanol) sprayed at 3.5 kV. The bottom plot zooms in on the transients marked in the top plot with a blue solid circle.

Figure 4.4 shows the example of differentiated data for the positive bias mode (i.e. positively charged droplets) used in the lower trace from Figure 4.3. It displays four transients produced from electrospray ions travelling through the tube consecutively. Non-differentiation data makes the transients' identification more difficult due to the differential signal noise which results from high-frequency noise. Applying the filtering using a low-pass filter to minimise a lot of the high-frequency noise has the same outcome as smoothing; therefore, there is no need to use a more time-consuming method.

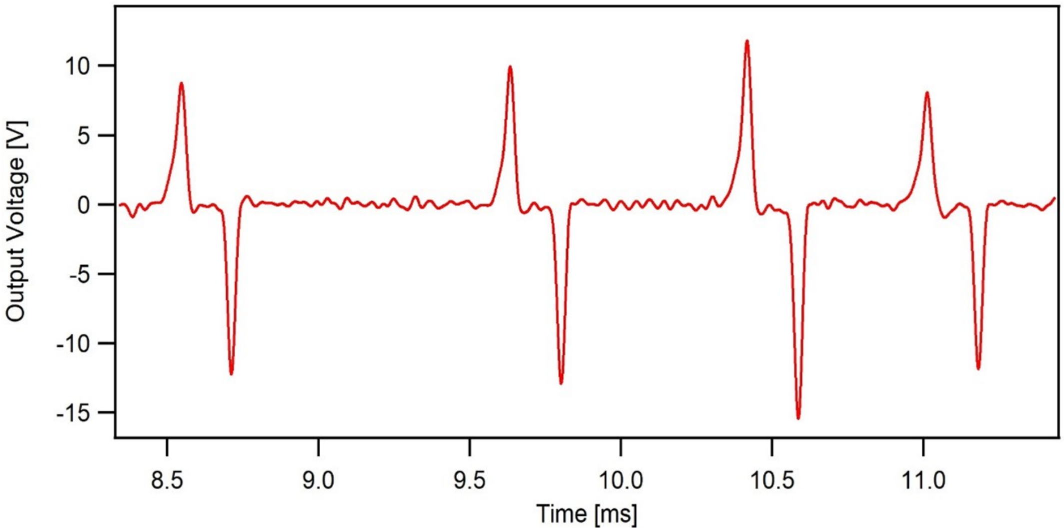

Fig. 4.4. Differentiated data collected of 1 mM fluorescein dye in (50:50 water:methanol) sprayed at 3.5 kV.

Figure 4.5 shows the example of differentiated data for the negative bias mode (i.e. negatively charged droplets). It presents four transients from electrospray ions travelling through the tube sequentially. As can be seen, the second transient at 16 ms indicates a double situation, and this is attributed to two ions entering the tube simultaneously, causing interference in both signals. According to peak heights in the differential signal, the two ions have the same charge. The electrospray can be detuned to reduce the event rate down to a level where individual events can be observed without them overlapping.

The positive peak refers to inserting a negatively charged ion into the tube, and the negative peak is produced when it leaves the tube, whilst the opposite occurs with a positively charged ion. The time elapsed between the two peaks in the differentiated signal exactly coincides with the ion's TOF [129].

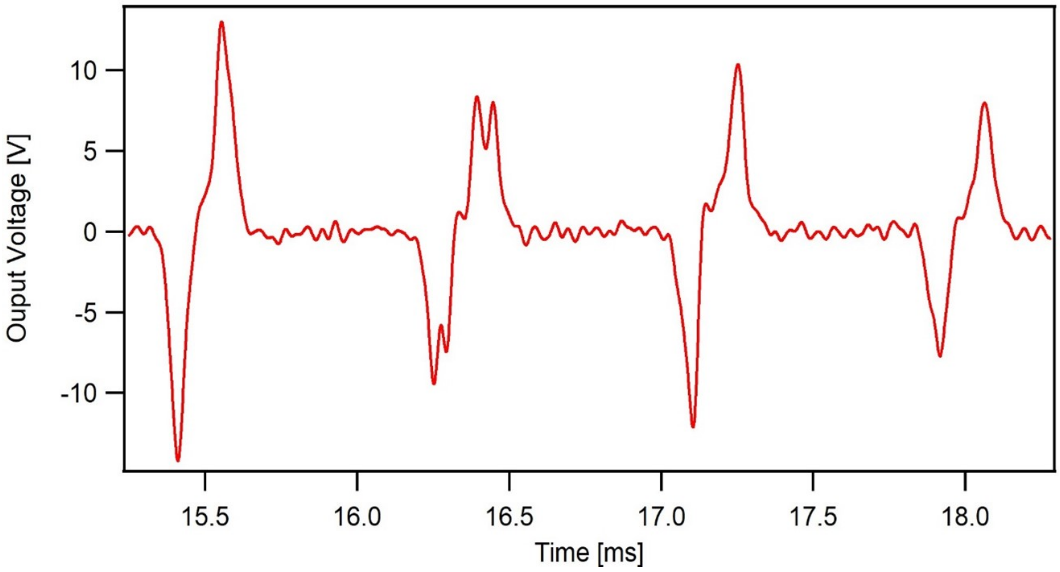

Fig. 4.5. Differentiated data collected of NaCl dissolved in 5 ml of water and methanol sprayed at -2.58 kV.

4.3 Results and Discussion

Velocity distributions measured for different spray biases (2.00 kV, 3.00 kV and 4.00 kV) are shown in Figure 4.6. A 0.1% solution of fluorescein in methanol was used, and the distance between the inlet capillary and first skimmer was 12.3 mm. In each case, a 1.25 MHZ sampling rate and the number of samples (50,000) were set. Within 0.5 seconds, a considerable number of transients were recorded. The time interval for each transient in this data was measured manually by taking the time difference between the positive and negative peaks in each transient signal, as shown in Figures 4.4 and 4.5. Each one of these then is added manually as a data point to the histograms, as presented in Figure 4.6. Manual measurement was performed, as efforts to automate the process may have led to unreliable results. The histograms produced from the mean and standard deviations of the speed values are presented in a Gaussian distribution (see Figure 4.6).

The plot (a) 2 kV indicates velocity distribution centred at 303 ms^{-1}, with a full-width at half maximum of 46 ms^{-1}. The histograms for 3 kV and 4 kV (b, c) are a little broader than 2 kV. Furthermore, the distributions, centred at 327

ms^{-1} and 333 ms^{-1} have FWHMs of 84 ms^{-1} and 64 ms^{-1}, respectively. When processing the data, it was clear in the 3 kV and 4 kV datasets that each transient had a very similar image charge because of their extremely reproducible form. However, the higher bias obviously increased the ions' speed. It is logical that using a high voltage or large electric field would accelerate the ions to a higher speed before entering the entrance capillary. The scatter plots showed that the distribution of velocity always depends on the clusters' charge where clusters with greater charge tend to be slower than ones with less charge. The charge-to-speed relationship can be fitted with $1/v^2$, suggesting that they might all have the same kinetic energy.

Another set of six examples of velocity distributions for the ions measured at 3.5 kV is shown in Figure 4.7. Various patterns were used in the distance position between the inlet capillary and the first skimmer: 12.3 mm in (a), 8.3 mm in (b), 14.8 mm in (c–e) and 4.6 mm in (f). The distance between the entrance capillary and skimmer 1 were modified to observe whether the velocity distribution varied. In all cases, 1 mM of a standard fluorescein solution (50:50 water:methanol) was utilised.

The histograms in Figure 4.7 (a–f) point out very similar distributions of velocity centred at 301 ms^{-1}, 294 ms^{-1}, 299 ms^{-1}, 296 ms^{-1}, 291 ms^{-1} and 307 ms^{-1}, with FWHMs of 61 ms^{-1}, 43 ms^{-1}, 34 ms^{-1}, 24 ms^{-1}, 32 ms^{-1} and 33 ms^{-1}, respectively. The histograms (b, c, e and f) show that each transient in the dataset has a fairly comparable image charge owing to their repeatable shape, while (a) and (d) are distinct from them because (a) has a larger width and (d) has a smaller width. Furthermore, repeating the data analysis distance of 14.8 mm three times, as shown in histograms (c–e), showed that their shapes were very similar together and demonstrated a narrower width in (d) than (c) and (e). The right-hand side of Figure 4.7 clearly demonstrates a relationship between charge and velocity. All the fastest moving drops have lower charges. The hypothesis in these experiments

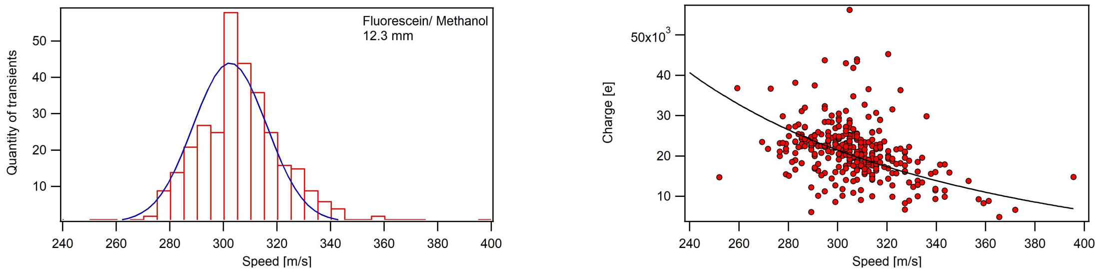

(a) 2 kV, ν =302.48 ms^{-1}, σ =19.414 ms^{-1}

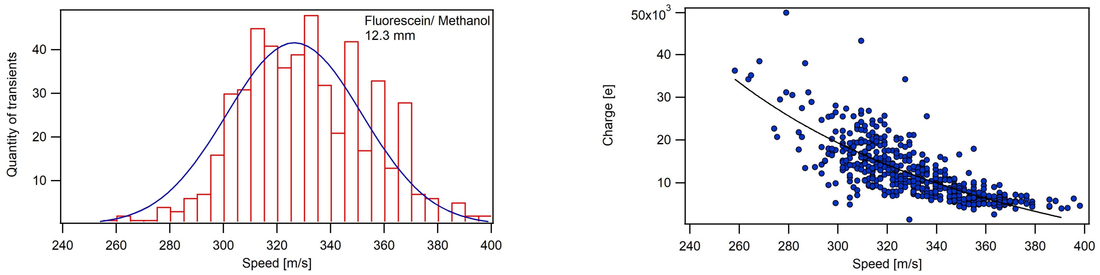

(b) 3 kV, ν =326.5ms^{-1}, σ =35.752 ms^{-1}

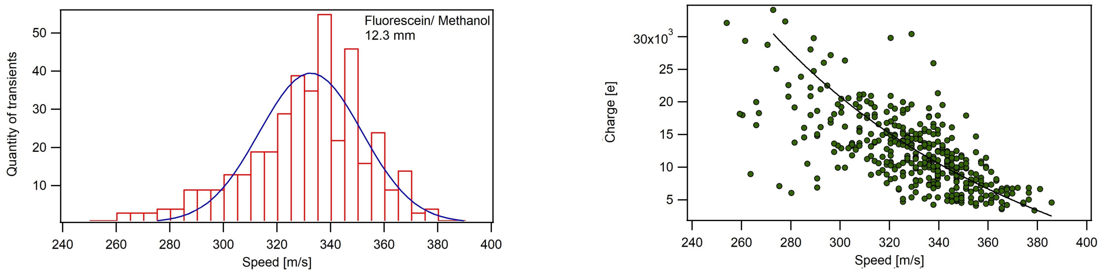

(c) 4 kV, ν=332.64 ms^{-1}, σ=27.076 ms^{-1}

Fig. 4.6. The left-hand side histograms of the velocity distributions for fluorescein dissolved in methanol sprayed at 2 kV, 3 kV, and 4 kV. The 12.3 mm was used as a distance between the entrance capillary and the first skimmer. The values cited as ν and σ indicate the mean and standard deviation measured from the data which is used to plot the Gaussian distributions. All histogram bins width is 5 ms^{-1}. The right-hand side plot is a scatter of the charge against velocity showing the correlation between these two quantities and fitting with a $1/v^2$ relationship.

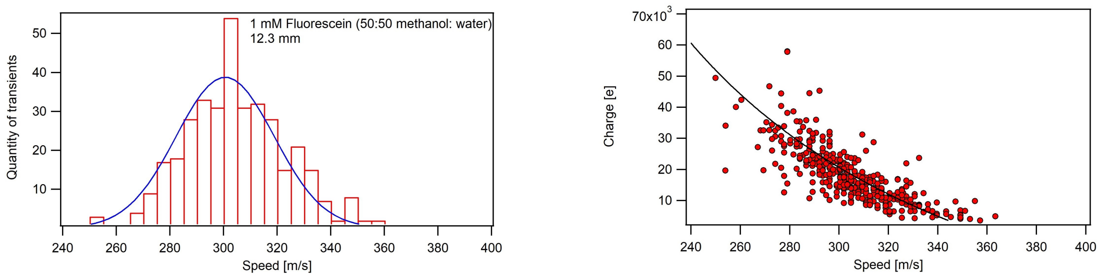

(a) 3.5 kV, ν =300.64 ms^{-1}, σ =25.89 ms^{-1}

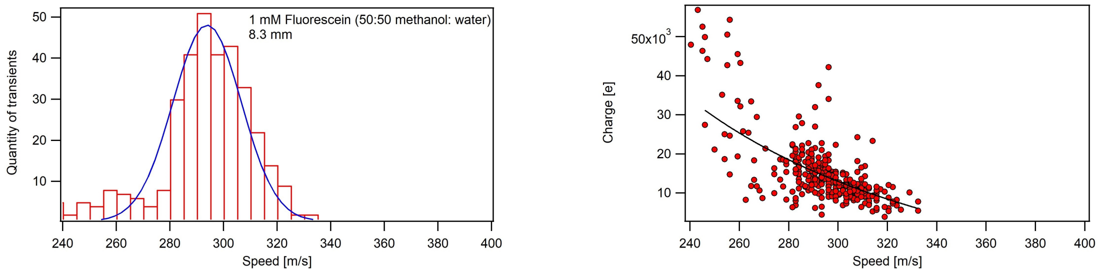

(b) 3.5 kV, ν =293.91 ms^{-1}, σ =18.063 ms^{-1}

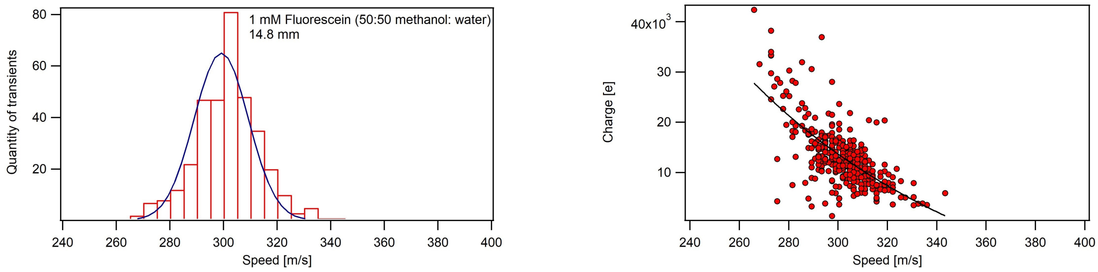

(c) 3.5 kV, ν =299.21 ms^{-1}, σ =14.314 ms^{-1}

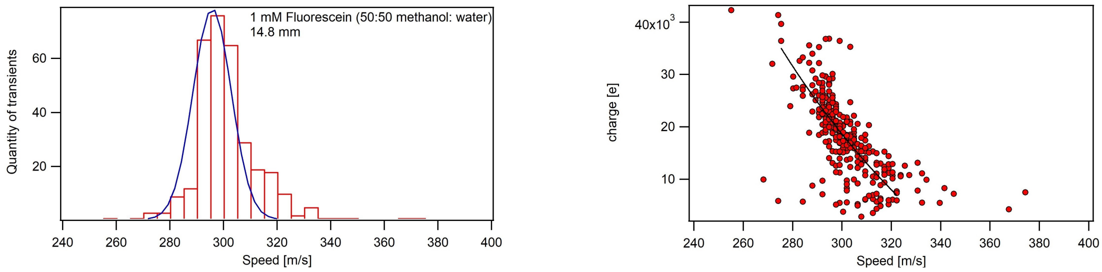

(d) 3.5 kV, ν =295.79 ms^{-1}, σ =10.073 ms^{-1}

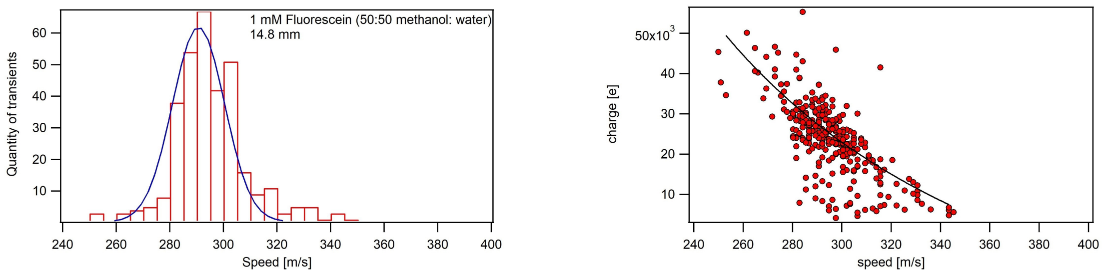

(e) 3.5 kV, ν =290.73 ms^{-1}, σ =13.748 ms^{-1}

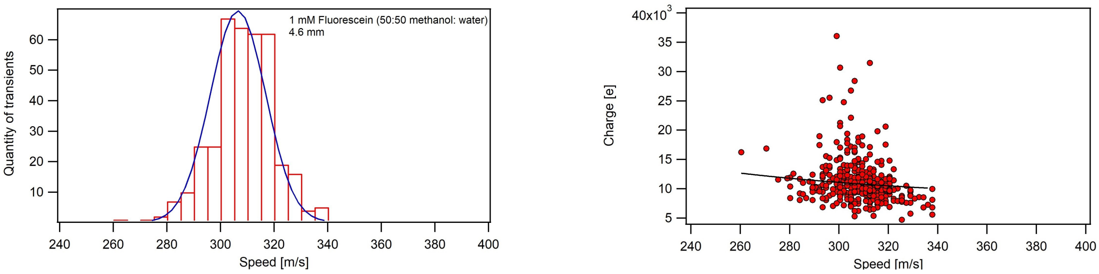

(f) 3.5 kV, ν =306.54 ms^{-1}, σ =14.613 ms^{-1}

Fig. 4.7. The left-hand side histograms of the velocity distributions for 1 mM a standard fluorescein solution (50:50 water: methanol) sprayed at 3.5 kV with differences between them in modifying the entrance capillary position in each case. The values ν and σ indicate the mean and standard deviation measured from the data which is used to plot the Gaussian distributions. All histogram bins width is 5 ms^{-1}. The right-hand side plot is a scatter of the charge against velocity showing the correlation between these two quantities and fitting with a $1/\mathrm{v}^2$ relationship

was that a shorter distance would make the histogram of velocity distribution narrow as can be seen in Figures 4.6 and 4.7, where all clusters are around 300 m/s to 330 m/s. Furthermore, the widths of the distributions suggest that they typically have narrow velocity distribution. The narrow distribution depends on the distance in stage 1 between where the ions exit the entrance capillary and where they enter skimmer 1. This hypothesis is not entirely correct since there is a dependence on mass. In fact, they do have a narrow speed, although there is a dependence on the mass where there is some evidence of speed dependence on charge, and by extension probably mass.

Figure 4.8 represents velocity distributions taken at various distances from Figure 4.7. It shows that there is a very slight dependence on the position of the first skimmer cone. This proves that decreasing this distance results in a slightly increased ion velocity due to sampling further into the adiabatic expansion within the Mach disc.

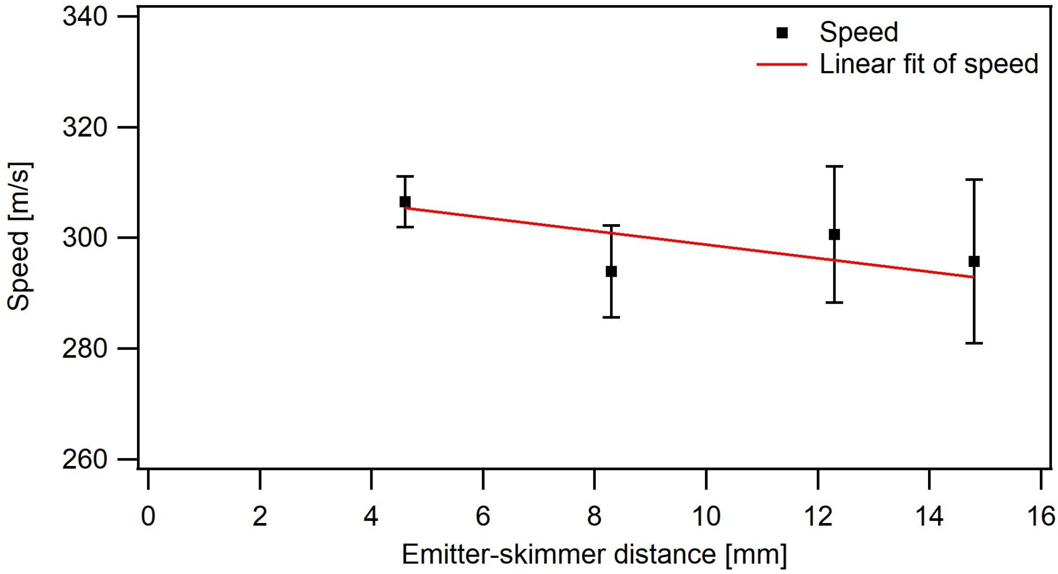

Fig. 4.8. Plotting data points between emitter-skimmer distance and speed to show similar velocity distributions.

In this system, it is expected that the speed of ions will be controlled by adiabatic expansion. Figure 4.9 is shown as a free-jet expansion after adding velocity distributions for all cases from histogram plots in Figure 4.7. The position of the Mach disc from the entrance capillary in stage 1 and skimmer 1 in stage 2 is given using the equation 2.2 (see section 2.2.1). The distance in the first vacuum-pumped stage was 5.3 mm. It was obtained by applying 0.25 mm for capillary diameter, an ambient pressure of 1,000 mbar and a vacuum pressure of 1 mbar, whilst the distance of 0.8 mm in the second vacuum-pumped stage was acquired using 0.4 mm for the first skimmer aperture diameter, an ambient pressure of 1 mbar and a vacuum pressure of 0.1 mbar. Adiabatic expansion in stage 1 with a position of skimmer 1 relative to Mach disc is shown in Figure 4.9a. All the speed distributions for distances 8.3 mm, 12.3 mm and 14.8 mm were outside the Mach disc, which means that they are less than the speed of sound except the speed distribution of distance 4.6 mm, which was inside the Mach disc. This means that the speed inside the Mach disc is much greater than the speed of sound, but the velocity measured in the image charge tube was less than the speed of sound. This is probably due to the position of the Mach disc in stage 2 which is so close to the first skimmer cone, where the ions always be captured outside the Mach disc if it

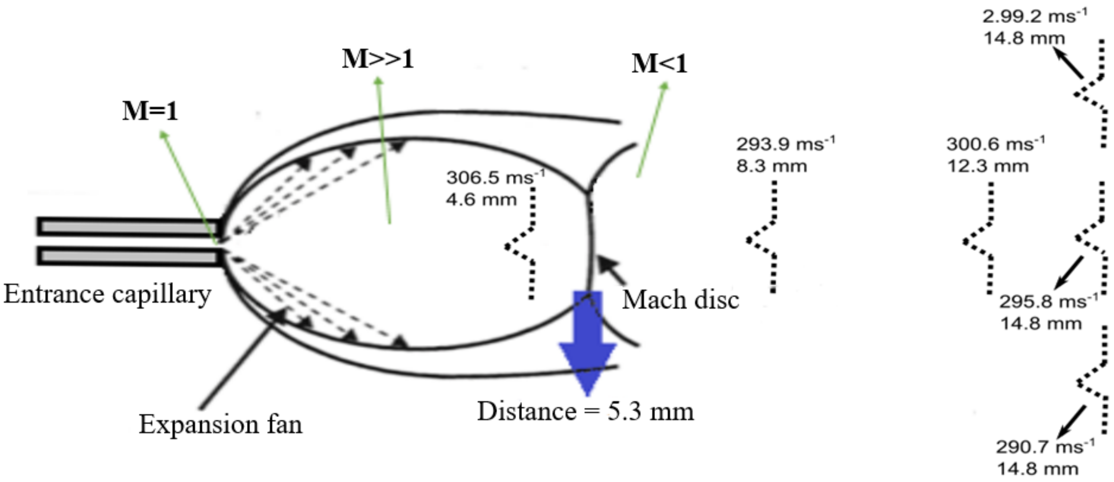

(a) Adiabatic expansion in stage 1 with skimmer 1 (not to scale)

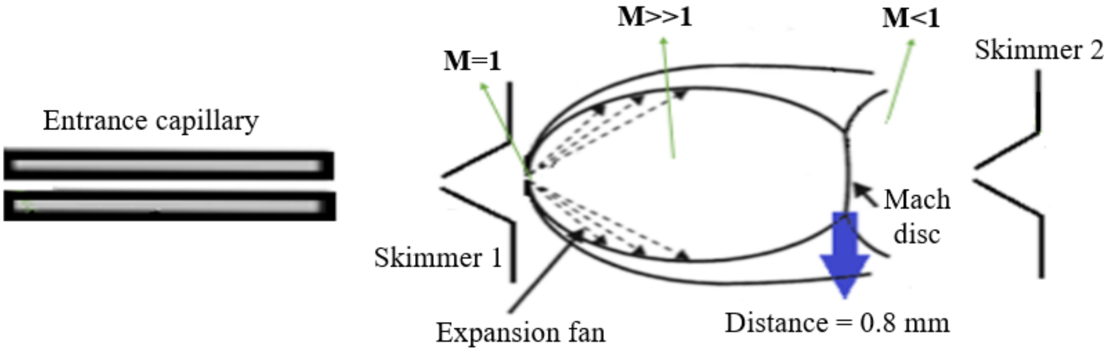

(b) Adiabatic expansion in stage 2 with skimmer 2 (not to scale)

Fig. 4.9. Adiabatic expansion after adding velocity distributions from previous Figure 4.7. The doted lines in (a) showing the position of skimmer 1 relative to Mach disc. The entire speed distributions out the Mach disc except for the velocity distribution of 307 ms^{-1}.

exists at all. Therefore, the opportunity for some thermalisation is always going to be there after that expansion because there will be residual gas molecules in stage 2, where the pressure is 0.1 mbar. So, there will be some scattering that probably reduces the overall velocity. In contrast, the adiabatic expansion in stage 2, where skimmer 2 is fixed with respect to skimmer 1, is seen in Figure 4.9b. All the speed distributions for 4.6 mm, 8.3 mm, 12.3 mm and 14.8 mm were on the external side of the Mach disc.

Briefly, the data showed that all the clusters were travelling through the drift tube with a speed within a rather small range despite having different sizes. However, the slowest clusters in all of these distributions tended to have a higher charge, giving them a lower speed. So, it is inferred that the heavy ions travel slower than the light ones. The fit with a $1/\mathrm{v}^2$ relationship indicated that they may all be thermalised in stage two, and they all have the same kinetic energy. It is worthwhile to keep in mind that dependence is only over a relatively narrow velocity distribution. If the ions are completely thermalised and all have the same kinetic energy, this would imply a relatively narrow size distribution. The reasons for this are not entirely clear but may indicate the preferential sampling of large ions in the image charge tube, as these will give clearly measurable signals, or it may be due to the preferential formation of large clusters in the beam. There is still scope for being able to deflect the ions using electrostatic deflectors further downstream, thus bending them based on their kinetic energy, but for this to lead to mass-selection, the kinetic energy would need to a large extent depend on their mass, while charge/speed data shown in this chapter are actually consistent with a constant kinetic energy model (see Chapter 5 for full details).

4.4 Conclusions

The data from an initial instrument with the ability to measure the charge and speed distributions of the ion beam were provided. The instrument was used to effectively measure the speed distribution for fluorescein sprayed from methanol using biases of 2 kV, 3 kV and 4 kV. The results showed that 3 kV and 4 kV give a mean velocity that is slightly greater than 2 kV, but 3 kV's and 4 kV's results were the same within uncertainty (they are both 330 ms^{-1}). In addition, the histogram data taken with 1 mM of a standard fluorescein solution sprayed at 3.5 kV with distance adjustments applied to the entrance capillary in each case (12.3 mm, 8.3 mm, 14.8 mm and 4.6 mm) demonstrated a narrow speed distribution, as illustrated in Figures 4.7 and 4.8.

Velocity distributions in adiabatic expansion showed that all were less than the supersonic speed, unlike the speed distribution for a distance of 4.6 mm, as shown in Figure 4.9. The 4.6 mm was inside the expansion fan, so it should be $v \gg 300$ m/s, but it is not. This might be because of the second expansion in skimmer 2, where the Mach disc is very close to skimmer 1, so the ions capture outside the expansion fan. There is sufficient gas in stage 2, as the pressure is 0.1 mbar in this stage, which slows down the speed of the ions and thus spends their energy as a result of exposure to collisions. In fact, we are not sure why there are no more differences, especially at the largest distance in stage 1. Perhaps a good follow-up experiment would be to increase this distance even further, although this would require redesigning the first stage to accommodate a larger distance.

These experiments have formed large clusters of relatively narrow distribution of cluster sizes with a correspondingly narrow distribution of speed. These clusters probably formed in adiabatic expansion in the first stage, regardless of where they sampled, or they may have formed in the rapid cooling of the plume where there is nothing happening afterwards in the system to break them into smaller clusters. Large clusters give nice large transient signals as they enter the drift tube, and they can be seen clearly by measuring the current using electronics. However, if these clusters are smaller, the signal becomes weaker, and therefore, this signal becomes buried in the noise where it cannot be seen. In order to see noise signals, there is need to use much more sensitive electronics and eliminating the noise somehow. Thus, the experiment should be performed on an isolation table, as the instrument is very sensitive to vibration. It is interesting to note, however, that there is not a continuous distribution of cluster sizes, as otherwise, it would observe transients of intermediate amplitudes in spectra such as those shown in Fig. 4.5. Instead, a series of transients all with very similar amplitudes has been observed. This would be the case if cluster formation in the system favoured a particular size. In this picture, it could still be the case that the beam contains very small clusters, and even individual molecules that would give signals masked by the background noise, but the only clusters formed are those within a relatively narrow size distribution.

Absolute charge information would require calibration against a known ion source, such as an Argon ion sputter gun, which it is not done. However, mass/charge information has been acquired, and this provides insight into the composition and energetics of the ion beam in our system. In the following chapter, the response of the ion beam to an electrostatic field in an attempt to deflect the beam is explored. This has two potential advantages. The first would be to separate the neutral molecules from the charged ions. The second could be a method to disperse the beam according to the mass of the molecules or clusters. However, this relies on the ions maintaining a constant velocity rather than constant kinetic energy.

Chapter 5

Towards A Supersonic Mass-selected Electrospray Deposition system and Separation of Neutral and Charged Species

5.1 Introduction

The electrospray technique is well established in mass spectrometry and has more recently been used in the deposition of a wide range of complex molecules in-situ with large organic molecules and inorganic clusters [59, 86]. Soft and reactive landing using mass-selected onto surfaces is considered the most popular addition to sources of electrospray deposition. Mass selection is typically utilised in mass spectrometry for one or more of the quadrupole mass filters [130]. Some literature [100, 101] has used systems with mass-selection integrated into their electrospray. The design includes a quadrupole mass filter and a bending quadrupole (a quadrupole deflector) to filter charged beam impurities and then prevent neutral species (i.e. solvent molecules) originating in the ion source from reaching the substrate in the high vacuum chamber.

The electrospray ionisation (ESI) process generates an ion beam from a solution that includes the molecules to be deposited. As shown in Figure 3.2 (see Section 3.3.2), this technique passes the solution through an electrospray capillary emitter by applying a high voltage (2–4 kV), which pulls the liquid out of the emitter into a sharp cone known as a Taylor cone. The electric field plays a significant role in disintegrating charged droplets, contributing to aerosol formation [6, 48]. The surface of the jet contains an excess of charged ions that divide the jet into a sequence of newly generated droplets charged near the theoretical Rayleigh limit [49]. The ionised droplets enter through the entrance capillary and a group of differentially pumped skimmer cones to minimise the pressure at all stages into the ultra-high vacuum (UHV) range, then exit the final skimmer of the system to the deposition chamber to be deposited on the surface.

In this simple method, no ion optics are used to control the beam through a series of differentially pumped skimmers compared with other developed electrospray deposition instruments, as mentioned in references [86, 100, 101], which include ion optics to control the molecular ion beam. The biggest downside of this method is that there is no mass selection of the ion beam used, where everything in the original solution has access to the surface. In certain situations, this is a significant obstacle, including solutions where counter ions occur, buffers and the distribution of molecules. In addition, it prevents any use of extremely reactive surfaces towards the carrier fluid. Thus, the main goal of this work is to present the solution to this issue by designing the mass-selected electrospray deposition instrument.

A few groups worldwide [91, 101] follow this method since the current mass-selected electrospray deposition systems are incredibly expensive when designing a device that can be installed in numerous research laboratories. In these systems, the mass selection is accomplished through high-priced precision devices with complex electronics, such as quadrupole radio frequency-direct current (RF-DC) filters, which, in most cases, cannot be used with massive molecules because quadrupole mass filters have a specific mass range determined by their geometry. A quadrupole mass filter is one such significant instrument in the field of multipole ion guides. The quadrupole mass filter (sometimes called a quadrupole mass analyser) is used for two primary purposes: to analyse ion beam characterisation. Besides this feature, it is utilised to transfer ions from one system phase to another [131]. The mass filtering is obtained using radio frequency and direct current voltages to produce an electric field. If the ions have a certain m/z, they flow steady and are permitted to pass through, but in the case of having a different m/z, they have an unsettled route and thus are unable to pass. Likewise, they are useless in preventing neutral molecules from reaching the surface because neutrals are unaffected by electrostatic fields, so the quadrupole cannot manipulate them. More high-precision equipment and electronic control systems are required; an electrostatic quadrupole deflector, also known as a quadrupole bender, uses an electric field to direct the ion beam at a 90-degree angle to eliminate them from neutral species. In this chapter, the use of simple electrostatic deflection plates to separate out two molecules from a solution to deposit selectively is explored, for example, fluorescein, ferrocene and a combination of fluorescein and ferrocene where the chemical structures are depicted in Figure 5.1. The aim of this work was to develop a very low-cost, compact method for manipulating an electrospray ion beam in terms of filtering based on kinetic energy and charge.

The ESI technique is most convenient for ionic or highly polar dyes, as Holcapek et al. mentioned in their paper on the effects of functional groups on the fragmentation of dyes in electrospray and atmospheric pressure chemical ionization mass spectra [132]. Adolf von Baeyer synthesised organic dyes in 1871, which won him the Nobel Prize in Chemistry in 1905 [133]. Fluorescein is an organic molecular compound, and it has the formula $C_{20}H_{12}O_5$. It is available as an orange-red powder dissolving in certain alcohol such as methanol and ethanol. Also, electrospray mass spectrometry (ESMS) has been developed to study thermally unstable and non-volatile materials, such as ferrocene compounds. Ferrocene compounds are particularly important elements to investigate through the electrospray ionisation mass spectrometry (ESI-MS) because of having characteristics of electrochemical oxidising on the electrospray needle [134]. Also, it has been observed that ferrocene and some of its derivatives readily oxidise with the ferrocenium cation formation through electrospraying [135, 136]. Ferrocene molecular ions are produced through the ferrocene oxidation technique during the gas stage under the 'reverse' ESI conditions in the presence of ferrocene vapour [137]. Ferrocene compounds have become a major focus of research in the past two decades because of their wide range of applications in catalysis, medicinal chemistry, organic synthesis and others [138–140]. Ferrocene is available as an orange-yellow powder, and its formula is $C_{10}H_{10}Fe$, as mentioned in its chemical structure (see Figure 5.1).

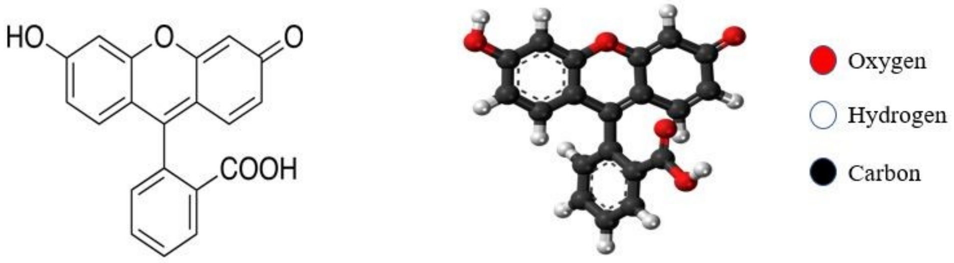

(a) Fluorescein

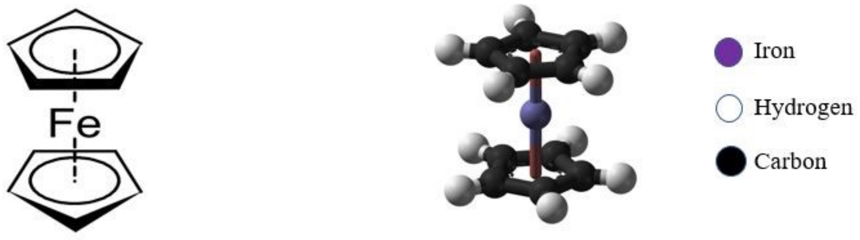

(b) Ferrocene

Fig. 5.1. 2D and 3D chemical structure of the a) fluorescein (consists of four benzene rings modified by the presence of a carboxylic (COOH), a carbonyl (C=O), a hydroxyl (-OH), and an ether type bonding (C-O-C)), b) ferrocene (iron centered between two cyclopentadienyl rings) [141–143].

In the case of using deflection voltage to bend the graphene oxide (GO) beam, the solvents are only deflected, and the GO continues straight. This may occur because GO is a considerably large molecule and forms very large clusters, much bigger than clusters of ferrocene and fluorescein. Therefore, GO clusters cannot be deflected since they have too much energy, so no deflection voltage has been employed in taken dataset.

In addition to simple electrostatic deflection plates, this chapter also explores the use of the electrostatic Einzel lens (called a unipotential lens), as shown in stage 4 in Figure 5.2. The Einzel lens is a widespread lens design. The unique characteristic of unipotential lenses is that both the object and image sides have the same stable potential. In principle, the Einzel lens would be extremely useful to focus electrospray beam in stage 1 of the system so that it can collect more of beam through the 0.4 mm aperture in the first skimmer cone. However, the Einzel lens in this region would require a high voltage to overcome the high energy of the accelerating ions at the pressures in this region. The high voltages cannot be applied as they may cause arc. Instead, the need to use advanced optics is required, such as ion funnels, to achieve this, which was not feasible in this project [144]. Instead, in this experiment, especially in stage 4, the Einzel lens has been used to spread the beam out over the sample or at least explore this approach since the pressure in this stage is low enough to sustain the high voltage without arcing. The dataset has been presented here to explore defocusing within the Einzel lens using a sodium chloride (NaCl) solution with x-ray photoelectron spectroscopy (XPS) measurements. This is an important goal because the formation of functional thin films on surfaces, in most cases, requires a homogeneous coverage of molecules over a larger area than the unmodified ion beam, which is typically only 2 mm in diameter.

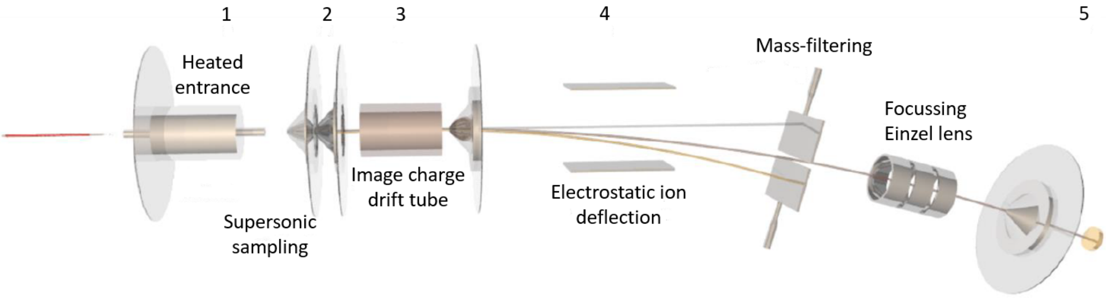

Fig. 5.2. A schematic instrument for mass-selected electrospray deposition. A supersonic sampling stage speeds up molecules to a narrow speed distribution that is measured using an image charge drift tube. The ion pathways will disperse in the electrostatic ion deflection stage based on the mass and charge where the neutral molecules continue straight, lighter ions are deflected beneath the exit slit, whilst heavier ions are directed toward the slit to the Einzel lens and then into the sample through the final system aperture.

5.2 Instrumentation

In the previous chapter, all distributions of cluster speeds (Gaussian distribution) are within a narrow range of 300 m/s ± 330 m/s. Therefore, in this chapter, the mass of the clusters is selected using deflection plates, as schematically illustrated in Figure 5.2, which bend the beam based on their kinetic energy, where their kinetic energy will be related to their m/z (and their speed - see Chapter 4).

The first two vacuum stages and the third stage are discussed in the previous section 4.2. The beam travels through the third skimmer to the deflection chamber, which contains an electrostatic deflection field in stage 4 at a pressure of 10^{-6} mbar range. The beam in the deflector stage incorporates low-mass molecular ions, high-mass molecular ions, and neutrals molecules. Assuming the starting hypothesis of near-constant ion velocity, the ion pathways distribute using deflector voltages based on the masses of the ions. The trajectory of ions is improved by controlling the high-voltage power supplies of the deflection connecting positive and negative biases via Bayonet Neill–Concelman (BNC) cables to deflection plates through an electrical feed-through flange. Neutral molecules keep going in a straight line, whereas the lighter and heavier molecules are deflected onto a parabolic path determined by their energy, which depends on their mass, as observed in Figure 5.2. Heavy molecules have higher kinetic energy than lighter molecules. The plates shall be placed at the center axis of the chamber and more than 5 mm away from any point of the chamber wall because even in a vacuum or the pressures that are using high voltages in the kilovolt range can still arc over short distances to the grounded chamber.

As shown in Figure 5.2, stage 4 also contains two moveable knife edges shaping a selection slit to assist the mass-filtering. The slit is closed to a narrow width and placed at a well-defined angle to permit the window of ion masses to reach the refocusing lens and then to the sample in the UHV chamber through the final aperture. The slit can also be applied to filter out heavy and low-mass solvent molecules using different widths, angles, and deflector voltages. To control the ion current hitting the slits, they ought to be linked separately to electrical feed-throughs using a picoammeter. The main reason for doing this is to improve the system and explore the distribution of ion energies in the beam. For characterising the system, The split targets (two targets) have been used instead of representing the knife edges and thus bending the beam to hit the two targets simultaneously as illustrated in Figure 5.3, which is the same as the beam going between the two edges of the knife edges. These targets are connected to two electrical feed-throughs using a picoammeter (Keithley) to observe the ions' current hitting the targets at different deflection voltages and discover the distribution of ion energies in the beam. These Keithley instruments are also coupled to the computer serial port using an RS-232 cable to record electrostatic ion deflection data as a graph on MATLAB program, which is considered the easiest way to know at which point in the graph has the same current. Both targets in this project do not cover the center of the vacuum flange, so the Keithley instrument cannot measure the straight beam on either target if the deflection voltage is not used. The main aim of using the central target is to check whether the electrospray is actually working as it should by measuring the straight beam. Ideally, three targets should be attached to three Keithley instruments, but to minimise cost, the target configuration is replaced and then changed back again. Similarly, in the fully integrated system, the targets are replaced by a 1 mm offset aperture to represent the knife edges where the sample was placed after the aperture to perform the deflected deposition experiments as shown in Fig. 5.4.

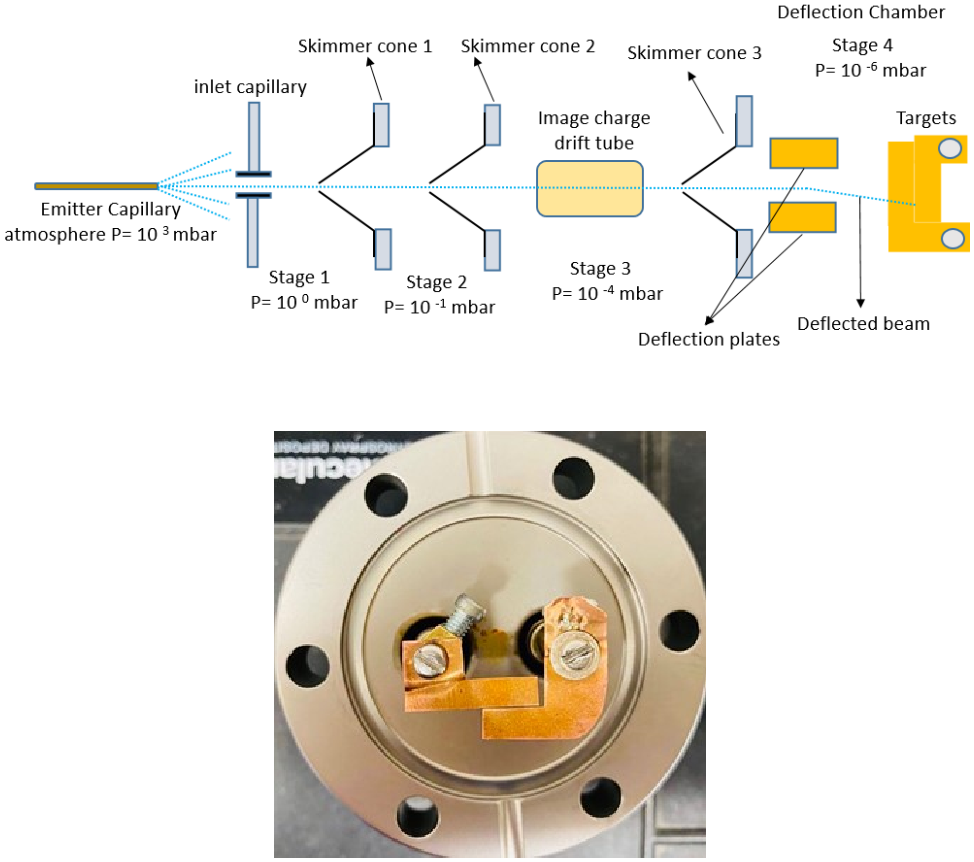

Fig. 5.3. A schematic of the electrospray source showing hitting the beam between the two targets when deflection voltage is applied to plates (top). Photograph of the targets placed away from the flange center (bottom).

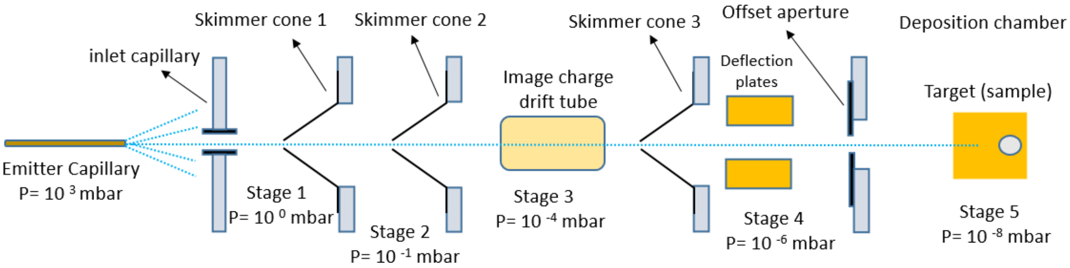

Fig. 5.4. Schematic drawing of the electrospray deposition system showing offset aperture to carry out the deflected deposition experiments.

As displayed in Figure 5.2, the heavier ion masses reach the refocusing lens and then the final skimmer cone slit, impinging on the sample. The main purpose of using this lens is to focus the ion beam through the aperture, causing the beam to diverge on the other side of the aperture to deposit over a large area on the sample surface. The Einzel lens consists of three ring electrodes arranged in a row to which a voltage is applied to the central electrode. In the defocusing experiments of this project, the Einzel lens replaces the deflection plates, and a sample is placed where the targets would be to perform deposition, as can be seen in Figure 5.5.

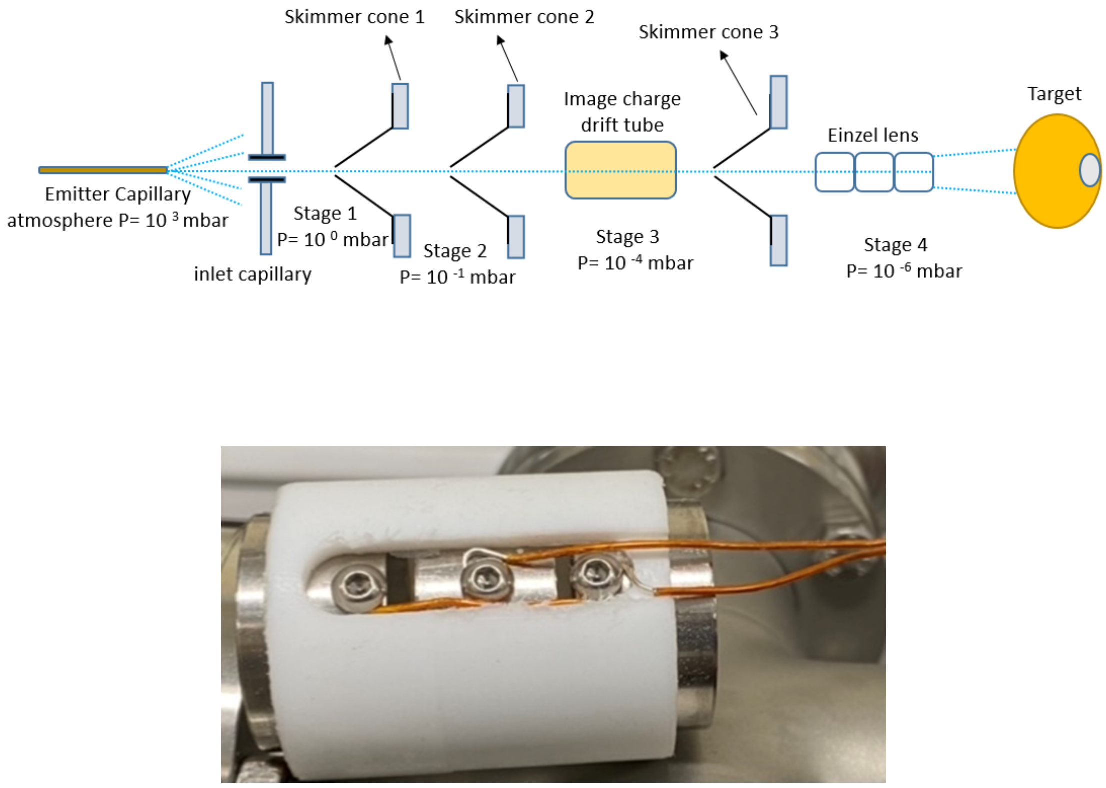

Fig. 5.5. The electrospray deposition source used the Einzel lens to defocus the beam (top). Photograph of the 20 mm internal diameter Einzel lens assembly taken in the laboratory (bottom).

Stage 5 is the UHV chamber, called the deposition chamber, in which the instrument is connected to an XPS. The pressure in this stage reaches 10^{-9} mbar range due to the removal of the solvent molecules from the beam and the differential pumping provided by the final skimmer slot.

5.3 Methods, Results and Discussion

5.3.1 Electrostatic ion deflection data from spraying fluorescein (50:50 methanol and water)

1 mM of the standard fluorescein solution was dissolved in 50:50 methanol and water and was sprayed at +2295 V. An electrostatic ion deflection experiment was taken in this research by following steps. Initially, during the electrospray process, the positive and negative voltages on the deflector plates were gradually raised from the voltage source to allow the ion beam to bend to hit the first target, continuing to increase the voltage on these plates to direct the ion beam to the second target. The two picoammeters were used simultaneously to measure the ion current hitting the targets and obtain roughly equivalent currents. Then, to attain equal current on both targets simultaneously, optimising the path of the beam through the system was needed by controlling the voltage supply of the deflection plates, which was generated as a graph with the MATLAB program, as shown in Figure 5.6.

At zero voltage, the ions beam passes straight through deflection plates; thus, it is infeasible to measure the current through the undeflected beam because the position of both targets is not in the middle of the vacuum's flange, as has already been shown in Figure 5.3. In Figure 5.6, the high blue data shows that the curved ions began to hit the top target at a deflection voltage of ±2000 V while hitting the second target occurred at ±3400 V, as demonstrated by the high red marks (This is not shown in the data since key measurements are when the currents are equal). Moreover, it can be seen that ions impinge both targets simultaneously between 600 seconds and 1000 seconds, with an average voltage of 3150 V ± 50 V. The blue data are clearly higher due to hitting the large droplets or ions in the upper target, whereas the red data rise is attributed to hitting the lower target through the small droplets or ions. Using high deflection voltage may cause some ions to deviate completely from the second target, so it is important to increase the deflection voltage slowly.

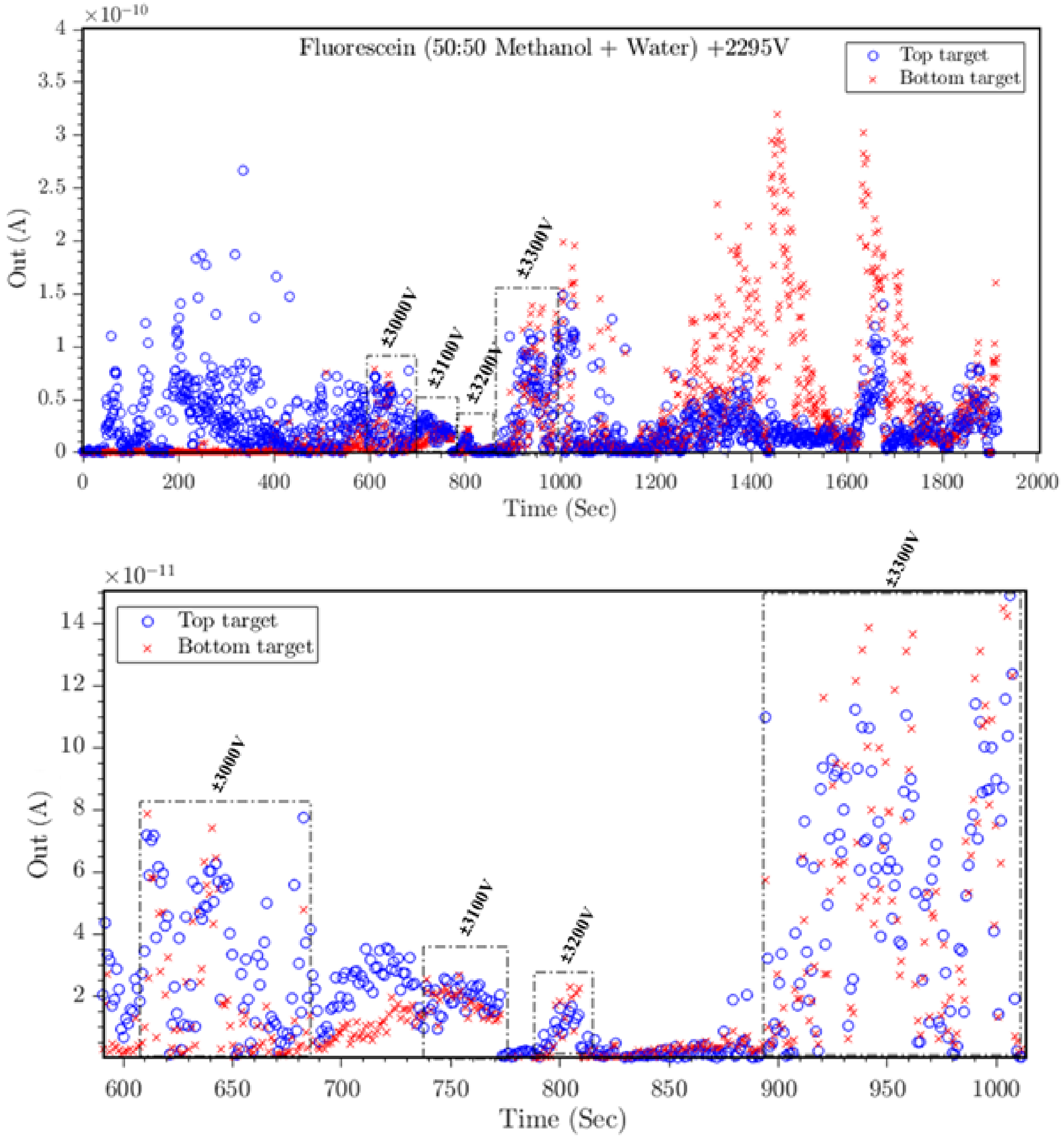

Fig. 5.6. Data collected using electrostatic ion deflection for 1 mM of a standard fluorescein solution (50:50 water and methanol) sprayed at +2295 V. Blue spots refer to the Top target, and red markers refer to the Bottom target. The dash-dotted lines indicate the different deflection voltages that were used to obtain equal ion currents at both targets. The bottom plot zooms in for equal currents marked in the top plot with dash-dotted lines.

5.3.2 Electrostatic ion deflection data from spraying fluorescein dissolved in methanol

In this experiment, a concentration of 0.1% (w.t.) solution of fluorescein dissolved in methanol was used. As illustrated in Figures 5.7 and 5.8, these data were collected using various electrospray voltages at +1880 V and +2100 V, respectively.

As in the previous experiment, the ions beam also started to hit the top target at deflection voltage of ±2000 V (not shown in the data). As shown in Figure 5.7, the current was equal at the average deflection voltage of 3150 V ± 50 V (appearing as blue and red data) represented by the dashed line sprayed at +1880 V. In addition, the ions reached the bottom target at deflection voltage ±3500 V, determined by the solid rectangular shape. On the other hand, at +2.1 kV, equal currents were achieved also with the average of 3150 V ± 50 V (viewed in Figure 5.8), which can be seen clearly by the dash-dotted line. The ions were deflected in the direction of the bottom target at ±3400 V, also defined by a solid rectangular form.

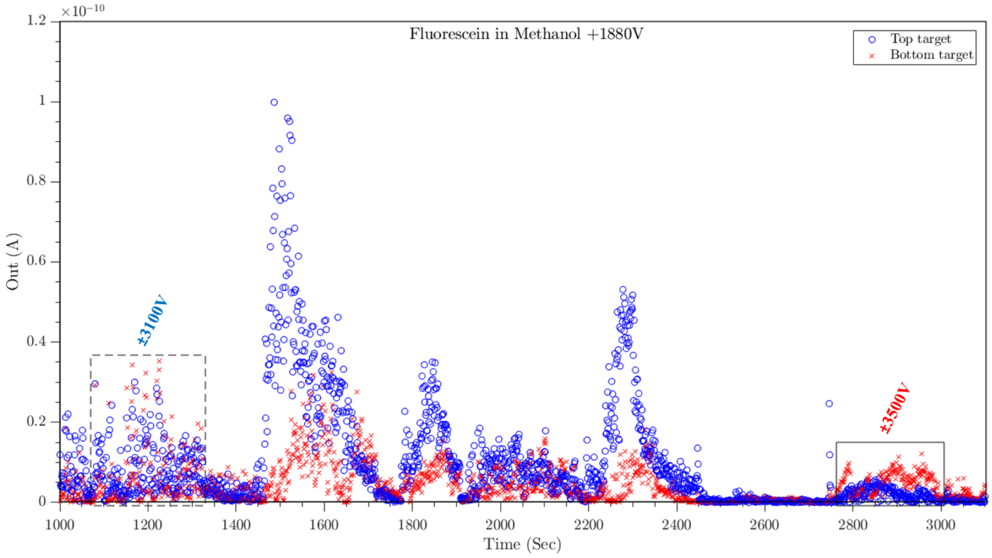

Fig. 5.7. Plot zoom of the data collected using electrostatic ion deflection for fluorescein solution in methanol sprayed at +1880 V. Blue data points indicate to out 1 (Top target). Red markers symbolize to out 2 (Bottom target). The dashed line applies for the equal currents. The solid rectangular shape refers to the ions struck the bottom target with deflection voltages of ±3500 V.

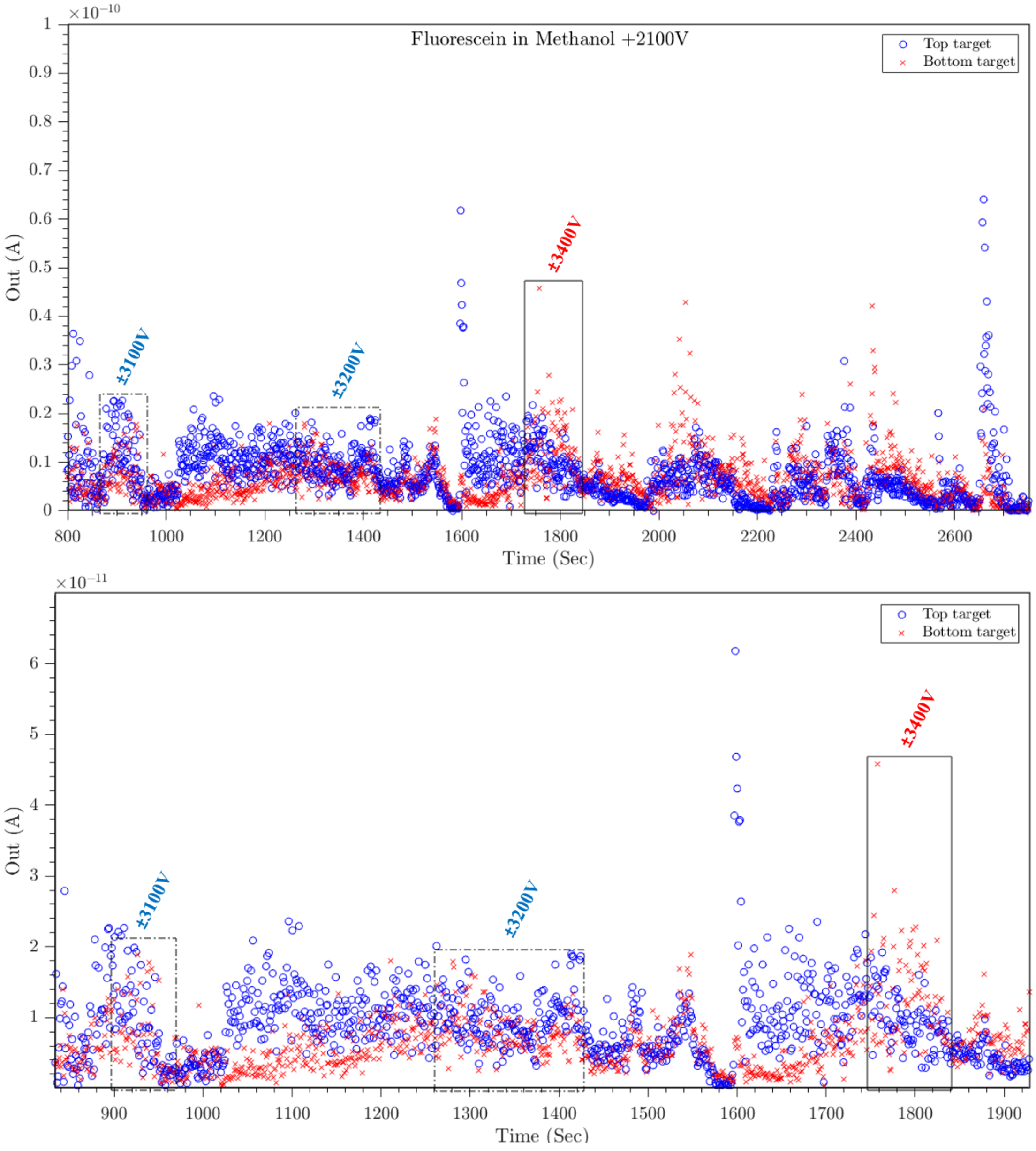

Fig. 5.8. Plot zoom of the data collected using electrostatic ion deflection for fluorescein solution in methanol sprayed at +2100 V. Blue data points indicate to out 1 (Top target). Red markers symbolize to out 2 (Bottom target). The dash-dotted lines indicate the same currents. The solid rectangular shape refers to the ions struck the bottom target with deflection voltages of ±3400 V. The bottom plot zooms in for marked data in the top plot.

The molecules that require a large deflection voltage have a higher ratio of kinetic energy to charge. In addition, the equal currents in these data are always found within a narrow deflection voltage range, implying that everything in the beam has similar kinetic energy. Several high blue data points in Figure 5.7 have been recorded near 1600, 1850, and 2300 seconds. This is due to the large droplets that have much more energy and would require a higher voltage to deflect them by the same amount to hit the upper target. Likewise, there are high blue data points at 1600 and 2700 seconds in Figure 5.8. This has been also attributed to larger droplets. But there are obviously smaller clusters within the beam that may change the electrospray conditions that we do not know exactly why they form. They are deflected more and thus hit the bottom target. Briefly, it is harder to bend the high-mass clusters and therefore hit the upper target, whereas the low-mass clusters bend more to hit the bottom target. After finishing the electrospray operation, the entrance capillary is regularly flushed with methanol for approximately an hour to prevent clogging by the highly concentrated solvent; however, dilute solutions usually make this manageable.

These data are the same as the data taken for fluorescein (50:50 water and methanol) shown in Figure 5.6. The currents are similar at the average deflection voltage of 3150 V ± 50 V, as can be seen in Figures 5.6, 5.7 and 5.8. In both cases, fluorescein clusters up, giving similar-sized clusters, which require a similar voltage to deflect. It should be considered that the electrospray voltage and flow rate on the syringe are important matters for obtaining a good spray. Electrospray voltage may vary with solvent mixtures, like methanol and water, compared to methanol.

5.3.3 Electrostatic ion deflection data from spraying ferrocene dissolved in methanol

A solution of ferrocene dissolved in methanol sprayed at +2 kV has been used. Ions, as usual, began to reach the first target at the deflection voltage of ±2000 V and attained the second target using a defection voltage of ±3800 V (not shown in the data). Figure 5.9 shows that the ion beam fell off on both targets at the same moment using the average of 3650 V ± 50 V given by the dash-dotted lines.

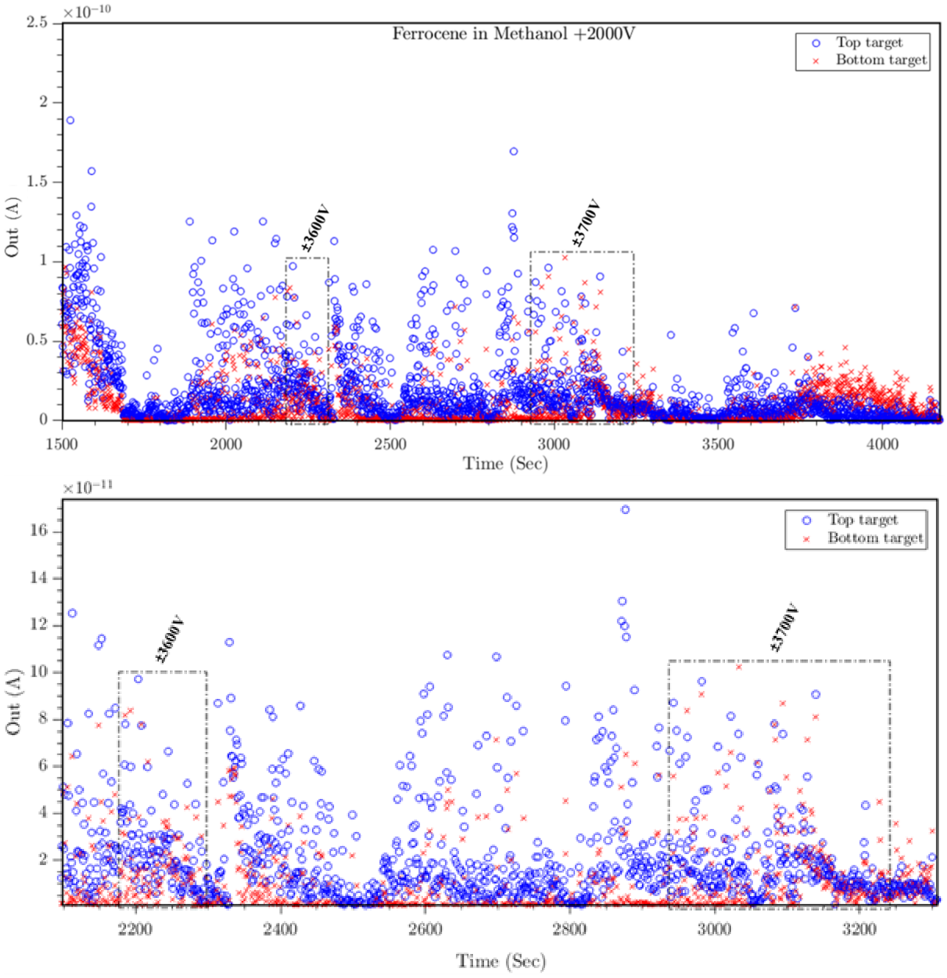

Fig. 5.9. Plot zoom of data collected using electrostatic ion deflection for ferrocene dissolved in methanol sprayed at +2000 V. Blue and red data refer to ions hitting the top and bottom target, respectively. The dash-dotted lines indicate the equalized currents on both targets at average of 3650 V ± 50 V. The bottom plot zooms in for equal currents marked in the top plot with dash-dotted lines.

By comparing ferrocene data in Figure 5.9 with fluorescein data as shown in Figures 5.6, 5.7 and 5.8, the results are completely different according to the mass of the formed clusters and not due to the molecular ions' mass. The ferrocene weight is 186.04 g mol^{-1}, whereas fluorescein is 332.31 g mol^{-1}. The fluorescein ions hit both targets simultaneously using the average deflection voltage of 3150 V ± 50 V, unlike the ferrocene, where ions hit both targets at the median deviation voltage of 3650 V ± 50 V. In all cases, what is changed between these two experiments is the molecules in the beam. Fluorescein and ferrocene form large clusters that require a higher voltage to deflect by the same amount. The very heavy ions will be explored in more detail with the SIMION simulations.

5.3.4 Electrostatic ion deflection data from spraying a mixture of ferrocene and fluorescein dissolved in methanol

A mixture of fluorescein and ferrocene in methanol sprayed at +2992 V was used. The idea of this experiment was to separate two components of the beam for the solution selectively, which are the lighter (low-mass) and heavy (high-mass) molecules using electrostatic ion deflection plates. These plates bend the beam based on its energy depending on its mass. The low-mass molecular ions are deflected more than the high-mass molecular ions.

As depicted in Figure 5.10, the ions at the deflection voltage of ± 3300 V have reached equal currents (i.e. hitting both targets simultaneously), determined by the dash-dotted lines. This is likely to have been created by clusters formed from heavier molecules (i.e. fluorescein). Similarly, the ions hit both targets again but by applying a mean deflection voltage of 3850 V ± 50 V, defined by the dash-dotted lines, which are supposed to be generated by clusters formed from the lighter molecules (i.e. ferrocene). These large clusters are formed from fluorescein and ferrocene molecules containing millions of molecules and lots of charges and therefore require more voltage to be deflected. Between 600 seconds and 1500 seconds, the high blue data points reoccur, which probably refers to the large drops hitting the top target simultaneously as the ions are deflected to obtain similar currents in the two targets. Furthermore, using ±4000 V allows the ions to strike the bottom target. The results of these experiments have been summarised in the following Table 5.1.

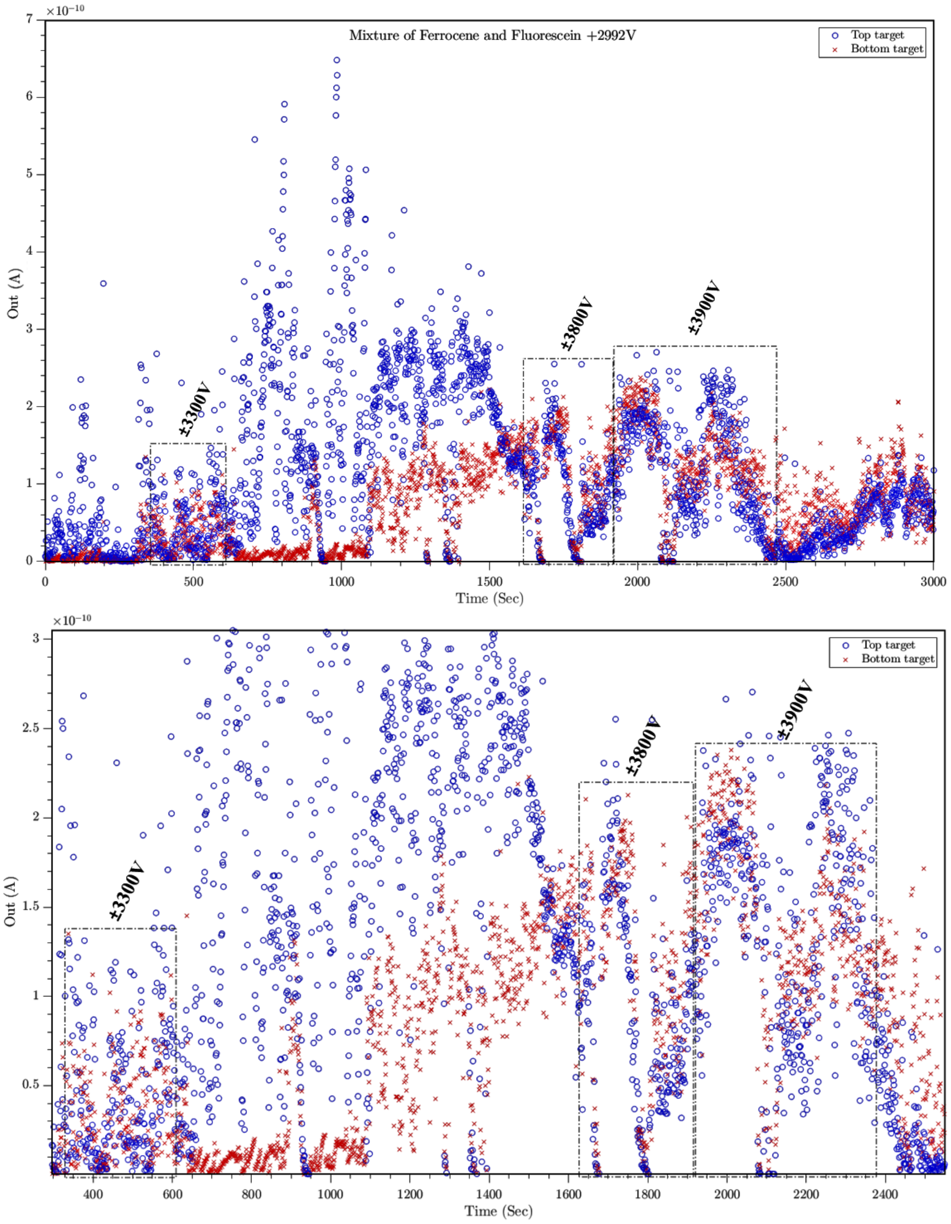

Fig. 5.10. Data collected using electrostatic ion deflection for a mixture of ferrocene and fluorescein dissolved in methanol sprayed at +2992 V. Blue data points indicate to top target, and the red cross markers symbolize to bottom target. The dash-dotted lines point out equalized currents. The bottom plot zooms in for equal currents marked in the top plot with dash-dotted lines.

Molecule	**Electrospray voltage**	**Deflection voltages applied to both negative and positive plates resulting in equal target currents**
Fluorescein (50:50 methanol:water)	+2295V	3150V ± 50V
Fluorescein in methanol	+1880V/+2100V	3150V ± 50V
Ferrocene in methanol	+2000V	3650V ± 50V
A mixture of fluorescein and ferrocene in methanol	+2992V	±3300V (created by fluorescein clusters) 3850V ± 50V (generated by ferrocene clusters)

Table 5.1. Results of the electrostatic ion deflection experiments when deflection voltages hitting both targets simultaneously.

The results are unexpectedly opposite of our predictions based only on the masses of the ions. Not measuring the velocity of the ions using ferrocene should be considered. Ferrocene requires a high voltage to be bent by the same amount, implying that the particles have a higher ratio of kinetic energy to charge. Ferrocene might be travelling with the same velocity as the fluorescein, where it forms either large clusters so that their kinetic energy is considerable or makes small clusters with lower amounts of charge and therefore is not affected by the electric field. The final suggestion might be that ferrocene clusters thermalise to a higher kinetic energy than fluorescein clusters, where the increased deflection only results from the difference in kinetic energy.

The ion drift tube can only detect the amount of the clusters' charge, not their precise size. It is worthwhile mentioning that the ions measured in the drift tube velocity experiment cannot be individual ions because a very wide range of charge values has been observed. For instance, if they are single ions with very small charges, thus a quantisation in the charge would be seen. Whilst there is no quantisation in the charge, rather there is a very smooth range of charges, which refers to a large number of charges on each cluster. The only way this can be achieved is to have clusters of molecules with a large overall charge. Therefore, the different deflection voltages required for the two molecules have no relation with the mass of the individual molecules themselves but rather the m/z of the large clusters they form. Any thermalisation that occurs with residual gas molecules in stages 1 and 2 might mean that they converge on a different kinetic energy. Therefore, the need to use SIMION simulation is required to gain insight into the size of these ions.

It requires the use of a voltage of less than 1 volt to bend individual molecular ions onto the upper target, which has never been attempted in these experiments because high-voltage power supplies have been used to bend large clusters. Future experiments should focus on very low voltage to see how the individual molecular ions would be performing. The only way to get some kind of idea of ion performance is to know the current has been measured on the central target. The typical current straight-through beam is 0.1 nA, and the typical deflected beam hitting the top target is up to 0.1 nA, as shown in Figures 5.7 and 5.9. If the straight-through beam has the same current as the bent beam, the deflected heavy clusters are the main contribution of the beam. Conversely, if the current of the bent beam, as shown in Figure 5.8, is less than the straight beam, this means there are other components within the ion beam that are not detected in the deflected beam because they are either very small or very large, and no voltage high enough has been applied to bend it to the target.

5.3.5 SIMION Simulations

An ion optics simulator software (SIMION) is compatible with a wide variety of systems, incorporating lenses, mass spectrometry and many types of particle optics devices. This method is employed to simulate the ions passing through the electrospray rig, allowing a comparison of ion masses with previous results of deflection experiments.

The deflection of ions via an electrospray system is determined by the voltage applied to deflection plates. This can be observed in several SIMION simulations in Figure 5.11, where the use of ±0.01 V on the deflection plates led fluorescein ions to travel through an electrostatic lens, ferrocene ions to hit the target and methanol ions to deflect further. In the other two instances, ferrocene and methanol ions were transmitted through the Einzel lens by applying deflection voltages of ±0.005 V and ±0.001 V, respectively. Sometimes, the ions are reflected due to insufficient kinetic energy to push them over the bump caused by the potential, as seen in Figure 5.12. Therefore, the kinetic energy should be increased to allow ions to pass through.

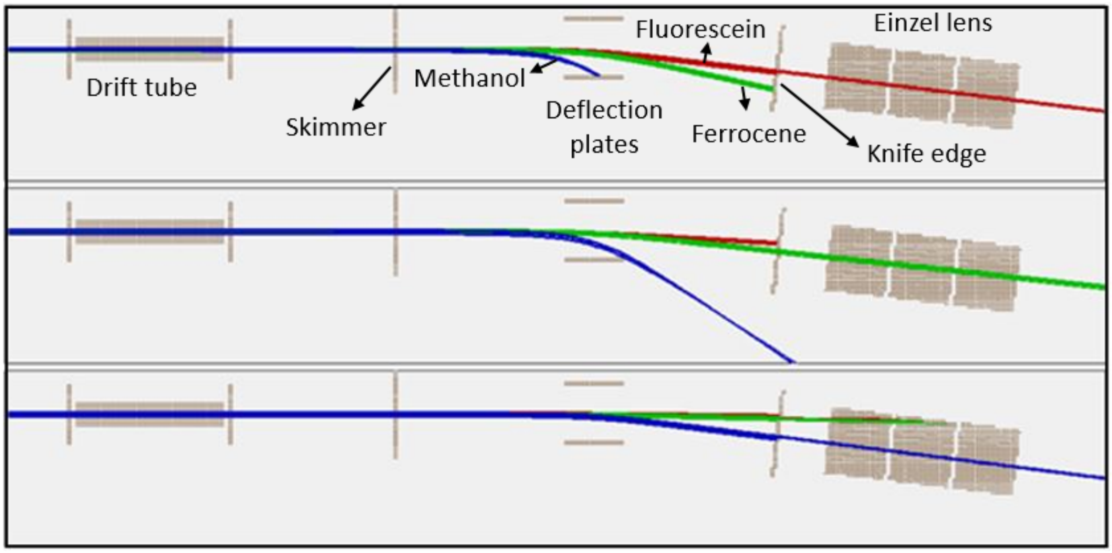

Fig. 5.11. SIMION simulations for an electrospray system. Red, green, and blue lines represent the paths followed by ions of fluorescein, ferrocene, and methanol travelling through the Einzel lens applying deflection voltages of ±0.01 V, ±0.005 V and ±0.001 V on plates, respectively.

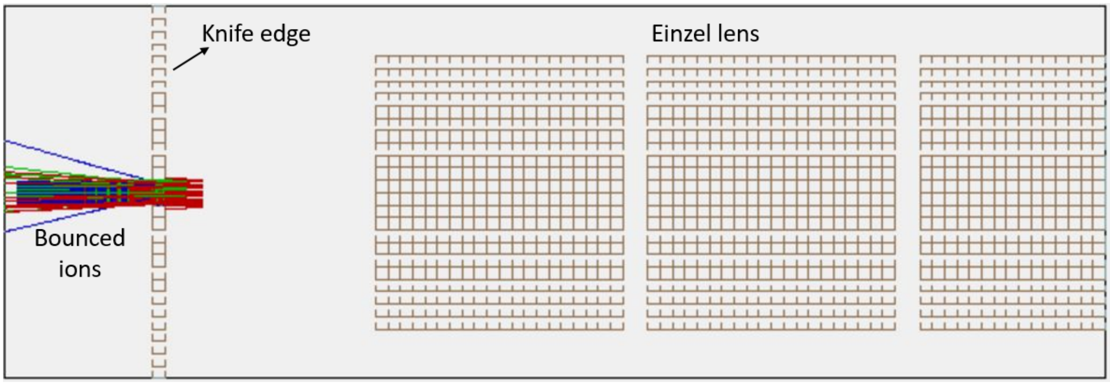

Fig. 5.12. Depiction of the path of bounced ions due to insufficient kinetic energy.

In order to compare the theoretical results with the experimental results, the voltage of the deflection plates in SIMION was set to a voltage of ±2000 V as used in our lab. A mass of 7×10^7 amu and speed of 300 m/s was employed to permit the ions beam to fly through the system, as presented in Figure 5.13. Moreover, as shown in Figure 5.14, applying a charge of +2e rather than +1e caused the electric field to bend more, preventing the ions beam from reaching the electrostatic lens. Therefore, doubling the mass is also required to make the ion trajectory pass through the whole system, which means that mass and charge are interdependent - i.e. depending on each other.

Fig. 5.13. SIMION simulations for an electrospray system showing flying one group of 20 ions passing through the system into the Einzel lens using charge +1e, a deflection voltage of ±2000 V and a mass of 7×10^7 amu.

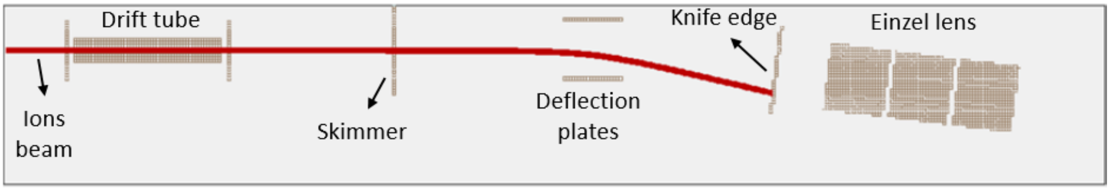

Fig. 5.14. SIMION simulations for an electrospray system using the same previous simulation parameters (see Figure 5.13) with setting charge to +2e.The ions in this event are unable to pass through the Einzel lens.

SIMION simulations suggest that the beam is not formed predominantly of individual molecular ions but rather clusters of molecules having very large masses in these experiments, as represented in Figure 5.15. Each cluster also in the simulations has only a single or double charge, whereas a smooth distribution of charges, that form clusters containing a very large number of charges, has been observed in the image charge tube experiments. In fact, the clusters will be even larger according to the SIMION simulations, as the mass will need to scale with the charge to observe the same deflection.

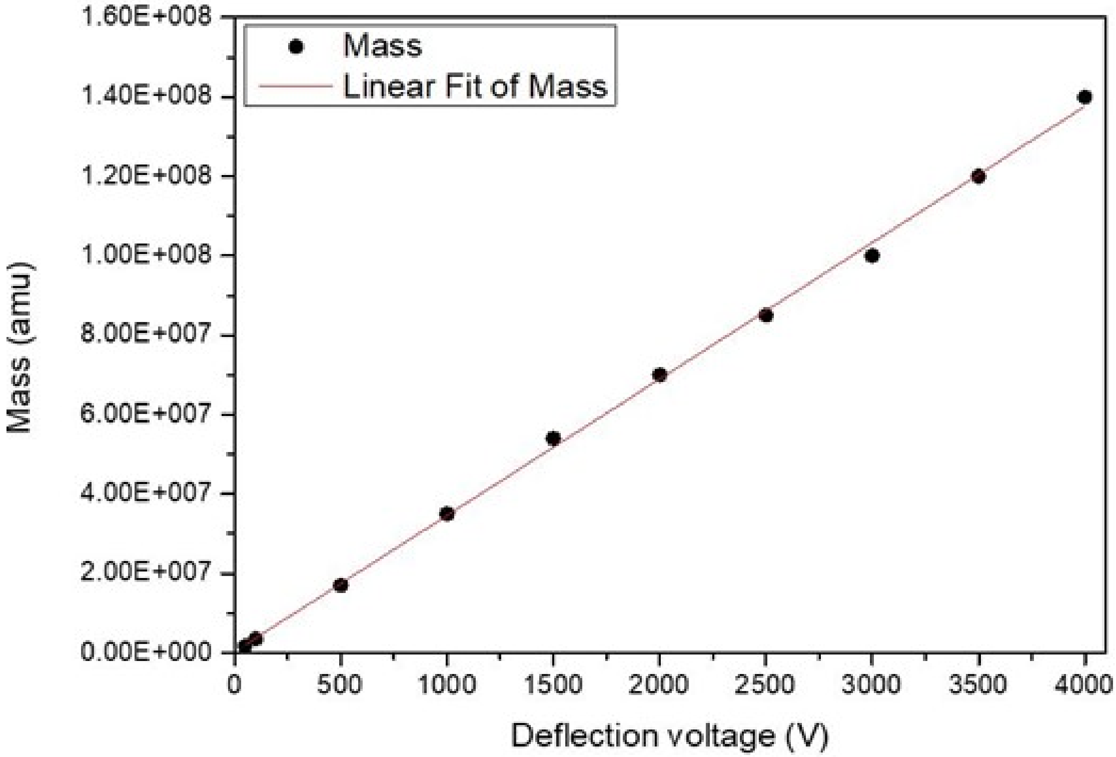

Fig. 5.15. A plot of the data shows using millions of masses by applying a charge of +1e to make ions beam travel through the whole system at different deflection voltages.

5.3.6 Defocusing Einzel lens

In electrostatic lenses, an electric field is formed within the cylinder region, which is used to focus the beam of ions to a focal point as dictated by voltages applied to lenses. Two-dimensional (2D) and potential energy surface views in Figures 5.16 and 5.17 show the path of fluorescein ions, which is affected by the electric field. The first and third electrodes are held at 0 V, whilst the second electrode is at 3800 V. The gradient of the electric field within the second electrode is defined by using the voltage given to that electrode, leading to determining the ion focusing strength on a centrepiece point.

Electrostatic lenses do not perform properly for ion beams with a wider range of kinetic energies. Hence, it is a good idea to utilise electrostatic lenses in areas of the instrument where the kinetic energies are likely to propagate less or where focusing the beam cannot be avoided.

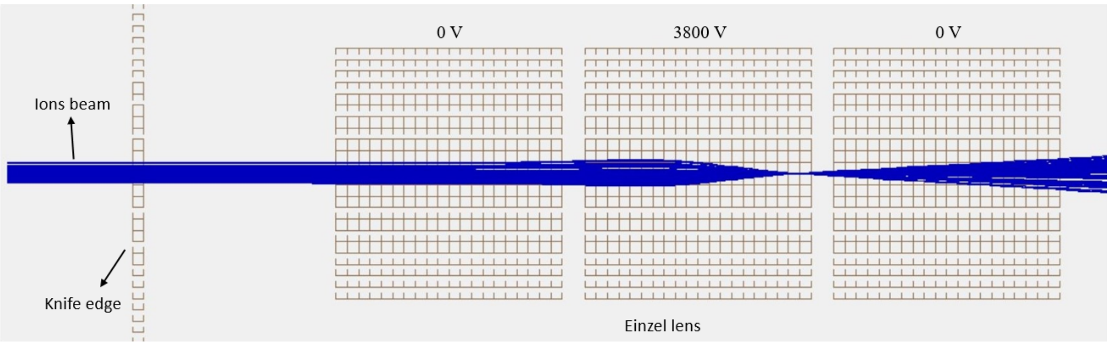

Fig. 5.16. A 2D view of ions trajectory showing the second lens voltage effect on focusing ions into a focal point. The used kinetic energy is 3700 eV.

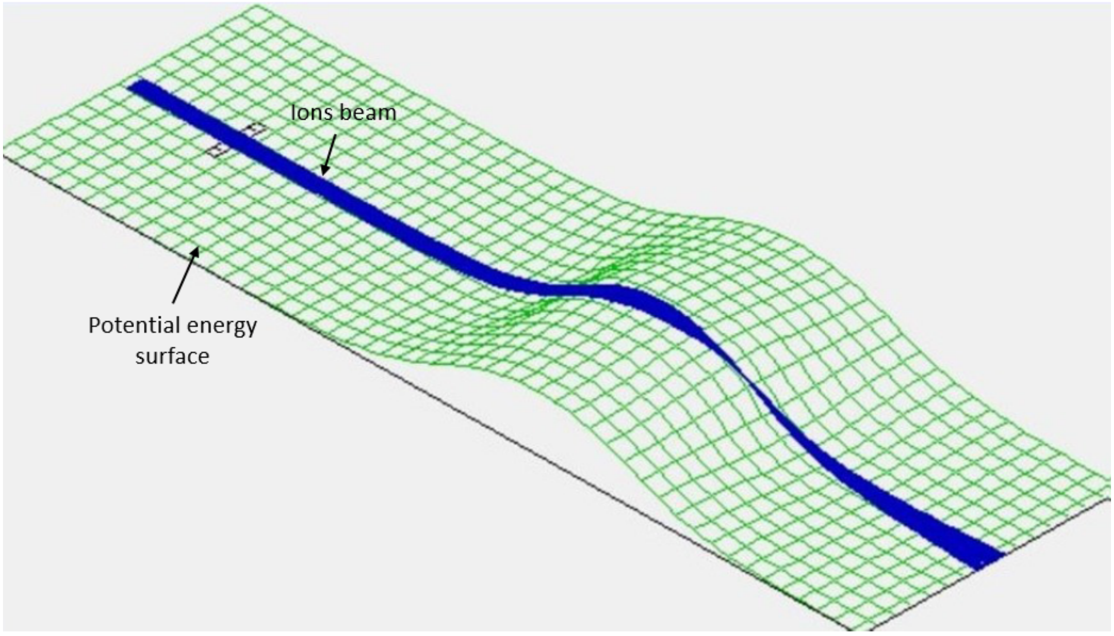

Fig. 5.17. Potential energy surface view of the ions path passing through a central cross-section of the Einzel lens.

The NaCl data is introduced to test the success of the Einzel lens in defocusing the beam in the actual experiment, with XPS measurements detailed in the following section.

5.3.7 Deposition of NaCl on SiO_2

The ability to form ionic clusters of salts such as a NaCl solution has been demonstrated by electrospray ionisation mass spectrometry (ESI-MS) and can be found in the literature [109, 145–147]. A 0.05 M NaCl was dissolved in 5 ml of methanol and further diluted with 5 ml of water to increase its conductivity. An electrospray system was used to deposit NaCl for an hour and a half, where the Einzel lens voltages were applied to defocus the beam. Defocusing the beam will be useful for future depositions over the whole sample.

5.3.7.1 Deposition with the use of the Einzel lens

Figure 5.18 shows Na 1*s* and Cl 2*p* spectra deposited of NaCl onto SiO_2 by electrospray with an Einzel lens to spread beam on the entire sample. An electrospray voltage of +1830 V and an Einzel lens voltage of +3800 V have been applied. The XPS measurements have taken place at various positions on the sample to see the Einzel lens effect - i.e. the positions of 13-18 mm are arbitrary values on the manipulator. As indicated in Figure 5.18, the 13 mm and 14 mm regions have a strong signal on both spectra due to the highest deposition coverage. The chlorine spectrum at 18 mm does not contain Cl 2*p* peak, and this spectrum signal is probably attributed to an Auger feature. The sodium spectrum is very weak because of the low deposition coverage. As a consequence, there will be a negligible amount of chlorine. Changing shape dramatically (i.e. not in the usual place for chlorine peak at around 201 eV) is also observed. The Shirley or linear background of all spectra has been subtracted. The chlorine spectrum at region 18 mm is eliminated from the signal by subtracting the spectrum of chlorine 18 from other chlorine spectra, and therefore a very flat chlorine peak is obtained (Cl 2*p* 18 spectrum is not shown since it can not subtract it from itself).

Figure 5.19 shows the intensity of the sodium and chlorine spectra taken from measured spectra at different Z positions on the sample. Igor Pro has been used to work out the intensity data for all spectra. The intensity values are calculated from the area located between molecule peaks, and the positions of peak intensity have been fitted with Gaussian curve fitting. The low-intensity values indicate the weak spectra peaks, whilst the high-intensity values refer definitely

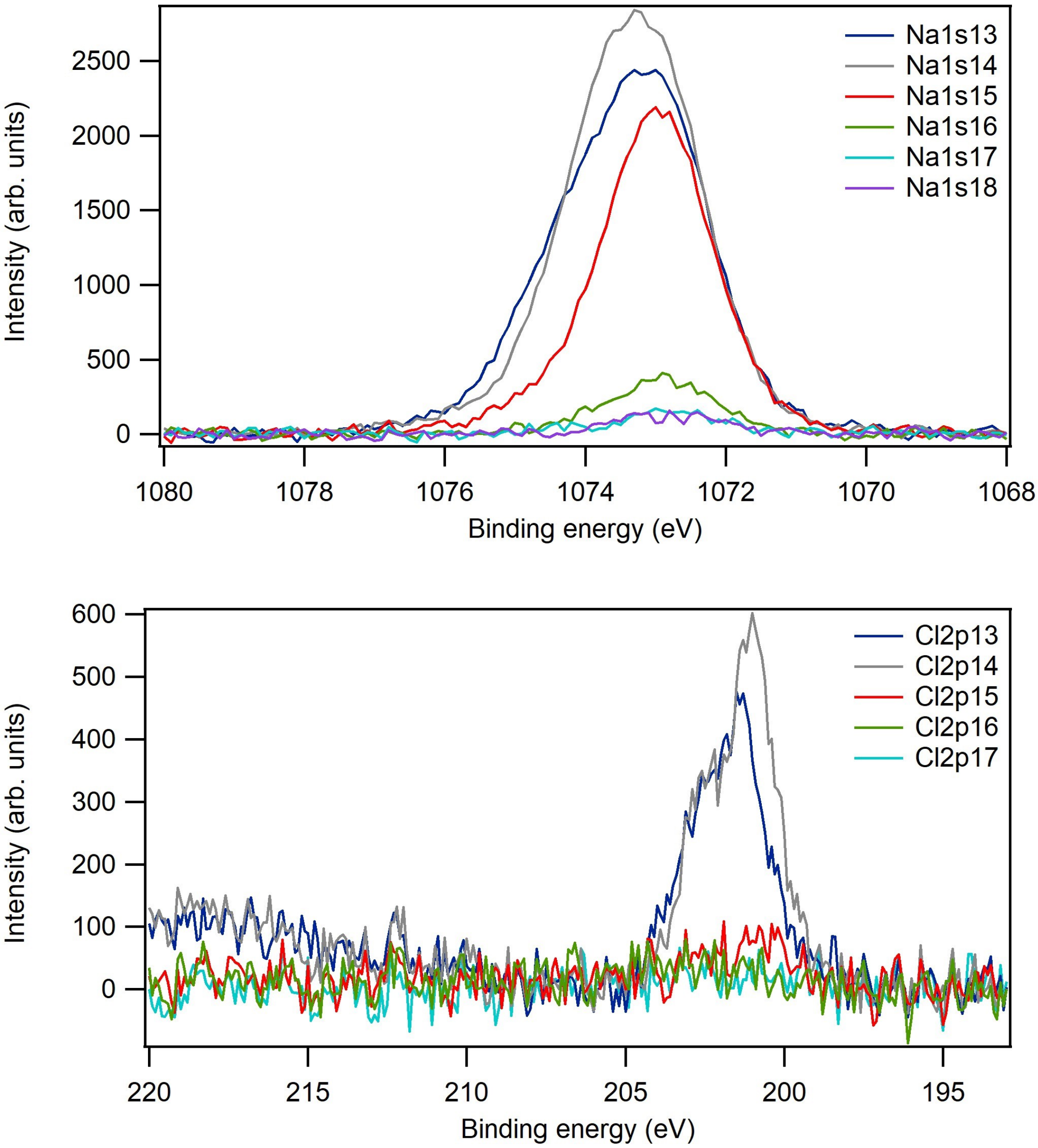

Fig. 5.18. Na 1*s* and Cl 2*p* spectra of NaCl deposition onto the SiO_2 substrate. The high-intensity peaks of Na 1*s* and Cl 2*p* correspond to the highest deposition coverage and the low-intensity peaks are attributed to the lowest coverage of molecules on the surface. The background has been subtracted from both spectra.

to the strong spectra peaks. The Gaussian full width at half maximum (FWHM) for the sodium and chlorine spectra is 3.5 mm ± 0.6 mm and 2.0 mm ± 0.3 mm, respectively. The FWHM is different even though the same beam is deposited. The reason might be that one set of ions is focused/defocused more than the other polarity, such as sodium being more defocused by the Einzel lens than chlorine.

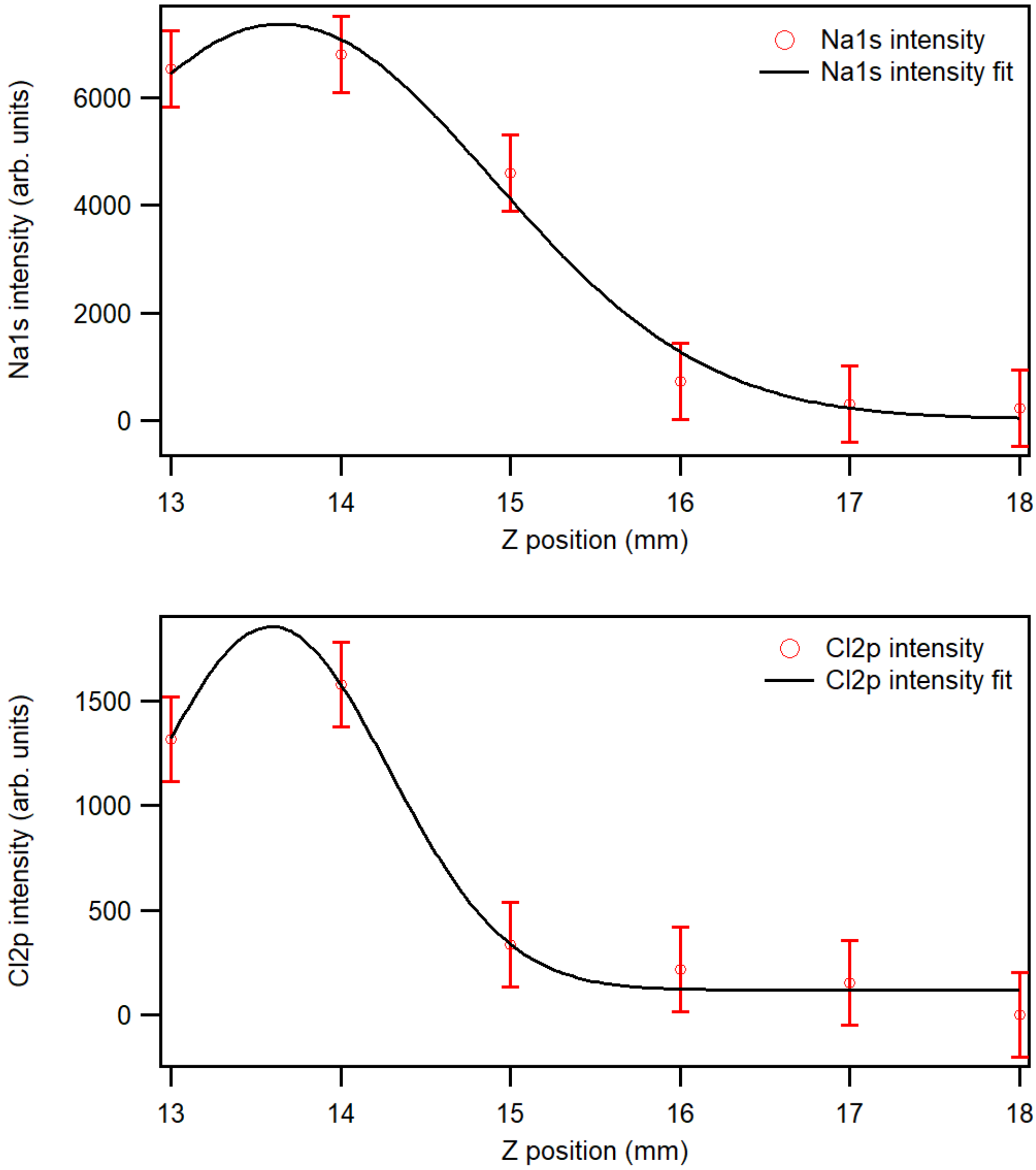

Fig. 5.19. A graph of Na 1s and Cl 2p intensity data for Z = 13 mm, 14 mm, 15 mm, 16 mm, 17 mm, and 18 mm. A Gaussian fitting is shown generated from the intensity data values.

Figure 5.20 shows C 1s and O 1s spectra resulting from NaCl deposition by the electrospray system. The spectra have had a Shirley background subtracted.

These spectra are measured to get the intensity data as presented in Figure 5.21. As can be seen, the intensity data of oxygen moves the other way, as it is expected, because it has not been deposited and has been attenuated slightly with some sodium and chlorine. Compared to the oxygen graph, the carbon curve has obviously followed the same shape as sodium and chlorine, even though there is no carbon in the NaCl molecule. This is attributed to the fact that, besides the electrospray, some of the solvents are deposited. The Gaussian fitting has not applied to these data because what matters is the deposited NaCl data.

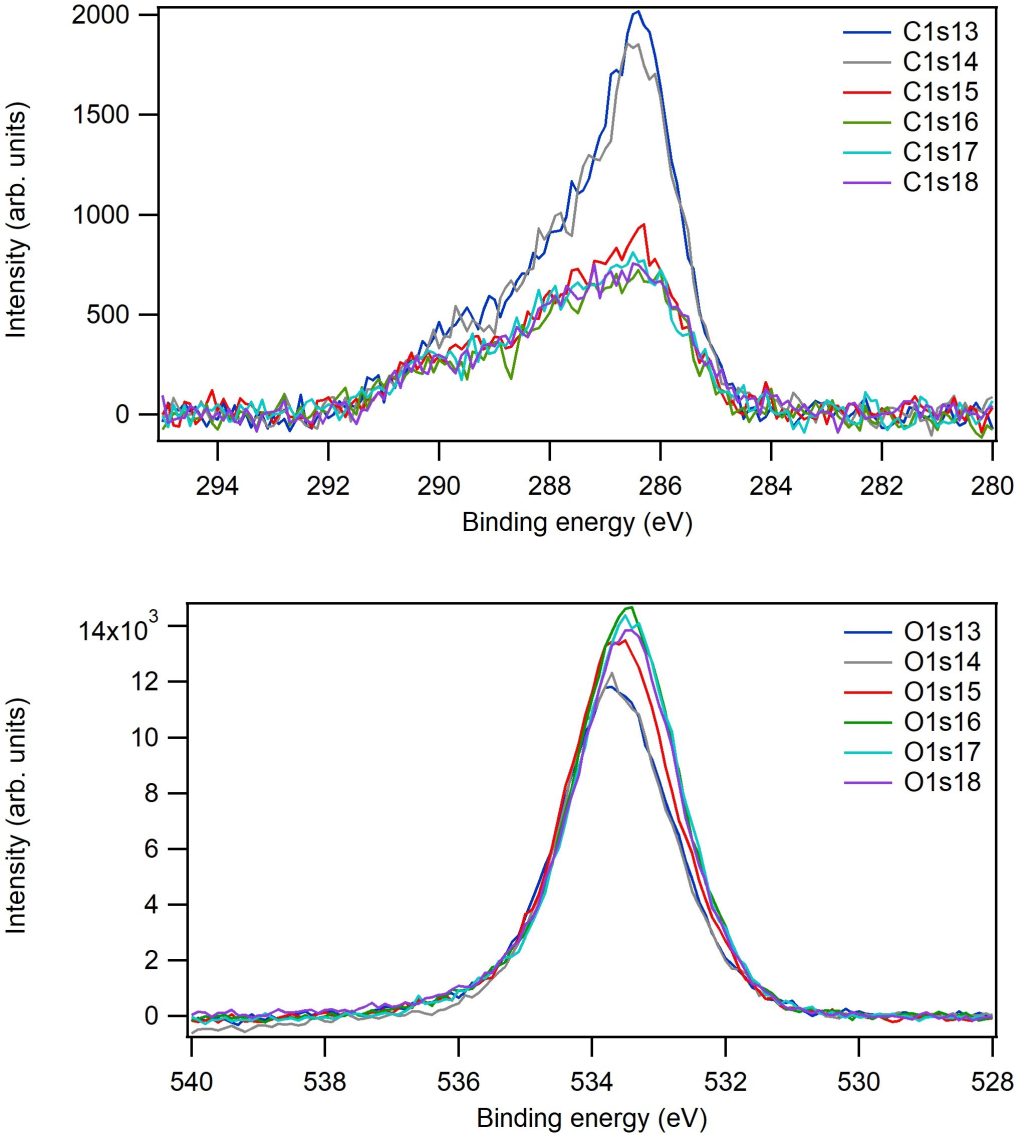

Fig. 5.20. C 1*s* and O 1*s* spectra of NaCl onto the SiO_2 substrate. The high-intensity peaks are attributed to the highest coverage and low-intensity peaks are due to the lowest coverage. A Shirley background has been subtracted from both spectra.

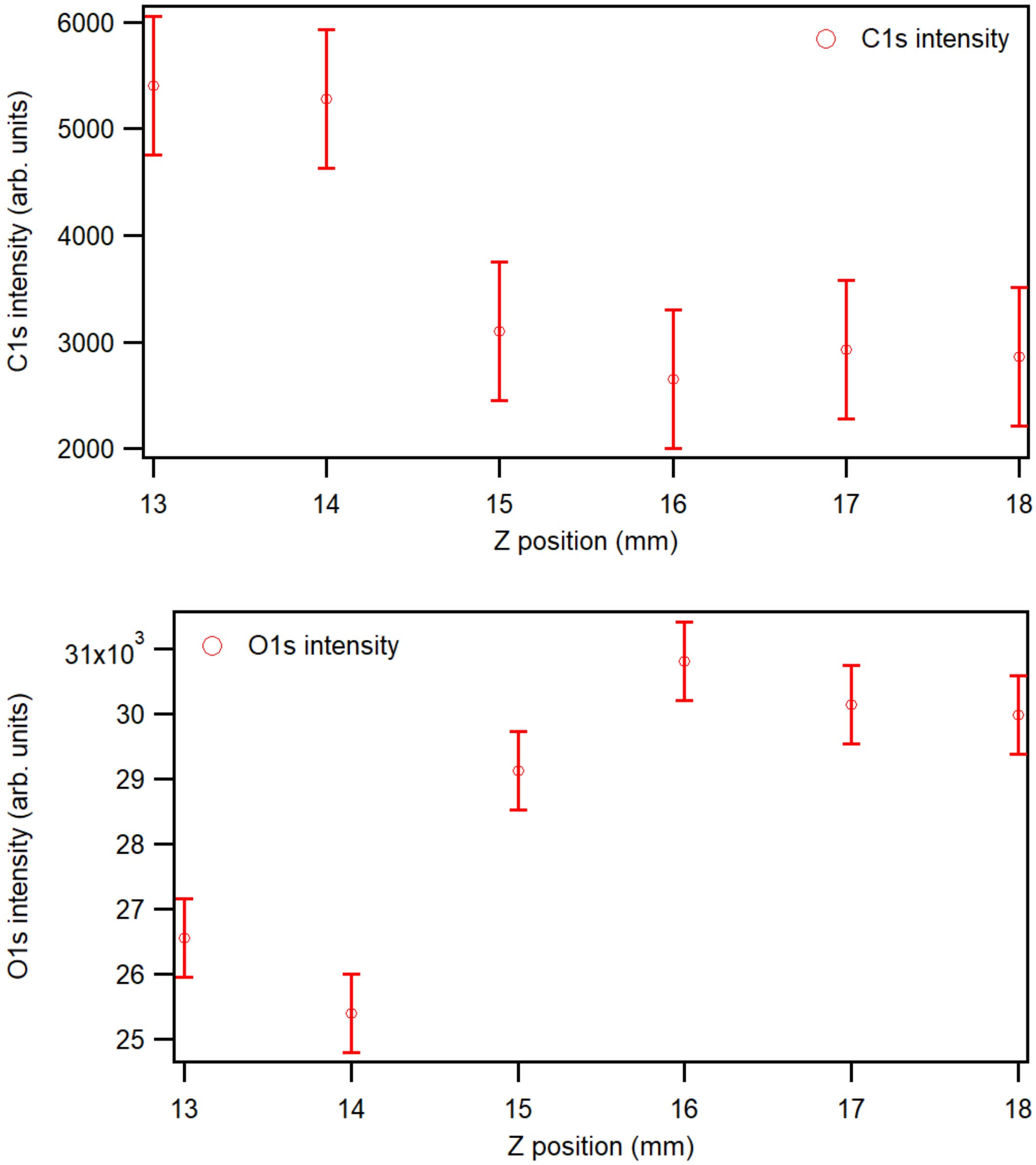

Fig. 5.21. C 1*s* and O 1*s* showing intensity data using different Z positions. These data are created by measuring the area of each spectrum.

Cl 2*p* spectra are in a doublet state with a spin-orbit splitting of 1.6 eV. Curve fitting software (XPST) has been employed to fit the peaks for the spectrum. An example of a curve fitting to the Cl 2*p* spectrum is outlined in Figure 5.22. XPST can also calculate the intensity values for every peak separately, which has been discussed in the next step.

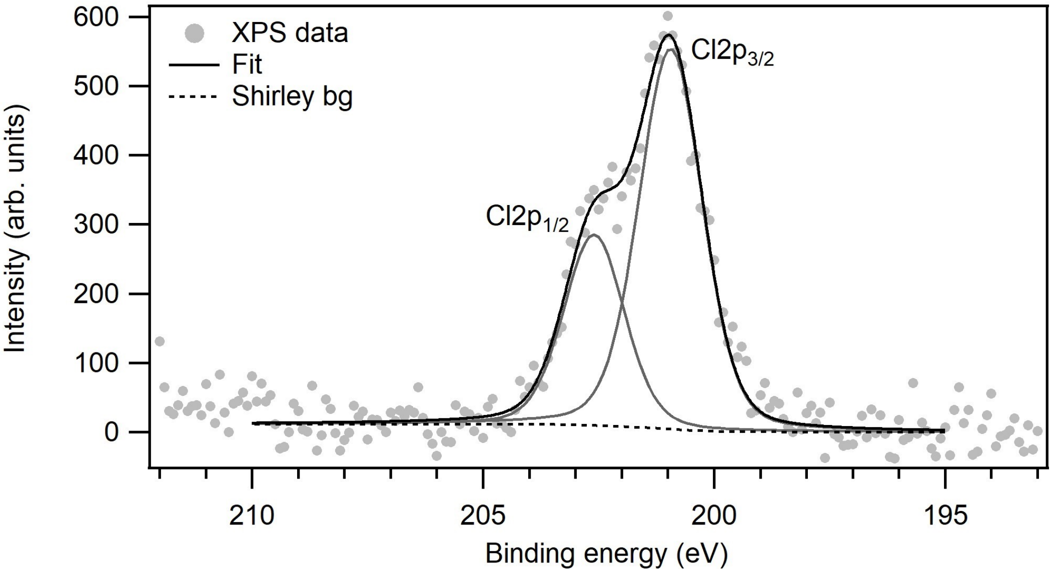

Fig. 5.22. Cl 2*p* XPS spectra of NaCl onto SiO_2. The data has had a Shirley background subtracted. The curve fitting shows two peaks which belong to Cl $2p_{3/2}$ and Cl $2p\ _{1/2}$ where the area of the Cl $2p_{1/2}$ peak is half of the Cl $2p_{3/2}$ peak.

The XPST is considered another way to compute the peak intensity. Figure 5.23 presents the intensity data of the chlorine spectra from Figure 5.18 using XPST curve fitting. The curve fitting has been carried out to obtain two peaks for every chlorine spectrum, as shown in the example in Figure 5.22. The Gaussian FWHM of the Cl 2*p*intensity data is 2.0 mm ± 0.1 mm. The shape and FWHM of the Cl 2*p* intensity data in Figure 5.23 are similar to the Cl2p intensity data in Figure 5.19.

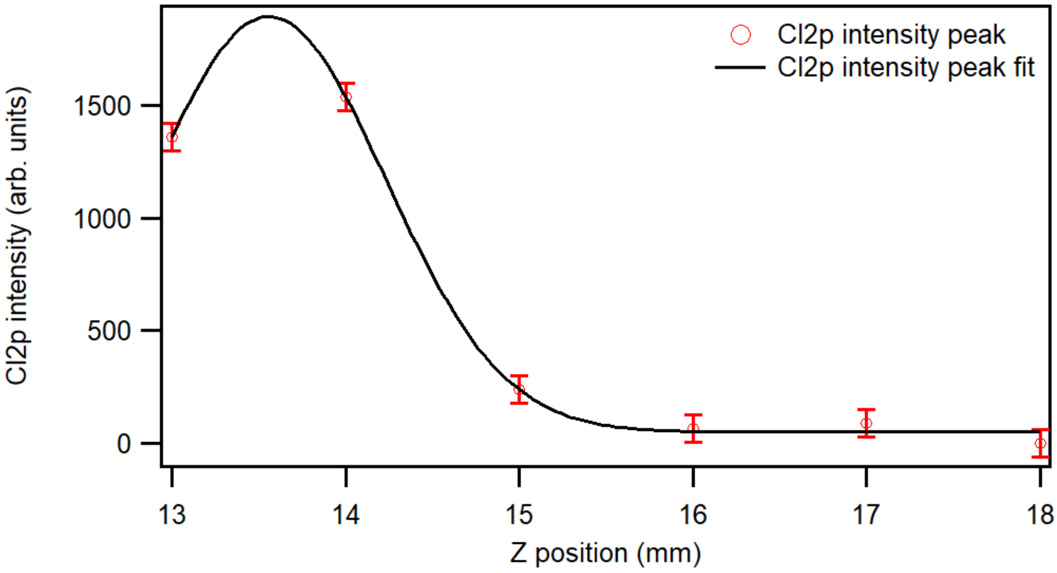

Fig. 5.23. Cl $2p$ intensity dataset given from spectra measurements at different regions. The peak fitting is carried out using Gaussian functions.

5.3.7.2 Deposition without the use of the Einzel lens

Na $1s$ and Cl $2p$ spectra deposited on NaCl onto SiO_2 by electrospray without using the Einzel lens are exhibited in Figure 5.24. The electrospray voltage +1829 V and no Einzel lens voltage have been applied. This experiment is to show whether or not the Einzel lens has an effect on beam propagation on the sample. The spectra of sodium and chlorine at 13 mm and 14 mm positions, as illustrated in Figure 5.24, have a good signal in contrast to spectrum 18, which has a very weak signal, as the previous data presented using the Einzel lens in Figure 5.18. All spectra have been background subtracted. The spectrum 18 does not contain chlorine $2p$ peak, so it is removed from the signal by dividing the spectrum of chlorine 18 from other chlorine spectra and subtracting it to zero to obtain a very flat chlorine peak (Cl $2p$ 18 spectrum is not shown since it can not subtract it from itself). As can be seen in Figure 5.24, the binding energies (BEs) of NaCl shift to higher BE as the coverage increases. This is because the thicker the NaCl layer, the more insulating the film becomes since NaCl is an insulating material. Therefore, steady-state charging will push the BE higher in sodium and chlorine. By comparing the intensity of the Na $1s$ and Cl $2p$ in the original data, the raio

1:1 for Na 1*s* and Cl 2*p* has been found when taking into account photoionisation cross-sections, implying that there is no preference to deposit in the positive ions.

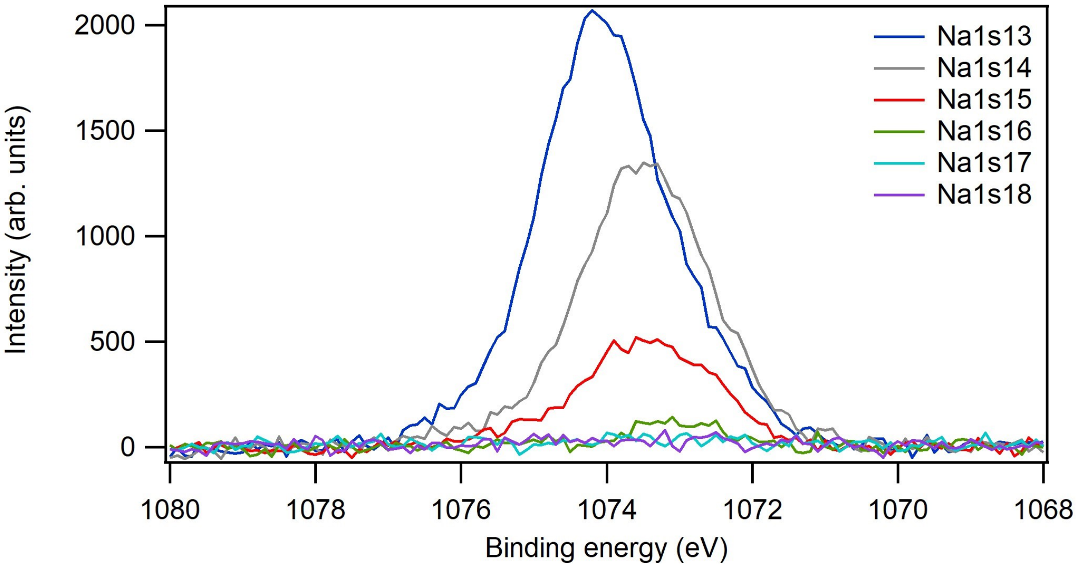

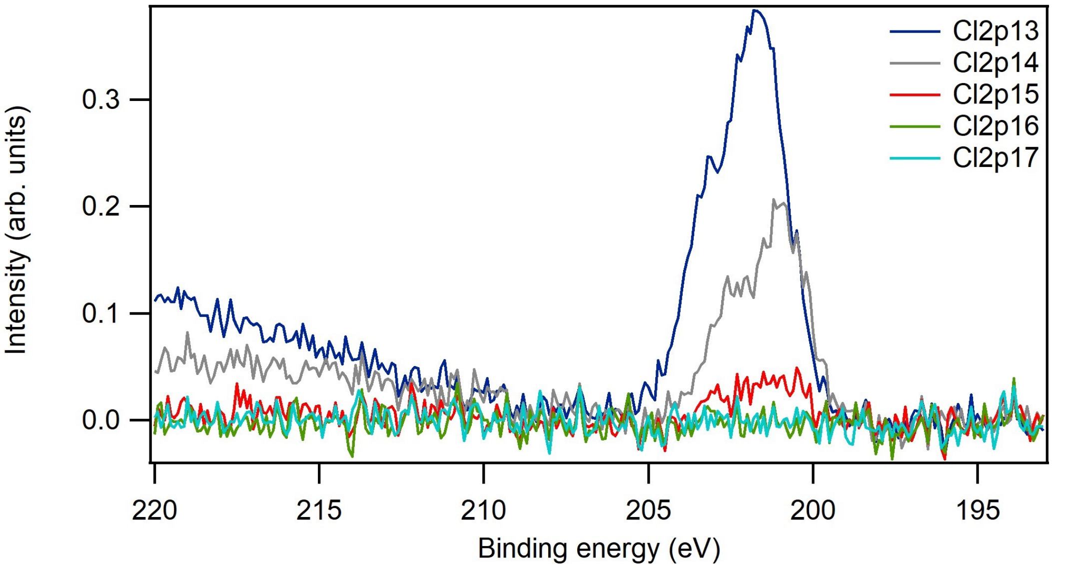

Fig. 5.24. Na 1*s* and Cl 2*p* spectra of NaCl deposition onto the SiO_2 substrate. The high-intensity peaks are attributed to the highest deposition coverage and low-intensity peaks correspond to the lowest coverage. The background has been subtracted from both spectra.

Figure 5.25 displays the Na 1*s* and Cl 2*p* spectra intensities taken from measured spectra at various locations on the sample. The intensity data is fitted using Gaussian fitting. The Gaussian FWHM for sodium and chlorine is 3.5 mm ± 0.2 mm and 2.4 mm ± 0.1 mm, respectively.

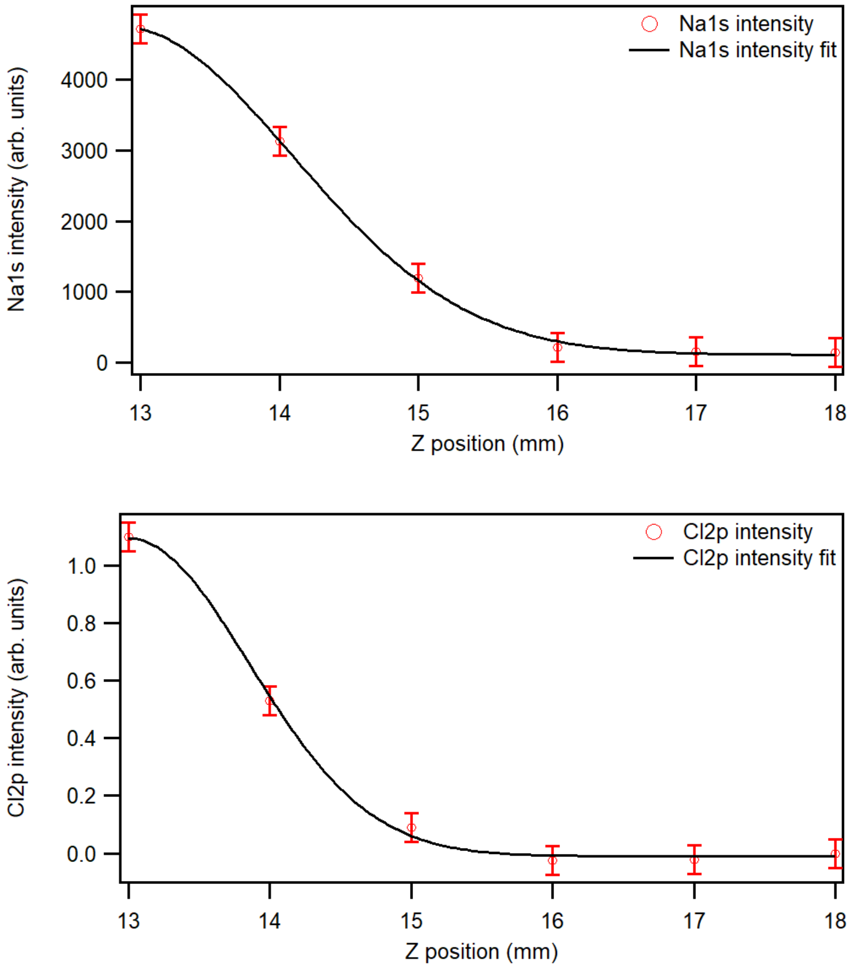

Fig. 5.25. Intensity data of Na 1*s* and Cl 2*p* spectra for Z = 13 mm, 14 mm, 15 mm, 16 mm, 17 mm, and 18 mm. A Gaussian fitting is shown generated from the intensity data values.

C 1*s* and O 1*s* spectra created from NaCl deposition are shown in Figure 5.26. Shirley and linear backgrounds are removed from spectra by subtraction. The intensity data presented in Figure 5.27 has been generated from measured spectra at different positions on the sample. The shape of the carbon intensity data is the same as the shape of the sodium and chlorine intensity dataset due to the depositing of some solvents from the electrospray, whilst the shape of the oxygen intensity data is different compared to them. These experimental data are very similar to data obtained using the Einzel lens. The results of these experiments have been summarised in the following Table 5.2.

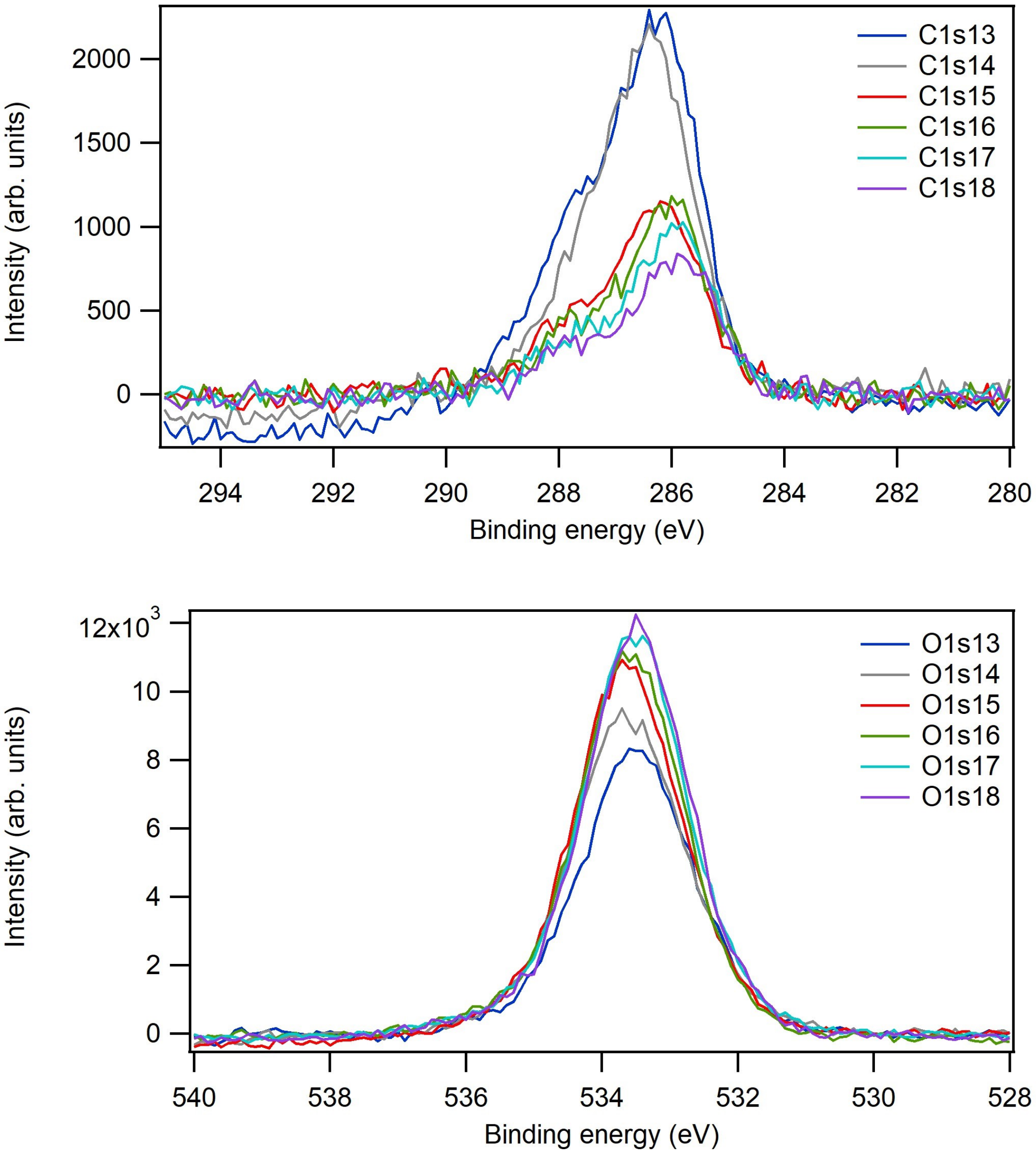

Fig. 5.26. C 1*s* and O 1*s* spectra of NaCl onto the SiO_2 substrate. The high-intensity peaks of C 1*s* and O 1*s* are attributed to the highest coverage and low-intensity peaks are due to the lowest coverage. The background has been subtracted from both spectra.

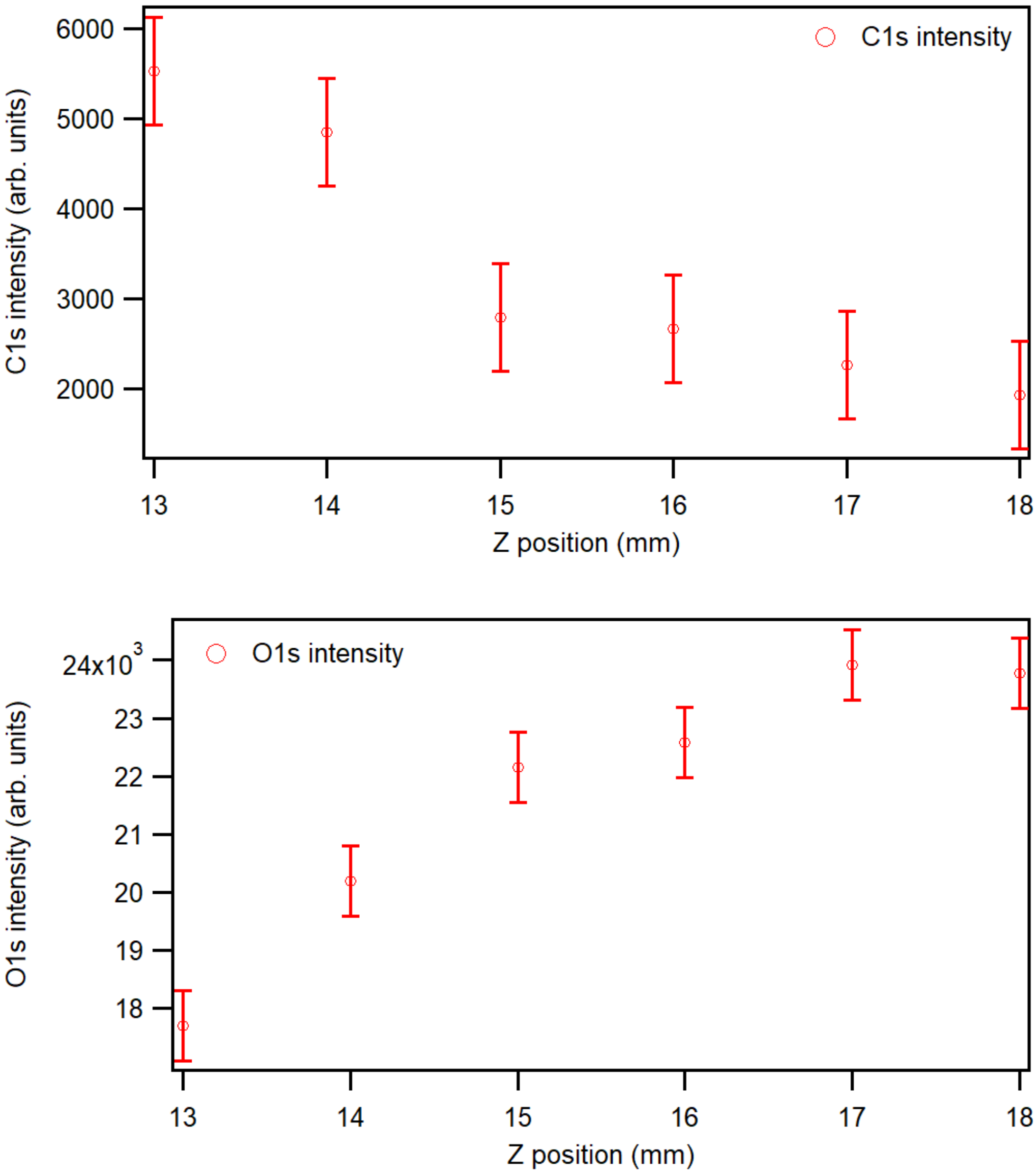

Fig. 5.27. C 1*s* and O 1*s* showing intensity data created from measured spectra data at various Z positions.

Experiment	**Electrospray Voltage**	**FWHM for Na Intensity Data**	**FWHM for Cl Intensity Data**
With Einzel Lens (+3800V)	+1830 V	3.5 mm ± 0.6 mm	2.0 mm ± 0.3 mm
Without Einzel Lens (0V)	+1829 V	3.5 mm ± 0.2 mm	2.4 mm ± 0.1 mm

Table 5.2. Table of FWHM for Na1s and Cl2p intensity data of NaCl experiments.

These data indicate that the Einzel lens has had no effect on the deposition of NaCl, which is likely because the NaCl beam contains many neutrals. The Einzel lens does not change the size of the deposition spot, and the spot size is always essentially the same, which can be observed by XPS. This was essentially a single-point experiment where the Einzel lens was set at a sufficiently high voltage during the deposition, which would surely make the beam smaller or more diffuse. We are certain that a higher voltage will achieve focusing or defocusing the beam because a voltage similar to that used to defocus the beam has been employed in the deflection plates. This experiment needs more time to explore more voltages because the Einzel lens must be set to a particular voltage during deposition and then map it out using XPS.

On the other hand, to explore the effect of the Einzel lens on the ions, a circle target is placed a long distance away in stage 4, as shown in a diagram in Figure 5.28. In this case, the voltage on the Einzel lens is changed and thus the current is measured. It has been noticed that the Einzel lens defocuses the beam until the spot is larger than the target; therefore, the current will drop, as shown in Figure 5.29.

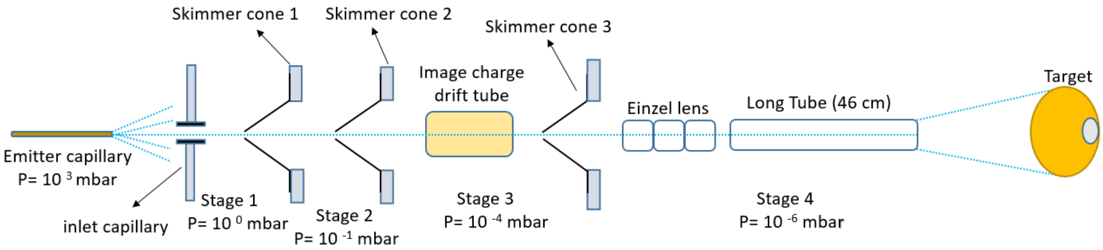

Fig. 5.28. A schematic of the electrospray deposition system showing the Einzel lens, long straight section, and target at the end to get deposition spot to be bigger than target.

.

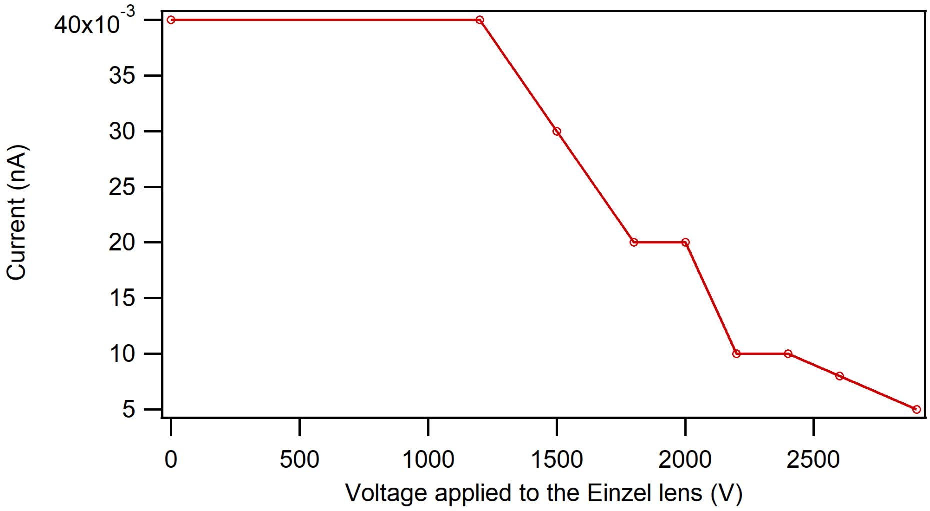

Fig. 5.29. Plot showing decrease of the current implying that the Einzel lens is working using the long tube.

5.3.8 Deposition of Graphene Oxide on SiO_2

Graphene is of great interest due to its use in many applications, including electronic devices, solar panels, sensors and anti-corrosion coatings. Electrospraying enables the deposition of graphene materials, such as graphene oxide (GO), reduced graphene oxide (rGO) and carbon nanofibers (CNF), onto a greater variety of substrates [108, 148, 149]. Graphene films were deposited through an electrospray deposition system for the first time by Beidaghi et al [150]. As illustrated in the chemical structure in Fig. 5.30 [151], GO is an oxidised form of graphene (i.e. an allotrope of carbon arranged in 2D) bound to oxygen-containing groups.

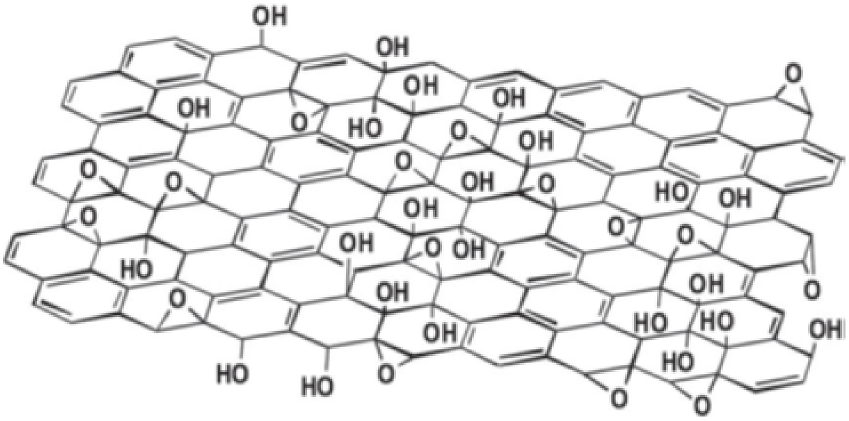

Fig. 5.30. Chemical structure of the graphene oxide molecule. Reproduced from ref. [151].

A solution made of GO in ethanol diluted to 0.04% (w.t.) was prepared. Because GO is a very large molecule, it forms suspension because it settles to the bottom of the bottle if it leaves for a few days. A silicon wafer substrate was cleaned by ultrasonication in acetone and methanol, and then the wafer was rinsed in de-ionised water. Graphene oxide was deposited using electrospraying onto the silicon dioxide surface. There was no deflection voltage applied to this experiment. The deposition time was an hour, and after the deposition, the sample was transferred into the photoemission electron microscopy (PEEM) for heating. The film morphology was analysed using atomic force microscopy (AFM), and images were captured at different scanning areas of 30×30 µm, 10×10 µm, 4×4 µm and 1×1 µm. The data had been processed by Gwyddion software.

Figure 5.31 illustrates AFM images measured by Bellamy-Carter (Nottingham) on different areas across a surface. AFM shows some circular deposits, presumably large droplets with a delivery mechanism for the GO on the scale of 2 microns produced from the electrospray. Even though the surface of SiO_2 is very rough, the graphene is clearly visible, especially in the phase imaging.

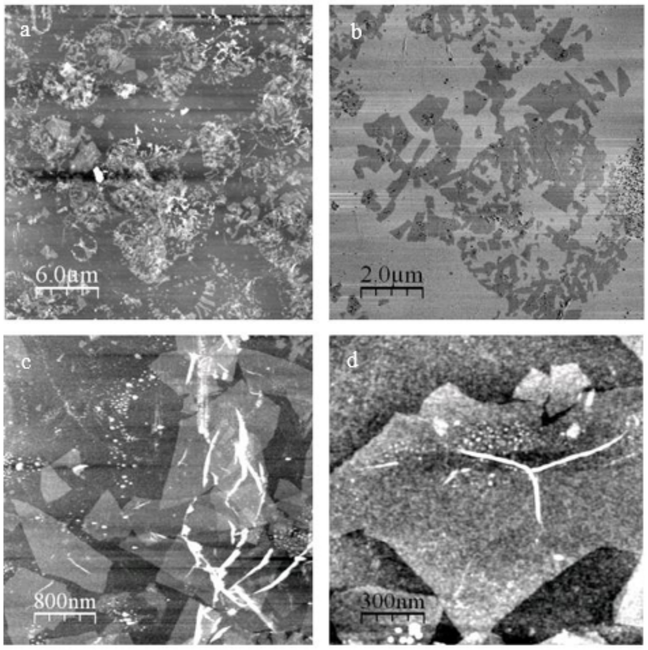

Fig. 5.31. AFM images of graphene oxide film on silica substrate using the electrospray. The scale bars are of length (a) 6.0 µm, (b) 2.0 µm, (c) 800 nm, and (d) 300 nm. AFM images are taken by Bellamy-Carter (Nottingham).

As shown in Figure 5.32, the optical micrograph at 5X, 50X and 100X displays small objects distributed on the silica substrate, which are GO flakes. These flakes are large enough to be visible by optical microscopy and lie flat on the surface with few wrinkles (actual size unknown), which means that it is promising to deposit these with electrospraying.

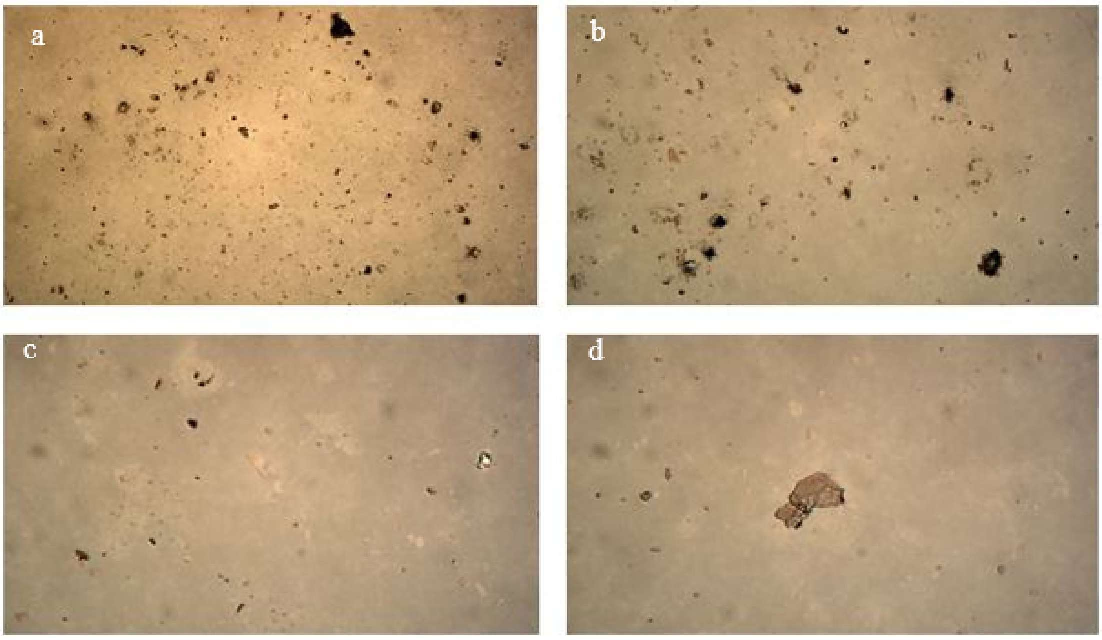

Fig. 5.32. Optical micrographs of graphene oxide film on silica substrate using the electrospray. Images taken at different magnifications starting from 20X (a), 50X (b), and 100X (c, d). Optical images are taken by Bellamy-Carter (Nottingham).

The split target was replaced with an offset aperture (the aperture is 5 mm off the flange centre) to attempt to deposit the GO onto a target placed behind the aperture using deflection plates to remove the large neutral droplets that appeared by deposition through the straight beam. This experiment did not work potentially because the GO formed very large clusters, making bending the beam through the offset aperture challenging.

5.4 Conclusions

The potential of the electrospray deposition method has shown remarkable success, as demonstrated by the experiments. The first four electrostatic ion deflection experiments using the electrospray technique were addressed. The fluorescein dataset has shown ions hitting both targets at the deflection voltages range of 3150 V ± 50 V. They are extremely similar since they have the same solution properties. Moreover, the results of spraying ferrocene solution at +2 kV clearly exhibited the difference in the deflection voltages used, which was the average of 3650 V ± 50 V compared with fluorescein data. The co-electrospray experiment (i.e. a mixture of fluorescein and ferrocene solutions) sprayed at +2992 V proved the energy selection's success in separating the two molecules into two different beams from the same solution. The deflection voltage of ± 3300 V has been used to separate the fluorescein beam, whilst the average deflection voltage of 3850 V ± 50 V has been applied to separate the ferrocene beam. Fluorescein and ferrocene have formed giant clusters that require a higher voltage to deflect, as suggested by the SIMION simulation and the smooth nature of the ion charge distribution. Modelling the electrospray system in SIMION simulation generates very large clusters of ions with a lot of kinetic energy flying at speed of approximately 300 m/s, and their masses are in the millions of amu.

The ability to measure individual molecule ions in both the image charge tube and the deflection experiment is likely substantially limited by the capability of the electronics. It is also likely that only the very large ion clusters were measurable in the charge tube, as these give clear transient signals. The smooth distribution of charges in drift tube data suggests a large number of charges on each ion, which means forming large clusters. The small ions, even if these made up the majority of the beam, would be below the detection limit. Similarly, if the very large ion clusters contribute a large current signal on the target in the deflection experiment, it could primarily be probing their deflection. The smaller molecular ions would be deflected by voltages in the low range, which would have been missed. Interestingly, there seems to be a preferred size of the clusters, which leads to a narrow range of deflection voltage to maintain a stable bent path for the ion beam.

These experiments have been conducted in a range that primarily focuses on the high voltage regime for the extremely large clusters that give a strong signal in the image charge tube and are easily detected with the deflection field. This has not been able to be demonstrated with smaller components and individual molecular ions, so more work is required on the low-voltage system to determine whether this voltage can be used to identify individual molecular ions because it would require creating more sensitive electronics for the image charge detector and eliminating noise from the system. Both future research experiments will benefit from removing the very large clusters from the beam, possibly by redesigning the first stage. However, the design of the first stage, where ions are deliberately extracted from within the silence zone, might be the real cause of large clusters in the beam, which can form during rapid expansion into a vacuum similar to what occurs in a gas aggregation source.

The electrospray source forms a deposition spot with range of coverages in the Gaussian distribution. The beam hitting the sample is about 2 mm in diameter, and the Einzel lens has been used to attempt to spread the beam out to 10×10 mm. The NaCl XPS measurements have proven the inability of the Einzel lens to defocus the beam practically, although SIMION simulation has shown a defocused beam. However, the data has shown that some regions are covered more than others. So the electrospray deposition time should be longer than expected to have high coverage. The experiments using negative voltages for both the electrospray and the Einzel lens and the experiment with no voltage applied to the Einzel lens have failed. On the other hand, the data presented using a long tube showed the success of the Einzel lens in defocusing the beam by observing the decrease in current when applying different voltages to the Einzel lens.

The AFM and optical images have revealed the inconsistency of deposition across the surface – some areas are heavily covered, and some are bare. Therefore, this is certainly worth further future studies.

Chapter 6

A Photoemission Study of Dye Molecules Deposited by Electrospray on rutile $TiO_2(110)$

6.1 Introduction

For decades, renewable energy sources have received considerable global interest due to the increase in fossil fuel consumption. The abundant energy produced by the sunlight makes dye-sensitised solar cells (DSSCs) a promising alternative compared to conventional silicon and thin film solar cells due to their transparency and tunable colours, which make them suitable for applications such as windows and glass facades [7, 152, 153]. The key components of a DSSCs device are a layer of semiconducting oxide materials, commonly TiO_2, a photosensitiser (dye), a redox-mediator (electrolyte) as $I^-/I_3{}^-$ and a counter electrode. The dye on the TiO_2 layer absorbs sunlight (photon) to excite electrons and then injects them into the conduction band of the titania. Subsequently, these injected electrons are transported to transparent conducting oxide. The oxidising dye at the counter electrode is reduced by transferring electrons from the redox mediator. The DSSCs mechanism is discussed in further detail in Section 1.2). Although a variety of dyes have been studied for use in the dye-sensitised solar cells model, ruthenium-based inorganic dyes are among the most effective when applying $I^-/I_3{}^-$ as a redox mediator [2].

The investigation of metal-organic dyes (i.e. ruthenium complex dyes) was the primary focus of early DSSC research. Nowadays, the study of organic dyes has become an interest of researchers [154, 155] due to ruthenium being a rare and expensive metal, and metal-free organic dyes have many features, such as high molar extinction coefficients, low manufacturing costs and ease of structural modification and synthesis [156]. There are, of course, some groups that have developed organic dyes and exhibited lower light-harvesting efficiency ranging between 4% and 8% [157–161]. The creation of dye aggregates on the surface of the semiconductor is one of the most significant issues contributing to the low conversion efficiency of organic dyes in the DSSC. To solve this problem and improve the light-harvesting efficiency, aggregation of dyes must be prevented to achieve the best performance, as this can be done by increasing both the surface area of the semiconductor oxide and adsorption on the substrate [5].

The electrospray deposition combined with photoelectron spectroscopies has become a good combination for the investigation of dye-sensitised surfaces [12, 13, 67]. The electrospray system is described previously (see Chapter 2), which allows non-volatile and complex molecules to be deposited at pressures between 10^{-7} and 10^{-9} mbar. Some literature studied XPS of free-metal organic dyes [162] and metal-organic dyes [12, 70]. The charge transfer interaction of N3 related to multicenter water splitting dye complex and its bi-isonicotinic acid ligand on TiO_2 has been reported by the O'Shea group [12, 70, 163], where 12 fs was the maximum limit charge transfer time from N3 to TiO_2 substrate [70]. The $TiO_2(110)$ substrate has received considerable attention in surface science studies due to its own versatility and multitude of applications, particularly in photocatalysis [164]. Also, a $TiO_2(110)$ surface is the most stable structure in terms of thermodynamics. Anatase $TiO_2(101)$ surface is considered a promising topic for further surface studies as well [165], as oxygen vacancies that are diffused on $TiO_2(110)$ tend to move to subsurface locations on $TiO_2(101)$ [166, 167]. Employing a single crystal substrate rather than a nanostructured is suitable for the surface science studies, as a periodic structure to obtain molecules in the same adsorption state is needed. In this chapter, all dyes were deposited in situ using the electrospray deposition technique combined with XPS. The system of organometallic (i.e N3 and RuP) and organic molecules (i.e D5, SC4 and R6) adsorbed onto rutile $TiO_2(110)$ is explored by XPS, which can be used to obtain element-specific information on the chemical structure and study bonding/interaction sites on the surface where analysis can be performed. The chemical structure of these dyes is given in their respective section.

6.2 Experimental Method

The sample used was a non-metallic wide band gap semiconductor surface of rutile $TiO_2(110)$ single crystal substrate. $TiO_2(110)$ was cleaned by cycles of sputtering 2 kV Ar^+ ions for 10 mins and then 1 kV for 5 mins, followed by annealing at 600°C until the C 1s peak was no longer observed in XPS spectra.

The electrospray source has been installed on the XPS system without applying instruments such as the drift tube, Einzel lens, and deflection plates presented in the previous results to use it for in-situ deposition experiments more conveniently. This comprises stages 1 to 3 of the electrospray, as presented in Chapter 5, and stage 4 is the XPS preparation chamber. A subtle but perhaps significant difference with the system used in this chapter is the larger separation between the entrance capillary and skimmer 1 and the increased separation between skimmers 1 and 2. These changes reflect the unwillingness to achieve a constant velocity to mass-select the ions by their kinetic energy. The deliberate shortening of these distances might cause the large clusters observed in the experiments in Chapters 4 and 5. A more molecular ion beam comprising smaller clusters might be reasonably expected, perhaps even individual molecular ions, in future experiments. This configuration is very similar to the one used in the deposition of C_{60}, fullerenes, single-molecule magnets (SMMs) and Self-decoupled tetrapodal perylene molecules in the literature [74, 85, 98, 168], where the spectroscopy and scanning probe microscopy is consistent with individual molecules being deposited rather than large clusters. All dyes (N3, RuP, D5 and SC4) were dissolved in ethanol except R6, which was dissolved in Tetrahydrofuran (THF) and sprayed at various times until 40 mins. The electrospray system is separated from the preparation chamber by a UHV gate valve. The preparation chamber pressure was 10^{-10} mbar when the gate valve was closed, whilst it was 10^{-8} mbar when the valve was open, and there was no electrospray procedure. The chamber pressure during the electrospray process rose to 10^{-7} mbar, whereas the presence of extra pressure was because of solvent molecules remaining in the molecule beam. As shown in Chapter 5, the deposition spot on the circular shape was with a range of coverages in the Gaussian profile. However, in this chapter, the coverage is changed by depositing for different times, such as 5 mins, 10 mins, 20 mins, 30 mins and 40 mins, then measuring after each deposition separately.

XPS data were calibrated to the Ti $2p_{3/2}$ substrate peak at 458.8 eV. Shirley [169] and linear backgrounds were removed from spectra, and curve-fitting analysis was carried out using pseudo-Voigt functions (a combination of Gaussian & Lorentzian) [170]. The dataset presented here has been fitted with a 30% Lorentzian and 70% Gaussian mix to approximate a Voigt lineshape.

Here, the widely used metal-organic ruthenium complex (N3) was examined again for comparison with the results already in the literature [12, 70] and to know what the data should look like when performing a new experiment. The XPS results are presented to characterise the bonding between the molecule and the surface in their respective section.

6.3 Results and Discussion

6.3.1 N3 on TiO_2 (110)

The surface coverage in the photoemission spectra samples is categorised into sub-monolayer, monolayer, few layers or multilayer. In the monolayer, molecules are directly adsorbed onto the surface, whilst the adsorption in the multilayer is deep, where the deep molecules cannot interact with the surface. To build a complete picture of how the molecules bond to the surface - particularly for new dyes used in this experiment – the N3 molecule in Figure 6.1 was tested as an example to ensure that the new experiments are working well.

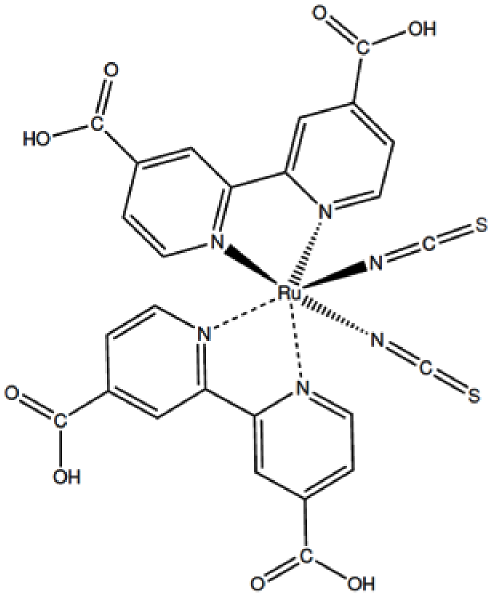

Fig. 6.1. Molecular structure of N3 dye (cis-bis(isothiocyanato)bis (2,2-bipyridyl-4,4'-dicarboxylato)-ruthenium(II)).

Figure 6.2 displays the O 1*s* XPS data at different sets of times to give a diverse range of coverages. The monolayers mean that the molecules are measured in direct chemical contact with the surface, whilst the multilayers predominantly imply molecules are not in contact with the surface. The monolayer at 5 mins deposition is fitted with two components, and the multilayer at 10 mins, 20 mins and 40 mins depositions with three. The dominant spectrum at 530.4 eV is attributed to the oxygen peak of TiO_2. For the monolayer, the peak at 531.4 eV is assigned to C=O and deprotonated to COO^- [12]. Deprotonation and configuration of the 2M-bidentate bridging method are typical advantages of aromatic carboxylic acid molecules adsorbed on TiO_2. Usually, oxygen bind to the surface in a 2M-bidentate bridging mode, where the two oxygen atoms in the O 1*s* spectrum are chemically equivalent upon adsorption [15], as shown in the schematic in Figure 6.3. The different anchoring modes of carboxylic acid onto a metal oxide have been clarified in the literature [171]. The bi-isonicotinic acid bonds with TiO_2 substrate are discussed in the previous studies as the 2M-bidentate (bridge) bonding geometry involves deprotonation of the carboxyl (COOH) groups [15, 16, 172]. The binding of pyridine carboxylic acids onto the TiO_2 surface can be obtained in the literature [173–175]. There is a problem that the N3 is incapable of deprotonating and bonding all 4 carboxylic acid groups onto the surface simultaneously. In the paper by Mayor [12], they found a 3:1 ratio of the COO^- and C–OH peaks in the monolayer, but a ratio of 1:0 has been observed in the monolayer data because the signal is weak enough to see C–OH.

In the case of 10 mins deposition, the small peaks at 531.4 eV and 533.4 eV are identified as the carbonyl (C=O) and hydroxyl (C-OH) groups, respectively, in the molecule's carboxylic acid ligand [15]. For the 40 mins deposition, the same event as 20 mins deposition is noticed with a suppression in the O 1*s* molecule component (C=O) relative to the substrate contribution because of increasing molecules number on the TiO_2 surface. Because of the equal intensities of carbonyl (C=O) at 531.7 eV and hydroxyl (C-OH) at 533.5 eV oxygen atoms in the N3 structure, it can anticipate the appearance of two O 1*s* peaks of comparable

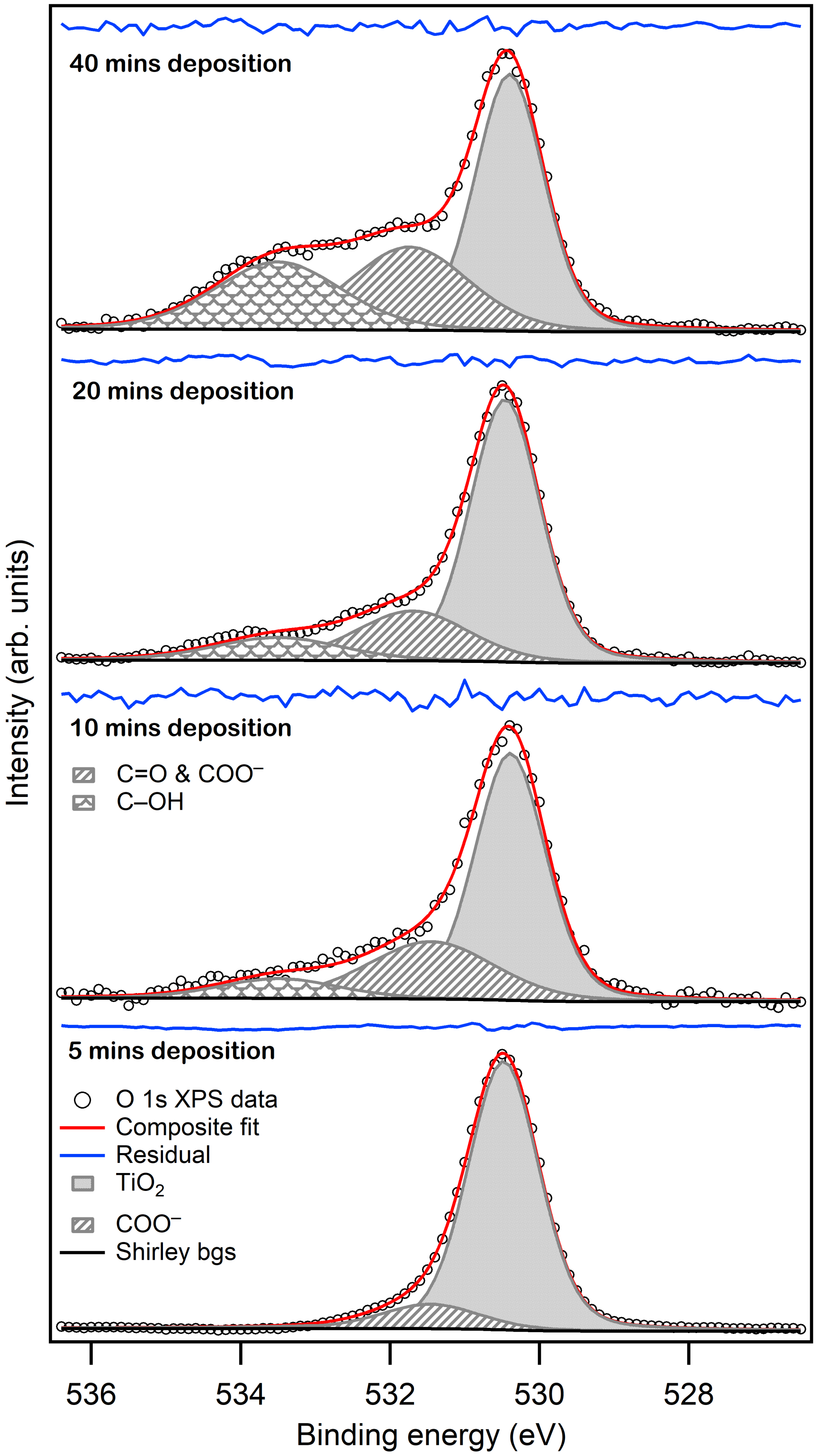

Fig. 6.2. O 1*s* photoemission spectra taken at different deposition times for N3 adsorbed on rutile $TiO_2(110)$, fitted using identical parameters. The dataset had Shirley's background subtracted. The residual spectra are shown above each spectrum.

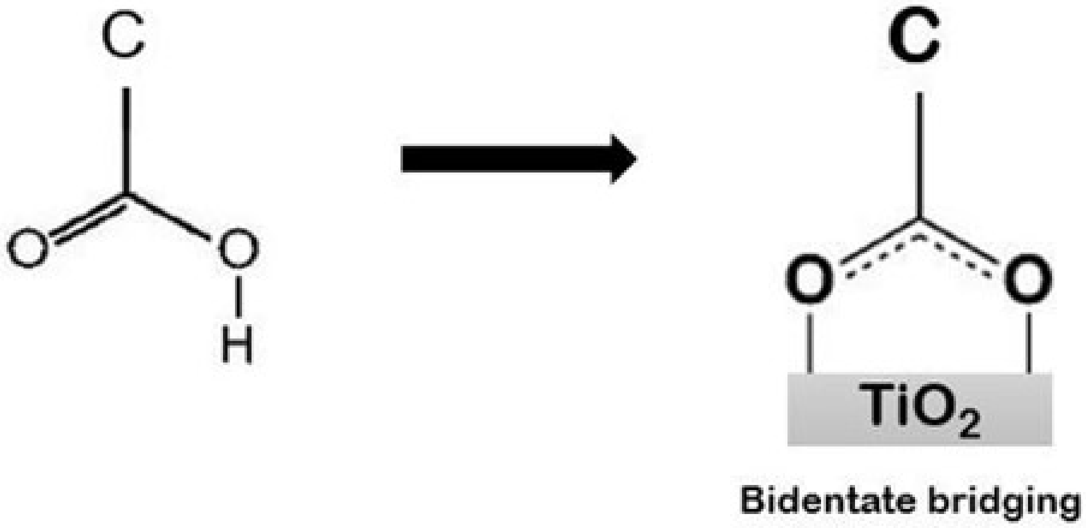

Fig. 6.3. Schematic representation of bidentate binding mode for carboxylic acid anchor onto titanium dioxide TiO_2(110).

intensity. As can be seen in the multilayer coverage (10 mins) and (40 mins), the intensity ratio of the O 1*s* peaks in (C=O) and hydroxyl (C-OH) are 3:1 and approximately ~1:1, respectively. This means most of the measured photoelectrons are from N3 molecules with limited intermolecular and molecule-surface bonding through the bi-isonicotinic acid ligands in the multilayer. In contrast, there is an interaction in the monolayer because of the deprotonation of the carboxylic acid groups.

The monolayer (a) and multilayer (b) of C 1*s* and Ru 3*d* spectra data are presented in Figure 6.4, which have been fitted with pyridine, carboxyl, thiocyanate groups and a doublet state Ru 3*d*. The atomic ratio of 10:2:1 is for carbon atoms in the pyridine ring, carboxylic acid and thiocyanate ligands. The actual ratio for the monolayer is 12:2:1. Hence the disagreement with the expected results is most probably attributable to the fact that half of these groups are bonded to the surface. The ratio found for the multilayer is 10:2:1, which corresponds to the ratio of these atoms in the molecule. The bi-isonicotinic acid (related to pyridine and carboxylic acid molecules) has been investigated previously [176, 177]. In both coverages, the main peak for the monolayer and multilayer at 285.9 eV and 285.7

eV is assigned to carbon-nitrogen (C–N) environments in the pyridine rings. The peak at 289.4 eV on both coverages is attributed to the carboxyl carbon atom in the carboxylic acid (COOH) anchoring group. The shoulder to the higher binding energy of the main peak is due to the thiocyanate groups at 287.3 eV and 287.1 eV for monolayer and multilayer. A slight change in the binding energy of the C 1*s* peaks in both coverages was observed, as shown in Table 6.1.

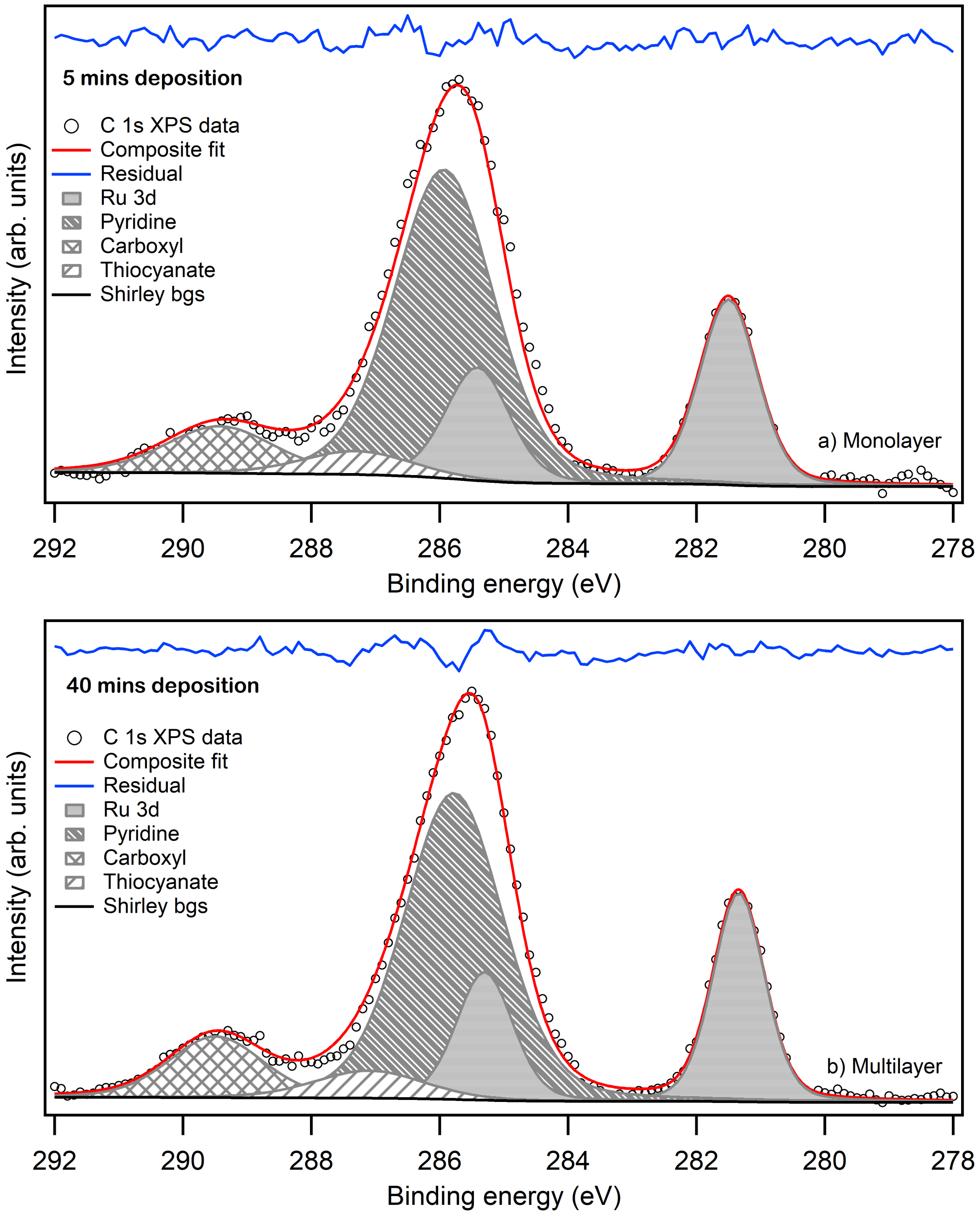

Fig. 6.4. C 1*s* core-level spectra taken at different deposition times adsorbed on rutile $TiO_2(110)$, fitted with Ru 3d, C-N, COOH, and N=C=S components. The spectra have had background subtracted.

Ru $3d$ is a doublet state with a well-defined separation of 4.2 eV [178]. The peak at the lower binding energy, 281.5 eV, is attributed to Ru $3d_{5/2}$, with the corresponding Ru $3d_{3/2}$, which can be seen in Figure 6.4. The intensity ratio of Ru $3d_{5/2}$ is 6, and the intensity ratio of Ru $3d_{3/2}$ is 4 (see Chapter 3 in the Section 3.4.6).

Figure 6.5 represents the N $1s$ photoelectron spectra of the monolayer and multilayer fitted with two components which are assigned to the nitrogen peaks in the pyridine ring (C-N) and thiocyanate (N=C=S). For the monolayer, the binding energies of these peaks are 400.5 eV and 398.6 eV, but 400.4 eV and 398.5 eV for the multilayer with a 2:1 ratio, respectively, corresponding to the atom ratio in the molecule. The monolayer of N $1s$ data shows no change in the intensity ratio related to pyridine and thiocyanate, implying that molecules reach the surface entirety. The C $1s$ and the N $1s$ spectra show that the molecule is intact on the surface since all the functional groups and the ruthenium atom are present. Also, the Ru $3d$ binding energy is is consistent with the Ru^{2+}, which supports the idea that the molecule is intact.

The XPS measurement of the S $2p$ spectra for monolayer and multilayer coverage is illustrated in Figure 6.6. S $2p$ is a doublet state with a spin-orbit coupling of 1.1 eV [179]. Previous studies revealed two different chemical environments of sulphur atoms for the monolayer [12], meaning that one of the thiocyanate ligands was included in the bonding to the surface. On the other hand, only one type of sulphur atom can be observed in this XPS data of both monolayer and multilayer films with an intensity ratio of 2:1. This implies no thiocyanate group involved in bonding to the surface, so both of these must be sticking out into the vacuum away from the surface, thus placing bi-isonicotinic acid ligands at the surface. This is consistent with the observation of complete deprotonation of the bi-isonicotinic ligands in the O $1s$ spectra for the monolayer, implying that all of the carboxylic acid groups are bound to the surface (both bi-isonicotinic acid

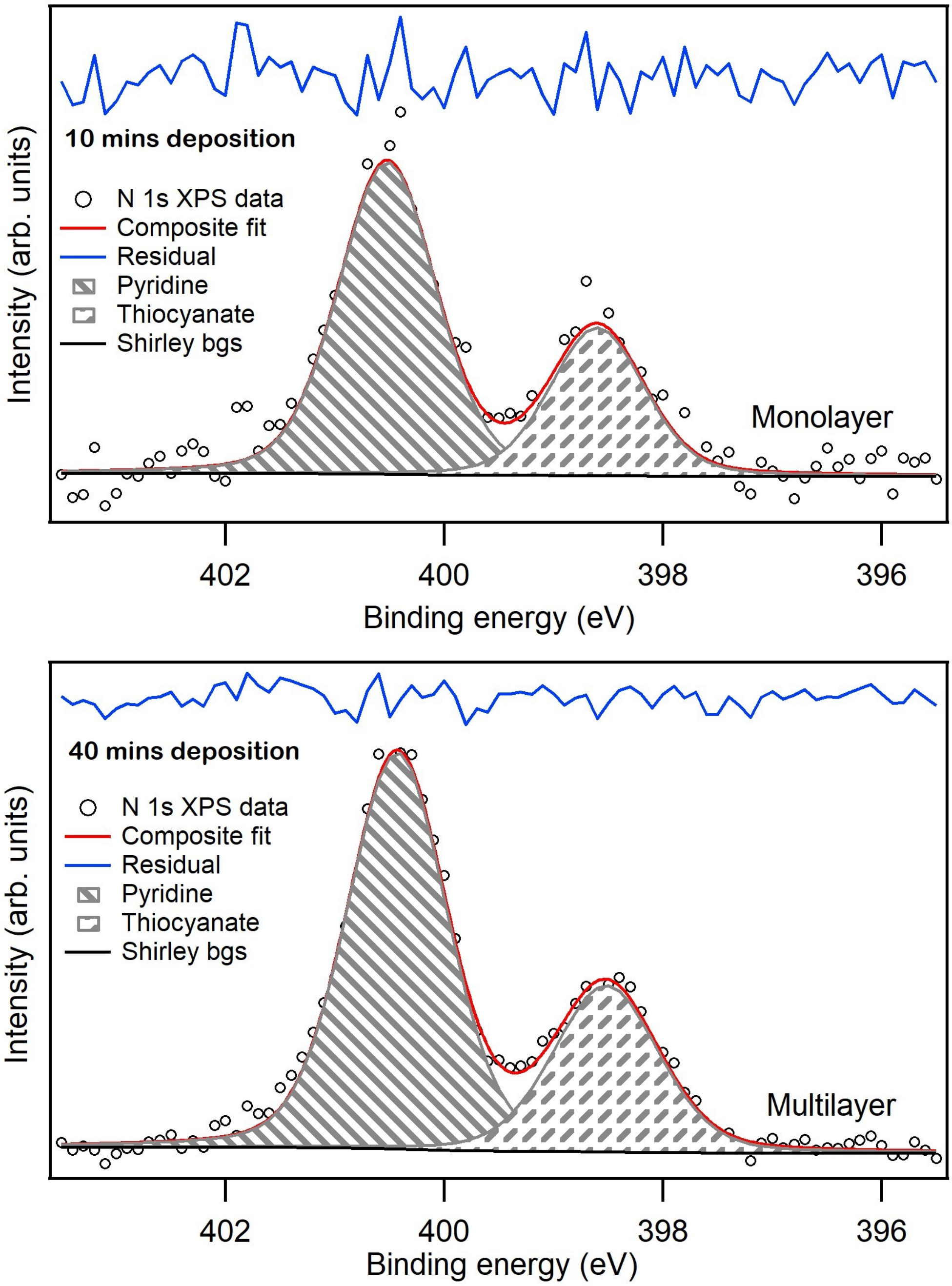

Fig. 6.5. N 1*s* XPS measured for a monolayer and multilayer of N3 on the rutile $TiO_2(110)$ surface. The large peak is attributed to nitrogen in the bi-isonicotinic acid ligands, whereas the small peak is assigned to the thiocyanate ligands.

ligands), making the sulphur atoms impossible to bond to the surface. In the paper by Mayor et al., different adsorption geometry is observed, where one sulphur atom is bound to the surface due to the bonding of a single bi-isonicotinic acid ligand to the surface [12].

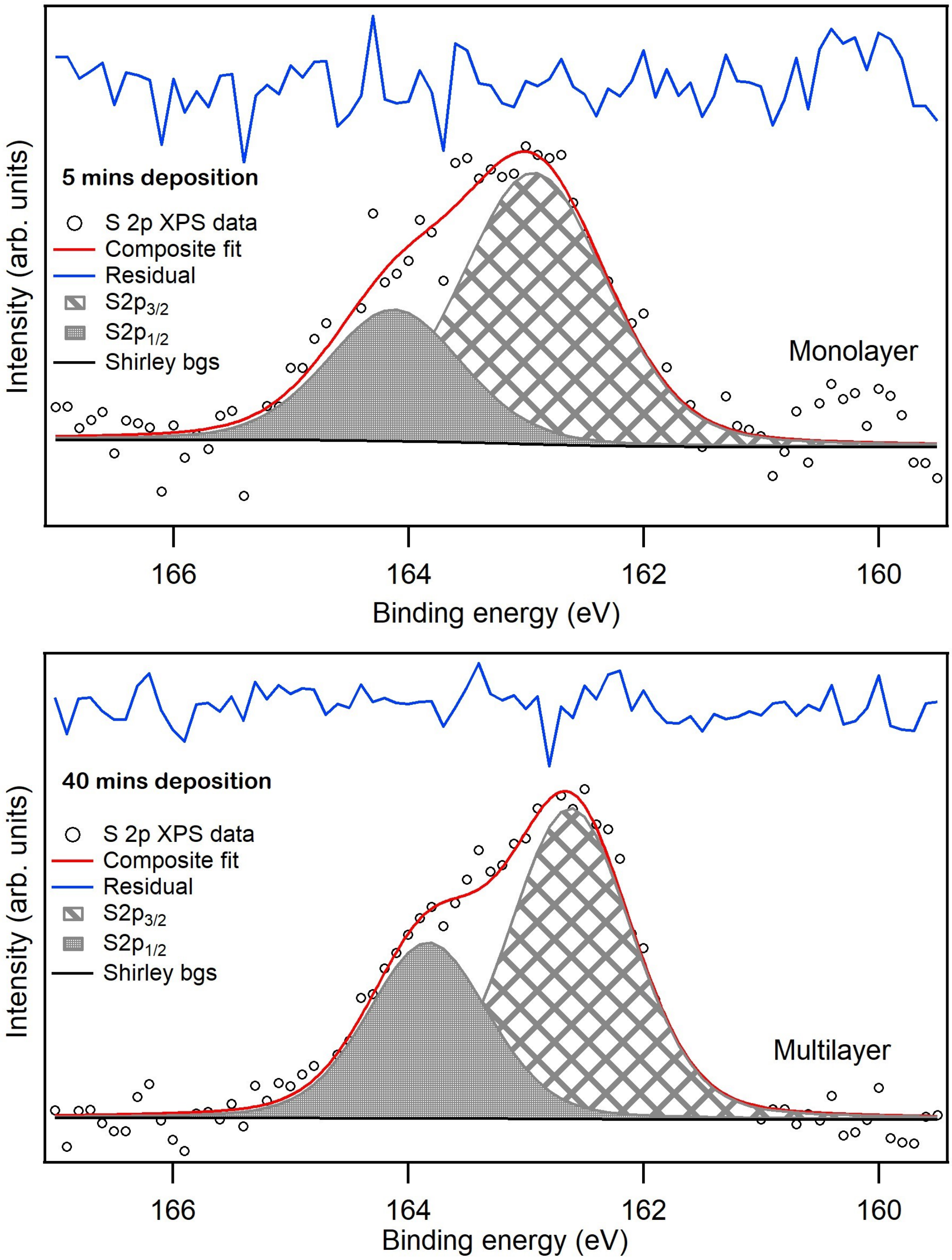

Fig. 6.6. S $2p$ XPS spectra indicate a single chemical state for S atoms (S $2p_{3/2}$ and S $2p_{1/2}$) with spin-orbit pairs of 1.1 eV.

The ratios of O, S, C and N in N3 molecule are 8:2:26:6 compared to photoionisation cross-sections ratios of the multilayer coverage 8.5:2:29.6:4.3 which have a reasonable agreement, but these ratios do not match exactly. This is probably because of the molecule's geometry on the surface, with some parts being attenuated by the other part of the molecule. The number of carbon atoms overestimates because some residual methanol is leftover from the deposition. Also, nitrogen is a bit low because it is on the inner part of the molecule, where some parts cover the nitrogen. A summary of core-level binding energy (BE) positions obtained from peak fitting of the XPS data is listed in Table 6.1.

		Peak BEs (eV)	
		Monolayer	**Multilayer**
	TiO_2	530.4	530.4
O 1*s*	C=O & COO^-	531.4	531.7
	C-OH		533.5
	Pyridine (C–N)	285.9	285.7
C 1*s*	Thiocyanate (N=C=S)	287.3	287.1
	Carboxyl (COOH)	289.4	289.4
Ru 3*d*		281.5	281.3
N 1*s*	Thiocyanate (N=C=S)	398.6	398.5
	Pyridine (C–N)	400.5	400.4
S 2*p*		162.9	162.6

Table 6.1. Parameters of the XPS component binding energies for N3 on the rutile $TiO_2(110)$ surface.

6.3.2 RuP on $TiO_2(110)$

Previous studies of water-splitting dye-sensitised photo-electrochemical cells have investigated a derivative of ruthenium with phosphonate anchoring groups as RuP [180–182]. RuP belongs to the ruthenium(II) bipyridyl dye family with phosphonic acid functional groups. It was synthesised and characterised, as reported by

Gillaizeau et al. [183]. The chemical structure of RuP is shown in Figure 6.7.

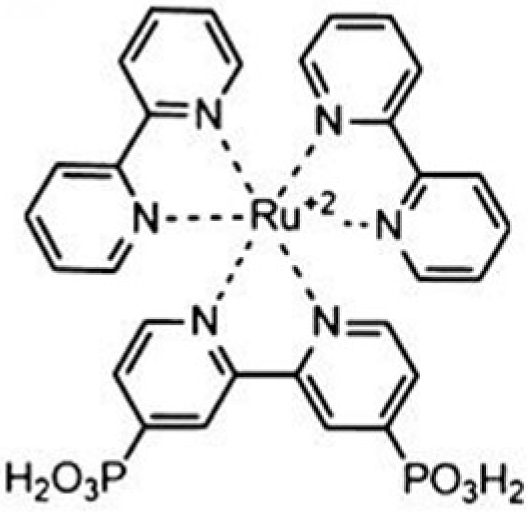

Fig. 6.7. Molecular structure of the RuP dye [Ru(bpy)2(4,4-PO3H2)2bpy]$^{2+}$.

Figure 6.8 shows the O 1*s* photoelectron spectra obtained for a range of RuP coverages, from 5 mins to 40 mins deposition. The oxygen peak in the oxide surface at 530.4 eV dominates the spectrum on both coverages. The two smaller peaks to higher binding energy are due to the phosphonic acid groups (i.e. P = O and P–OH environments) [183]. Phosphonic acid anchors to the surface of TiO_2 are illustrated in Figure 6.9 through the adsorption of O_2 on the surface mediated by the 2M-bidentate bridging mode. In the lower coverage (5 mins deposition), these two peaks, at 531.3 eV and 532.6 eV, respectively, have a ratio of 4:1. When the phosphonic acid groups are bound to the TiO_2 surface, it causes some loss of OH (i.e deprotonated as bonded to the surface) which makes the O 1*s* peak resemble the binding energy of P=O as seen in the rest of deposition times. In the high coverage (40 mins deposition), P=O and P–OH peaks at 531.7 eV and 533.2 eV, respectively, have a ratio of 1:1 in the unbound molecule, as the phosphonic acid groups remain protonated.

Figure 6.10 exhibits a photoelectron spectra of the C 1*s* and Ru 3*d* core levels for the monolayer and multilayer. The carbon environments are bonded into

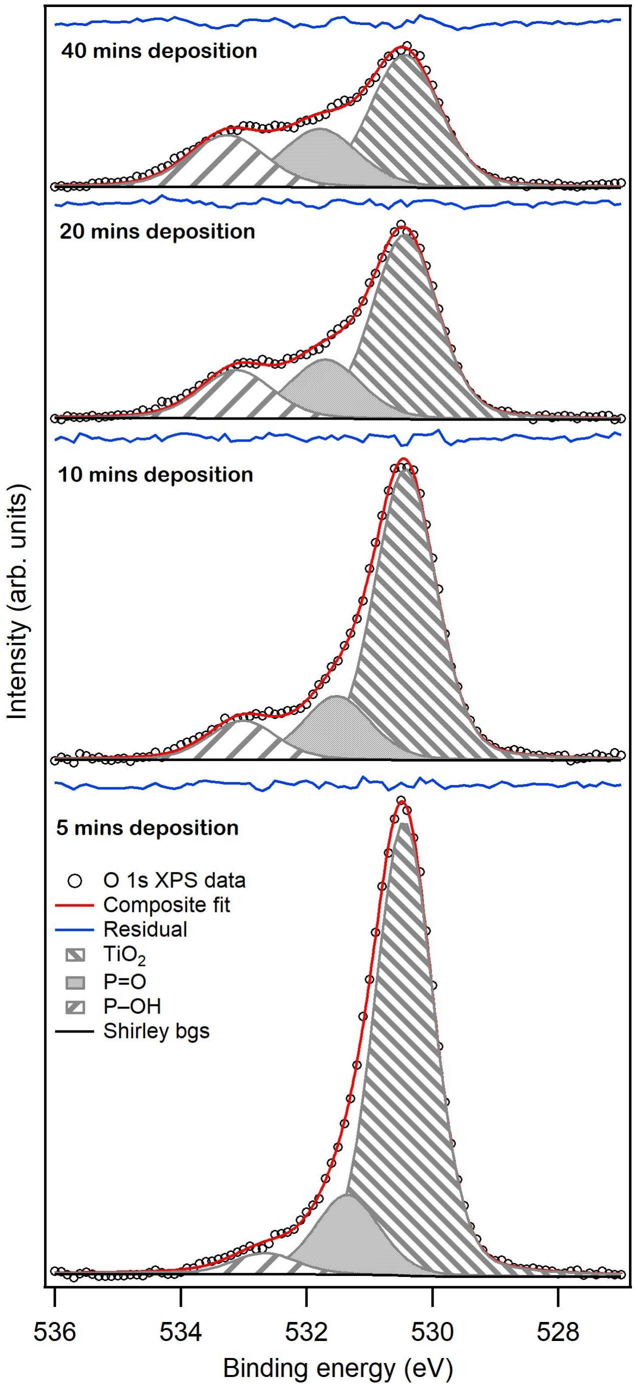

Fig. 6.8. O 1*s* core-level photoemission spectra measured for different surface coverages of RuP adsorbed on rutile $TiO_2(110)$.

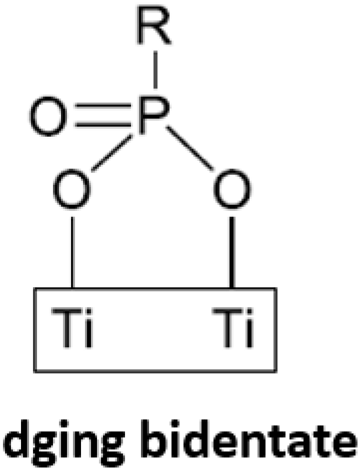

Fig. 6.9. Schematic representation of bidentate binding mode for phosphonic acid group anchor onto titanium dioxide TiO_2(110) [184].

pyridine ring C–C, pyridine ring C–N and phosphonic acid. In both coverages, the most intense peak to be dominated by XPS is from C–C in the pyridine ring. The binding energy of pyridine ring C–C at 285.7 eV in the low coverage whilst 285.5 eV in high coverage. The second intense peak in both coverages at 286.8 eV and 286.6 e is due to carbon atoms bound to nitrogen in the pyridine ring, whilst the phosphoryl carbon atom in the PO_3H_2 group is fitted to a small shoulder at 287.3 eV for both coverages. The intensity ratio representing pyridine ring C–C, pyridine ring C–N and phosphoryl carbon is 8:6:1 for monolayer and multilayer which is consistent with the expected ratio based on the stoichiometry. The C–C and C–N pyridine rings and phosphoryl carbon are in the same chemical environment in both films, implying these have not participated in bonding to the surface. The Ru $3d$ peaks are resolved as a doublet of Ru $3d_{5/2}$ and Ru $3d_{3/2}$ at 281.9 eV and 286.1 eV in the monolayer, and binding energy of 281.7 eV and 285.9 eV is to the multilayer.

N $1s$ XPS spectra are displayed in Figure 6.11, exhibiting a single pyridine C–N peak in both films. This peak is consistent with the single bonding shown by nitrogen atoms. However, the binding energy of C–N is 401.04 eV for the monolayer and 400.9 eV for the multilayer coverage.

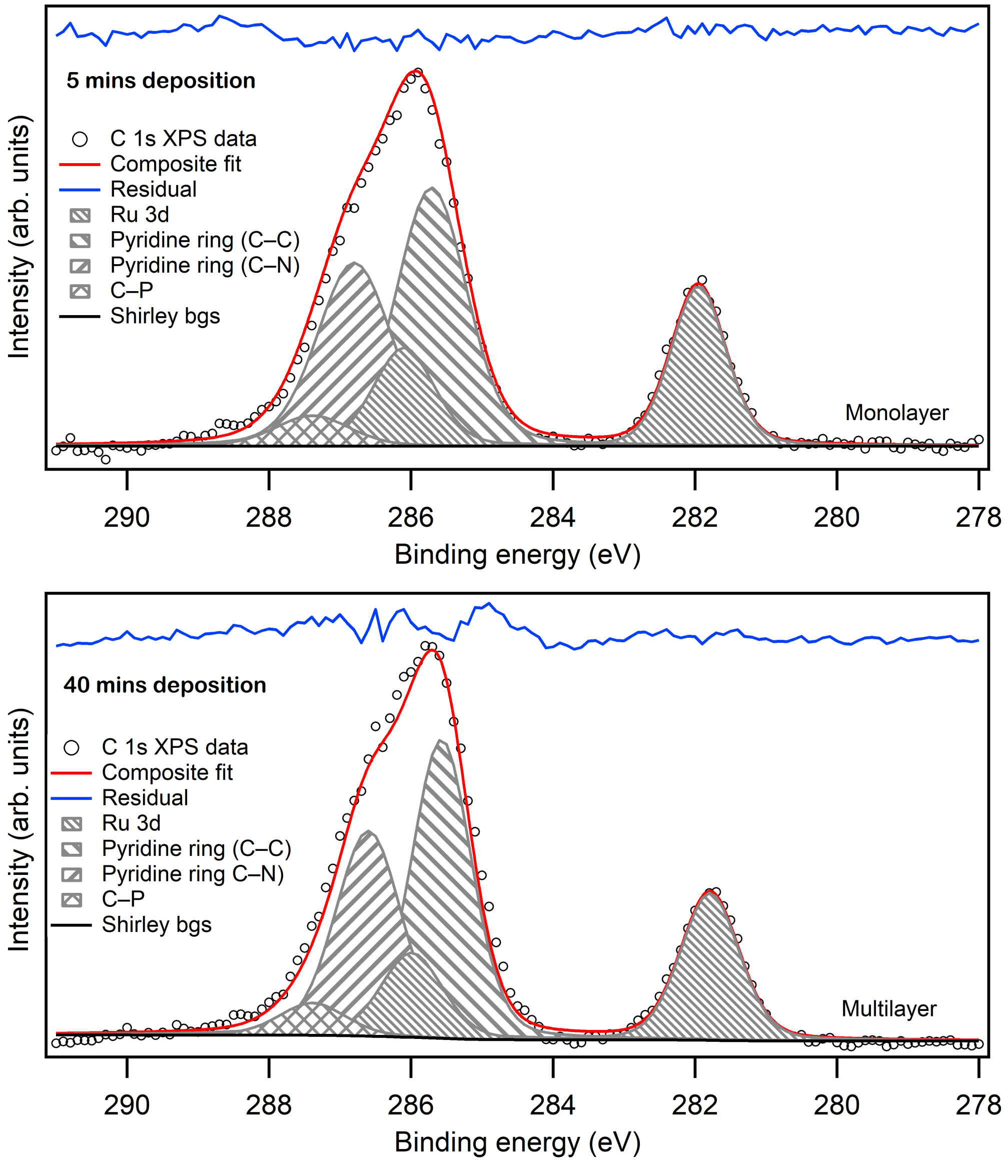

Fig. 6.10. C 1*s* photoemission spectra of a RuP monolayer and multilayer film adsorbed on rutile $TiO_2(110)$.

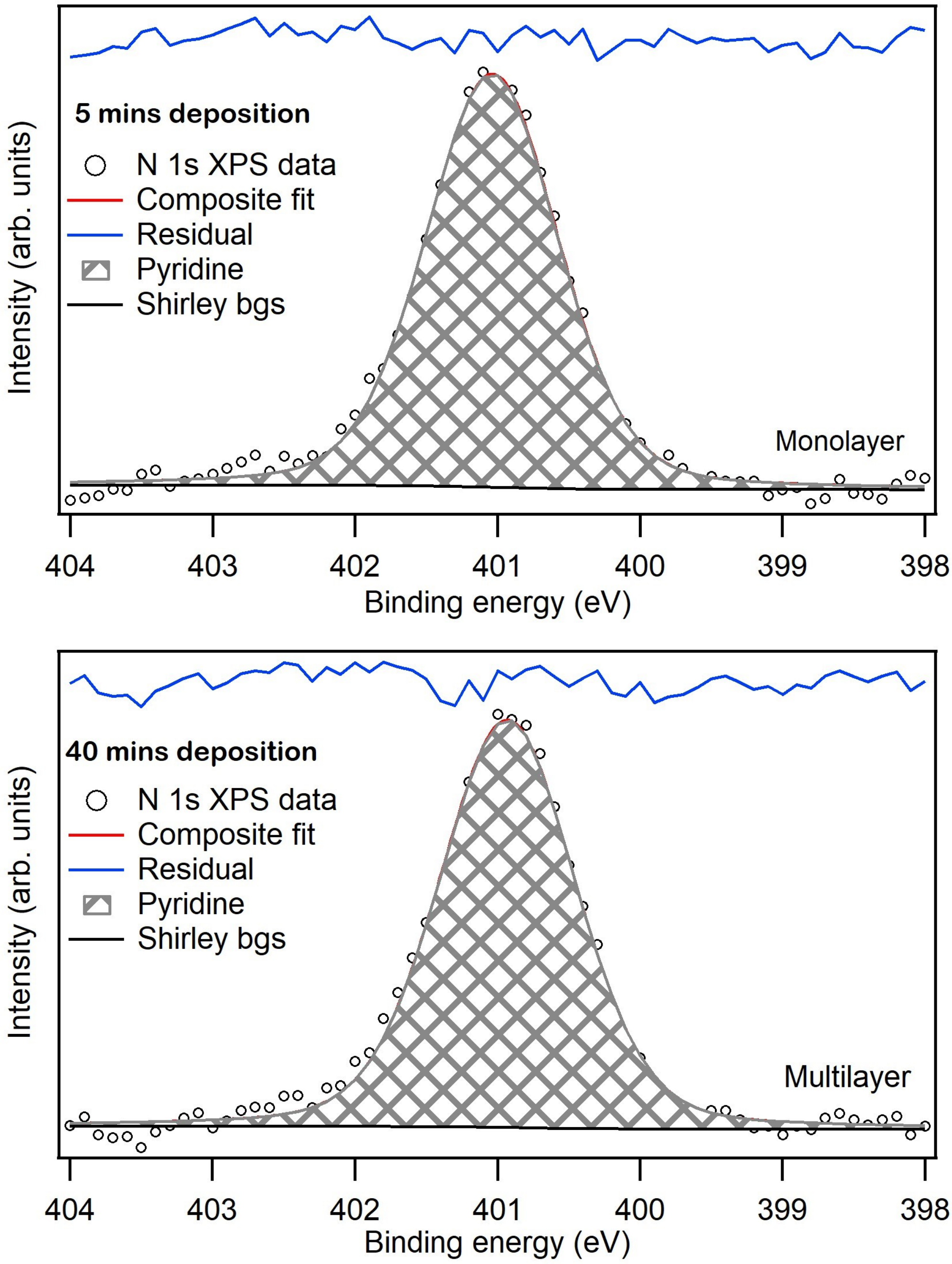

Fig. 6.11. N 1*s* XPS spectra for the monolayer and multilayer film fitted with one component attributed to the pyridine C–N environment.

Figure 6.12 presents the P 2*p* core-level spectra for the monolayer and multilayer film and the P 2*p* paired state with the spin-orbit splitting of 0.87 eV [179]. The corresponding peaks of P2p can be deconvoluted into double peaks (P $2p_{3/2}$ and P $2p_{1/2}$). The lower binding energy of the P $2p_{3/2}$ peak can be seen clearly in the monolayer spectrum at 133.4 eV, and similarly, it is 133.5 eV for the multilayer. It is worth noting that a 0.1 eV shift is not really significant. This shift can occur as the coverage is increased due to less screening of the core holes from the surface, causing a small amount of steady charging. All P 2*p* spectra coverages have a ratio of 2:1. When calculating the photoionisation cross-sections of the O, P, C and N, it was observed that the ratios 4.4:2:27:3.9 do not match completely with the proportions based on the stoichiometry 6:2:30:6, although there is a good similarity. The binding energies of the XPS peaks are summarised in Table 6.2.

		Peak BEs (eV)	
Core Level		**Monolayer**	**Multilayer**
O 1*s*	TiO_2	530.4	530.4
	P=O	531.3	531.7
	P–OH	532.6	533.2
C 1*s*	Pyridine ring (C–C)	285.7	285.5
	Pyridine ring (C–N)	286.8	286.6
	Phosphoryl (C–P)	287.3	287.3
Ru 3*d*		281.9	281.7
N 1*s*	Pyridine (C–N)	401.04	400.9
P 2*p*		133.4	133.5

Table 6.2. Core levels of the XPS component binding energies for RuP on the rutile $TiO_2(110)$ surface.

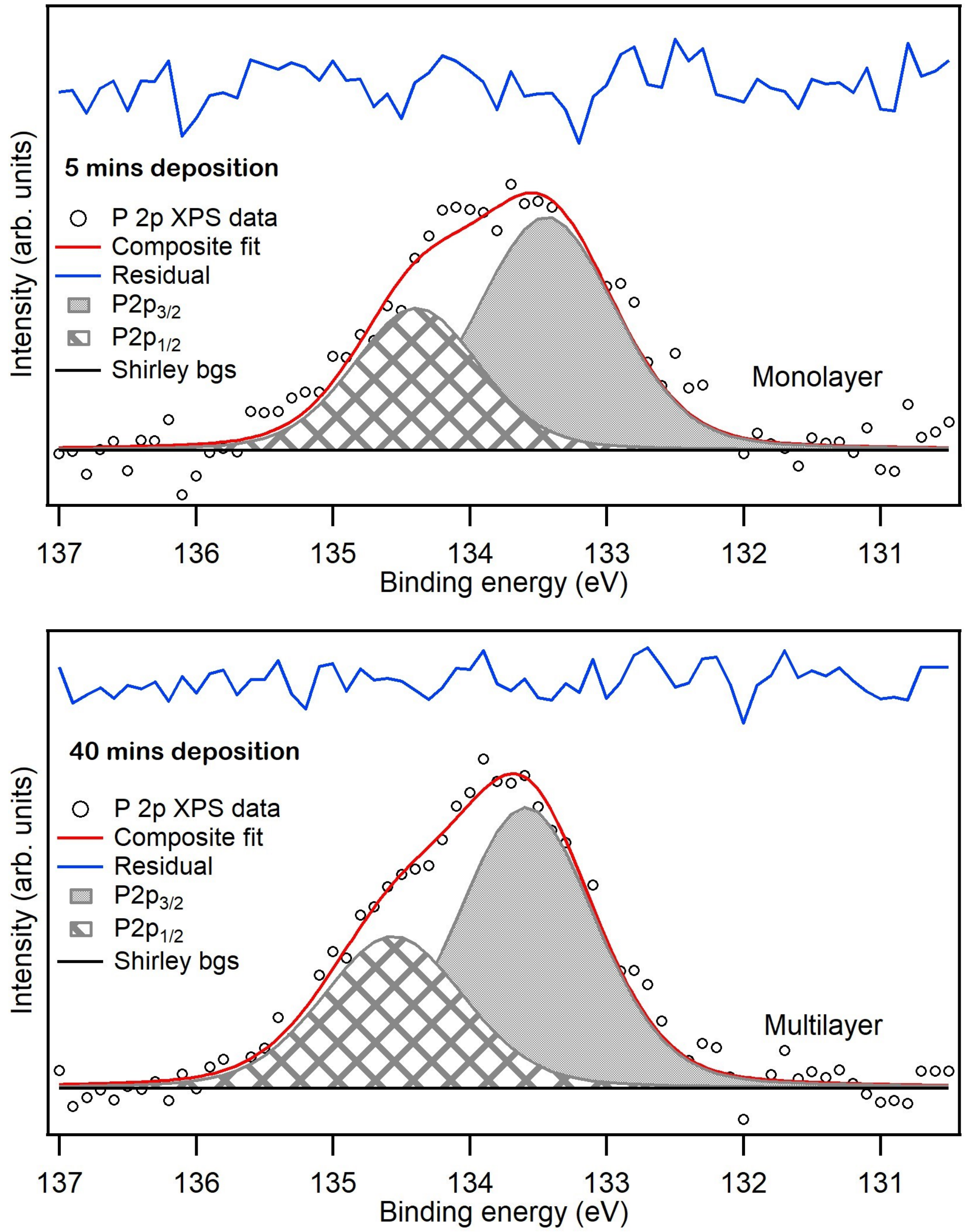

Fig. 6.12. P $2p$ photoemission spectroscopy of monolayer and multilayer coverage of RuP showing the spin-orbit split P $2p_{3/2}$ (right) and P $2p_{1/2}$ (left).

6.3.3 D5 on $TiO_2(110)$

The D5 molecule is known as the polyene-diphenylaniline dye. The diphenylaniline group donates an electron, whereas the cyanoacetic acid group accepts it. Moreover, the cyanoacetic acid acts as an anchoring group onto the nanostructured TiO_2 surface [161] (see chemical structure in Figure 6.13). The electronic structure of D5 and triphenylamine on TiO_2 had previously been studied using photoelectron spectroscopy (PES) [162, 185, 186].

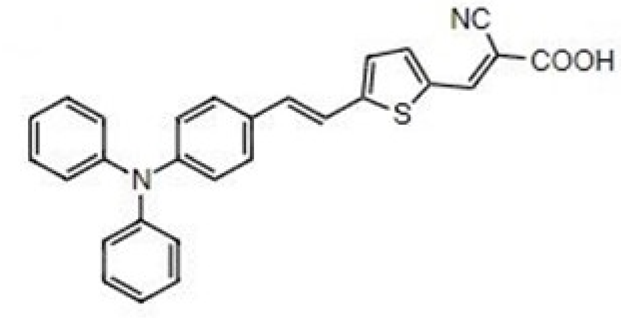

Fig. 6.13. Molecular structure of D5 dye (3-(5-(4-(dip–henylamino) styryl) thiophen-2-yl)-2-cyanoacrylic acid.

A comparison of the O 1*s* X-ray photoemission spectra for surface coverages ranging from 5 mins to 40 mins deposition is shown in Figure 6.14. As usual, the prominent peak at 530.4 eV in all spectra is attributed to the substrate oxygen atom. In the first spectrum for 5 mins deposition, there is a single molecule O 1*s* peak at 531.8 eV, which is assigned to the COO^-. This arises because of the deprotonation of the COOH groups and the bonding of the O1s atoms to TiO_2 atoms on the surface by the 2M-bidentate process (see section 6.3.1). As the coverage is increased, the same situation is clearly observed for 10 mins deposition with an increase in the number of molecules on the surface. In the case of 20 mins and 40 mins deposition, the two components to higher binding energy are referred to C=O at 531.8 eV, which presents in the carboxylic acid group and is thus deprotonated to COO^- [12]. The oxygen atoms of the O–H feature at 534.0 eV indicates that not all molecules are bound to the surface. The expected ratio of the C=O & COO^{-}:C–OH should be 1:1, but it was 4:1, which means some O–H group lost proton (i.e. deprotonated as bounded to the surface) or it did not receive thick coverage (i.e. just a little more than one monolayer).

C 1*s* core-level photoelectron spectra are presented in Figure 6.15. There are four chemical environments for C 1*s* in D5: ring carbon, triphenylamine N, thiophene and carboxyl groups. The main carbon peak can be fitted to three components representing the carbon bound to nitrogen in the triphenylamine moiety and cyanoacrylic acid group at 286.3 eV, carbon bound to sulphur in the thiophene at 287 eV and the dominant peak to lower binding energy at 285.3 eV, which comprise 21 ring carbon atoms of the molecule (see Figure 6.13). The peak at 288.7 eV is attributed to a carboxylic carbon atom. The same molecular components are observed for 40 mins deposition coverage, where the binding energies of 285.2 eV, 286.2 eV, 287.0 eV and 289.0 eV are attributed to ring carbons, triphenylamine N, thiophene and COOH groups, respectively. The 5 mins deposition (sub-monolayer) contributes to this deprotonated carboxylic, whilst the 40 mins deposition (a little more than one monolayer) is not deprotonated. The atomic ratio of molecules in the chemical structure is 21:4:2:1, whereas 22:5:2:1 is the intensity ratio for the sub-monolayer. There is a slight difference in the ratio because some molecule parts close to the substrate are bound to the surface, whilst the rest of the molecules attenuate them.

N 1*s* XPS data is illustrated in Figure 6.16 and is fitted with two components for all coverages. These are attributed to the nitrogen atoms in the triphenylamine (C–N) at binding energy of 400.6 eV and nitrile ($C \equiv N$) at 399.7 eV for the 5 mins and 40 mins deposition. A previous study has the same moieties of triphenylamine and nitrile, which have been used to investigate the comparison of N 1*s* binding energies in D5 [187]. The 5 mins and 40 mins deposition data indicate that the ratio of nitrogen atoms in the triphenylamine and nitrile groups is 1:1.

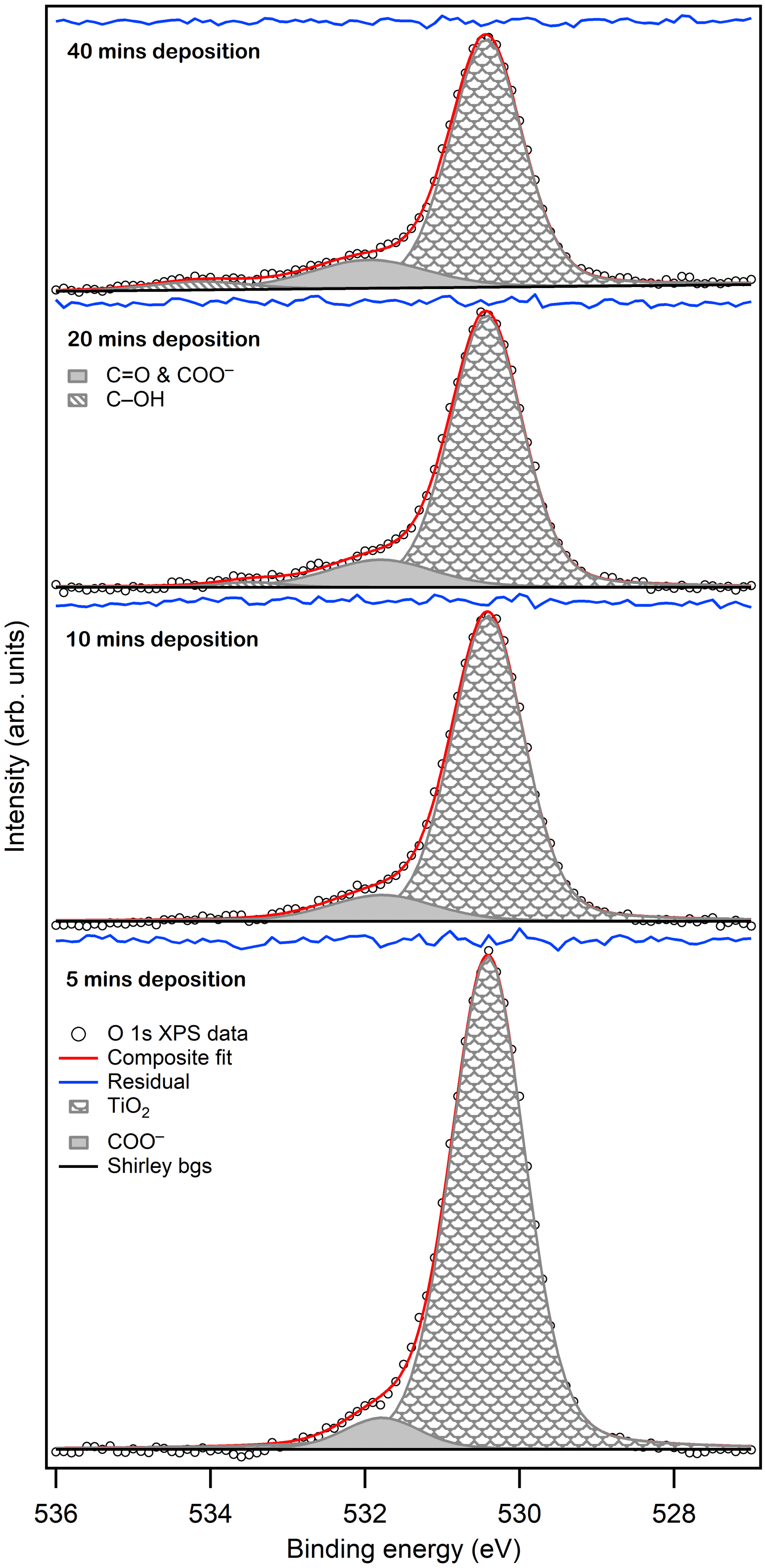

Fig. 6.14. O 1*s* core-level XPS spectra using different time deposition coverages of D5 adsorbed onto nanostructured $TiO_2(110)$.

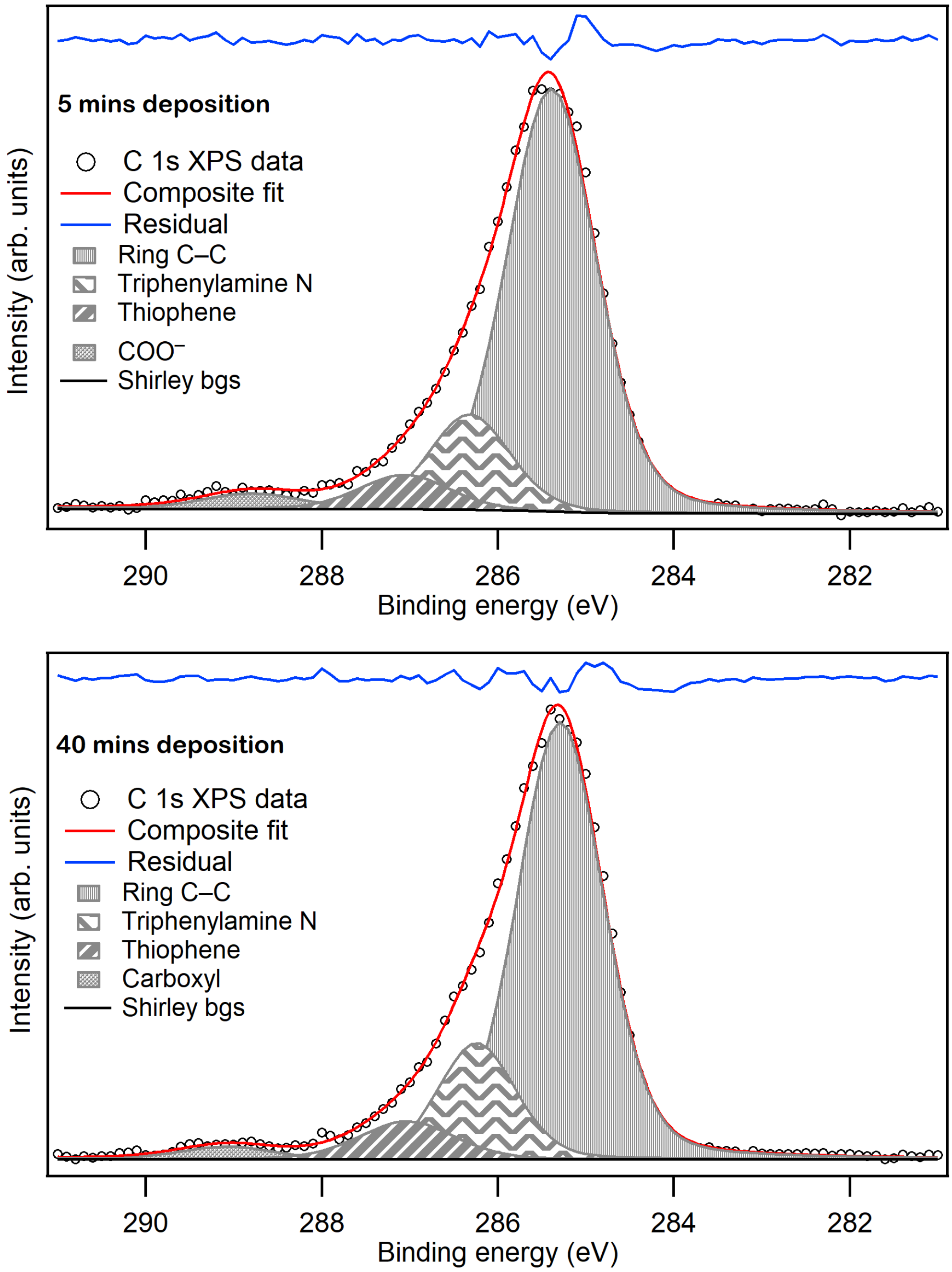

Fig. 6.15. C 1*s* photoemission measured spectra of D5 coverages adsorbed on rutile $TiO_2(110)$ surface.

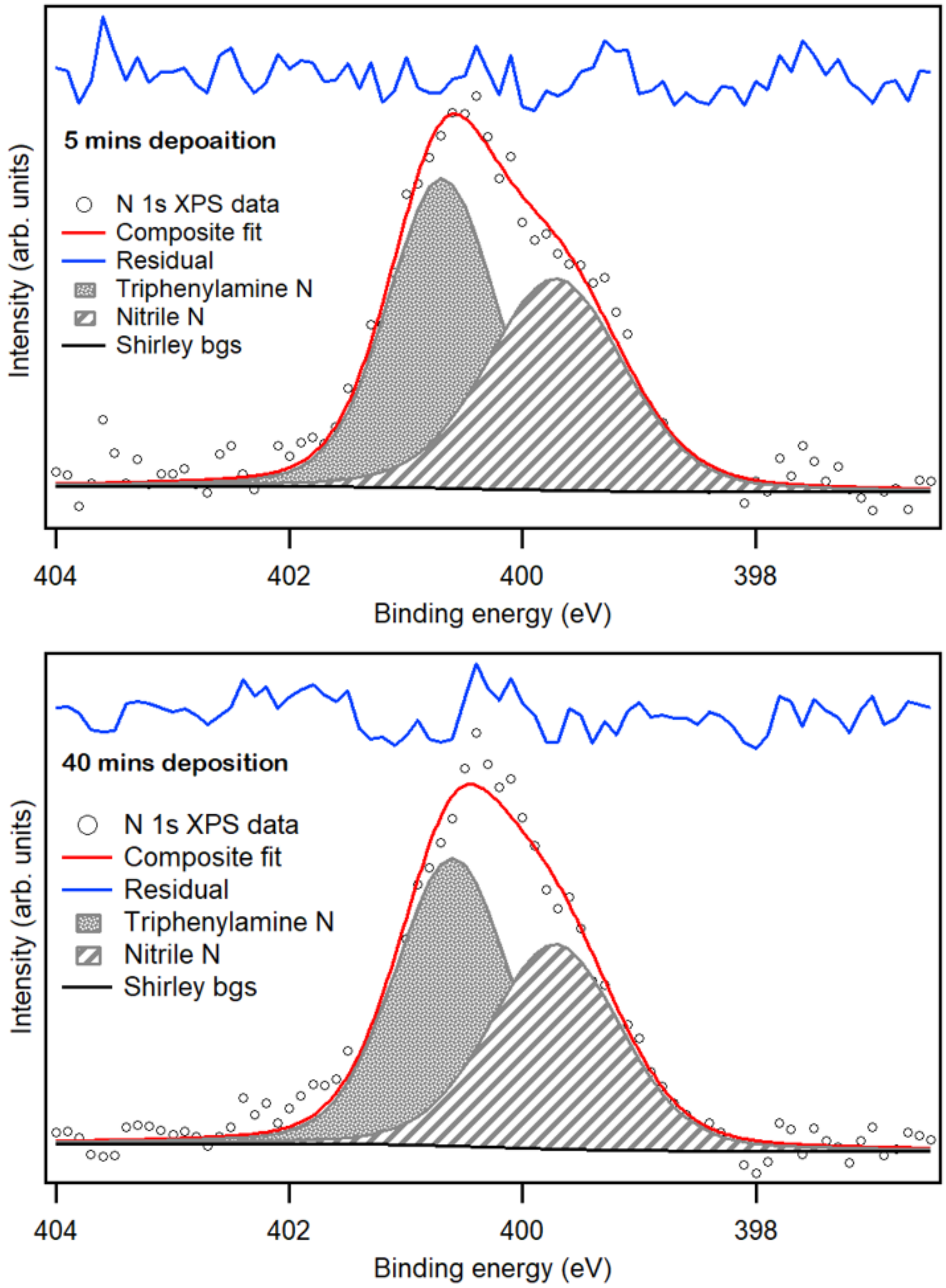

Fig. 6.16. N 1*s* XPS spectra for 5 and 40 mins deposition coverages of D5 adsorbed on $TiO_2(110)$ referring to no change in chemical environment between different coverages.

Figure 6.17 shows the S $2p$ photoemission spectra of the 5 mins and 40 mins deposition films, fitted with two component pairs corresponding to the sulphur environments in the thiophene moiety (C–S $2p_{3/2}$ and C–S $2p_{1/2}$). The spin-orbit splitting 1.1 eV [179] between 3/2 and 1/2 doublet components were used. The 2:1 is the intensity ratio for 5 mins and 40 mins deposition coverages. The lower binding energy of the C–S $2p_{3/2}$ peak can be observed clearly in the spectra at 164.8 eV [188]. The atomic ratios of O, S, C and N in D5 molecule are 2:1:28:2 which also does not coincide perfectly when considering the photoionisation cross-sections ratios of 1.4:1:24.4:1.6, where the oxygen ratio is low due to its bonding to the surface. The spectral parameters are given in Table 6.3.

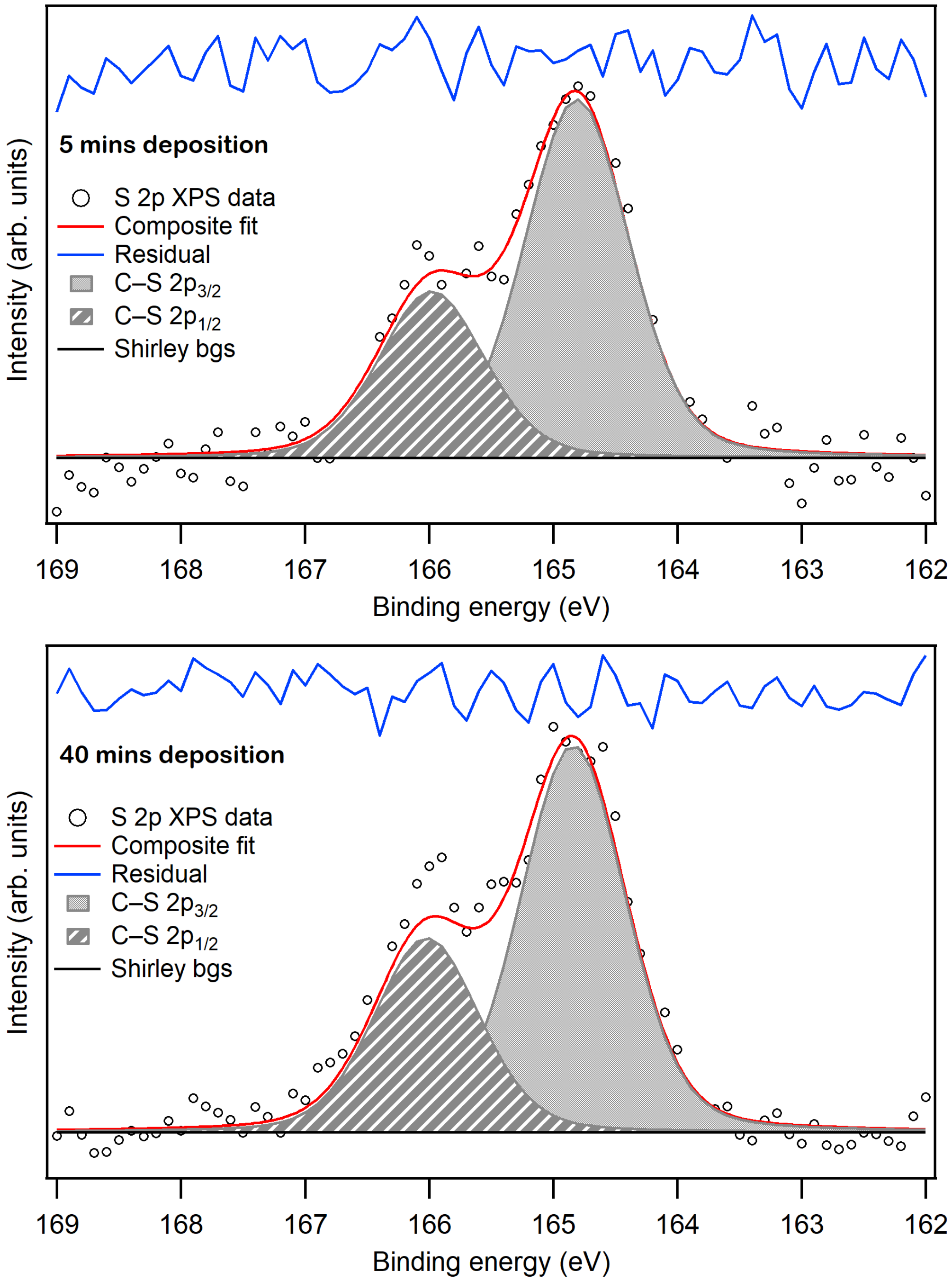

Fig. 6.17. S 2*p* core-level spectra of D5 coverages adsorbed onto rutile $TiO_2(110)$ surface.

		Peak BEs (eV)	
		5 mins deposition film	**40 mins deposition film**
O 1*s*	TiO_2	530.4	530.4
	C=OH & COO^-	531.8	531.8
	C−OH		534.0
C 1*s*	Ring (C−C)	285.3	285.2
	Triphenylamine N	286.3	286.2
	Thiophene	287.0	287.0
	COO^-	288.7	289.0
N 1*s*	Triphenylamine N	400.6	400.6
	Nitrile N	399.7	399.7
S 2*p*	Thiophene	164.8	164.8

Table 6.3. Parameters of the XPS component binding energies for D5 on the rutile $TiO_2(110)$ surface.

6.3.4 SC4 on $TiO_2(110)$

SC4 has a similar chemical structure to D5 with an addition of an incorporated moiety of 4-(benzo[c][1,2,5]thiadiazol-4-yl)benzoic acid as shown in Figure 6.18. The previous study has reported a triphenylamine-dihexylbithiophene in SC4 dye-sensitiser molecule as an electron donor and a 4-(benzo[c][1,2,5]thiadiazol-4-yl)benzoic acid as the electron acceptor. There has been an investigation using UV-visible and photoluminescence spectroscopies to study metal-free dye SC4 [189], but it has not been attempted for XPS.

Figure 6.19 shows a comparison of the O 1*s* photoemission spectra coverages taken at different deposition times. The substrate oxide signal clearly dominates the binding energy at 530.4 eV. There are two peaks fitted to the O 1*s* spectrum assigned to COO^- and C–O–C at 531.7 eV and 533.7 eV as it is visible in the 5 min deposition. The COO^- peak is generated due to the deprotonation of the carboxyl groups and the ligation of O 1*s* atoms to the TiO_2 substrate, whilst C–O–C is formed due to oxygen atom in the ether group (–O–). There is only one OH group, and it disappears completely in the monolayer due to deprotonated

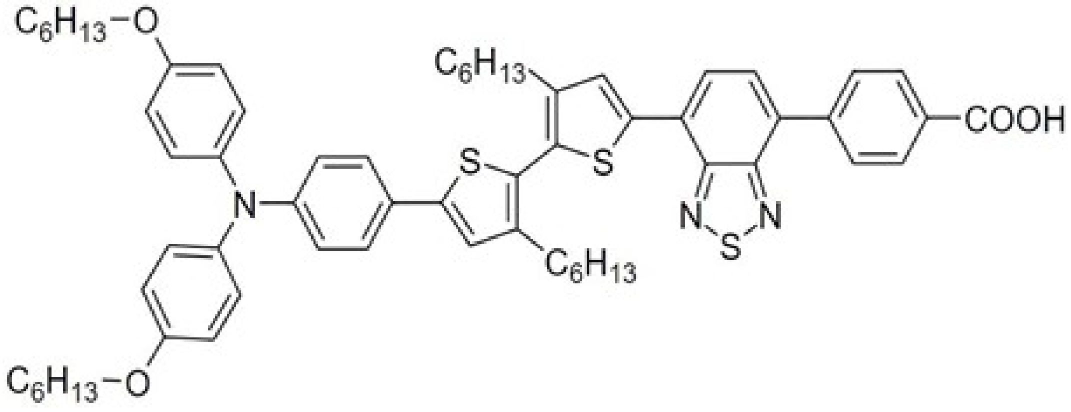

Fig. 6.18. Molecular structure of the SC4 dye 4-(7-(5'-(4-(bis (4-(hexyloxy) phenyl) amino) phenyl) -3,3'-dihexyl-[2,2'-bithiophen]-5-yl)benzo[c] [1,2,5] thiadiazol-4-yl) benzoic acid.

and bonding to the surface. The same condition is observed in the 10 mins deposition except for the intensity difference where it is closer to 1:1. These peaks should have the same intensity, but if the molecule is bound to the surface through COOH, C–O–C would be much stronger than COOH. The reason is that COOH will be buried underneath the C–O–C part of the molecule. The oxygen atoms may interact with the surface but will not create strong covalent bonds as if they were deprotonated. In the 20 mins and 40 mins deposition, two different chemical environments are presented. The high binding energy environment is attributed to the C–OH & C–O–C oxygen group, whilst the low binding energy is assigned to the C=O oxygen of the carboxyl acid group [15]. The C–OH & C–O–C: C=O intensity ratio is approximately 3:1, which agrees with the molecular stoichiometry.

Figure 6.20 displays the C 1*s* photoelectron spectra for surface coverage ranging from 5 mins to 40 mins deposition. The C 1*s* spectra have been fitted using five peaks. The most intense peak in the spectra is attributed to carbon atoms in the aromatic ring carbons at 285.2 eV in 5 mins and 10 mins deposition. As the coverage is increased, the binding energy position of aromatic carbon shifts upwards from 285.2 eV in the monolayer to 285.8 eV in the multilayer relative to carboxylic carbon. The neighbour peak is due to aliphatic chains. The aliphatic chains were shifted by 0.6 eV from aromatic carbons previously using photoemis-

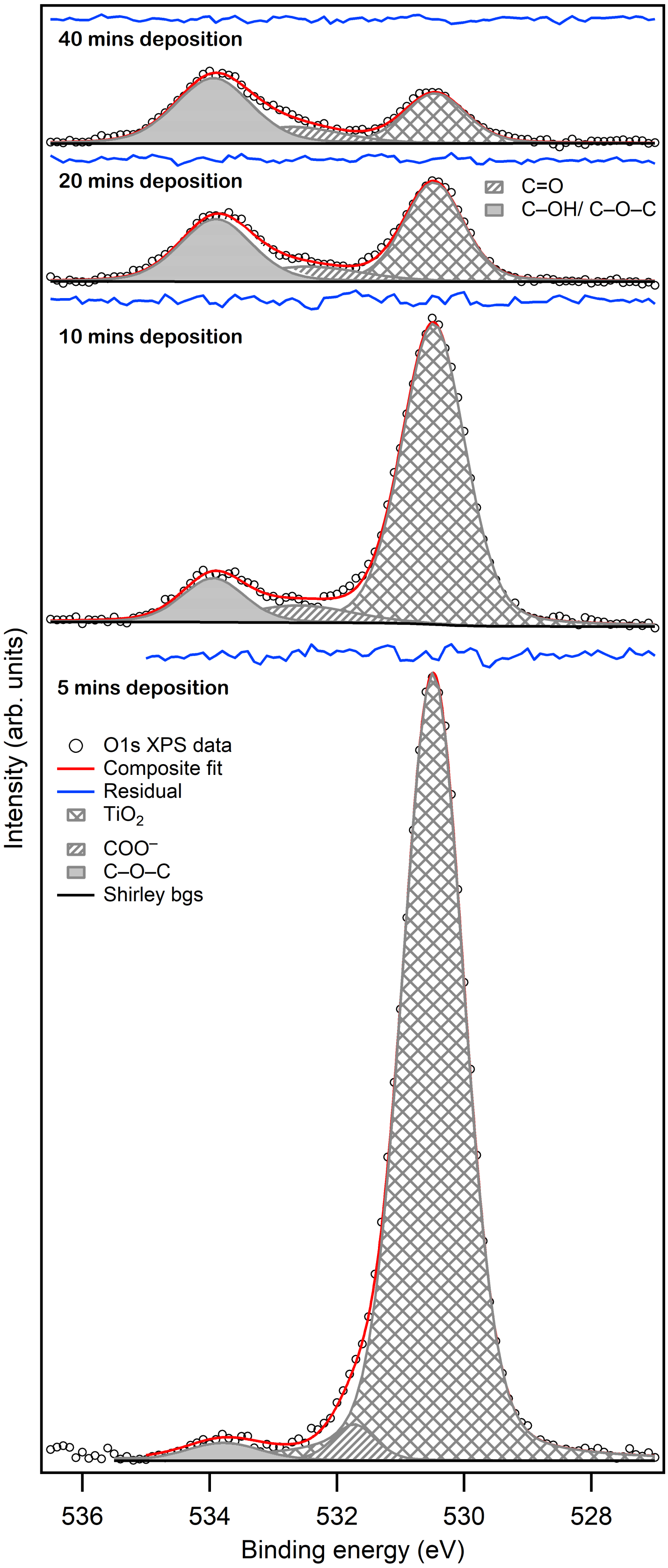

Fig. 6.19. O 1*s* core-level photoemission spectra for different time deposition coverages of SC4 adsorbed onto $TiO_2(110)$.

sion spectroscopy of zinc protoporphyrin adsorbed on rutile $TiO_2(110)$ [72], which is similar to our shift between these two peaks. The shoulder to the higher binding energy is fitted with triphenylamine and thiophene. The carboxyl peak is invisible but still there, which is identifiable from the previous study of the D5 molecule on TiO_2. According to the SC-4 molecule, the atomic ratios of aromatic carbons, aliphatic carbons, triphenylamine, thiophene and carboxyl is 29:24:5:4:1, which is consistent with the intensity ratios observed in Fig. 6.20.

N 1s photoemission spectra of the film coverages are shown in Figure 6.21. There is a nitrogen atom in the triphenylamine (C–N) ligands and two nitrogen atoms bound to sulfur (N–S), and thus the ratio is 2:1. The binding energy of N–S compounds in the thiadiazole varies from 399.3 eV to 401.6 eV [190] and is close to the binding energy of C–N, which is 400 eV or 400.5 eV [185, 186]. Therefore they are fitted with one peak at 400.2 eV and 400.4 eV for both coverages, respectively.

S 2p photoelectron spectra for the surface coverages are illustrated in Figure 6.22. S 2p is a doublet state and always comprises two peaks corresponding to two pairs of spin orbitals doublets (S $2p_{3/2}$ and S $2p_{1/2}$). The S $2p_{3/2}$ peak has to be twice the size of the S $2p_{1/2}$ peak using a spin-orbit split pair of 1.1 eV [179]. The coverages require two doublets to obtain a good curve fit, as can be observed in Figure 6.22. The two doublets are attributed to C–S ligands, and the other doublets are relative to N–S ligands. The low binding energy for the chemical states in the monolayer at 164.5 eV and 166.1 eV significantly correspond to sulphur atoms bound to carbon and nitrogen, respectively, whilst they are around 164.7 eV and 166.3 eV in the multilayer. The ratio of the doublets is 2:1 for both coverages, as expected from the sulphur atomic ratio in the molecule. The O, S, C and N ratios of 4:3:63:3 in the SC4 have not corresponded precisely with the 3.4:3:53.7:2.1 ratios obtained by photoionisation cross-sections, which is perhaps due to the geometry of the molecule on the surface where some parts are attenuated by the other part of the molecule. Information about the binding energies and the

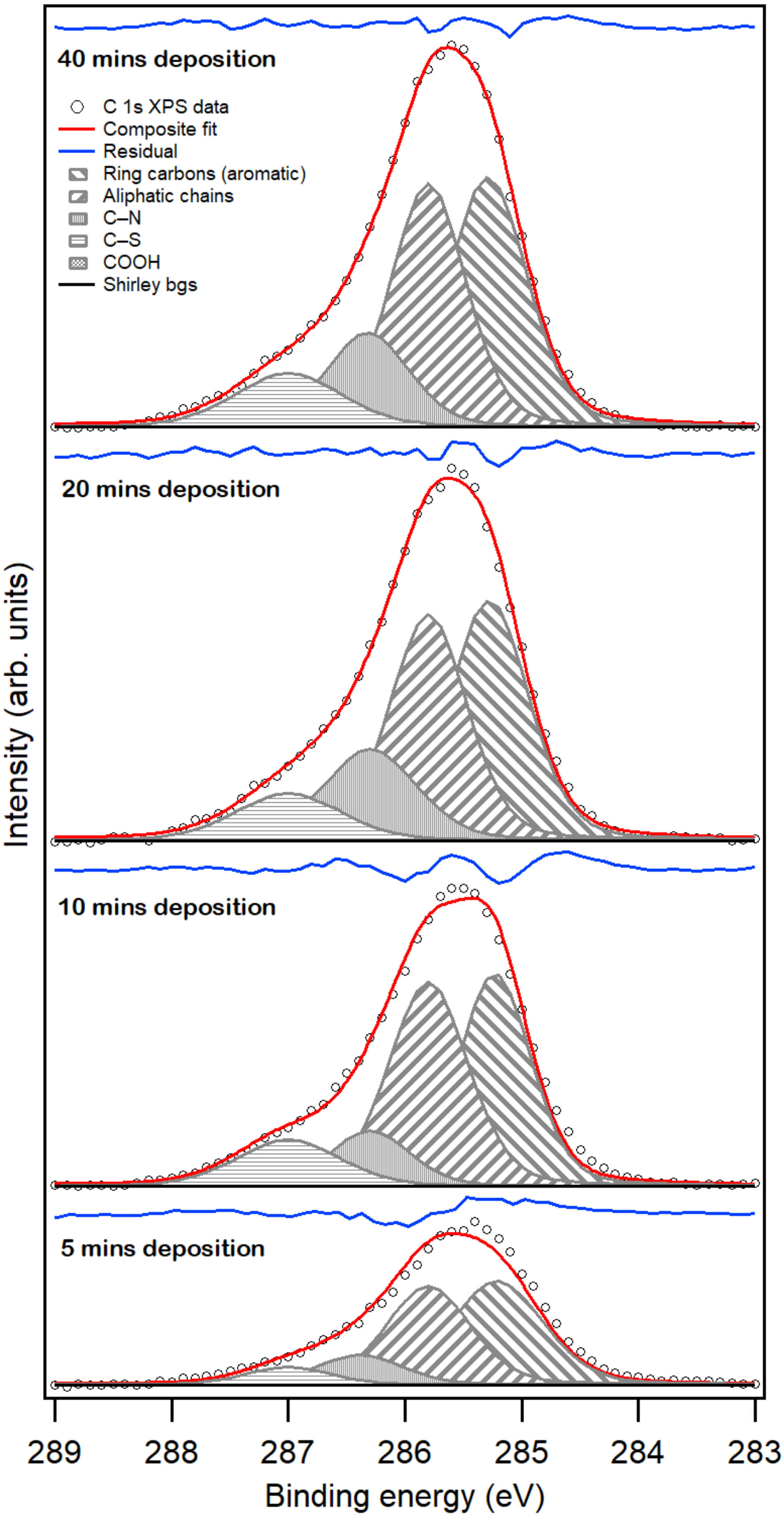

Fig. 6.20. C 1*s* core-level photoemission spectra for different surface coverages of the SC4 dye onto $TiO_2(110)$.

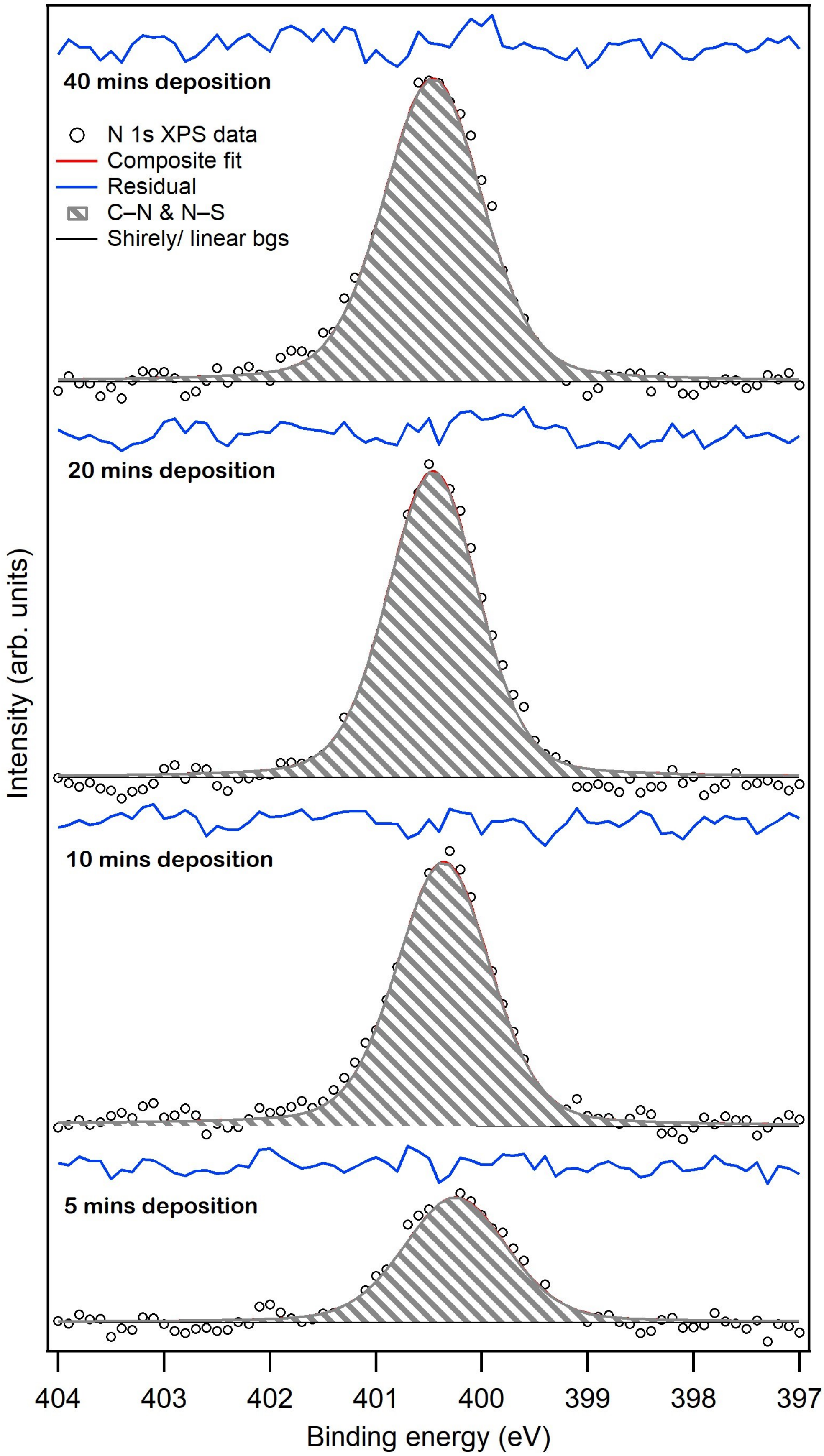

Fig. 6.21. N 1*s* core-level photoelectron spectra of SC4 for all coverages adsorbed on rutile $TiO_2(110)$.

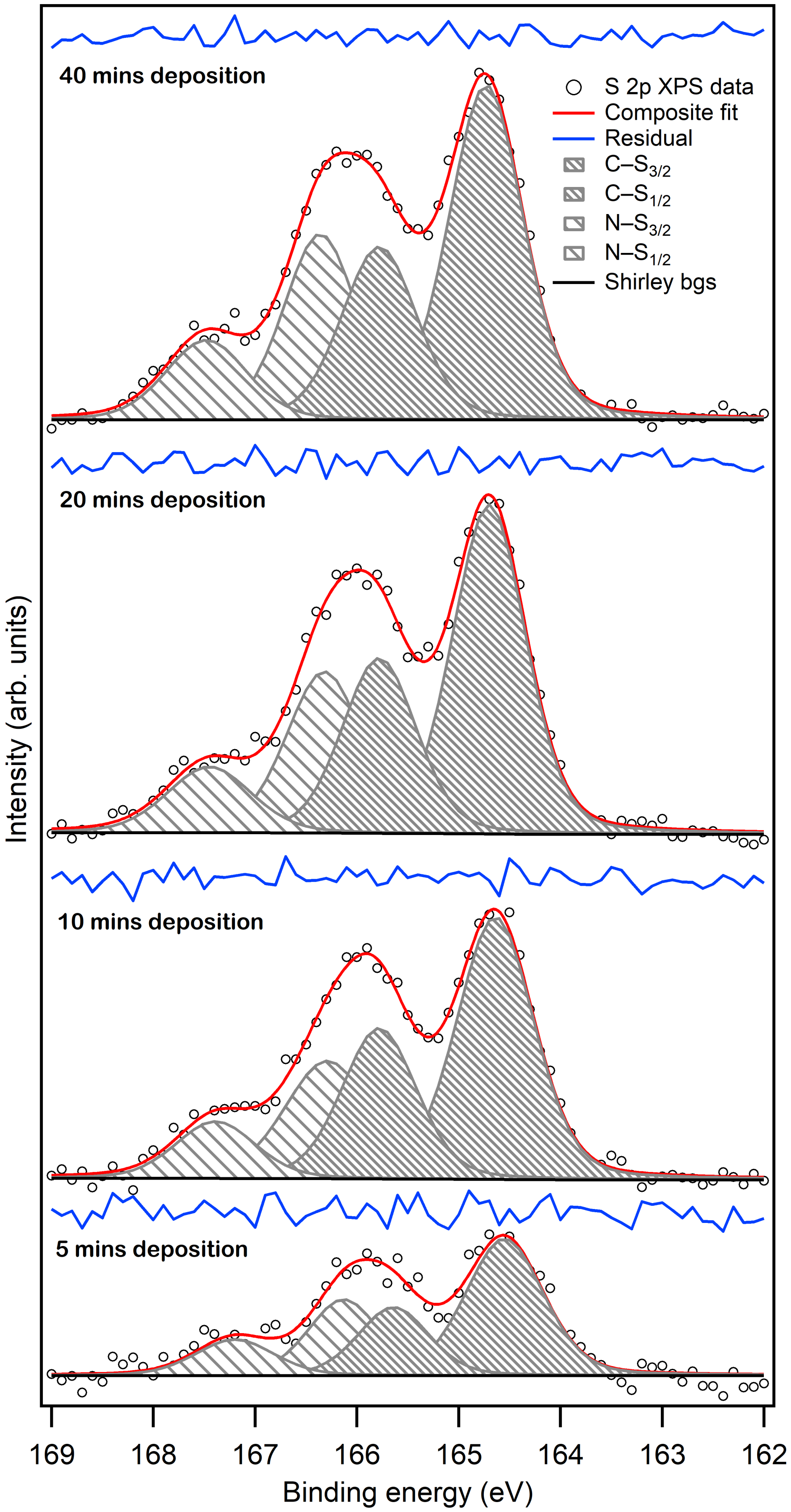

Fig. 6.22. S 2*p* XPS spectra of SC4 onto TiO_2 refer to four components related to C–$S_{3/2}$, C–$S_{1/2}$, N–$S_{3/2}$, and N–$S_{1/2}$ moieties using spin-orbit separation of 1.1 eV.

XPS peaks can be found in Table 6.4.

Core Level		**Thin Film**	**Thick Film**
O 1*s*	TiO_2	530.4	530.4
	COO^- & C=O	531.7	532.6
	C-O-C & C-OH	533.7	533.9
C 1*s*	Ring C	285.2	285.2
	Aliphatic C	285.8	285.8
	Triphenylamine	286.3	286.3
	Thiophene	287.0	287.0
	Carboxyl C	289.0	289.0
N 1*s*	Triphenylamine N & N-S	400.2	400.4
S 2*p*	C-S	164.5	164.7
	N-S	166.1	166.3

Table 6.4. Parameters of the XPS component binding energies for SC4 on the rutile $TiO_2(110)$ surface.

6.3.5 R6 on $TiO_2(110)$

A blue dye called R6 is presented in a schematic diagram in Figure 6.23. The Samanta group in Ireland has previously studied the electronic properties of R6 and its binding interaction on a TiO_2 anatase-101 surface [191]. Ren and co-workers reported an organic dye, R6, achieving a 12.6% power conversion efficiency measured under sunlight [4, 192].

Figure 6.24 displays the O 1*s*photoemission spectra at different times of deposition. The dominant peak at 530.4 eV is assigned to the oxide surface on both coverages. The 5 mins deposition data are weak because it is not easy to make a reliable fit due to not having sufficient statistics from the molecule compared to the substrate. In the 10 mins deposition, there are two peaks fitted to the O 1*s* spectrum attributed to C=O & COO^- and C–OH & C–O–C at 531.6 eV and 533.2 eV, respectively. The C=O & COO^- and C–OH & C–O–C peaks have reached

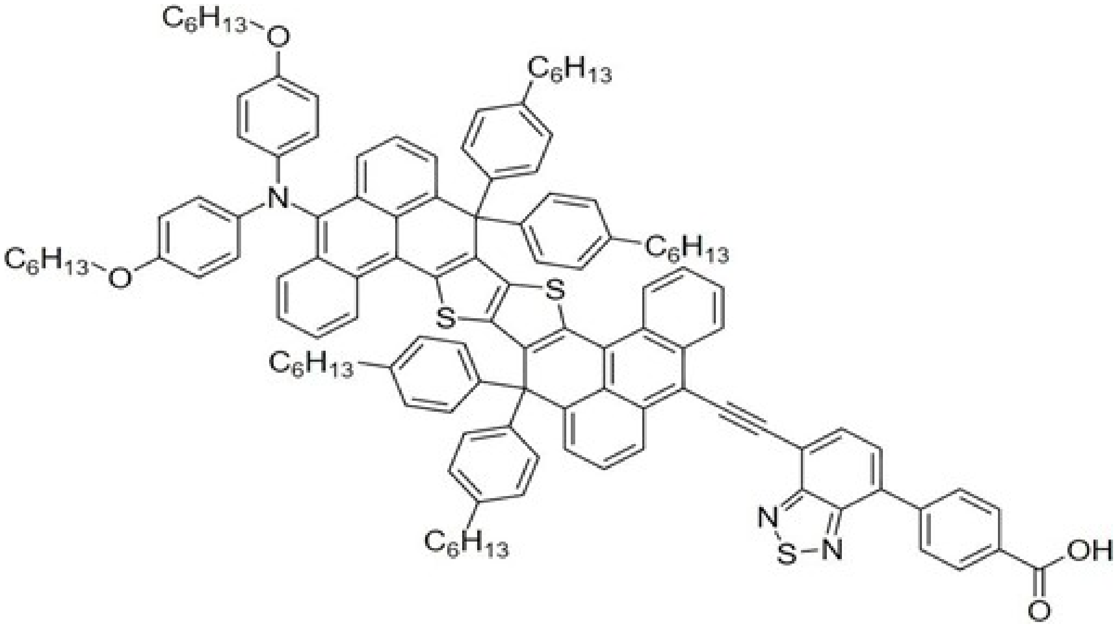

Fig. 6.23. Molecular structure of the R6 dye 4-(7-((15-(Bis (4-(hexyloxy) phenyl) amino) -9,9,19,19-tetrakis (4-hexylphenyl)-9,19 -dihydrobenzo [1',10'] phenanthro [3',4':4,5] thieno [3,2-b] benzo [1,10] phen–anthro [3,4-d] thiophen-5-yl) ethynyl) benzo[c] [1,2,5] thiadiazol-4-yl) benzoic acid.

a ratio approximately 1:1 in the case of complete deprotonation of the carboxylic acid group in bonding to the surface.

The multilayer coverages (20 mins and 40 mins deposition), as shown in Figure 6.24, has presented same components as in 10 mins deposition. The atomic structure ratio for C=O & COO$^-$ and C–OH & C–O–C should be 3:1 (i.e. 3 is related to two oxygen atoms in the ether group and one oxygen atom in –OH whilst 1 is related to one oxygen atom in =O group) in the case of the absence of deprotonation of the carboxylic group in the isolated molecule. The multilayer is likely estimated to be two or three layers as a 1:1 ratio of the C=O & COO$^-$ and C–OH & C–O–C peaks are seen.

Figure 6.25 presents the C 1*s* photoelectron spectra of the surface coverages. The most intense peak at 285.0 eV corresponds to ring aromatic carbons; however, the second intense peak at 285.5 eV is due to aliphatic chains. The shoulder side to the higher binding energy of the main peak is fitted with two peaks attributed to triphenylamine and thiophene. The carboxyl carbon atom in

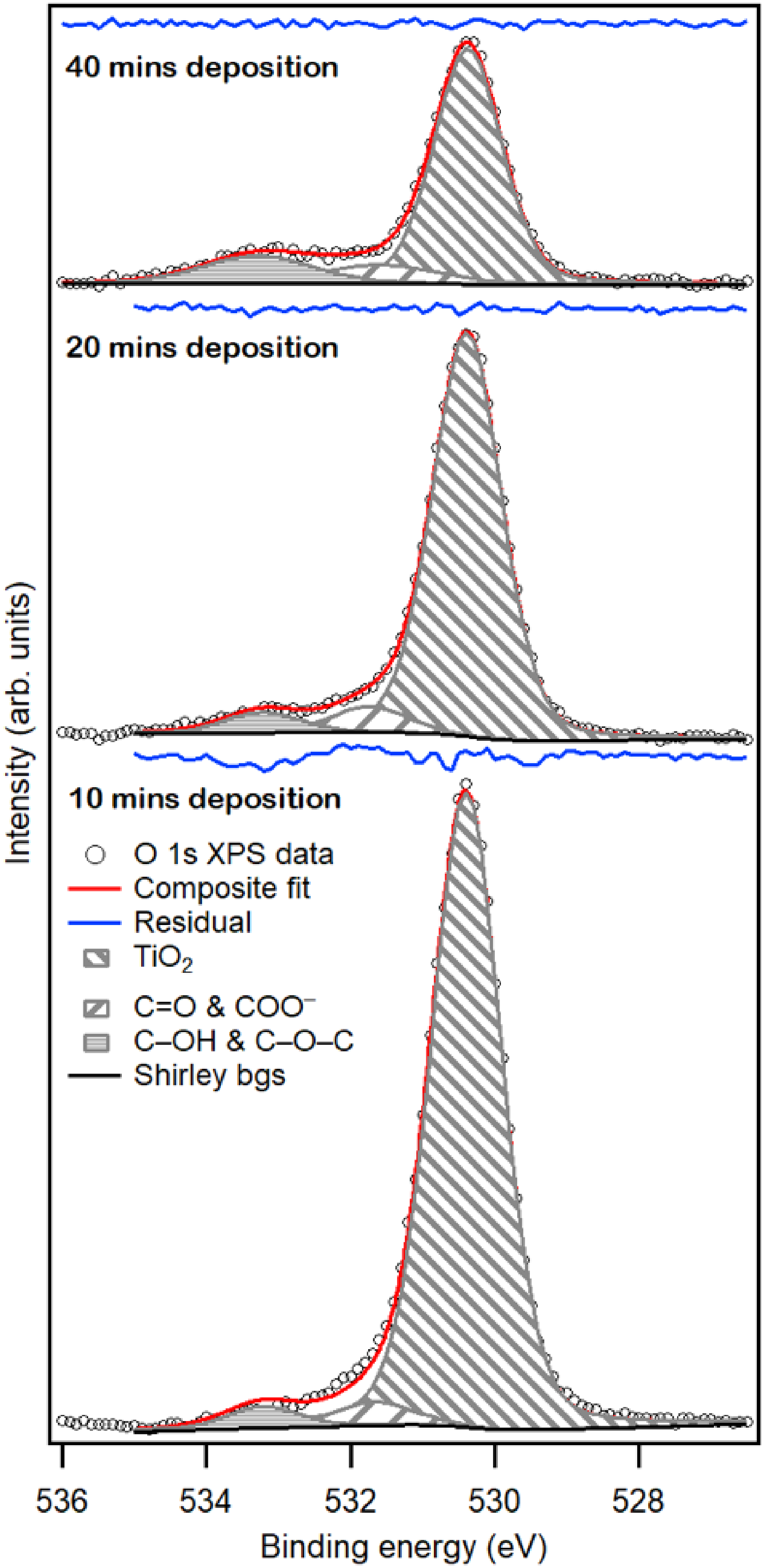

Fig. 6.24. O 1*s* core-level photoemission spectra for surface coverages obtained at different deposition times of R6 adsorbed on rutile $TiO_2(110)$.

the carboxylic acid anchoring group is the higher binding energy peak in the C 1*s* spectra. Since the spectra are quite complicated, the width of each peak for all coverages has been constrained to be the same (see Figure 6.25). The fits of C 1*s* are very similar to the SC4 molecule because they have the same moieties. The atomic ratio of 84:36:5:4:1 is for carbon atoms in the aromatic carbon, aliphatic chains, triphenylamine, thiophene and carboxylic acid group, which is consistent with the actual ratio of the layers.

The photoemission spectra of the N 1*s* region have been exhibited in Figure 6.26. The measurements of the N 1*s* show no different change for all coverages where C–N and N–S moieties are represented as one peak, as a result of the convergence in the binding energy at 400.1 eV, as occurred in SC4 dye previously.

Figure 6.27 shows two chemical environments in the S 2*p* region for different coverages. Both the 5 mins and 40 mins deposition are bound into two peaks related to C–S and N–S ligands. These peaks are corresponded to two pairs of spin orbitals doublets ($2p_{3/2}$ and $2p_{1/2}$) using separation between the two peaks of 1.1 eV [179]. The chemical state peaks located at low binding energies are attributed to C–S $2p_{3/2}$ and N–S $2p_{3/2}$ environments. The atomic ratios of 4:3:122:3 in the R6 molecule do not coincide with multilayer coverage ratios of 8.4:3:177.6:2.4 based on photoionisation cross-sections. In fact, this may be due to the geometry of the molecule on the surface, where some regions of the molecule attenuated other molecular regions on the surface. The XPS parameters are discussed briefly in Table 6.5.

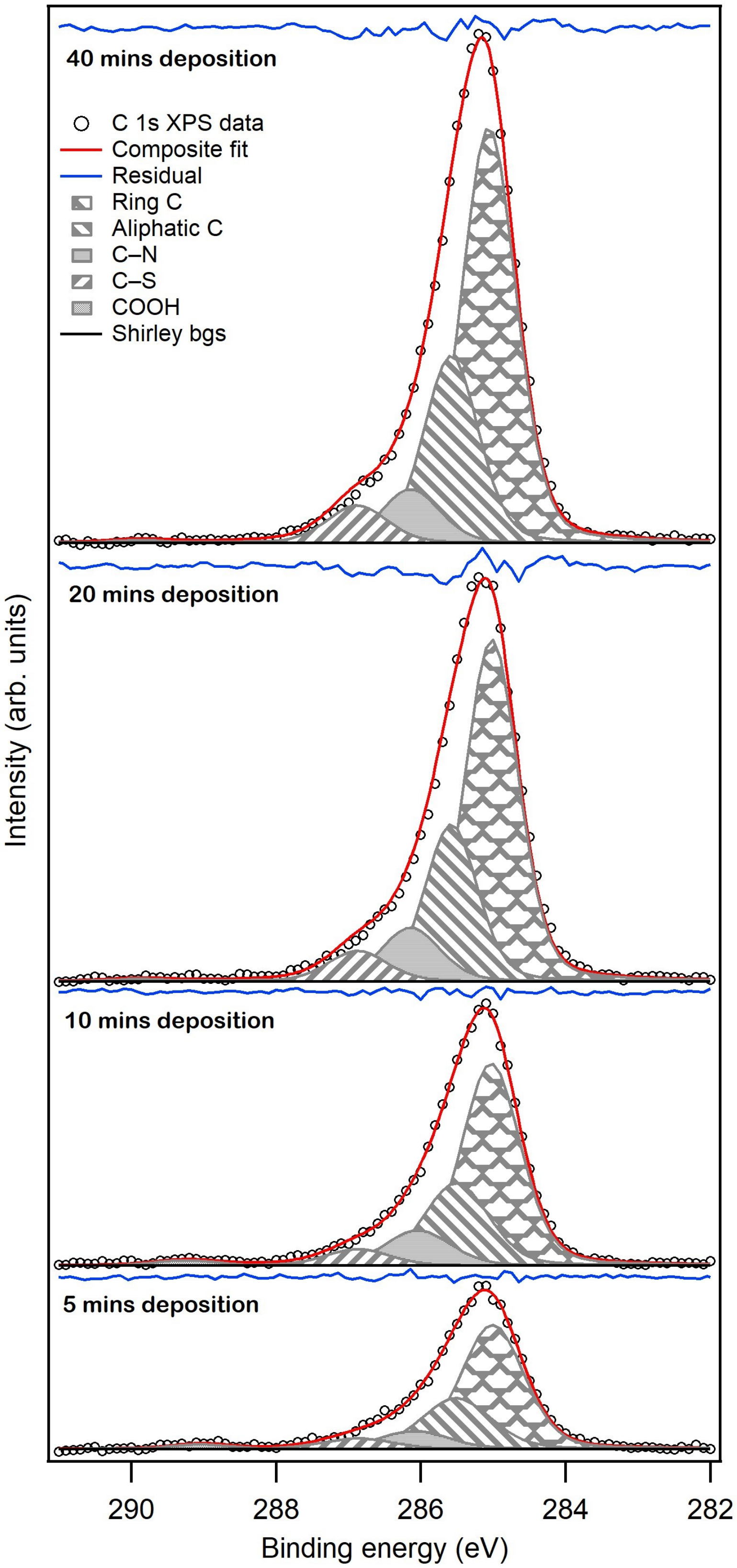

Fig. 6.25. C 1*s* core-level photoelectron spectra for different surface coverages of the R6 on rutile $TiO_2(110)$.

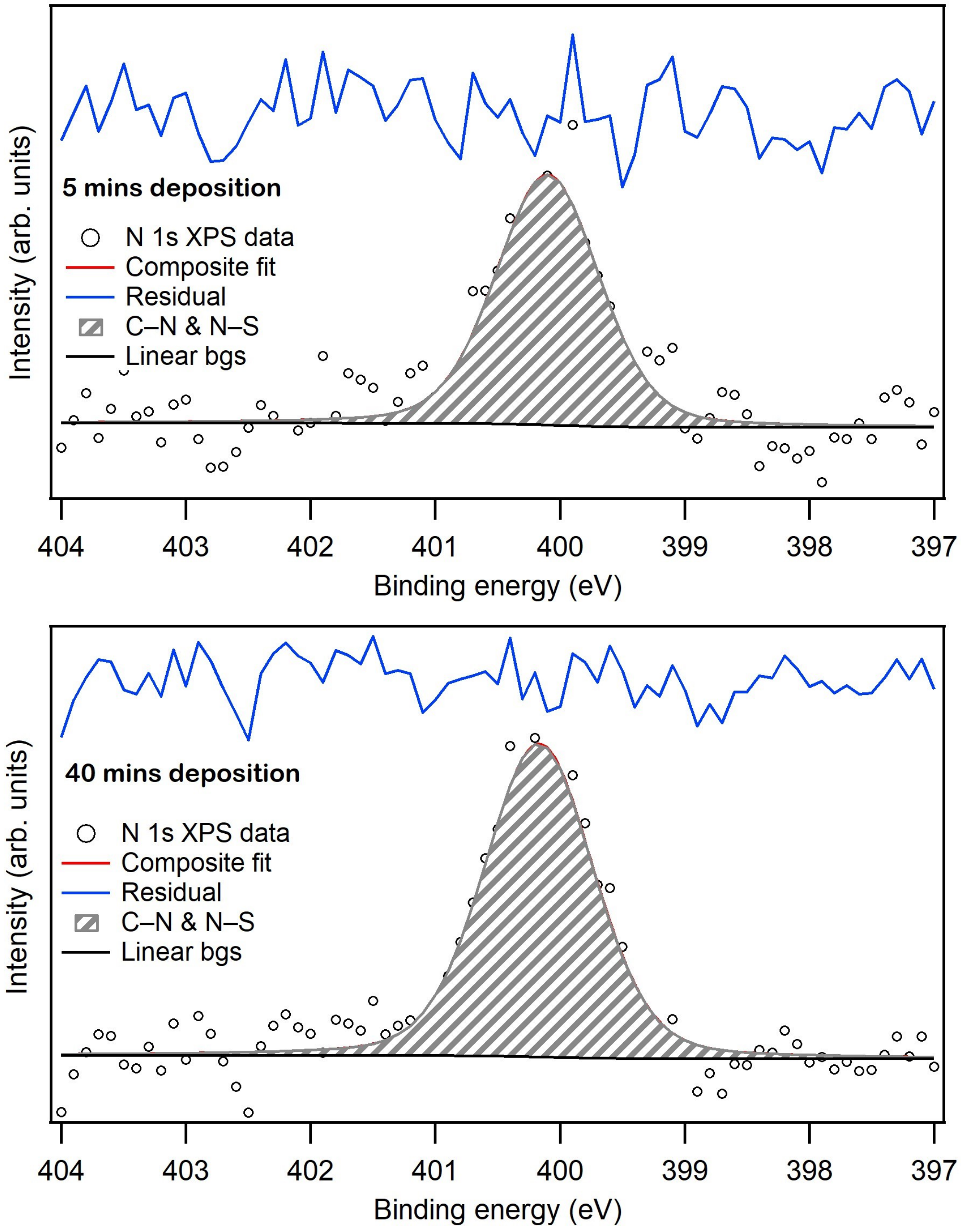

Fig. 6.26. N 1*s* core-level photoemission spectra for 5 mins and 40 mins deposition times of R6 on the $TiO_2(110)$ surface.

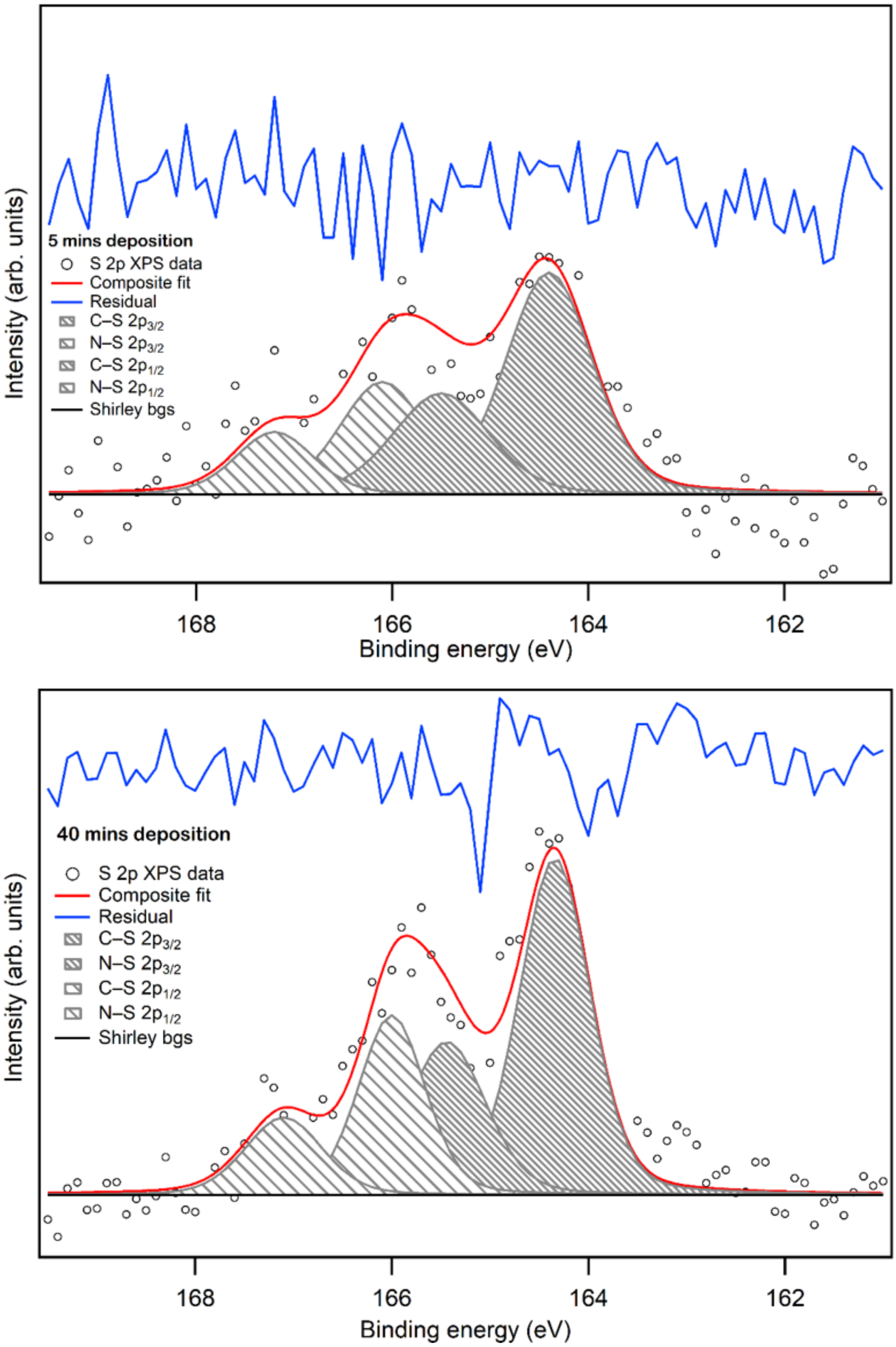

Fig. 6.27. S 2*p* XPS spectra for surface coverages of R6 onto TiO_2 substrate showing the spin-orbit split C–S $2p_{3/2}$, N–S $2p_{3/2}$, C–S $2p_{1/2}$, and N–S $2p_{1/2}$ contributions.

Core Level		**Low Coverage**	**High Coverage**
O 1*s*	TiO_2	530.4	530.4
	C=O & COO^-	531.6	531.6
	C-OH & C-O-C	533.2	533.2
C 1*s*	Ring C	285.0	285.0
	Aliphatic C	285.5	285.5
	Triphenylamine	286.0	286.1
	Thiophene	286.8	286.8
	Carboxyl C	289.0	289.8
N 1*s*	Triphenylamine N & N-S	400.1	400.1
S 2*p*	C-S	164.4	164.3
	N-S	166.1	166.0

Table 6.5. Parameters of the XPS component binding energies for R6 on the rutile $TiO_2(110)$ surface.

6.4 Conclusions

The UHV electrospray source and the XPS system have been used to deposit some dye complexes, such as N3, RuP, D5, SC4 and R6, onto the rutile $TiO_2(110)$ substrate in situ. The surface coverages were obtained by depositing at different times to construct the film thickness and then taking measurements after each deposition process. The molecules' bonding geometry and chemical interaction with the oxide surface have been inferred from photoemission spectroscopy. The XPS data collected for monolayer and multilayer coverages of dyes present convincing evidence of chemical interactions with the surface TiO_2. The O 1*s* photoemission in the monolayer coverages shows that the carboxylic acid and phosphonic acid groups are anchored to the titanium atoms of the oxide surface through deprotonation by 2M-bidentate bridging mode, bonding their oxygen atoms to the surface. The C 1*s* spectra, along with N 1*s*, provide strong evidence that the molecule is still intact on the surface and has not fragmented upon deposition; moreover, the ruthenium binding energy is consistent with the Ru^{2+} oxidation state within the molecule. If the ruthenium fell out of the molecule and the ruthenium was simply sitting on the surface, it would probably cluster together, become metallic and have a different binding energy. Moreover, there is a sensible agreement between atomic ratios for all molecules and photoionisation cross-section proportions, even though they are not perfectly matched. The main reason is likely to be due to the geometry of the molecule on the surface, where part of the molecule attenuated the other parts. The importance of the bonding for the electronic characteristics of each dye complex for the orbitals studied here should be subject to further study.

Chapter 7

Conclusions and Future Work

This chapter summarises a series of experiments demonstrating the unique capabilities of electrospraying. Future work suggestions also are covered in this chapter.

7.1 The Characterisation of Velocity Distributions in Electrospray Ionisation

An image charge detection instrument was used to determine the charge and speed distributions of ions in the UHV electrospray system. The geometry of the vacuum interface was investigated, where the speed of ions could be controlled by adiabatic expansion. This instrument will aid future ion optics studies in electrospraying by knowing the size values and the velocity measurements of the ions. In this chapter, large clusters with a narrow velocity distribution of the cluster sizes between 300 m/s and 330 m/s was formed. The evidence suggests that the ions measured in the drift tube cannot be individual molecular ions as there is a very smooth band of charges implying the formation of large clusters. So, the next stage incorporates the electrostatic deflectors to separate these clusters by mass (more details in

Chapter 5).

7.2 Towards A Supersonic Mass-selected Electrospray Deposition System and Separation of Neutral and Charged Species

The first section of this chapter presents four electrostatic ion deflection experiments using the electrospray technique. These deflection experiments showed that fluorescein and ferrocene form large clusters that need high voltages to be deflected, as proposed by the SIMION simulation and the smooth nature of the ion charge distribution. The deflection of small molecular ions using low voltages has not been proven because the experimental setup has concentrated on the high-voltage regime. In future work, more sensitive electronics will be created for the image charge detector and eliminate noise from the system to measure individual molecular ions on the low voltage regime. In the second section, XPS measurements of NaCl were studied to test the electrospray's spot size and the ability of the Einzel lens to defocus the beam in the real life, especially since the SIMION simulation proved successful. These measurements have shown that, under the conditions studied, the Einzel lens did not change the spot size. In the future, a specific target will be made to test defocusing again; however, it is worth remembering that the Einzel lens will not affect the neutral component of the electrospray beam, which may be significant in this case. Future experiments on the Einzel lens should therefore filter these out first to observe the effect on the ions. AFM to study the morphology of the graphene oxide films and optical microscopy have been employed in the last section of Chapter 5, which showed successful deposition of flat-lying graphene oxide flakes but a very inhomogeneous coverage due to the large droplets delivering those flakes.

7.3 A Photoemission Study of Dye Molecules Deposited by Electrospray on rutile TiO_2(110)

This chapter studied the adsorption of the dye molecules of N3, RuP, D5, SC4 and R6 on the rutile TiO_2 (110) surface using a combination of electrospray with XPS to deposit in situ to make layered deposits and films comprising blends of materials. Their chemical interaction and bonding geometry with the titanium oxide surface are investigated by XPS. The results of the core-level photoemission spectra for dyes indicate that the first layer of dye molecules creates a strong chemical anchor to Ti atoms of the oxide substrate by deprotonating the carboxyl and phosphoryl groups as the 2M-bidentate bridging mode. The spectra of C $1s$, along with N $1s$, provide strong evidence that the molecule is intact on the surface due to the presence of all functional groups and a ruthenium atom where the binding energy of Ru3d is consistent with the Ru^{2+}.

7.4 Future Work Suggestions

For future research that could build on this thesis, a potentially important experiment could be conducted regarding the electrospray instrument development. The beam in these experiments is about 2 mm in diameter when hitting the sample. For example, it is required to spread the beam to at least 10x10 mm in order for a solar cell device to be made. The defection plates can deflect the beam at least +/- 5 mm. Having two more plates in the other direction would help direct the beam anywhere within a 10x10 mm square on the sample. Therefore, the deflection voltages are controlled using a computer to quickly move the beam over that 10x10 mm area during the deposition to create a homogenous film over the whole sample. One simple way to start might be to place a window instead of the target and then have a camera focused on it (possibly with a microscope attachment). After that, the solution is sprayed onto the window and attempted to be controlled, with the beam transmitted using the existing plates. If this works, a four-plate system is designed and then determined how to control the voltages. Again, it should be noted that any netural component of the beam will not be deflected, so these would need to be filtered out first. The future work of defocusing the Einzel lens could be by manufacturing a target containing a series of rings and then measuring the current on each ring to find the voltage that would make the beam the smallest. Using XPS will enable seeing the effect. Alternatively, increasing the distance to the surface might also spread the beam out to a larger diameter simply because of the beam's divergence, which could be tested by constructing a long tube for the source.

Another future experiment related to the drift tube experiment is that it would be worth to carry out further studies on ion drift tube measurements for one more molecules that can be bent because this study focused only on fluorescein. For example, the ferrocene needs a large voltage to be deflected, which suggests that the ferrocene forms a large cluster.

It would also be interesting to extend the work in Chapter 6 by depositing more molecules such as N719, Ru455, D45, PY1, C239 and R4. Some of these dye molecules have a carboxylic acid group, and it is useful to study their adsorption geometries on the TiO_2 surface to compare them with the other dyes described in Chapter 6. Also, it would be worth to study the dipyrrin-based bonds in PY1, which has a different chemical structure than the bi-isonicotinic acid ligands, to discover how the molecules adsorbed onto the surface. These experiments will be carried out to determine the primary factors affecting charge transfer efficiency. Finally, it is interesting to incorporate a solar simulator to study dye complexes adsorbed onto a TiO_2 surface in operation.

Bibliography

[1] B Podolsky, N Rosen, JF Clauser, AM Steinberg, RY Chiao, A Vaziri, G Weihs, A Zeilinger, RS Bennink, SJ Bentley, et al. Efficient hybrid solar cells based on meso-superstructured organometal halide perovskites. *Science*, 338(6107):643–647, 2012.

[2] Kristofer Fredin, Kenrick F Anderson, Noel W Duffy, Gregory J Wilson, Christopher J Fell, Daniel P Hagberg, Licheng Sun, Udo Bach, and Sten-Eric Lindquist. Effect on cell efficiency following thermal degradation of dye-sensitized mesoporous electrodes using N719 and D5 sensitizers. *The Journal of Physical Chemistry C*, 113(43):18902–18906, 2009.

[3] Jun Hyuk Yang, Chung Wung Bark, Kyung Hwan Kim, and Hyung Wook Choi. Characteristics of the dye-sensitized solar cells using TiO_2 nanotubes treated with $TiCl_4$. *Materials*, 7(5):3522–3532, 2014.

[4] Gerrit Boschloo. Improving the performance of dye-sensitized solar cells. *Frontiers in chemistry*, 7:77, 2019.

[5] Gabriella Di Carlo, Daniela Caschera, Roberta G Toro, Cristina Riccucci, Gabriel M Ingo, Giuseppina Padeletti, Luisa De Marco, Giuseppe Gigli, Giovanna Pennesi, Gloria Zanotti, et al. Spectroscopic and morphological studies of metal-organic and metal-free dyes onto titania films for dye-sensitized solar cells. *International Journal of Photoenergy*, 2013, 2013.

[6] Robert H Temperton. *Complex molecules on surfaces: In-situ electrospray*

deposition and photoelectron spectroscopy. PhD thesis, University of Nottingham, 2017.

[7] Brian O'regan and Michael Grätzel. A low-cost, high-efficiency solar cell based on dye-sensitized colloidal TiO2 films. *nature*, 353(6346):737–740, 1991.

[8] Khushboo Sharma, Vinay Sharma, and SS Sharma. Dye-sensitized solar cells: fundamentals and current status. *Nanoscale research letters*, 13(1):1–46, 2018.

[9] Hitoshi Kusama, Hideo Orita, and Hideki Sugihara. TiO_2 band shift by nitrogen-containing heterocycles in dye-sensitized solar cells: a periodic density functional theory study. *Langmuir*, 24(8):4411–4419, 2008.

[10] M Khaja Nazeeruddin, Amin Kay, Ignacio Rodicio, Robin Humphry-Baker, E Müller, Petr Liska, Nick Vlachopoulos, and M Grätzel. Conversion of light to electricity by cis-X_2bis (2, 2'-bipyridyl-4, 4'-dicarboxylate) ruthenium (II) charge-transfer sensitizers (X= Cl^-, Br^-, I^-, CN^-, and SCN^-) on nanocrystalline titanium dioxide electrodes. *Journal of the American Chemical Society*, 115(14):6382–6390, 1993.

[11] A. Stierle. Surface core level shift observed on NiAl(110). *Surface Science*, 529:L263–L268, 04 2003.

[12] Louise C Mayor, J Ben Taylor, Graziano Magnano, Anna Rienzo, Christopher J Satterley, James N O'Shea, and Joachim Schnadt. Photoemission, resonant photoemission, and x-ray absorption of a Ru (II) complex adsorbed on rutile TiO_2 (110) prepared by in situ electrospray deposition. *The Journal of chemical physics*, 129(11):114701, 2008.

[13] Louise C Mayor, Alex Saywell, Graziano Magnano, Christopher J Satterley, Joachim Schnadt, and James N O'Shea. Adsorption of a Ru (II) dye complex

on the Au (111) surface: Photoemission and scanning tunneling microscopy. *The Journal of chemical physics*, 130(16):164704, 2009.

[14] Andrew J Gibson, Robert H Temperton, Karsten Handrup, Matthew Weston, Louise C Mayor, and James N O'Shea. Charge transfer from an adsorbed ruthenium-based photosensitizer through an ultra-thin aluminium oxide layer and into a metallic substrate. *The Journal of chemical physics*, 140(23):234708, 2014.

[15] L Patthey, H Rensmo, Petter Persson, K Westermark, L Vayssieres, A Stashans, Å Petersson, PA Brühwiler, H Siegbahn, S Lunell, et al. Adsorption of bi-isonicotinic acid on rutile TiO_2 (110). *The Journal of chemical physics*, 110(12):5913–5918, 1999.

[16] J Schnadt, JN O'shea, L Patthey, J Schiessling, y J Krempaskỳ, M Shi, Nils Mårtensson, and PA Brühwiler. Structural study of adsorption of isonicotinic acid and related molecules on rutile TiO_2 (110) II: XPS. *Surface science*, 544(1):74–86, 2003.

[17] Joachim Schnadt, Anders Henningsson, Martin P Andersson, Patrik G Karlsson, Per Uvdal, Hans Siegbahn, Paul A Brühwiler, and Anders Sandell. Adsorption and charge-transfer study of bi-isonicotinic acid on in situ-grown anatase TiO_2 nanoparticles. *The Journal of Physical Chemistry B*, 108(10):3114–3122, 2004.

[18] Joachim Schnadt, Paul A Brühwiler, Luc Patthey, James N O'shea, Sven Södergren, Michael Odelius, Rajeev Ahuja, Olof Karis, Margit Bässler, Petter Persson, et al. Experimental evidence for sub-3-fs charge transfer from an aromatic adsorbate to a semiconductor. *Nature*, 418(6898):620–623, 2002.

[19] J Ben Taylor, Louise C Mayor, Janine C Swarbrick, James N O'Shea, Cristina Isvoranu, and Joachim Schnadt. Adsorption and charge transfer dy-

namics of bi-isonicotinic acid on Au (111). *The Journal of chemical physics*, 127(13):134707, 2007.

[20] Mohammad K Nazeeruddin, Peter Pechy, Thierry Renouard, Shaik M Zakeeruddin, Robin Humphry-Baker, Pascal Comte, Paul Liska, Le Cevey, Emiliana Costa, Valery Shklover, et al. Engineering of efficient panchromatic sensitizers for nanocrystalline TiO_2-based solar cells. *Journal of the American Chemical Society*, 123(8):1613–1624, 2001.

[21] Guocan Li, Aswani Yella, Douglas G Brown, Serge I Gorelsky, Mohammad K Nazeeruddin, Michael Grätzel, Curtis P Berlinguette, and Michael Shatruk. Near-IR photoresponse of ruthenium dipyrrinate terpyridine sensitizers in the dye-sensitized solar cells. *Inorganic Chemistry*, 53(11):5417–5419, 2014.

[22] Catherine E McCusker and Felix N Castellano. Design of a long-lifetime, earth-abundant, aqueous compatible Cu (I) photosensitizer using cooperative steric effects. *Inorganic Chemistry*, 52(14):8114–8120, 2013.

[23] Yizhu Liu, Petter Persson, Villy Sundström, and Kenneth Wärnmark. Fe N-heterocyclic carbene complexes as promising photosensitizers. *Accounts of chemical research*, 49(8):1477–1485, 2016.

[24] Pavel Chábera, Yizhu Liu, Om Prakash, Erling Thyrhaug, Amal El Nahhas, Alireza Honarfar, Sofia Essén, Lisa A Fredin, Tobias CB Harlang, Kasper S Kjær, et al. A low-spin Fe (III) complex with 100-ps ligand-to-metal charge transfer photoluminescence. *Nature*, 543(7647):695–699, 2017.

[25] Saif A Haque, Emilio Palomares, Hari M Upadhyaya, Lucy Otley, Robert J Potter, Andrew B Holmes, and James R Durrant. Flexible dye sensitised nanocrystalline semiconductor solar cells. *Chemical Communications*, (24):3008–3009, 2003.

[26] Peng Wang, Bernard Wenger, Robin Humphry-Baker, Jacques-E Moser, Joël Teuscher, Willi Kantlehner, Jochen Mezger, Edmont V Stoyanov, Shaik M

Zakeeruddin, and Michael Grätzel. Charge separation and efficient light energy conversion in sensitized mesoscopic solar cells based on binary ionic liquids. *Journal of the American Chemical Society*, 127(18):6850–6856, 2005.

[27] Udo Bach, Donald Lupo, Pascal Comte, Jacques-E Moser, F Weissörtel, J Salbeck, H Spreitzer, and Michael Grätzel. Solid-state dye-sensitized mesoporous TiO_2 solar cells with high photon-to-electron conversion efficiencies. *Nature*, 395(6702):583–585, 1998.

[28] Brian O'Regan and DT Schwartz. Solid state photoelectrochemical cells based on dye sensitization. In *AIP Conference Proceedings*, volume 404, pages 129–136. American Institute of Physics, 1997.

[29] VPS Perera, PKDDP Pitigala, PVV Jayaweera, KMP Bandaranayake, and K Tennakone. Dye-sensitized solid-state photovoltaic cells based on dye multilayer- semiconductor nanostructures. *The Journal of Physical Chemistry B*, 107(50):13758–13761, 2003.

[30] Markus Clark Scharber and Niyazi Serdar Sariciftci. Efficiency of bulk-heterojunction organic solar cells. *Progress in polymer science*, 38(12):1929–1940, 2013.

[31] Tae Eui Kang, Han-Hee Cho, Chul-Hee Cho, Ki-Hyun Kim, Hyunbum Kang, Myounghee Lee, Sunae Lee, BongSoo Kim, Chan Im, and Bumjoon J Kim. Photoinduced charge transfer in donor–acceptor (DA) copolymer: fullerene bis-adduct polymer solar cells. *ACS Applied Materials & Interfaces*, 5(3):861–868, 2013.

[32] Harald Hoppe and Niyazi Serdar Sariciftci. Organic solar cells: An overview. *Journal of materials research*, 19(7):1924–1945, 2004.

[33] Tohru Shiga and Tomoyoshi Motohiro. Photosensitization of nanoporous TiO_2 film with porphyrin-linked fullerene. *Thin Solid Films*, 516(6):1204–1208, 2008.

[34] Sandro Cattarin, Paola Ceroni, Dirk M Guldi, Michele Maggini, Enzo Menna, Francesco Paolucci, Sergio Roffia, and Gianfranco Scorrano. Synthesis and photoelectrochemical properties of a fullerene–azothiophene dyad. *Journal of Materials Chemistry*, 9(11):2743–2750, 1999.

[35] Daigo Hirayama, Kazuo Takimiya, Yoshio Aso, Tetsuo Otsubo, Taku Hasobe, Hiroko Yamada, Hiroshi Imahori, Shunichi Fukuzumi, and Yoshiteru Sakata. Large photocurrent generation of gold electrodes modified with [60] fullerene-linked oligothiophenes bearing a tripodal rigid anchor. *Journal of the American Chemical Society*, 124(4):532–533, 2002.

[36] Ken-ichi Yamanaka, Mamoru Fujitsuka, Yasuyuki Araki, Osamu Ito, Toshihide Aoshima, Takanori Fukushima, and Tsutomu Miyashi. Intramolecular Photoinduced Electron-Transfer Processes in Tetrathienylethylene-Quaterthiophene-[60] Fullerene Triad in Solutions. *The Journal of Physical Chemistry A*, 108(2):250–256, 2004.

[37] Shigeki Hattori, Kei Ohkubo, Yasuteru Urano, Hisato Sunahara, Tetsuo Nagano, Yuji Wada, Nikolai V Tkachenko, Helge Lemmetyinen, and Shunichi Fukuzumi. Charge separation in a nonfluorescent donor- acceptor dyad derived from boron dipyrromethene dye, leading to photocurrent generation. *The Journal of Physical Chemistry B*, 109(32):15368–15375, 2005.

[38] Paul Kebarle and Udo H Verkerk. Electrospray: from ions in solution to ions in the gas phase, what we know now. *Mass spectrometry reviews*, 28(6):898–917, 2009.

[39] L Frs. On the equilibrium of liquid conducting masses charged with electricity', Lond. *Edinb. Dublin Philos. Mag. J. Sci*, 14:87, 1882.

[40] John Zeleny. The electrical discharge from liquid points, and a hydrostatic method of measuring the electric intensity at their surfaces. *Physical Review*, 3(2):69, 1914.

[41] J Zeleny. On the conditions of instability of electrified drops, with applications to the electrical discharge from liquid points. *Proc. Cambridge Philos. Soc.(1915, 18, 71–83).*

[42] John Zeleny. Instability of electrified liquid surfaces. *Physical review*, 10(1):1, 1917.

[43] Malcolm Dole, Lawrence L Mack, Robert L Hines, Ralph C Mobley, Lowell D Ferguson, and Martin B Alice. Molecular beams of macroions. *The Journal of chemical physics*, 49(5):2240–2249, 1968.

[44] John B Fenn, Matthias Mann, Chin Kai Meng, Shek Fu Wong, and Craig M Whitehouse. Electrospray ionization for mass spectrometry of large biomolecules. *Science*, 246(4926):64–71, 1989.

[45] Matthias Wilm. Principles of electrospray ionization. *Molecular & cellular proteomics*, 10(7), 2011.

[46] John B Fenn. The nobel prize in chemistry 2002. https://www.nobelprize.org/prizes/chemistry/2002/fenn/facts/.

[47] Takashi Nohmi and John B Fenn. Electrospray mass spectrometry of poly (ethylene glycols) with molecular weights up to five million. *Journal of the American Chemical Society*, 114(9):3241–3246, 1992.

[48] Geoffrey Ingram Taylor. Disintegration of water drops in an electric field. *Proceedings of the Royal Society of London. Series A. Mathematical and Physical Sciences*, 280(1382):383–397, 1964.

[49] James N Smith, Richard C Flagan, and JL Beauchamp. Droplet evaporation and discharge dynamics in electrospray ionization. *The Journal of Physical Chemistry A*, 106(42):9957–9967, 2002.

[50] Marjan Enayati, Ming-Wei Chang, Felix Bragman, Mohan Edirisinghe, and Eleanor Stride. Electrohydrodynamic preparation of particles, capsules and

bubbles for biomedical engineering applications. *Colloids and Surfaces A: Physicochemical and Engineering Aspects*, 382(1-3):154–164, 2011.

[51] Bhupendra G Prajapati and Manoj Patel. A technology update: Electro spray technology. *International Journal of Pharmaceutical Sciences Review and Research*, 1(1):12–13, 2010.

[52] Hyun-Ha Kim, Jong-Ho Kim, and Atsushi Ogata. Time-resolved high-speed camera observation of electrospray. *Journal of Aerosol Science*, 42(4):249–263, 2011.

[53] Christina G Drosou, Magdalini K Krokida, and Costas G Biliaderis. Encapsulation of bioactive compounds through electrospinning/electrospraying and spray drying: A comparative assessment of food-related applications. *Drying technology*, 35(2):139–162, 2017.

[54] Hassan Rezaeinia, Behrouz Ghorani, Bahareh Emadzadeh, and Nick Tucker. Electrohydrodynamic atomization of Balangu (Lallemantia royleana) seed gum for the fast-release of Mentha longifolia L. essential oil: Characterization of nano-capsules and modeling the kinetics of release. *Food Hydrocolloids*, 93:374–385, 2019.

[55] JV Iribarne and BA Thomson. On the evaporation of small ions from charged droplets. *The Journal of chemical physics*, 64(6):2287–2294, 1976.

[56] BA Thomson and JV Iribarne. Field induced ion evaporation from liquid surfaces at atmospheric pressure. *The Journal of Chemical Physics*, 71(11):4451–4463, 1979.

[57] Lars Konermann, Antony D Rodriguez, and Jiangjiang Liu. On the formation of highly charged gaseous ions from unfolded proteins by electrospray ionization. *Analytical chemistry*, 84(15):6798–6804, 2012.

[58] Simon J Gaskell. Electrospray: principles and practice. *Journal of mass spectrometry*, 32(7):677–688, 1997.

[59] Enzo Fornari, Clive J Roberts, Robert H Temperton, and James N O'Shea. Electrospray deposition in vacuum as method to create functionally active protein immobilization on polymeric substrates. *Journal of colloid and interface science*, 453:252–259, 2015.

[60] Janine C Swarbrick, J Ben Taylor, and James N O'Shea. Electrospray deposition in vacuum. *Applied surface science*, 252(15):5622–5626, 2006.

[61] Bon Ki Ku and Sang Soo Kim. Electrospray characteristics of highly viscous liquids. *Journal of Aerosol Science*, 33(10):1361–1378, 2002.

[62] Bon Ki Ku and Sang Soo Kim. Electrohydrodynamic spraying characteristics of glycerol solutions in vacuum. *Journal of electrostatics*, 57(2):109–128, 2003.

[63] Matthias Pauly, Mario Sroka, Julius Reiss, Gordon Rinke, Alyazan Albarghash, Ralf Vogelgesang, Hannes Hahne, Bernhard Kuster, Jörn Sesterhenn, Klaus Kern, et al. A hydrodynamically optimized nano-electrospray ionization source and vacuum interface. *Analyst*, 139(8):1856–1867, 2014.

[64] Hans Pauly. *Atom, Molecule, and Cluster Beams I: Basic Theory, Production and Detection of Thermal Energy Beams*, volume 1. Springer Science & Business Media, 2000.

[65] M Barr, KM O'Donnell, A Fahy, W Allison, and PC Dastoor. A desktop supersonic free-jet beam source for a scanning helium microscope (SHeM). *Measurement Science and Technology*, 23(10):105901, 2012.

[66] Christopher S Kley, Christian Dette, Gordon Rinke, Christopher E Patrick, Jan Čechal, Soon Jung Jung, Markus Baur, Michael Dürr, Stephan Rauschenbach, Feliciano Giustino, et al. Atomic-scale observation of multiconformational binding and energy level alignment of ruthenium-based photosensitizers on TiO_2 anatase. *Nano letters*, 14(2):563–569, 2014.

[67] Andrew J Britton, Matthew Weston, J Ben Taylor, Anna Rienzo, Louise C Mayor, and James N O'Shea. Charge transfer interactions of a Ru (II) dye complex and related ligand molecules adsorbed on Au (111). *The Journal of chemical physics*, 135(16):164702, 2011.

[68] Matthew Weston, Thomas J Reade, Andrew J Britton, Karsten Handrup, Neil R Champness, and James N O'Shea. A single centre water splitting dye complex adsorbed on rutile TiO_2 (110): Photoemission, x-ray absorption, and optical spectroscopy. *The Journal of chemical physics*, 135(11):114703, 2011.

[69] Matthew Weston, Karsten Handrup, Thomas J Reade, Neil R Champness, and James N O'Shea. Experimental observation of sub-femtosecond charge transfer in a model water splitting dye-sensitized solar cell. *The Journal of chemical physics*, 137(22):224706, 2012.

[70] Matthew Weston, Andrew J Britton, and James N O'Shea. Charge transfer dynamics of model charge transfer centers of a multicenter water splitting dye complex on rutile TiO_2 (110). *The Journal of chemical physics*, 134(5):054705, 2011.

[71] Matthew Weston, Thomas J Reade, Karsten Handrup, Neil R Champness, and James N O'Shea. Adsorption of dipyrrin-based dye complexes on a rutile TiO_2 (110) surface. *The Journal of Physical Chemistry C*, 116(34):18184–18192, 2012.

[72] Anna Rienzo, Louise C Mayor, Graziano Magnano, Christopher J Satterley, Evren Ataman, Joachim Schnadt, Karina Schulte, and James N O'Shea. X-ray absorption and photoemission spectroscopy of zinc protoporphyrin adsorbed on rutile TiO_2 (110) prepared by in situ electrospray deposition. *The Journal of chemical physics*, 132(8):084703, 2010.

[73] Usharani Nagarajan, Kohsaku Kawakami, Shaoling Zhang, Bangaru Chan-

drasekaran, and Balachandran Unni Nair. Fabrication of solid collagen nanoparticles using electrospray deposition. *Chemical and Pharmaceutical Bulletin*, 62(5):422–428, 2014.

[74] Christopher J Satterley, Luís MA Perdigão, Alex Saywell, Graziano Magnano, Anna Rienzo, Louise C Mayor, Vinod R Dhanak, Peter H Beton, and James N O'Shea. Electrospray deposition of fullerenes in ultra-high vacuum: in situ scanning tunneling microscopy and photoemission spectroscopy. *Nanotechnology*, 18(45):455304, 2007.

[75] James N O'Shea, John B Taylor, Janine C Swarbrick, Graziano Magnano, Louise C Mayor, and Karina Schulte. Electrospray deposition of carbon nanotubes in vacuum. *Nanotechnology*, 18(3):035707, 2007.

[76] Melanie C O'Sullivan, Johannes K Sprafke, Dmitry V Kondratuk, Corentin Rinfray, Timothy DW Claridge, Alex Saywell, Matthew O Blunt, James N O'Shea, Peter H Beton, Marc Malfois, et al. Vernier templating and synthesis of a 12-porphyrin nano-ring. *Nature*, 469(7328):72–75, 2011.

[77] Dmitry V Kondratuk, Luis MA Perdigao, Melanie C O'Sullivan, Simon Svatek, Gareth Smith, James N O'Shea, Peter H Beton, and Harry L Anderson. Two vernier-templated routes to a 24-porphyrin nanoring. *Angewandte Chemie*, 124(27):6800–6803, 2012.

[78] Maria B Wieland, Luis MA Perdigão, Dmitry V Kondratuk, James N O'Shea, Harry L Anderson, and Peter H Beton. Height dependent molecular trapping in stacked cyclic porphyrin nanorings. *Chemical Communications*, 50(55):7332–7335, 2014.

[79] Dmitry V Kondratuk, Johannes K Sprafke, Melanie C O'Sullivan, Luis MA Perdigao, Alex Saywell, Marc Malfois, James N O'Shea, Peter H Beton, Amber L Thompson, and Harry L Anderson. Vernier-Templated Synthesis,

Crystal Structure, and Supramolecular Chemistry of a 12-Porphyrin Nanoring. *Chemistry–A European Journal*, 20(40):12826–12834, 2014.

[80] Dmitry V Kondratuk, Luis Perdigão, Ayad Esmail, James N O'shea, Peter H Beton, and Harry L Anderson. Supramolecular nesting of cyclic polymers. *Nature Chemistry*, 7(4):317–322, 2015.

[81] Alex Saywell, Andrew J Britton, Nassiba Taleb, Maria del Carmen Giménez-López, Neil R Champness, Peter H Beton, and James N O'Shea. Single molecule magnets on a gold surface: in situ electrospray deposition, x-ray absorption and photoemission. *Nanotechnology*, 22(7):075704, 2011.

[82] Steffen Kahle, Zhitao Deng, Nikola Malinowski, Charlène Tonnoir, Alicia Forment-Aliaga, Nicha Thontasen, Gordon Rinke, Duy Le, Volodymyr Turkowski, Talat S Rahman, et al. The quantum magnetism of individual manganese-12-acetate molecular magnets anchored at surfaces. *Nano letters*, 12(1):518–521, 2012.

[83] Karsten Handrup, Victoria J Richards, Matthew Weston, Neil R Champness, and James N O'Shea. Single molecule magnets with protective ligand shells on gold and titanium dioxide surfaces: In situ electrospray deposition and x-ray absorption spectroscopy. *The Journal of Chemical Physics*, 139(15):154708, 2013.

[84] Philipp Erler, Peter Schmitt, Nicole Barth, Andreas Irmler, Samuel Bouvron, Thomas Huhn, Ulrich Groth, Fabian Pauly, Luca Gragnaniello, and Mikhail Fonin. Highly ordered surface self-assembly of Fe_4 single molecule magnets. *Nano letters*, 15(7):4546–4552, 2015.

[85] Fabian Paschke, Philipp Erler, Luca Gragnaniello, Jan Dreiser, and Mikhail Fonin. Electrospray Deposition and Magnetic Properties of Prototypical Molecular Magnets. *Quantum Materials Research*, 1, 2020.

[86] Stephan Rauschenbach, Frank L Stadler, Eugenio Lunedei, Nicola Malinowski, Sergej Koltsov, Giovanni Costantini, and Klaus Kern. Electrospray ion beam deposition of clusters and biomolecules. *small*, 2(4):540–547, 2006.

[87] Alex Saywell, Johannes K Sprafke, Louisa J Esdaile, Andrew J Britton, Anna Rienzo, Harry L Anderson, James N O'Shea, and Peter H Beton. Conformation and packing of porphyrin polymer chains deposited using electrospray on a gold surface. *Angewandte Chemie*, 122(48):9322–9325, 2010.

[88] Soohyung Park, Younjoo Lee, and Yeonjin Yi. Vacuum-integrated electrospray deposition for highly reliable polymer thin film. *Review of Scientific Instruments*, 83(10):105106, 2012.

[89] Julia Laskin, Peng Wang, and Omar Hadjar. Soft-landing of peptide ions onto self-assembled monolayer surfaces: an overview. *Physical chemistry chemical physics*, 10(8):1079–1090, 2008.

[90] Shalinee Kavadiya and Pratim Biswas. Electrospray deposition of biomolecules: Applications, challenges, and recommendations. *Journal of Aerosol Science*, 125:182–207, 2018.

[91] Zhitao Deng, Nicha Thontasen, Nikola Malinowski, Gordon Rinke, Ludger Harnau, Stephan Rauschenbach, and Klaus Kern. A close look at proteins: submolecular resolution of two-and three-dimensionally folded cytochrome c at surfaces. *Nano letters*, 12(5):2452–2458, 2012.

[92] Jean-Nicolas Longchamp, Stephan Rauschenbach, Sabine Abb, Conrad Escher, Tatiana Latychevskaia, Klaus Kern, and Hans-Werner Fink. Imaging proteins at the single-molecule level. *Proceedings of the National Academy of Sciences*, 114(7):1474–1479, 2017.

[93] Gordon Rinke, Stephan Rauschenbach, Ludger Harnau, Alyazan Albarghash, Matthias Pauly, and Klaus Kern. Active conformation control

of unfolded proteins by hyperthermal collision with a metal surface. *Nano letters*, 14(10):5609–5615, 2014.

[94] Nadine Hauptmann, Christian Hamann, Hao Tang, and Richard Berndt. Soft-landing electrospray deposition of the ruthenium dye N3 on Au (111). *The Journal of Physical Chemistry C*, 117(19):9734–9738, 2013.

[95] Girjesh Dubey, Roberto Urcuyo, Sabine Abb, Gordon Rinke, Marko Burghard, Stephan Rauschenbach, and Klaus Kern. Chemical modification of graphene via hyperthermal molecular reaction. *Journal of the American Chemical Society*, 136(39):13482–13485, 2014.

[96] Martin Knudsen. Die Gesetze der Molekularströmung und der inneren Reibungsströmung der Gase durch Röhren. *Annalen der Physik*, 333(1):75–130, 1909.

[97] Martin Knudsen. Experimentelle Bestimmung des Druckes gesättigter Quecksilberdämpfe bei 0 und höheren Temperaturen. *Annalen der Physik*, 334(6):179–193, 1909.

[98] Alex Saywell, Graziano Magnano, Christopher J Satterley, Luís MA Perdigão, Neil R Champness, Peter H Beton, and James N O'Shea. Electrospray deposition of C_{60} on a hydrogen-bonded supramolecular network. *The Journal of Physical Chemistry C*, 112(20):7706–7709, 2008.

[99] P Kratochvil, RFT Septo, and UW Suter. Glossary of basic terms in polymer science. *Pure and Applied Chemistry*, 68:2287–2311, 1996.

[100] Omar Hadjar, Peng Wang, Jean H Futrell, Yury Dessiaterik, Zihua Zhu, James P Cowin, Martin J Iedema, and Julia Laskin. Design and performance of an instrument for soft landing of biomolecular ions on surfaces. *Analytical chemistry*, 79(17):6566–6574, 2007.

[101] Chr Hamann, R Woltmann, I-Po Hong, N Hauptmann, S Karan, and R Berndt. Ultrahigh vacuum deposition of organic molecules by electrospray ionization. *Review of Scientific Instruments*, 82(3):033903, 2011.

[102] Alex Saywell, Graziano Magnano, Christopher J Satterley, Luís Perdigão, Andrew J Britton, Nassiba Taleb, María del Carmen Giménez-López, Neil R Champness, James N O'shea, and Peter H Beton. Self-assembled aggregates formed by single-molecule magnets on a gold surface. *Nature communications*, 1(1):1–8, 2010.

[103] Hanqiong Hu, Sofia Rangou, Myungwoong Kim, Padma Gopalan, Volkan Filiz, Apostolos Avgeropoulos, and Chinedum O Osuji. Continuous equilibrated growth of ordered block copolymer thin films by electrospray deposition. *ACS nano*, 7(4):2960–2970, 2013.

[104] Yunhua Gan, Zhengwei Jiang, Haige Li, Yanlai Luo, Xiaowen Chen, Yanling Shi, Yuying Yan, and Yunfei Yan. A comparative study on droplet characteristics and specific charge of ethanol in two small-scale electrospray systems. *Scientific Reports*, 9(1):1–12, 2019.

[105] Jingwei Xie and Chi-Hwa Wang. Electrospray in the dripping mode for cell microencapsulation. *Journal of colloid and interface science*, 312(2):247–255, 2007.

[106] Lee Chuin Chen, Satoru Tsutsui, Tsubasa Naito, Satoshi Ninomiya, and Kenzo Hiraoka. Electrospray ionization source with a rear extractor. *Journal of Mass Spectrometry*, 53(5):400–407, 2018.

[107] Ryan T Kelly, Aleksey V Tolmachev, Jason S Page, Keqi Tang, and Richard D Smith. The ion funnel: theory, implementations, and applications. *Mass spectrometry reviews*, 29(2):294–312, 2010.

[108] Maria Mustafa, Muhammad Naeem Awais, Ganeshthangaraj Pooniah, Kyung Hyun Choi, Jeongbeom Ko, and Yang Hui Doh. Electrospray de-

position of a graphene-oxide thin film, its characterization and investigation of its resistive switching performance. *Journal of the Korean Physical Society*, 61(3):470–475, 2012.

[109] Reinhard Juraschek, Thomas Dülcks, and Michael Karas. Nanoelectrospray—more than just a minimized-flow electrospray ionization source. *Journal of the American Society for Mass Spectrometry*, 10(4):300–308, 1999.

[110] Heinrich Hertz. Ueber einen Einfluss des ultravioletten Lichtes auf die electrische Entladung. *Annalen der Physik*, 267(8):983–1000, 1887.

[111] Albert Einstein. On a heuristic point of view concerning the production and transformation of light. *Annalen der Physik*, pages 1–18, 1905.

[112] Klaus Wandelt. *Encyclopedia of interfacial chemistry: surface science and electrochemistry*. Elsevier, 2018.

[113] SD Kevan. Design of a high-resolution angle-resolving electron energy analyzer. *Review of Scientific Instruments*, 54(11):1441–1445, 1983.

[114] M Dogan, M Ulu, GG Gennarakis, and TJM Zouros. Experimental energy resolution of a paracentric hemispherical deflector analyzer for different entry positions and bias. *Review of Scientific Instruments*, 84(4):043105, 2013.

[115] David Phillip Woodruff. *Modern techniques of surface science*. Cambridge university press, 2016.

[116] Peter Guttmann and Carla Bittencourt. Overview of nanoscale NEXAFS performed with soft X-ray microscopes. *Beilstein journal of nanotechnology*, 6(1):595–604, 2015.

[117] Yougui Liao. Practical Electron Microscopy and Database-An Online Book. *can be found under http://www. globalsino. com/EM/, nd*, 2018.

[118] Anne Thorne, Ulf Litzén, and Sveneric Johansson. *Spectrophysics: principles and applications*. Springer Science & Business Media, 1999.

[119] Peter W Atkins and Ronald S Friedman. *Molecular quantum mechanics*. Oxford university press, 2011.

[120] Othmar Marti, B Drake, and PK Hansma. Atomic force microscopy of liquid-covered surfaces: Atomic resolution images. *Applied Physics Letters*, 51(7):484–486, 1987.

[121] Gerd Binnig, Calvin F Quate, and Ch Gerber. Atomic force microscope. *Physical review letters*, 56(9):930, 1986.

[122] Othmar Marti. AFM instrumentation and tips. *Handbook of micro/nanotribology*, pages 81–144, 1999.

[123] David A Dahl. SIMION for the personal computer in reflection. *International Journal of Mass Spectrometry*, 200(1-3):3–25, 2000.

[124] David Manura. Chapter 2. SIMION Basics (SIMION® 8.0 User Manual). `https://simion.com/manual/chap2.html`, 2006.

[125] Stephan Rauschenbach, Ralf Vogelgesang, N Malinowski, Jurgen W Gerlach, Mohamed Benyoucef, Giovanni Costantini, Zhitao Deng, Nicha Thontasen, and Klaus Kern. Electrospray ion beam deposition: soft-landing and fragmentation of functional molecules at solid surfaces. *ACS nano*, 3(10):2901–2910, 2009.

[126] Sarah R Mabbett, Lloyd W Zilch, Joshua T Maze, John W Smith, and Martin F Jarrold. Pulsed acceleration charge detection mass spectrometry: application to weighing electrosprayed droplets. *Analytical chemistry*, 79(22):8431–8439, 2007.

[127] Stephen D Fuerstenau and W Henry Benner. Molecular weight determination of megadalton DNA electrospray ions using charge detection time-of-flight mass spectrometry. *Rapid Communications in Mass Spectrometry*, 9(15):1528–1538, 1995.

[128] John W Smith, Elizabeth E Siegel, Joshua T Maze, and Martin F Jarrold. Image charge detection mass spectrometry: pushing the envelope with sensitivity and accuracy. *Analytical Chemistry*, 83(3):950–956, 2011.

[129] Joshua T Maze, Thaddeus C Jones, and Martin F Jarrold. Negative droplets from positive electrospray. *The Journal of Physical Chemistry A*, 110(46):12607–12612, 2006.

[130] Philip E Miller and M Bonner Denton. The quadrupole mass filter: basic operating concepts. *Journal of chemical education*, 63(7):617, 1986.

[131] Daniel A Warr. *Investigating the Structure and Composition of Macromolecules Using Electrospray Deposition Coupled with Scanning Tunnelling Microscopy.* PhD thesis, University of Warwick, 2018.

[132] Michal Holčapek, Kateřina Volná, and Dana Vaněrková. Effects of functional groups on the fragmentation of dyes in electrospray and atmospheric pressure chemical ionization mass spectra. *Dyes and Pigments*, 75(1):156–165, 2007.

[133] Timothy J Bennett, David A Quillen, and Rolly Coronica. Fundamentals of fluorescein angiography. *Curr Concepts Ophthalmology*, 9(3):43–9, 2001.

[134] Roman S Skazov, Yury S Nekrasov, Sergey A Kuklin, and Alexander A Simenel. Influence of experimental conditions on electrospray ionization mass spectrometry of ferrocenylalkylazoles. *European Journal of Mass Spectrometry*, 12(2):137–142, 2006.

[135] Yu S Nekrasov, Yu A Borisov, RS Skazov, AN Rodionov, AA Simenel, and Yu A Belousov. On the mechanism of ferrocene oxidation under the conditions of electrospray ionization. *Russian Chemical Bulletin*, 58(7):1521–1523, 2009.

[136] Yu S Nekrasov, Yu A Borisov, RS Skazov, AA Simenel, LV Snegur, Yu A Belousov, and AN Rodionov. The reactivity of ferrocenylalkyl azoles under the

conditions of electrospray ionization. *Journal of Organometallic Chemistry*, 694(12):1807–1812, 2009.

[137] Yu S Nekrasov, NS Ikonnikov, Yu A Belousov, and SS Kiselev. Comparative studies of the behavior of neutral and ionic ferrocene derivatives under different conditions of electrospray ionization. *Journal of Analytical Chemistry*, 66(13):1291–1297, 2011.

[138] J Bariyanga. Electrospray mass spectrometry analysis of ferocenylketimines and their platinum (II) complexes. *Journal of Molecular Structure*, 570(1-3):109–118, 2001.

[139] Amandeep Singh, Isha Lumb, Vishu Mehra, and Vipan Kumar. Ferrocene-appended pharmacophores: An exciting approach for modulating the biological potential of organic scaffolds. *Dalton transactions*, 48(9):2840–2860, 2019.

[140] Sijongesonke Peter and Blessing Atim Aderibigbe. Ferrocene-based compounds with antimalaria/anticancer activity. *Molecules*, 24(19):3604, 2019.

[141] Andrew R Barron. *Physical methods in chemistry and nano science*. Rice University, 2015.

[142] Francesco Buonocore and Andrea di Matteo. New insights into oxidation properties and band structure of fluorescein dyes from ab initio calculations. *Theoretical Chemistry Accounts*, 131(2):1–9, 2012.

[143] Marvin Rausch, Martin Vogel, and Harold Rosenberg. Ferrocene: A novel organometallic compound. *Journal of Chemical Education*, 34(6):268, 1957.

[144] Miklos Szilagyi. *Electron and ion optics*. Springer Science & Business Media, 2012.

[145] Lars Konermann, Robert G McAllister, and Haidy Metwally. Molecular dynamics simulations of the electrospray process: formation of NaCl clusters

via the charged residue mechanism. *The Journal of Physical Chemistry B*, 118(41):12025–12033, 2014.

[146] Duxi Zhang and R Graham Cooks. Doubly charged cluster ions $[(\mathrm{NaCl})_m(\mathrm{Na})_2]^{2+}$: magic numbers, dissociation, and structure. *International Journal of Mass Spectrometry*, 195:667–684, 2000.

[147] Chunyan Hao, Raymond E March, Timothy R Croley, Jeffrey C Smith, and Steven P Rafferty. Electrospray ionization tandem mass spectrometric study of salt cluster ions. Part 1—Investigations of alkali metal chloride and sodium salt cluster ions. *Journal of mass spectrometry*, 36(1):79–96, 2001.

[148] Anthony P Taylor and Luis F Velásquez-García. Electrospray-printed nanostructured graphene oxide gas sensors. *Nanotechnology*, 26(50):505301, 2015.

[149] Aïda Varea, Oriol Monereo, Elena Xuriguera, J Daniel Prades, and Albert Cirera. Electrospray as a suitable technique for manufacturing carbon-based devices. *Journal of Physics D: Applied Physics*, 50(31):315301, 2017.

[150] Huaichao Tang, Cheng Yang, Ziyin Lin, Quanhong Yang, Feiyu Kang, and Ching Ping Wong. Electrospray-deposition of graphene electrodes: a simple technique to build high-performance supercapacitors. *Nanoscale*, 7(20):9133–9139, 2015.

[151] Heyong He, Jacek Klinowski, Michael Forster, and Anton Lerf. A new structural model for graphite oxide. *Chemical physics letters*, 287(1-2):53–56, 1998.

[152] Michael Grätzel. Recent advances in sensitized mesoscopic solar cells. *Accounts of chemical research*, 42(11):1788–1798, 2009.

[153] Anders Hagfeldt and Michael Grätzel. Light-induced redox reactions in nanocrystalline systems. *Chemical reviews*, 95(1):49–68, 1995.

[154] M Chandrasekharam, B Chiranjeevi, KSV Gupta, Surya Prakash Singh, A Islam, L Han, and M Lakshmi Kantam. Simple Metal-Free Organic D-π-A Dyes with Alkoxy-or Fluorine Substitutions: Application in Dye Sensitized Solar Cells. *Journal of nanoscience and nanotechnology*, 12(6):4489–4494, 2012.

[155] Amaresh Mishra, Markus KR Fischer, and Peter Bäuerle. Metal-free organic dyes for dye-sensitized solar cells: From structure: Property relationships to design rules. *Angewandte Chemie International Edition*, 48(14):2474–2499, 2009.

[156] Karl Martin Karlsson, Xiao Jiang, Susanna K Eriksson, Erik Gabrielsson, Håkan Rensmo, Anders Hagfeldt, and Licheng Sun. Phenoxazine dyes for dye-sensitized solar cells: relationship between molecular structure and electron lifetime. *Chemistry–A European Journal*, 17(23):6415–6424, 2011.

[157] Daniel P Hagberg, Jun-Ho Yum, HyoJoong Lee, Filippo De Angelis, Tannia Marinado, Karl Martin Karlsson, Robin Humphry-Baker, Licheng Sun, Anders Hagfeldt, Michael Grätzel, et al. Molecular engineering of organic sensitizers for dye-sensitized solar cell applications. *Journal of the American Chemical Society*, 130(19):6259–6266, 2008.

[158] Kohjiro Hara, Tadatake Sato, Ryuzi Katoh, Akihiro Furube, Yasuyo Ohga, Akira Shinpo, Sadaharu Suga, Kazuhiro Sayama, Hideki Sugihara, and Hironori Arakawa. Molecular design of coumarin dyes for efficient dye-sensitized solar cells. *The Journal of Physical Chemistry B*, 107(2):597–606, 2003.

[159] Tamotsu Horiuchi, Hidetoshi Miura, Kouichi Sumioka, and Satoshi Uchida. High efficiency of dye-sensitized solar cells based on metal-free indoline dyes. *Journal of the American Chemical Society*, 126(39):12218–12219, 2004.

[160] Sanghoon Kim, Jae Kwan Lee, Sang Ook Kang, Jaejung Ko, J-H Yum,

Simona Fantacci, Filippo De Angelis, D Di Censo, Md K Nazeeruddin, and Michael Grätzel. Molecular engineering of organic sensitizers for solar cell applications. *Journal of the American Chemical Society*, 128(51):16701–16707, 2006.

[161] Daniel P Hagberg, Tomas Edvinsson, Tannia Marinado, Gerrit Boschloo, Anders Hagfeldt, and Licheng Sun. A novel organic chromophore for dye-sensitized nanostructured solar cells. *Chemical Communications*, (21):2245–2247, 2006.

[162] Erik MJ Johansson, Tomas Edvinsson, Michael Odelius, Daniel P Hagberg, Licheng Sun, Anders Hagfeldt, Hans Siegbahn, and Håkan Rensmo. Electronic and molecular surface structure of a polyene- diphenylaniline dye adsorbed from solution onto nanoporous TiO_2. *The Journal of Physical Chemistry C*, 111(24):8580–8586, 2007.

[163] J Ben Taylor, Louise C Mayor, Janine C Swarbrick, James N O'Shea, and Joachim Schnadt. Charge-transfer dynamics at model metal-organic solar cell surfaces. *Journal of physical chemistry. C*, 111(44):16646–16655, 2007.

[164] Amy L Linsebigler, Guangquan Lu, and John T Yates Jr. Photocatalysis on TiO_2 surfaces: principles, mechanisms, and selected results. *Chemical reviews*, 95(3):735–758, 1995.

[165] Ulrike Diebold, Nancy Ruzycki, Gregory S Herman, and Annabella Selloni. One step towards bridging the materials gap: surface studies of TiO_2 anatase. *Catalysis today*, 85(2-4):93–100, 2003.

[166] Yunbin He, Olga Dulub, Hongzhi Cheng, Annabella Selloni, and Ulrike Diebold. Evidence for the predominance of subsurface defects on reduced anatase TiO_2 (101). *Physical Review Letters*, 102(10):106105, 2009.

[167] Hongzhi Cheng and Annabella Selloni. Surface and subsurface oxygen va-

cancies in anatase TiO_2 and differences with rutile. *Physical Review B*, 79(9):092101, 2009.

[168] Talha Ijaz, Ben Yang, Ruipu Wang, Jiazhe Zhu, Aftab Farrukh, Gong Chen, Grégory Franc, Yang Zhang, André Gourdon, and Zhenchao Dong. Self-decoupled tetrapodal perylene molecules for luminescence studies of isolated emitters on Au (111). *Applied Physics Letters*, 115(17):173101, 2019.

[169] Dave A Shirley. High-resolution X-ray photoemission spectrum of the valence bands of gold. *Physical Review B*, 5(12):4709, 1972.

[170] John F Kielkopf. New approximation to the Voigt function with applications to spectral-line profile analysis. *JOSA*, 63(8):987–995, 1973.

[171] Lei Zhang and Jacqueline M Cole. Anchoring groups for dye-sensitized solar cells. *ACS applied materials & interfaces*, 7(6):3427–3455, 2015.

[172] Joachim Schnadt, J Schiessling, JN O'shea, SM Gray, L Patthey, MK-J Johansson, M Shi, J Krempaskỳ, J Åhlund, PG Karlsson, et al. Structural study of adsorption of isonicotinic acid and related molecules on rutile TiO_2 (110) I: XAS and STM. *Surface science*, 540(1):39–54, 2003.

[173] JN O'Shea, Yi Luo, J Schnadt, L Patthey, H Hillesheimer, J Krempasky, D Nordlund, M Nagasono, PA Brühwiler, and N Mårtensson. Hydrogen-bond induced surface core-level shift in pyridine carboxylic acids. *Surface science*, 486(3):157–166, 2001.

[174] James N O'Shea, Joachim Schnadt, Paul A Brühwiler, Hendrik Hillesheimer, Nils Mårtensson, Luc Patthey, Juraj Krempasky, ChuanKui Wang, Yi Luo, and Hans Ågren. Hydrogen-bond induced surface core-level shift in isonicotinic acid. *The Journal of Physical Chemistry B*, 105(10):1917–1920, 2001.

[175] James N O'Shea, Janine C Swarbrick, Katharina Nilson, Carla Puglia, Barbara Brena, Yi Luo, and Vin R Dhanak. Molecular ordering in isonicotinic

acid on rutile TiO_2 (110) investigated with valence band photoemission. *The Journal of chemical physics*, 121(20):10203–10208, 2004.

[176] Joachim Schnadt, JN O'Shea, L Patthey, J Krempaskỳ, Nils Mårtensson, and PA Brühwiler. Alignment of valence photoemission, x-ray absorption, and substrate density of states for an adsorbate on a semiconductor surface. *Physical Review B*, 67(23):235420, 2003.

[177] James N O'Shea, J Ben Taylor, Louise C Mayor, Janine C Swarbrick, and Joachim Schnadt. Molecular damage in bi-isonicotinic acid adsorbed on rutile TiO_2 (110). *Surface science*, 602(9):1693–1698, 2008.

[178] John C Fuggle and Nils Mårtensson. Core-level binding energies in metals. *Journal of Electron Spectroscopy and Related Phenomena*, 21(3):275–281, 1980.

[179] J Kirz, DT Attwood, BL Henke, MR Howells, KD Kennedy, K-J Kim, JB Kortright, RCC Perera, P Pianetta, JC Riordan, et al. Center for X-ray Optics, X-ray Data Booklet. 1986.

[180] John R Swierk and Thomas E Mallouk. Design and development of photoanodes for water-splitting dye-sensitized photoelectrochemical cells. *Chemical Society Reviews*, 42(6):2357–2387, 2013.

[181] Kenneth Hanson, M Kyle Brennaman, Hanlin Luo, Christopher RK Glasson, Javier J Concepcion, Wenjing Song, and Thomas J Meyer. Photostability of phosphonate-derivatized, RuII polypyridyl complexes on metal oxide surfaces. *ACS applied materials & interfaces*, 4(3):1462–1469, 2012.

[182] Pengtao Xu, Nicholas S McCool, and Thomas E Mallouk. Water splitting dye-sensitized solar cells. *Nano Today*, 14:42–58, 2017.

[183] Isabelle Gillaizeau-Gauthier, Fabrice Odobel, Monica Alebbi, Roberto Argazzi, Emiliana Costa, Carlo Alberto Bignozzi, Ping Qu, and Gerald J

Meyer. Phosphonate-based bipyridine dyes for stable photovoltaic devices. *Inorganic Chemistry*, 40(23):6073–6079, 2001.

[184] Yaron Paz. Self-assembled monolayers and titanium dioxide: From surface patterning to potential applications. *Beilstein journal of nanotechnology*, 2(1):845–861, 2011.

[185] Maria Hahlin, Michael Odelius, Martin Magnuson, Erik MJ Johansson, Stefan Plogmaker, Daniel P Hagberg, Licheng Sun, Hans Siegbahn, and Håkan Rensmo. Mapping the frontier electronic structures of triphenylamine based organic dyes at TiO_2 interfaces. *Physical Chemistry Chemical Physics*, 13(8):3534–3546, 2011.

[186] Shun Yu, Sareh Ahmadi, Marcelo Zuleta, Haining Tian, Karina Schulte, Annette Pietzsch, Franz Hennies, Jonas Weissenrieder, Xichuan Yang, and Mats Göthelid. Adsorption geometry, molecular interaction, and charge transfer of triphenylamine-based dye on rutile TiO_2 (110). *The Journal of chemical physics*, 133(22):224704, 2010.

[187] WJ Gammon, O Kraft, AC Reilly, and BC Holloway. Experimental comparison of N (1s) X-ray photoelectron spectroscopy binding energies of hard and elastic amorphous carbon nitride films with reference organic compounds. *Carbon*, 41(10):1917–1923, 2003.

[188] Tingming Jiang, Walter Malone, Yongfeng Tong, Diana Dragoe, Azzedine Bendounan, Abdelkader Kara, and Vladimir A Esaulov. Thiophene derivatives on gold and molecular dissociation processes. *The Journal of Physical Chemistry C*, 121(50):27923–27935, 2017.

[189] Shu Chen, Lin Yang, Jing Zhang, Yi Yuan, Xiandui Dong, and Peng Wang. Excited-state and charge Carrier dynamics in a high-photovoltage and thermostable dye-sensitized solar cell. *ACS Photonics*, 4(1):165–173, 2017.

[190] Erin L Ratcliff, Ronald C Bakus Ii, Gregory C Welch, Tom S Van Der Poll, Andres Garcia, Sarah R Cowan, Bradley A MacLeod, David S Ginley, Guillermo C Bazan, and Dana C Olson. Formation of interfacial traps upon surface protonation in small molecule solution processed bulk heterojunctions probed by photoelectron spectroscopy. *Journal of Materials Chemistry C*, 1(39):6223–6234, 2013.

[191] Pralok K Samanta and Niall J English. Opto-electronic properties of stable blue photosensitisers on a TiO_2 anatase-101 surface for efficient dye-sensitised solar cells. *Chemical Physics Letters*, 731:136624, 2019.

[192] Yameng Ren, Danyang Sun, Yiming Cao, Hoi Nok Tsao, Yi Yuan, Shaik M Zakeeruddin, Peng Wang, and Michael Grätzel. A stable blue photosensitizer for color palette of dye-sensitized solar cells reaching 12.6% efficiency. *Journal of the American Chemical Society*, 140(7):2405–2408, 2018.